Temperature Induced Deformations in Match-Cast Segments and their Effects on Precast Segmental Bridges

Vom Promotionsausschuss der
Technischen Universität Hamburg-Harburg
zur Erlangung des akademischen Grades
Doktor-Ingenieur
genehmigte Dissertation

von

M.Sc Ra'ed Abendeh

aus Jordanien

2006

1. Gutachter :   Univ.-Prof. Dr.-Ing. Günter Rombach

2. Gutachter :   Univ.-Prof. Dr.-Ing Wolfgang Maier

Prüfungsvorsitzender   Univ.-Prof. Dr.-Ing Jürgen Grabe

Tag der mündlichen Prüfung :   30. Oktober 2006

Acknowledgment

Table of contents

Notations

Latin capital notations

A Total cross-sectional area of a concrete section

A_P Area of a prestressing tendon or tendons

D Diffusivity

E Secant modulus of elasticity

E_b black-body emissive power

E_c Modulus of elasticity of normal weight concrete

E_s Modulus of elasticity of reinforcement or prestressing steel

I Second moment of inertia of a section

L Length of a segment

M_{eq} Equivalent moment

P Prestress force

Q_{ik} Characteristic axle load, of a design truck (LM1)

Q Internal heat source (heat generated per unit time per unit volume)

T Temperature of the solid surface; at the solid/fluid interface

T_∞ Temperature of the fluid – ambient temperature

Latin small notations

a_c Coefficient of thermal diffusivity of concrete

b Width of the segment

b_i Real flange width

b_w Width of a web

c Specific heat capacity

f_c Compressive strength of concrete

f_{ck} Characteristic compressive cylinder strength of concrete at 28 days

f_{pk} Characteristic tensile strength of prestressing steel

f_{yk} Characteristic yield strength of reinforcement

h thickness of formwork

k Convection coefficient of formwork

l	Length; span
q	Heat conducted (heat flux)
q_h	Solid-fluid surface-convection heat flux
q_t	Heat of hydration of concrete
q_{ik}	Uniformly distributed live load
t	Time
t_0	Time of loading
u	velocity of a fluid (air)
w	Width of a segment, wind speed
x,y,z	Cartesian coordinates

Greek notations

Δ	Maximum deflection of segments (gap)
ΔU	Change in stored energy
$\alpha(t)$	Degree of hydration
α_T	Thermal expansion coefficient
α_k	Heat transfer or convection coefficient
ε_c	Compressive strain in the concrete
$\varepsilon_{c,s}$	Mean shrinkage strain of concrete
$\varepsilon_{c,c}$	Mean creep strain of concrete
ε_u	strain of reinforcement or prestressing steel at maximum load
ϕ	Curvature of the segment
$\varphi(t,t_\circ)$	Ratio of creep strain to the instantaneous strain (creep coefficient) between time t and t_0
λ	Thermal conductivity coefficient
λ_f	Thermal conductivity coefficient of a particular formwork material
μ	Coefficient of friction
ν	Poisson's ratio
ρ	Oven-dry density of concrete in kg/m^3

σ_x Compressive stress in x direction

σ_y Compressive stress in y direction

σ_z Compressive stress in z direction

1   Introduction and scopes

Segmental construction in the field of prestressed hollow box girders concrete bridges can be considered one of the most interesting and important achievements in bridge engineering in the last decades. The usage of precast elements instead of in-situ concrete leads to an economical, durable and safe design and a fast and versatile construction. That is the reason why precast segmental hollow box girder bridges have become the preferred constructions method for many elevated highway projects in the last years. In urban areas the very fast erection without interrupting the traffic underneath is an important advantage for these types of bridges.

In contrast to classical monolithic constructions, a segmental bridge consists of small pieces or slices called segments, which maybe precast, cast in place in their final position in the structure or a combination of precast and cast in place. In other words, it is opposite to the precast girder concept where the bridge is cut longitudinally. In the precast segmental method, the bridge is cut transversally, each slice being a segment. Thereafter the segments are stressed together by external or internal tendons. The erection process of a segmental bridge can be seen in Figure 1.1.

Figure 1.1 Segmental bridge construction in Bangkok [Br5]

Segmental construction is not a new technique. In the years 1944 - 1946 the first segmental bridges with about 55 *m* span were built over the Marne River in France by Eugene

Freyssinet [Lal]. The main breakthrough came with the usage of hollow box girder segments. More than 300 such structures were constructed between 1950 and 1965 in Europe. Thereafter the concept has spread throughout the world. Nowadays the main segmental bridge construction is carried out in Southeast Asia, where there is a great need to improve the road systems.

Match-cast method especially the short line match casting is most of the time used as a segment production technique for post-tensioned hollow box girder segmental bridges to guarantee a perfect fitting of adjacent segments. When a new segment is to be cast against an old one, a problem can appear. In the quite high heat of concrete hydration the newly concreted segment (new cast segment) causes a thermal gradient in the hardened preceding segment (match cast segment), which acts like a mould to form the contact joint. This gradient leading to spatial deformation causes a bowing of the match cast segment (or banana shape) before the fresh new cast concrete has reached its initial set, which becomes a permanent curvature in the new segment. The resulting segments have one straight and one curved side, whereas the old segments keep bowing in time and return to their original shape after cooling down to constant temperature. The resulting gap between two adjacent elements may significantly reduce the durability and the load bearing capacity of the structure. Few experimental data has been published about this phenomenon and a systematic study is still missing.

A thermo-mechanical finite element model has been developed to simulate the behaviour of segments during match-casting. The temperature distribution within a body and the subsequent thermal stresses and deformations under any stable or variable boundary condition with respect to time can be analyzed. Included in this model is the evolution of temperature produced from the heat of hydration in the new cast segment, the non-linear time dependant behaviour of concrete and the temperature flux between the new and old segment. The method of equivalent moment is used to calculate the deformations due to the thermal gradients, as well as in-situ test results from the San Antonio (*Y* project) and the Bang Na (BBBE) segmental bridges were used to verify the complex numerical model. A good agreement has been obtained. The influence of different environmental conditions, the shape of the segment, and use of insulating materials on the bowing effect have been studied.

At the erection site, the bow shaped segments have particular problems during the epoxy and temporary post-tensioning operations. One may have problems in closing the joints and the bowing deformation reduces the required compressive stresses for the epoxy resin. Moreover, this phenomenon not only poses problems in construction but it also raises questions about stress distribution across joints and it could lead to areas of reduced compression in the segment's centreline, meanwhile stress peaks occur at the tips of the segment's cantilever slab. In some cases, it could be detrimental by causing cracking in the segments. It can be said that bowing effect could cause a reduction in the load bearing capacity and influence the serviceability of segmental bridges. Reported scientific research is quite limited and none, up to date, was conducted to investigate the impact of using match-cast segment on the behaviour of precast segmental bridges.

A numerical simulation of two typical real segmental bridges, namely the Second Stage Expressway System (SES) and Bang Na segmental bridges, consisting of perfectly fitted or bow shape segments with dry joints will be presented in this thesis. The results show that compressive stresses and the load bearing capacity of the structure as well as the durability and deflections are highly influenced by the bowing effect.

This thesis is organized as follows: The state of the art is presented in chapter 2. There the construction and design of segmental bridges, the previous studies including the main problems appearing during the manufacturing of the precast segments will be presented. Furthermore the investigations and studies of heat development and transfer in the early age of concrete, which contain the previous concrete thermal measurements and models conducted in order to analyze the temperature distribution within a body will be discussed. Chapter three presents the approaches and measurements made to conduct the bowing and to estimate the temperatures and deformations during the match-cast process of San Antonio and Bang Na segmental bridges. Numerical simulations and modelling of match-cast segments and the transient thermo-mechanical process will be introduced to conduct the unavoidable complicated behaviour of match-cast segments. In order to verify the thermo-mechanical model, comparisons of the model will be shown with measurements taken in San Antonio and Bang Na bridges. The numerical models will also be compared to a mathematical approach based on the equivalent moment formula.

In chapter four the behaviour of a real segmental span with perfect and imperfect segments is studied. First a numerical simulation of a real segmental bridge (Second Stage Expressway System in Bangkok) will be introduced and verified using the measurements taken from the SES segmental bridge. The mechanical finite element model will be extended to simulate segments having gaps produced from the match-cast method. Their influences on the serviceability and the bearing capacity of the whole structure under the short-term and the long-term loading including creep and shrinkage effects of concrete will be predicted. The time dependant behaviour of the structure could be detrimental or helpful in redistributing the compressive stresses and closing the gaps. The study of the whole structure during different periods of time could give answers about the efficiency as well as prestressing losses of the whole structure. In addition to the before mentioned investigations the Bang Na segmental bridge consisting of very slender elements will be modelled in order to show the obvious influences of large gaps on the structure.

Chapter four finally will include the recommendations and construction approaches in order to predict and to minimize the risks of impact bow shaped segments in the structure. The conclusions are presented in chapter five.

The objectives of this study can be summarized as follows:

1. **Numerical simulation of the match cast process to study the behaviour of match-cast segments during the evolution of temperature produced from the heat of hydration. Characterize relevant measures to reduce the bowing effect.**

2. **To study the impact of using imperfect match-cast segments with gaps concerning the serviceability and load bearing capacity of segmental bridges.**

3. **Investigate the behaviour of segmental bridges under long-term loads including time dependant behaviour of concrete.**

2   Present state of knowledge

This chapter gives a brief description of precast segmental bridge technology and the different production methods of segments. The main problems during the manufacturing of the precast segments will be presented. The various investigations and studies of heat development and heat transfer in the early age of concrete will be discussed, which will include the previous concrete thermal measurements and numerical models conducted in order to analyze the temperature distribution within a body.

2.1   Segmental bridges – Segment production

Segmental bridges with hollow box girder are considered relatively a new development in concrete construction. Hence, most of the segmental field research related to design and improvement of this new technique has been investigated during the past 30 years. The research investigated by Breen [Br1- Br4], Podolny and Muller [Po1, Po2] is considered to be the basics of construction and design of segmental bridges in USA. In Germany, many investigations were conducted by Kupfer [Ku1, Ku2], Kordina [Kor], Fischer [Fi1, Fi2], Eibl [Ei1], Rombach [Ro1- Ro4], Specker [Sp2], and Chaffo [Cha] in construction and design of segmental bridges. The 'Deutsche Beton-Verein' published recommendations for the design of hollow box girder segmental bridges in 1999 [Deu].

Segmental construction can be defined as a method of construction in which the primary load-carrying members are composed of individual precast or cast-in-place segments external and/or internal post-tensioned longitudinally and/or transversely tendons together to form simple or continuous-span bridges. In this research work precast segmental bridges will be treated only. The prefabrication can shorten the construction period without a disruption in traffic. In addition it can be more economical by reducing the mild reinforcement as well as higher quality of concrete can be achieved.

In spite of their disadvantages, which can be represented in bad corrosion protection of steel in the joints and their need of thicker webs, the internal tendons were being little applied in segmental construction. In 1992, the Department of Transport in the UK issued a memorandum pointing out the problem of corrosion in post-tensioned prestressed tendons and banned the classical option of internal tendons. The use of external tendons can reduce the period and cost by simplifying the concreting procedures and constructability, besides

the tendons can be more readily inspected and replaced. Figure 2.1 shows the external tendons layout of a typical segmental span of the Second Stage Expressway System (SES) in Bangkok. Superstructures of segmental construction are generally of single or multiple box sections or a combination thereof, but precast beam-type sections may also be used.
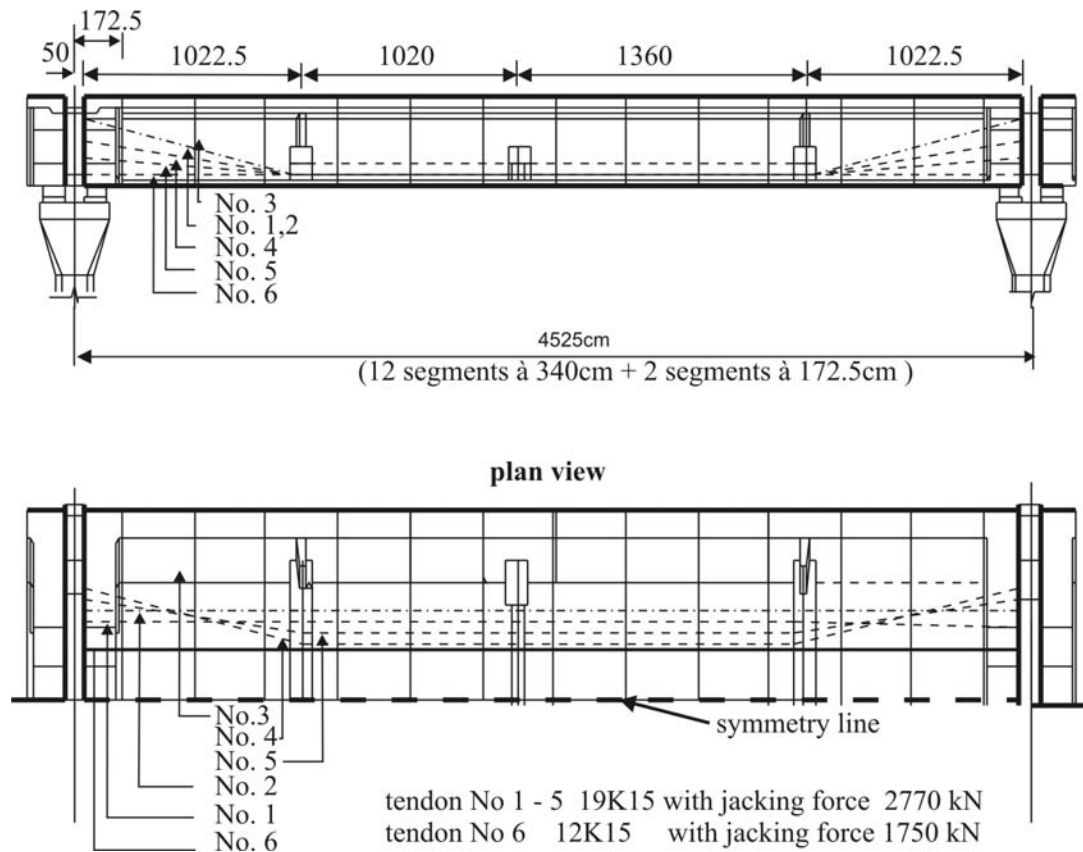

Figure 2.1 External prestressed segmental bridge (SES Bangkok) [Ro1]

Three different segments used in segmental bridges, as a result of using external post tensioning, are called pier, deviator and standard segments, and they can be seen in Figure 2.2.

- Pier segment: Is used to stiffen the webs by using a thick diaphragm to diffuse the support forces and for the anchorage of the external tendons process. The external tendons are not anchored in the webs; therefore the eccentric forces are considerable.

- Standard segment: In this element, the dead load could be minimized as a result of thinner webs of 35 *cm* or less relied on the shear forces. Neither tendons are deviated nor anchorages are carried out herein.

- Deviator segment: The layout of the external tendons needs some regions where the tendons must be deviated; this leads to high vertical loads, which have to be diffused to the webs.

The shear keys are designed to carry the shear loads at the joints, where also the friction between the joint surfaces takes part in resisting shear forces.

The dimensions and weight of the segments can depend on the possibility of transportation available since normally the precast plant does not lie in the project site [Br6, Rog].

In precast segmental construction, segments are generally manufactured in a plant due to the need of big storage area or near the erection site, and then transported to their final position for assembly. Initially, joints between segments were of a conventional type: either concrete poured wet joints or dry mortar packed joints (Fig. 2.5). Modern segmental construction calls for the match-casting technique, whereby the segments are precast against each other, preferably in the same relative order they will have in the final structure. The joints are either left dry in areas where climate permits, or made of a very thin film of epoxy resin or mineral complex, which does not change the match-casting properties. There is no need for any waiting period for a joint cure, and final assembly of segments by prestressing may proceed as fast as practical.
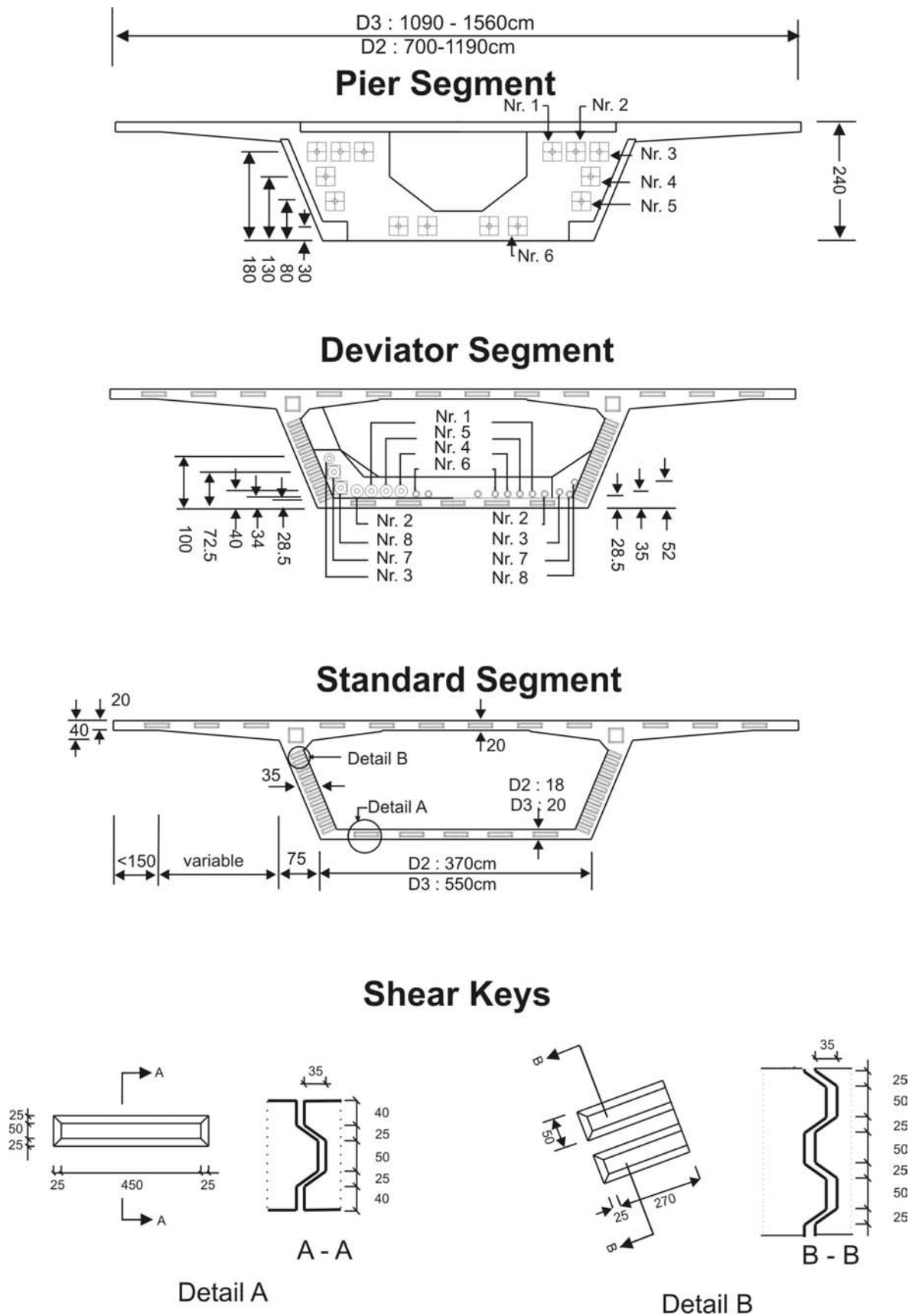
Figure 2.2 Cross-sections of segments and shear keys (SES) [Ta1]

The various methods used until now for precasting segments fall into two basic categories:

1. Long-line casting, where all segments of a span are manufactured on a fixed bed with the formwork moving along the bed for the successive casting operations as can be seen in Figure 2.3. In this technique the segments are cast in their correct supposed position on a long bed, which represents the profile of the real structure at one time. The pier segment is cast first between the fixed bulkhead and the removable formwork, then the next segments. As segment casting continues, the first cast segments can be removed for storage. This method was used for constant-depth box girders; thereafter it was extended to the case of variable-depth decks. The advantages of this technique can be seen in its simplicity of set out and control deck geometry after removing of the form as well as it is not necessary to move the segments directly to storage. The relatively big manufacturing space, all the equipment for casting and curing must be mobile and a firm foundation that should resist the casing bed are considered to be disadvantages in the long-line method.
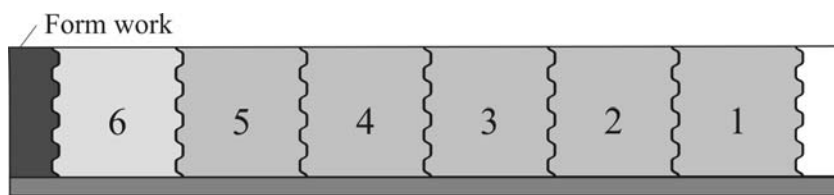

Figure 2.3 Long-line match-cast method

2. Short-line casting, where segments are manufactured in a step-by-step procedure with the forms maintained at a stationary position. Figure 2.4 shows the standard old match-cast segment of the SES Bangkok bridge against the formwork prepared to cast the new match-cast segment.

In the short-line casting method all segments are required to be cast at the same site using stationary forms, next to the previously cast segment in order to get a homogeneous perfect fitting match-cast joint. The previously cast segment is removed for storage after casting and initial curing, and the freshly cast segment is placed into its position; the cycle of casting is then repeated. The larger the segments get, the more the tendency is going towards the short-line method. The small space where all equipment remains at a stationary site is a basic advantage of the short-line method, besides the horizontal and vertical curves as well as the superelevation are obtained more readily than in the long-line casing method that

requires change in soffit configuration. The bowing effect and the accuracy of adjustment of the match-cast segments represent the major potential disadvantages of this technique. The short-line match-cast method will be discussed in detail in the next section.
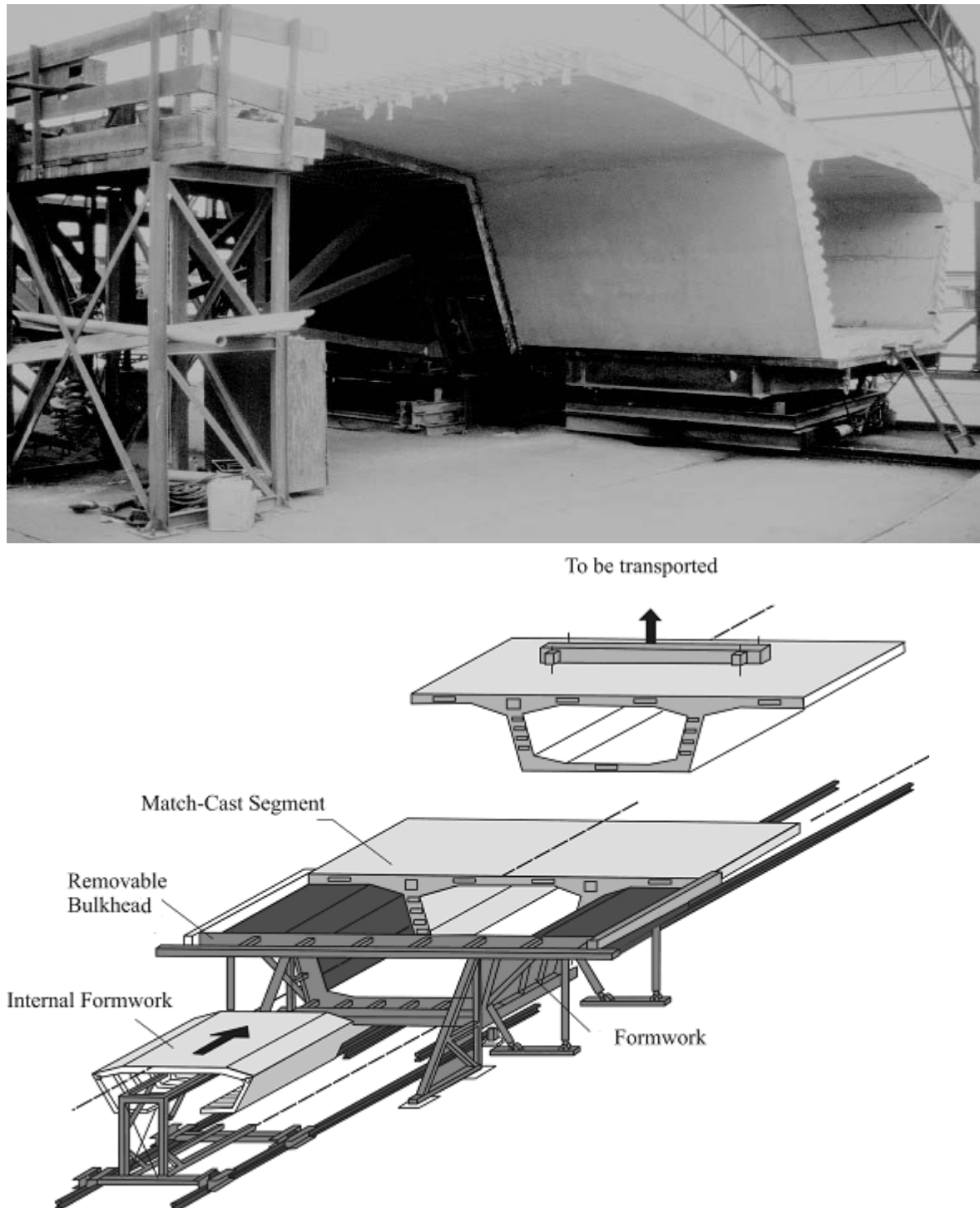

Figure 2.4 Short line match – cast method [Ro1, Po1]

Many experiments for application of joints between concrete precast structures were carried in the last 50 years. The simplest form of joint type is the flat joint. After that joints with brackets were applied. Figure 2.5 shows a segment joint with reinforced bracket.

In the last 15 years, the joints are in the vast majority of cases either left dry (where climate permits) or made of a very thin film of epoxy resin or mineral complex, which does not change the match casting properties. Table 2.1 lists the types of joints that can be used between adjacent segments. Figure 2.6 shows the application of dry and concrete joints between two segments. It can be seen that the concrete joint allows the use of extended steel rebars.
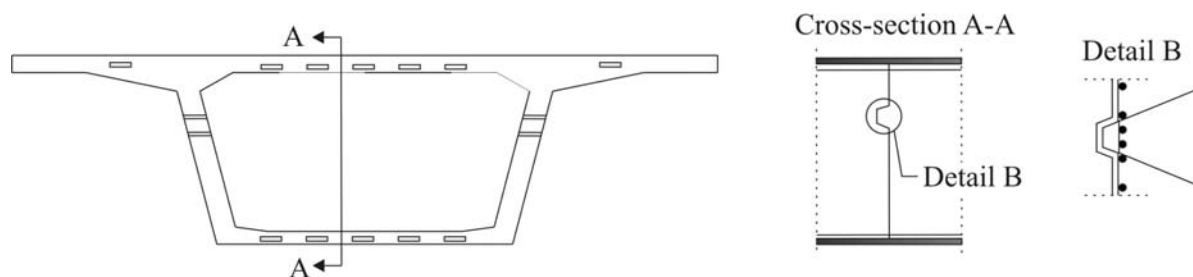

Figure 2.5 Segment joint with reinforced bracket [Ku2, Top]

Table 2.1 Types of the joints [Sp1, Sp2]

Joint type	Width of the gap
Concrete joint	20 - 60 *cm*
Mortar joint	7 - 12 *cm*
Cement paste joint	2 - 5 *cm*
Epoxy joint	less than 3 *mm*
Dry joint	≈ 0
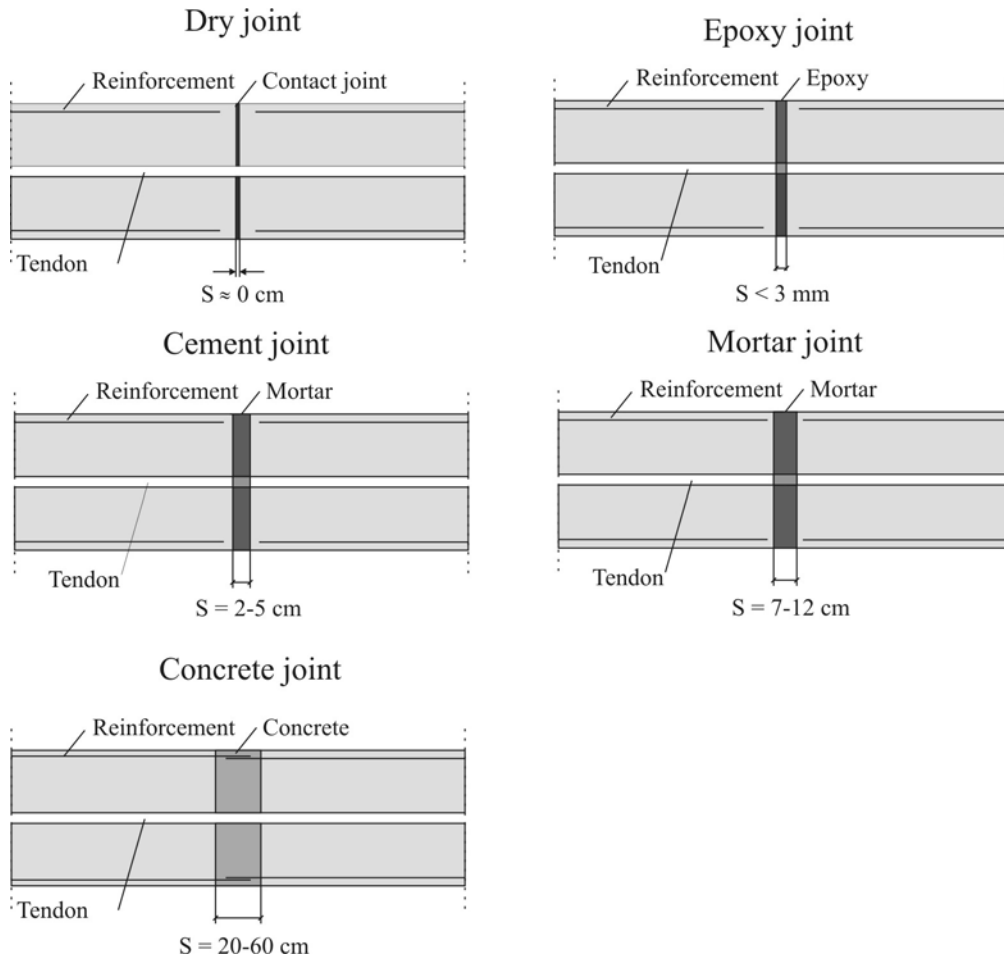
Figure 2.6 Types of joints used in segmental bridges [Ro4]

Dry jointing is a new technique for use in building modern precast segmental bridges. All dry-jointed segments behave in a similar manner to a monolithic or epoxy-jointed structure up to the point when longitudinal bending stresses give rise to decompression of the joints or shear stresses cause the joint to slip. Its use in the Bangkok Second Stage and the Bang Na Expressway, one of the world's largest bridge construction projects [Ta1, Ta2, Ro1, Ba2] demonstrates the main advantage of this technique. During the life of the bridge and according to the serviceability requirements, the dry joint must keep closed and have a minimum compression of 1.4 *MPa* by AASHTOO [Aa3] and 2.0 *MPa* according to German regulations [Bmv] under certain loading conditions. These measures are taken to prevent the risk of cracking of unreinforced concrete in the vicinity of joints. Moreover, an opening of joints would decrease the stiffness of the structure extremely.

Shear keys are used on the surface of the joint to help in the alignment process of the segments during erection and then to transfer shear forces between segments. In the case of using epoxy joints, shear transfer through shear keys is needed only during erection and until the epoxy layer has set. Otherwise, dry joints are used with shear keys, where shear forces are transferred in the erection time and permanent conditions.

Either a few large or multiple small shear keys are provided, as shown in Fig. 2.7. Both are designed to avoid a shear failure occurring through the joint. Normally, it is common practice to use additional shear keys more than the minimum number required by the design to take under consideration the inaccuracy of the simplified design model, possible damage to some of the keys during storage or handling and imperfections.
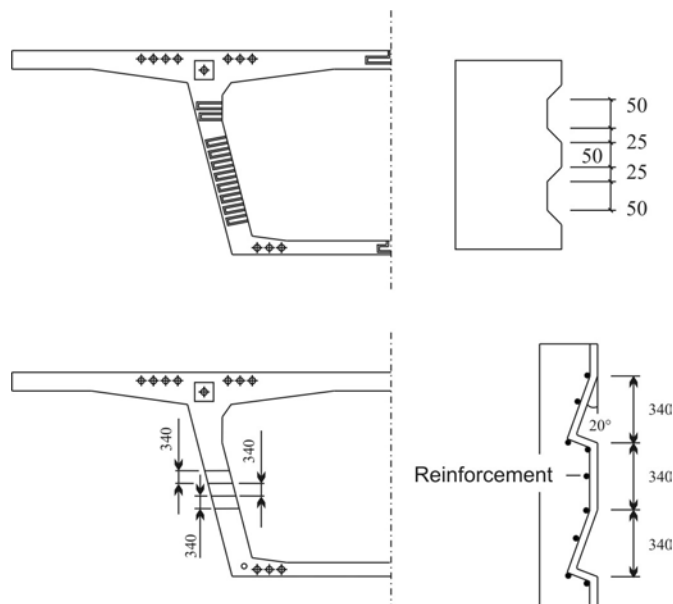
Figure 2.7 Shear key arrangements [Nig]

Segments with epoxy joints are designed similar to *in situ* box girders. In the current study only dry joints were treated and the shear keys were ignored (no indentation) for simplification of the numerical model.

2.2   Short-line match-cast method – Bowing effect

In this section the mechanism of match casting and the various problems, which may arise, will be discussed. The principles of the match casting have been described in section 2.1 (see Figure 2.4).

Figure 2.8 shows a plan view of the deck for different steps of production. In the short-line match casting method the first segment of a span, which is not the pier segment, is cast between one fixed and one removable bulkhead, as can be seen in Figure 2.8a The subsequent pieces are cast between the fixed bulkhead and the previously cast segment after it reaches enough hardening (Figure 2.8b). A problem can appear as the significant heat of hydration of the concrete in the new segment causes a non-linear thermal gradient in the match cast segment due to the low conductivity of concrete and ambient different temperatures. This gradient can cause an unsteady expansion in the concrete near the joint and/or in some cases a contraction may occur in the other side if a negative value in the thermal gradient appears. The deformation in the match cast segment results in a bowing of the segment (banana shape) as can be seen in Figure 2.8c.

The fresh concrete will follow the deformation of the match-cast segment and will flow to close the space resulted during the bowing of match-cast segment till it achieves enough setting or hardening. Thereafter a same permanent curvature like the bowing curvature occurs in the new segment. The new segment has one straight and one curved side, whereas the old segment keeps bowing then returns to its original shape after cooling to constant temperature, as can be seen in Figure 2.8d. Δ represents the deflection value, which is the gap that appears in each segment in the final position in segmental bridges.
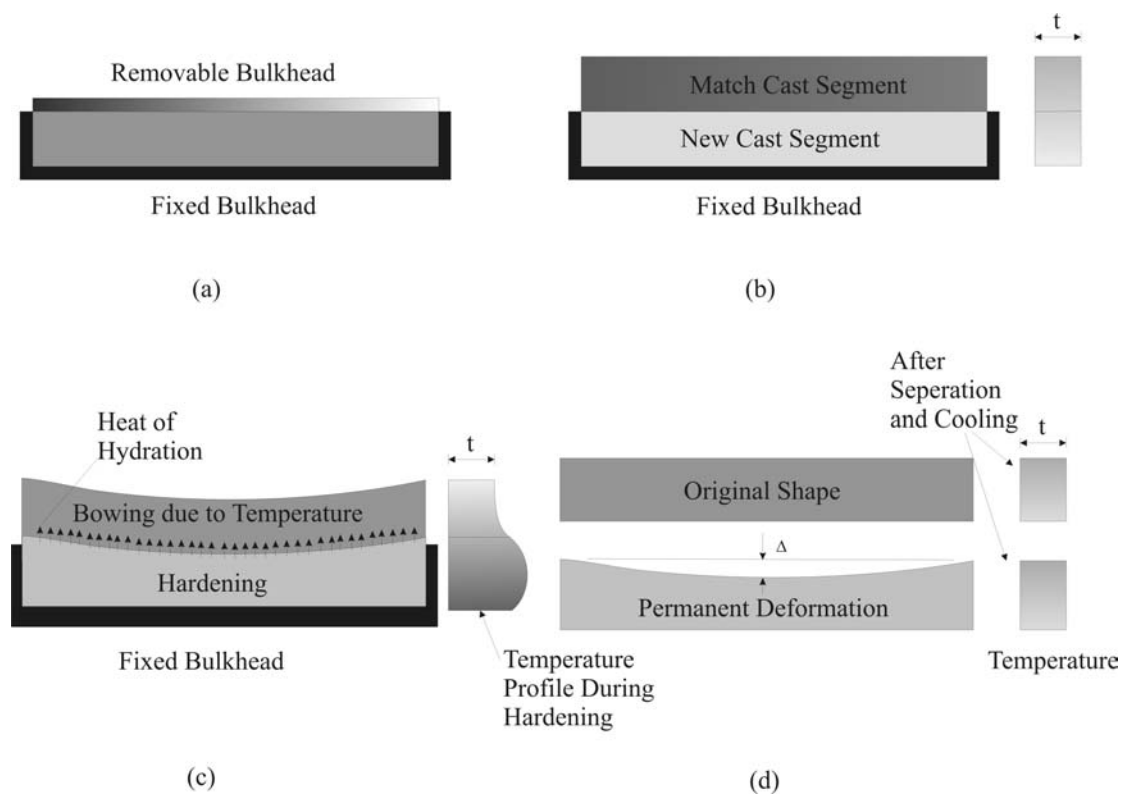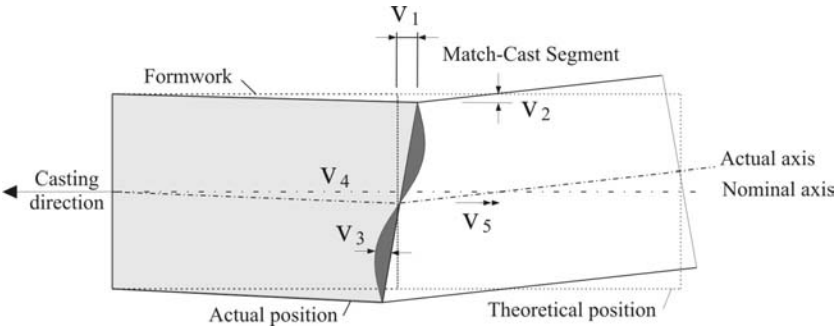

Figure 2.8 Bowing of match cast segments – top view of the deck [Fi2, Br3, Br4]

The permissible gap, which may effect the load bearing capacity and the durability of the structure is very small and always a matter of discussion between the manufacturer and the designer. Allowable tolerances at the manufacturing process of the match-cast segments according to German Regulations [Bun] are given in Table 2.2. These values are mainly based on practical experience and constraints rather than scientific research. It is very difficult to guarantee these values. Please note that V_3 is ±0.5 *mm* only. No value is given for the permissible bowing of the segment, which is regarded as one of the most critical parameter.

Table 2.2 Permissible tolerances [Bun]

Mould dimensions	
Longitudinal deviations	$V_1 = \pm 5.0$ mm
Vertical deviations	$V_2 = \pm 2.5$ mm
Curvature of the segmental joint	$V_3 = \pm 0.5$ mm
Angle deviation from the nominal axis	$V_4 = \pm 0.001$ rad
Angle deviations from the transverse slope	$V_5 = \pm 0.0005$ rad
After concrete casting	
Dimension of a segment	± 10.0 mm
The position of the non-concrete elements	± 5.0 mm
The change in the profile of the two meeting segments (after applying of the transverse prestressing)	± 2.5 mm
The horizontal and vertical change in the nominal axis	± 10.0 mm
Angular deviation from the nominal axis	± 0.003 rad
Angular deviation from the transverse slope	± 0.001 rad
Total longitudinal deviation of all segments of a span after the erection process	± 25.0 mm

It has been given little mention about the temperature-induced deformations in match cast segments. It is found that the width-to-length ratio (w/L) of the segment affects significantly the bowing phenomenon. Podolny [Po2] claimed that the effect is particularly significant for segments with width-to-length (w/L) ratios exceeding 6. He described the problem and noted that in order to eliminate the gaps, it is important to enclose both the newly cast and the match cast segments in an isothermal enclosure.

Similarly Fig. and Muller Engineers [Fig] described the problem in their "Prestressed Concrete Segmental Bridge Construction Manual". They attributed the problem to inaccurate heating during accelerated curing, which is sometimes used to reduce the construction cycle time. They also noted that the problem is of particular significance in segments with a large width-to-length ratio (w/L). They asserted that proper curing of both segments could eliminate the problem completely.

The previous authors not only did not mention the significant effect of heat of hydration but also did not deal with the factors, which can affect the thermal gradient. Some authors edited about problems caused during the construction of segmental bridges. Prescon Corporation [Br3] conducted a study of the bow-shaped segment phenomenon that was causing problems in the construction of phase *IIIA* and *B* of the San Antonio "*Y*" Project (see section 3.1). The segments had a very big width of $w = 17.7\ m$ and a short length $L = 1.8\ m$ ($w/L = 9.8$). The erection crews reported gaps in joints and difficulties in closing these gaps with the temporary post-tensioning system, as can be seen in Figure 2.9.
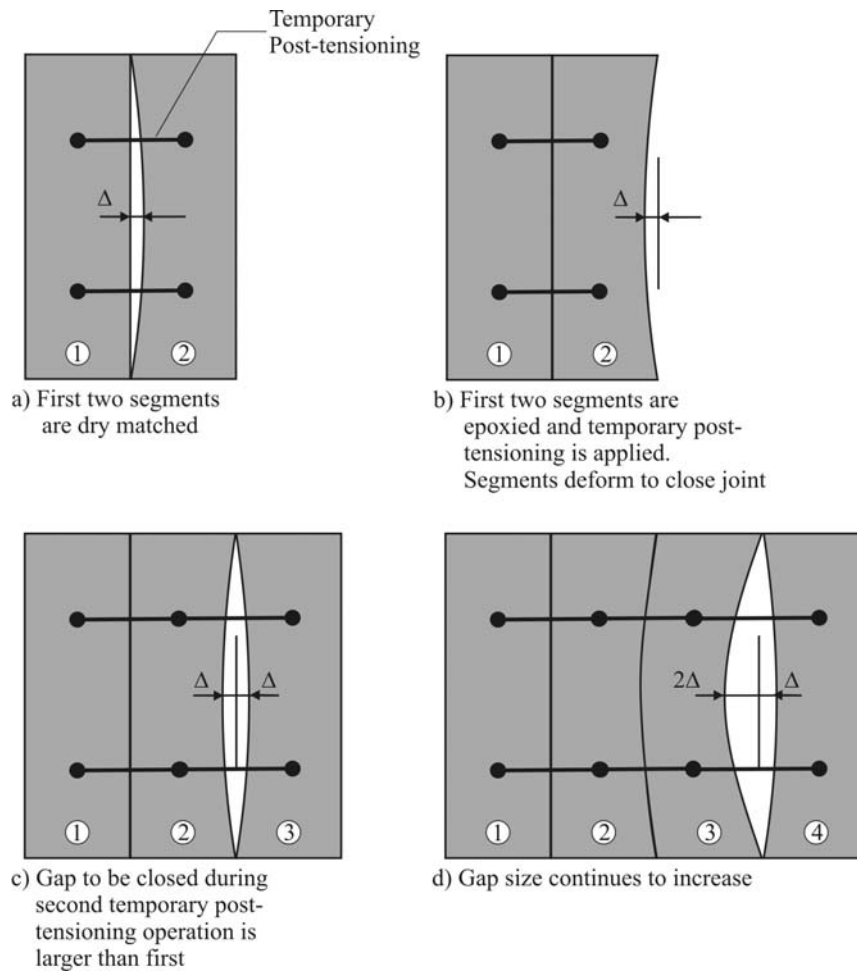
Figure 2.9 Plan view (bridge deck) of temporary post-tensioning operations [Br3]

In order to study this problem, Prescon [Br3] used thermocouples in eight segments of one span and measured the resulting segment deformations. They measured temperature-induced deformations, Δ, of up to 3 *mm* (see chapter 3.3.1). An analysis based on a linear thermal gradient from the match cast face to the exposed face resulted in deformations similar to the measured values. The maximum-recorded temperature difference between the match cast face and the open face was 18 *°C*. The description of the measurements and the results will be discussed in details in chapter three.

Fukunaga *et al* [Ten] described the design and construction of Tenryugawa bridge in Japan. The 1.58 *km* bridge with typical spans of 85.5 *m* represents the longest continuous concrete girder bridge in Japan. After one month from starting cantilever erection from the pier head, some cracks were observed at the end of the cantilever slab of the pier segment and segment No. 1. A nonlinear finite element thermal stress analysis was conducted, which showed that at the end of the cantilever slab, longitudinal tensile stresses are caused by the heat of hydration of the newly cast segment and by the progress of drying shrinkage. They found

that the deck width and segment length ratio which was ($w/L = 4.5$) has a large effect on the local tensile stress value. To solve this problem, they installed longitudinal prestressing strands and reinforcing bars in the cantilever slab.

The main dimensions of many constructed precast segmental bridges are given in Table A.1. There is a broad range of parameters. The width to length ratio varies from 2.8 to 13.8. Thus it is important to study the whole range of slenderness ratios.
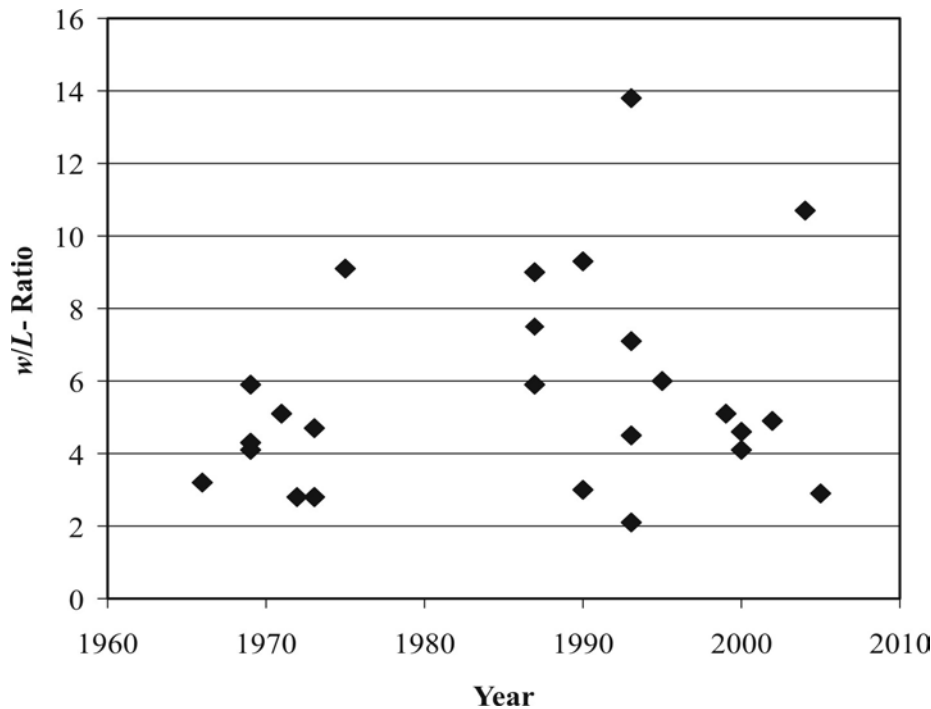
Figure 2.10 Width to length ratio of various precast segmental bridges

2.3   Bowing of the match-cast segment

In order to study the phenomenon of "bowing of match-cast segments", the heat development during hydration of concrete, the distribution of the temperature within a body and the formation of the thermal gradient as well as the mechanical properties, thermal stresses and resulting deformations should be studied. Finite Element simulations will be used for these investigations. In the following chapters, the main parameters will be discussed.

From decades of practical experience and from theoretical considerations, it is well known that early age temperatures and temperature-induced stresses may have a great influence on the quality of the concrete and concrete structures. Therefore, control of these temperatures

and of the associated thermal stresses was of paramount importance to enhance the quality of the concrete and concrete structures. Knowledge of the expected temperature rise during the hydration of cement in the match-cast method is desirable in order to conduct thermal stresses and deformations which can lead to bowing of segments, and to minimize the risk of thermal cracking in concrete structures.

Numerical simulation techniques can be used for quantification of the effectiveness of technical and technological measures for improving the quality. Simulation programs must be able to predict the evolution of temperatures, strength, stresses, and the risk of early age cracking [Sp3, Sp4, Zei, Po2].

Tetmayer [Tet] was one of the first who considered the importance of the influences of temperature in early-age concrete. As early as 1883 he performed temperature measurements.

In the last years the risk of thermal cracking is discussed particularly in connection with durability. Incompatibility of thermal strains of the cement matrix and aggregate and the associated risk of microcracking and loss of durability as well as thermal gradients due to cooling of concrete surfaces has pushed forward the need for control of maximum temperatures in concrete's early lives, in particular with regard to high strength concrete. These concretes are known to be very susceptible to early age cracking.

2.3.1   Heat of hydration

The raw materials used in the manufacturing of Portland cement consist mainly of lime, silica, alumina and iron oxide. These compounds interact with one another in the kiln to form a series of more complex products. Four compounds are regarded as the major constituents of cement: Tricalcium silicate (C_3S), Dicalcium silicate (C_2S), Tricalcium aluminate (C_3A) and Tetracalcium aluminoferrite (C_4AF).

In the presence of water, the silicates and aluminates of Portland cement form products of hydration of hydrates, which in time produce a firm and hard mass. In common with many chemical reactions, the hydration of cement compounds is exothermic. The quantity of heat per mass of unhydrated cement, evolved upon complete hydration at a given temperature, is defined as the heat of hydration [Ne1, Ne2]. For the usual range of Portland cements, about one-half of the total heat is liberated between 1 and 3 days, about three-quarters in 7 days,

and nearly 90 per cent in 6 months [Zei]. Figure 2.11 shows the typical development of heat of hydration versus time.
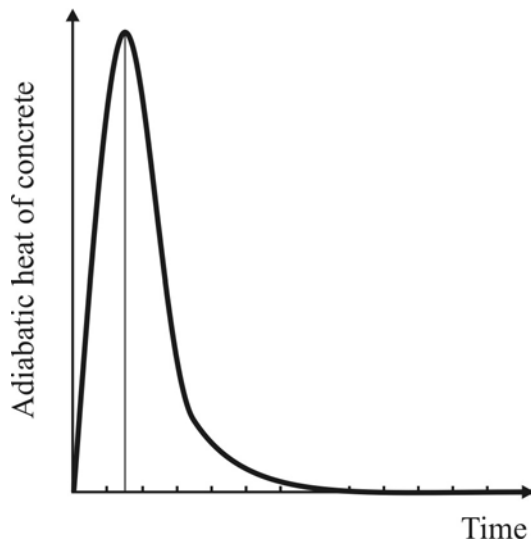

Figure 2.11 Typical development of the adiabatic heat of concrete [Zei]

The heat of hydration relies mainly on the chemical constitution of the cement, and is equal to the amount of the heat of hydration of separated compounds. Typical heat of hydration values of pure compounds are given in Table 2.3.

Table 2.3 Heat of hydration of pure compounds [Ros]

Compound	Heat of hydration	
	J/g	*cal/g*
C_2S	250	60
C_3S	500	120
C_3A	1340	322
C_4AF	420	101

The percentages of main compounds in cement can be calculated as given below. The terms in brackets are the percentage of the oxide in the total weight of cement according to table 2.4 [Ne1].

$$C_3S = 4.07(CaO) - 7.60(SiO_2) - 6.72(Al_2O_3) - 1.43(Fe_2O_3) - 2.85(SO_3) \qquad (2.1)$$

$$C_2S = 2.87(SiO_2) - 0.754(3CaO.SiO_2) \qquad (2.2)$$

$$C_3A = 2.65(Al_2O_3) - 1.69(Fe_2O_3) \tag{2.3}$$

$$C_4AF = 3.04(Fe_2O_3) \tag{2.4}$$

The oxide composition limits of Portland cements are listed in table 2.4.

Table 2.4 Approximate composition limits of Portland cement [Ne1]

Oxide	Content, weight %
CaO	$60 \div 67$
SiO$_2$	$17 \div 25$
Al$_2$O$_3$	$3 \div 8$
Fe$_2$O$_3$	$0.5 \div 6.0$
MgO	$0.1 \div 4.0$
Alkalis	$0.2 \div 1.3$
SO$_3$	$1.0 \div 3.0$

Equations 2.1 to 2.4 and Table 2.4 results in a composition of Portland cement as listed in Table 2.5. Further the heat of hydration of the various components is given.

Table 2.5 Approximate composition limits of Portland cement [Bk3]

Oxide	Content, weight %	Heat of hydration J/g cement
C$_2$S	$15 \div 50$	$38 \div 125$
C$_3$S	$25 \div 60$	$125 \div 300$
C$_3$A	$3 \div 12$	$40 \div 161$
C$_4$AF	$8 \div 12$	$34 \div 50$

Figure 2.12 shows the transient development of heat of hydration of cement chemical composition, where about one-half of the total heat is liberated in about one day [Tac, Lea].
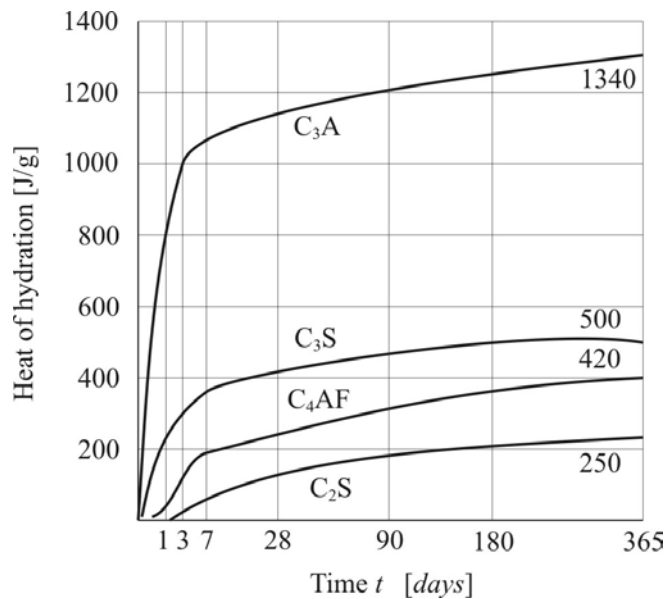
Figure 2.12 Heat of hydration of pure compounds versus time [Lea]

In real concrete, the factors influencing the rate of temperature rise, the maximum temperature and the temperature distribution are complex and many. They may include mix proportions, composition of cement, aggregate type, dimensions of cast concrete and environmental conditions such as wind and relative humidity. Some of these parameters will be discussed in the following.

Numerous laboratory techniques and methods have been developed in order to determine the temperature rise in concrete, ranging from sophisticated calorimeters used to monitor the temperature in very small samples of cement to temperature measurements at the centre of a large insulated block of concrete. The testing methods being used can be classified into the following categories: isothermal, adiabatic and semi-adiabatic. Isothermal methods are usually applied to pure cement pastes and make them possible to measure the heat generated by samples kept at a constant temperature. Adiabatic methods use calorimeters for measuring the temperature rise in a sample being hydrated with no heat exchanges with the external medium. The adiabatic temperature curve is shown in Figure 2.13. Semi-adiabatic methods use calorimeters or equipment where heat exchange with the external environment is limited.
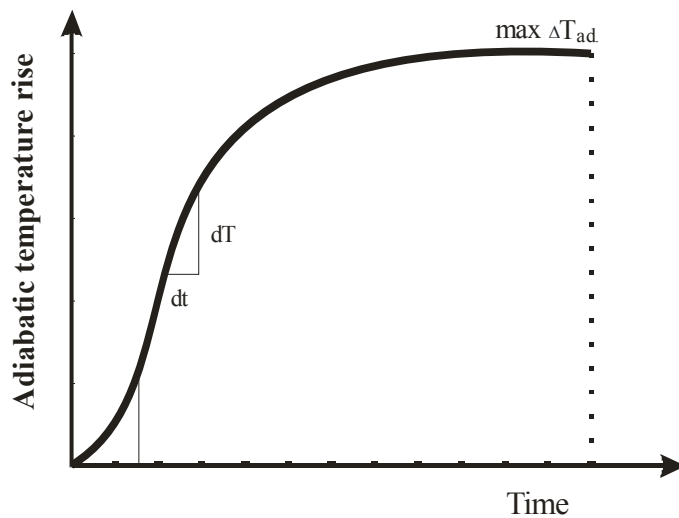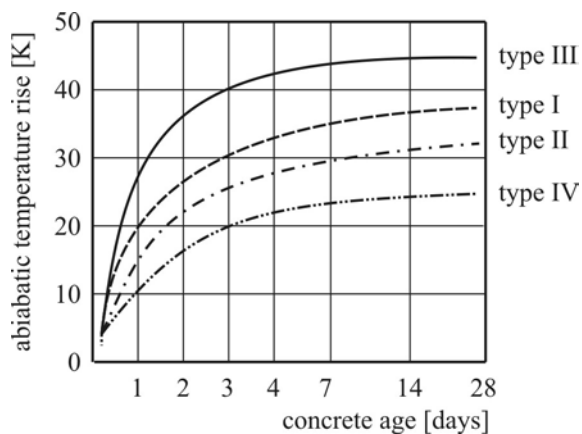
Figure 2.13 Typical adiabatic temperature development of concrete [Sp4, Zei]

Figure 2.14 shows the hydration curves for different types of cement, i.e. for type *I*, *II*, *III* and *IV* cement according to the American Concrete Institute. It can be said that the shape of these curves is a function of the chemical composition of the cement.

Concrete type acc. to American Concrete Institute [Am1]

type I: Ordinary Portland

type II: Modified cement

type III: Rapid-hardening Portland

type IV: Low-heat Portland

Figure 2.14 Impact of using different cement types on the adiabatic concrete heat of hydration [Am1]

Figure 2.15 shows different curves representing the influence of the initial mix temperature on the adiabatic concrete heat of hydration (ordinary concrete).
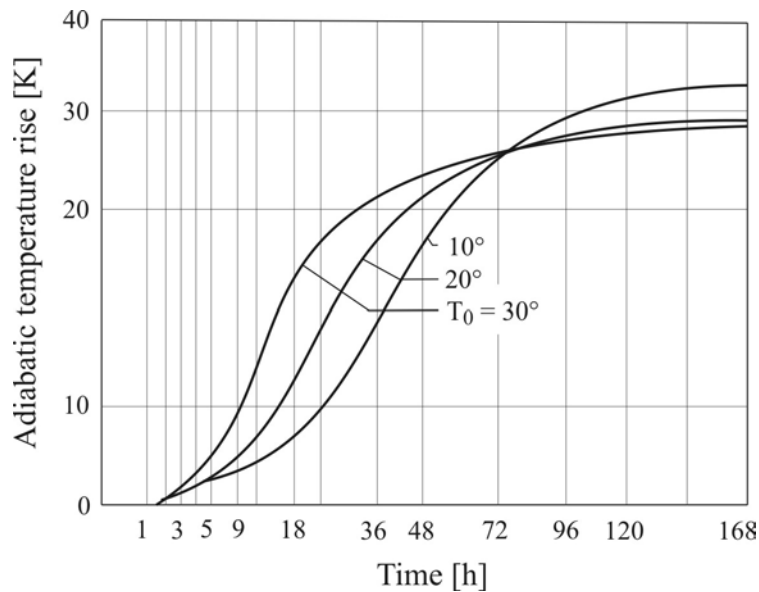
Figure 2.15 Effect of initial mix temperature on adiabatic heat of hydration curves [Lau]

To measure the adiabatic temperatures of five different concrete mixes as listed in Table 2.5, Zeitler [Zei] used a special cubic setup, which was designed with a polystyrene insulation material to read the developed temperature from the heat of hydration with almost no effect of the surrounding temperatures. Figure 2.16 shows the adiabatic temperatures of the five different concrete mixes.

Table 2.5 Mix proportion for different concrete mixes used by Zeitler [Zei]

	Concrete Type	1	2	3	4	5
Cement	kg/m^3	PZ 45 F 375	PZ 45 F 375	PZ 45 F 375	PZ 35 F 277	HOZ 35 L 329
Aggregate	kg/m^3	gravel 1780	Liapor [1] 985	Berwilit [2] 995	gravel-sand 1845	gravel-sand 1845
Water	kg/m^3	185	290	240	175	176
Concrete Density	kg/m^3	2340	1650	1610	2300	2350
Compressive Strength (28d)	N/mm^2	50.5	47.0	35.2	32.1	35.8

[1] expanded clay   [2] expanded shale

Normal concrete (type 1) with its high compressive strength as given by Zeitler is used in the construction of concrete bridges, whereas concretes type (2) and (3) are lightweight concretes. In normal concrete construction usually concrete type (4) is used, the blast

furnace concrete (concrete type 5) produces the lowest heat of hydration among the five types.
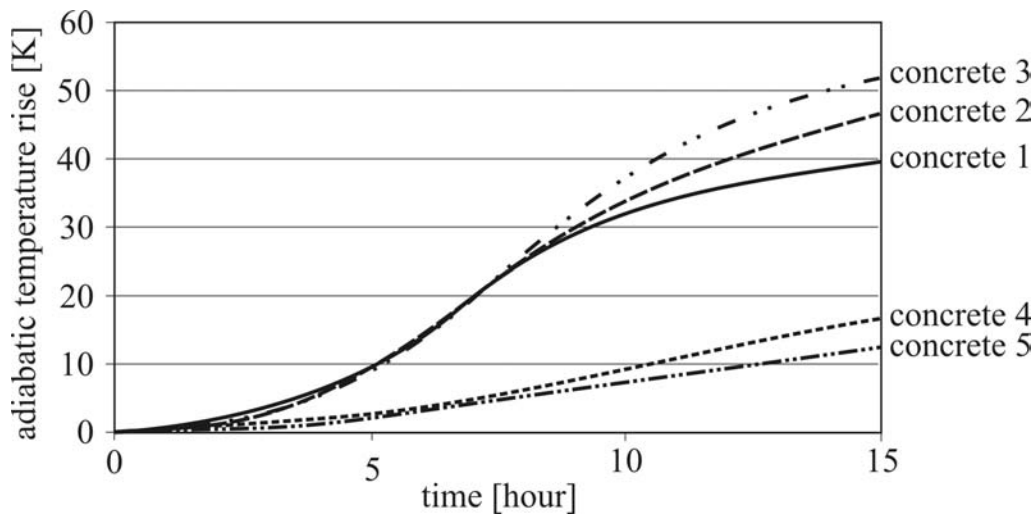

Figure 2.16 Adiabatic temperature curves of the five concrete mixes versus time [Zei]

Numerical models were also used to study and to predict temperature development in cement-based systems like cement paste, mortar and concrete. They can be subdivided into micro level and macro level models. Micro level models are developed in the area of materials science. They allow for simulation of physicochemical processes and mechanisms, which occur on the micro- or even nano-level scale. Their main disadvantage lies in the limited number of particles, which can be used due to the limited computer capacity. Macro level models are developed for the prediction of temperature fields in real concrete structures. These models are used in the engineering practice as an aid in decision-making regarding time of formwork stripping, the effectiveness of various curing methods like application of insulation or cooling of the concrete.

For reasons of simplicity the degree of hydration $\alpha(t)$ generally indicates the state of the hydration process at time t. Moreover many parameters are used to indicate the degree of hydration and the amount of chemically bound water. However, one must bare in mind that the four major cement compounds hydrate at different rates, while binding different amounts of water per unit mass and librating different amounts of heat per unit mass. This indicates that the degree of hydration of cement must be considered as a weighted average of degrees of hydration of the constituents. The knowledge of the degree of hydration and

its characteristics can help in giving solutions to decrease the risks of the development heat of hydration i.e. by decreasing the degree before the setting of concrete.

The degree of hydration should be equalized with the degree of heat development as a result of many practical engineering purposes:

$$\alpha(t) = \frac{Q(t)}{Q_{max}}$$ (2.5)

In which $Q(t)$ and Q_{max} represent the amounts of heat liberated at time t and at complete hydration respectively.

The degree of hydration process is particularly affected by:

- The chemical composition of the cement
- The fineness and particle size distribution of the cement
- The water/cement ratio
- The initial reaction temperature
- The presence and type of admixtures

These parameters influence the shape of the hydration curves $\alpha(t)$. The rate of hydration of concrete is faster the finer the cement, the higher the temperature and the higher the water/cement ratio (*w/c* ratio) as can be seen in Figure 2.17.
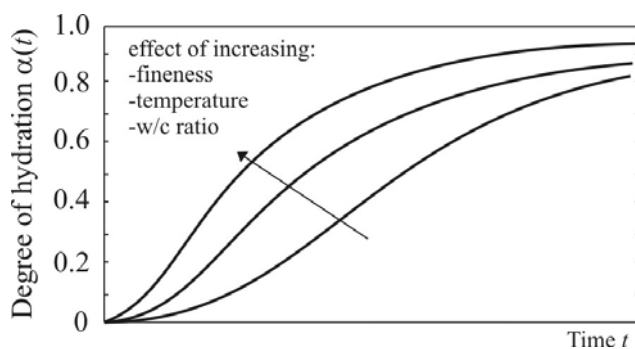

Figure 2.17 Effect of variations in cement paste parameters on the rate of hydration [Sp4]

It can be noticed from the curves that the maximum degree of hydration achieved in an ordinary concrete mix is determined generally by the fineness of the cement and the *w/c* ratio. In fact even if the *w/c* ratio exceeds the critical value of 0.4, Figure 2.18 shows that

the degree of hydration will generally not exceed 70 to 80%, the latter value being considered the lowest value at which complete hydration would theoretically be possible.
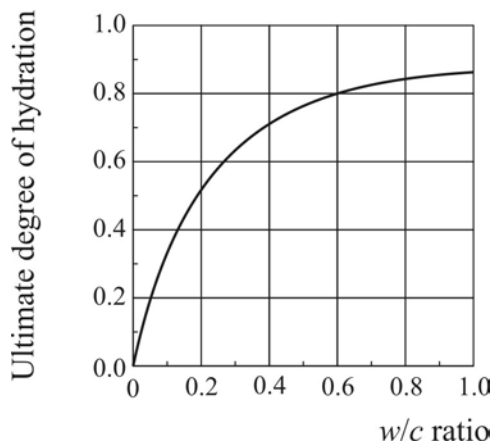

Figure 2.18 Effect of the water/cement ratio on the ultimate degree of hydration [Mil]

The realization that the degree of hydration is a predominant parameter in numerical analysis for the conduction of early-age thermal problems, besides its importance for the development of the material properties and the probability of early age thermal cracking appearance, reveals itself as a distinct approach in modern numerical predictive models. Fundamentally a reliable prediction of temperatures without simultaneous calculation of the development of hydration process is impossible.

2.3.2   Prediction of temperature development in hardening concrete

A study of the heat-transfer problem will reveal the temperature development and distribution within a body. We can then determine the amount of heat moving into or out of the body, and the subsequent thermal stresses and deformations.

Heat transfer can be defined as the thermal energy transport within a medium or among adjacent media by molecular interaction called conduction, fluid motion called convection, and electromagnetic waves called radiation, produced from a spatial difference in temperature. This difference in temperature is governed by the law of energy conservation, which if applied to a control volume or a control mass. It is stated that the sum of the flow of energy and heat across the system, the work done on the system, and the energy stored and converted within the system, is zero.

The study of heat transfer is based on the principles and laws of thermodynamics for conducting the chemical and physical states, the conservation of energy, and the physics of heat conduction, fluid motion for convection, electromagnetic fields for radiation, and the physics of thermal energy conversion.

Almost all the numerical analytical methods for the determination of temperature fields studied and discussed in the thirties [Ca1, Mch] were based on the Fourier differential equation where the temperature gradient in $°C/m$ can be given as:

$$\frac{\partial T}{\partial t} = a_c \cdot \left(\frac{\partial^2 T}{\partial x^2} + \frac{\partial^2 T}{\partial y^2} + \frac{\partial^2 T}{\partial z^2} \right) + Q(t, x, y, z) \qquad (2.6)$$

where: a_c is the coefficient of thermal diffusivity of concrete [m^2/s]

T is the temperature of the concrete

x, y, z are the coordinates of a particular point in the structure

$Q(t, x, y, z)$ is the source term, which represents the heat liberation function [J/g]

t is time

For heat transfer analysis purposes, we need to identify the boundaries of a system as well as its contents. Such controlled boundaries and volume are called the control surface and control volume. We consider a control volume to allow for flow of heat across the boundaries. The thermal system analysis will consist of two processes: At first the thermal processes and heat exchange occurring within the control volume, and then the interaction with the surroundings occurring at the control surfaces.

The control surface is situated on the boundary marking the separation of the system to be studied from its surroundings, i.e., the boundary surface. This boundary can be a phase boundary such as: solid-fluid or liquid-gas, where a discontinuity in the thermodynamic and transport properties occurs, or it can be within the same phase or medium.
Heat flows along the direction of decreasing temperatures in a certain system. In a case there is a moving fluid, heat also flows along the direction of this fluid flow. Therefore, the heat flow has a magnitude and a direction, in other words the heat flow is a vector quantity.

The magnitude of the heat transfer rate per unit area and its direction are presented by the heat flux vector q.

By conservation of energy, we have for a one dimensional heat flow [Log]:

{The energy entering the control volume}+{The rate of internal heat generation} = {The change in stored energy}+{The energy transferring out of control volume}

or, $$q_x \cdot A \cdot dt + Q \cdot A \cdot dx \cdot dt = \Delta U + q_{x+dx} \cdot A \cdot dt \qquad (2.7)$$

where: q_x is the heat conducted (heat flux) into the control volume at surface edge x for one-dimensional problem as shown in Figure 2.19.

ΔU is the change in stored energy

A is the cross-sectional area perpendicular to heat flow q

t is time

Q is the internal heat source (heat generated per unit time per unit volume)

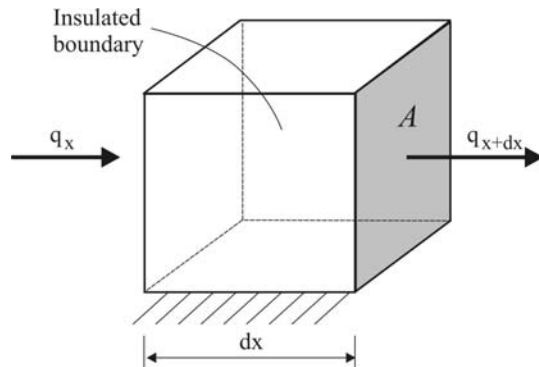q_{x+dx} is the heat conducted out of control volume at the surface edge $(x+dx)$

Figure 2.19 Control volume

The heat flux q_x is given by:

$$q_x = \lambda_{xx} \cdot \frac{dT}{dx} \qquad (2.8)$$

where: λ_{xx} is the thermal conductivity in the x direction in $W/(m\,°C)$

In addition to heat flux vectors describing heat transfer within a medium there is a special designation for the fluid conduction at the interface of a fluid stream and a stationary, impermeable solid. This is defined as the surface-convection heat flux, where on the solid

surface, due to the fluid stream no-slip condition, due to impermeability and fluid viscosity, we have a velocity of $u = 0$. However, this interface heat flux is influenced by the fluid velocity adjacent to the surface interface. Then the heat flowing through a solid by conduction flows by surface convection through the interface of this solid and its adjacent moving fluid, and it flows then by convection through the moving fluid.

It would be convenient to describe the convection in control volume with convection, as shown in Figure 2.20.
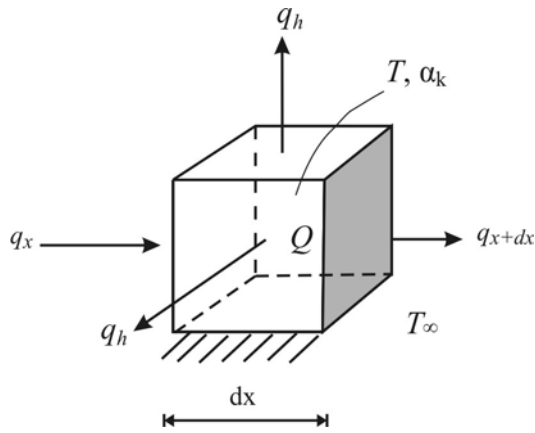

Figure 2.20 Control volume with convection

In terms of a heat transfer coefficient α_k and the temperature T and T_∞ the surface convection is given by:

$$q_h = \alpha_k (T - T_\infty) \tag{2.9}$$

Equation 2.9 is known as Newton's law of cooling. The convection heat transfer coefficient α_k is discussed in chapter 2.3.3.2.

This solid-fluid surface-convection heat flux is especially designated as q_h. Equation 2.7 becomes

$$q_x \cdot A \cdot dt + Q \cdot A \cdot dx \cdot dt = c\,(\rho \cdot A \cdot dx)\,dT + q_{x+dx} \cdot A \cdot dt + q_h \cdot P \cdot dx \cdot dt \tag{2.10}$$

where: α_k is the heat-transfer or convection coefficient, in $W/(m^2\,°C)$

   T is the temperature of the solid surface, at the solid/fluid interface

   T_∞ is the temperature of the fluid – ambient temperature

P is the perimeter around the constant cross-sectional area A

ρ   is the mass density

c is the specific heat in $W \cdot s \, / \, kg \cdot^{o} C$ or $J/(kg\,^{o}C)$

The derived quantities of the heat transfer and their units are listed in Table 2.6.

Table 2.6 Primary and derived units for heat transfer [Kav]

Derived Quantity	Unity
Specific heat capacity (c)	$J/(kg\ K)$ or $J/(kg\,^{o}C)$
Energy	J (Joule)
Thermal conductivity (λ)	$W/(m\ K)$ or $W/(m\,^{o}C)$
Heat flux (q_x)	W/m^2
Heat flow rate	Watt or $J\,s$
Internal heat source (Q)	W/m^3
Convection coefficient (α_k)	$W/(m^2\,^{o}C)$
Mass density (ρ)	kg/m^3

The finite element formation of heat-transfer is shown in Appendix B.

2.3.3   Heat Transfer Parameters

Wherever a temperature difference takes place in a medium or between mediums heat transfer must occur. When a temperature gradient exists in a stationary medium, which may be a solid, or a fluid, the term *conduction* refers to the heat transfer that will occur across the medium. In contrast, the term *convection* refers to heat transfer that will occur between a surface and a moving fluid when they are at different temperatures. The third term of heat transfer is the thermal radiation. All surfaces of finite temperature emit energy in the form of electromagnetic waves. Hence, in the absence of an intervening medium, there is net heat transfer by radiation between two surfaces at different temperatures.

A medium of heat transfer could be a single-phase medium such as solid, liquid, or gas. The medium could have many phases; such as a brick which has a volume of void space filled by air. Thus, the brick is a solid-gas, two-phase medium, or it could be in another example multiphase medium.

Because the heat transfer is a result of non-uniformity in temperature, it can be stated that the presence of spatial temperature non-uniformity is considered as the existence of thermal non-equilibrium. When heat transfer is considered between a control volume and its surroundings, it is generally addressing the non-uniformity of temperature within the system, as well as in the surroundings.

It could be considered in some cases only the heat transfer, i.e., the thermal non-equilibrium, between the surroundings and the surface of the controlled mass or volume. In other cases we may be interested in thermal non-equilibrium between this surface and its interior.

The thermal system is defined as a part of the universe chosen for analysis. The thermal system exchanges thermal energy with its thermal surroundings, when it is in thermal non-equilibrium with these surroundings, where the thermal surroundings are that part of the universe affected by this thermal energy exchange. A thermal system contains substance or matter and this substance may change by transformations and by mass exchange with the surroundings.

To study and analyze a thermal system, we need to use thermodynamics principles, which allow for a quantitative description of the state of substance. This can be done by defining the boundaries of the system, applying the conservation laws, and examining the way that the system participates in thermal energy variation and conversion.

The heat flux vector q is the sum of the conduction, convection and radiation heat flux vectors represented by the thermal energy flow per unit time and per unit area. The surface A is designated by a unit normal vector.

2.3.3.1   Thermal conductivity λ

The process of carrying heat by molecular contact among molecules in thermal non-equilibrium is called conduction heat transfer. The thermal conductivity is defined as the ratio of heat flow rate (or heat flux q) to temperature gradient per unit length (see eq. 2.3.3), and represents the uniform flow of heat through a solid (concrete) of unit thickness over a unit area subjected to a unit temperature difference between the two opposite faces. Table 2.7 shows the thermal conductivities λ of some solids and liquids.

Table 2.7 Typical thermal conductivities (λ) of some solids and liquids [*W/(m ℃)*]

Material	[Log]	DIN 4108 [Di1]
Aluminium, 0 ℃	202	160
Steel (1% carbon), 0 ℃	35	17 ÷ 50
Fiberglass, 20 ℃	0.035	
Earth, coarse gravelly, 20 ℃	0.52	0.70 ÷ 2.0
Wood, oak, radial direction, 20 ℃	0.17	0.13 ÷ 0.18
Engine oil, 20 ℃	0.145	
Dry air, atmospheric pressure, 20 ℃	0.0243	
Reinforced concrete		2.0 ÷ 2.5

The thermal conductivity of concrete at normal temperatures depends on several factors of which are content and type of aggregate, moisture content at the time of heating, porosity, density and temperature. Concrete made with siliceous aggregates will generally have higher thermal conductivities than those made with other normal weight aggregates, as can be seen in Table 2.8. The thermal conductivity of saturated Portland cement paste at $5 \div 15 \, °C$ is between 1.1 and 1.6 *W/(m ℃)*, which is less than for normal aggregate [Zol].

Table 2.8 Typical values of the coefficient of thermal conductivity of concrete (λ) made with different types of aggregates [Am1]

Type of aggregate	Thermal conductivity of concrete λ in *W/(m ℃)*
Quartzite	3.5
Dolomite	3.2
Limestone	2.6 ÷ 3.3
Granite	2.6 ÷ 2.7
Rhyolite	2.2
Basalt	1.9 ÷ 2.2

The thermal conductivity of water at 20 $°C$ ($\lambda = 0.515$ $W/(m \ °C)$) is much more than that of air ($\lambda = 0.0034$ $W/(m. °C)$); air-dried concrete with a moisture content of about 50 percent less than saturated concrete, could experience a 25 percent reduction in conductivity [Baz]. The thermal conductivity of ordinary concrete at normal temperatures ranges between 1.4 and 3.6 $W/(m \ °C)$ [Cam, Mit, Rho, Usb, Zol].

2.3.3.2   Convection q

Convection heat transfer can occur between a fluid or air in motion or even constant and a boundary surface when the two are at different temperatures. The basic objective of studying convective heat transfer is to predict the value of the coefficient of convective heat transfer α_k. The fluid can be motionless $u = 0$, or it can be in motion, orderly time varying, or randomly time-varying (turbulent) motion, where $u = u\ (x, t) \neq 0$. If the fluid is at rest i.e. its velocity is zero, then the problem can be reduced to simple conduction where there are temperature gradients normal to the interface. If the fluid has a motion $u \neq 0$, heat is transferred by both simple conduction and by the movement of the fluid itself [Gho].

Assume fluid flow over the heated surface of Figure 2.21 [Inc], the existence of the fluid-surface interaction is due to the development of a region in the fluid through which the velocity varies from zero at the surface to a finite value u_∞ associated with the flow. This region of the fluid is called the velocity boundary layer. If the flow and surface temperatures are different, there shall be a region of the fluid through which the temperature varies from T_s at $y = 0$ to T_∞ in the outer flow. If T_s is less than T_∞, convection heat transfer can occur between the surface and the outer flow.
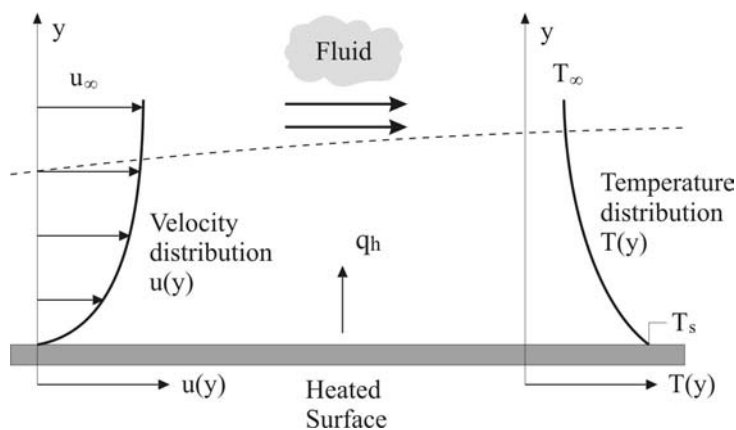

Figure 2.21 Boundary layer development in convection heat transfer [Inc]

Convection could be classified according to the nature of the flow as can be seen in Table 2.9. Forced flow occurs when the flow is resulted by external means, such as by a fan to provide forced convection air-cooling of hot electrical components on a stack of printed circuit boards. On the other side, for free or natural convection the flow is induced by buoyancy forces, which arise for density differences produced by temperature changes in the fluid.

Table 2.9 Approximate values of convection heat-transfer coefficients α_k [Log, Inc]

Mode	Convection coefficient α_k in $W/(m^2\ {}^\circ C)$
Free convection, air	5 ÷ 25
Forced convection, air	10 ÷ 500
Forced convection, water	100 ÷ 15,000
Boiling water	2,500 ÷ 25,000
Condensation of water vapour	5,000 ÷ 100,000

The convection heat transfer coefficient α_k for concrete can be given as [Rec, Vdi]:

$$\alpha_k = 5.8 + 4 \cdot w \qquad \text{for } w \leq 5 \text{ m/sec} \tag{2.11}$$

$$\alpha_k = 7.15 \cdot w^{0.78} \qquad \text{for } w > 5 \text{ m/sec} \tag{2.12}$$

Where, w is the wind speed, in [*m/sec*].

2.3.3.3   Specific heat *c*

The development of a temperature distribution in any structure is governed by the thermal properties of the material, specially heat capacity and heat conductivity. The thermal or heat capacity of a material, also called the specific heat *c*, is the amount of heat per unit mass, required to change the temperature of the material by one degree. The specific heat of ordinary concrete aggregates at $21^\circ C$ ranges between 0.5 and 0.92 *kJ/(kg·K)* (0.2 and 0.22 *cal* /(*g·${}^\circ C$*)), while that of hardened cement paste can range between 0.63 and 1.72 *kJ/(kg· K)* (0.15 and 0.41 *cal* /(*g·${}^\circ C$*)) [Br7, Baz]. The specific heat of ordinary concrete at normal temperatures can vary from *c* = 0.5 to 1.13 *kJ/(kg K)* (0.12 to 0.27 *cal* /(*g ${}^\circ C$*)).

For fresh mixes and water saturated concretes the higher values apply, the lower values for dry concretes and lightweight concrete. Carman and Nelson [Ca2] and the US Bureau of

Reclamation [Usb] have reported that changes in aggregate type, mix proportions and age do not have a great effect on the specific heat of ordinary concretes at normal temperatures.

2.3.3.4   Thermal diffusivity D

Thermal diffusivity D is defined as the rate at which temperature changes may take place in a material and is used for estimating temperature distributions under transient conditions.

Diffusivity can be expressed as: $D = \lambda / (c \cdot \rho)$ (2.13)

where: λ is the thermal conductivity;

        c is specific heat

        ρ is the density of the material.

The values for ordinary concrete are about 15 percent less than those for the aggregate and have been reported to range from $D = 0.69 \times 10^{-6} m^2 / s$ for concrete made with basalt to $D = 1.89 \times 10^{-6} m^2 / s$ for concrete made with quartz aggregate [Baz].

In the match-cast process, the low conductivity of concrete normally decreases the bowing of match-cast segments by reducing the amount of transferred heat, whereas less specific heat coefficient or less density of the concrete can increase the bowing resulting in a gap. Hence, the lower the thermal diffusivity, the smaller the resulting gap in the match-cast method.

The main influence on the thermal diffusivity of normal weight concrete comes from the type of aggregate as shown in Table 2.10.

Table 2.10 Diffusivity D of different types of aggregate [Am1]

Aggregate type	Diffusivity of concrete D in m^2 / s
Quartzite	1.50 e-6
Limestone	1.30 e-6
Dolomite	1.28 e-6
Granite	1.11 e-6
Rhyolite	0.92 e-6
Basalt	0.83 e-6

2.3.3.5   Thermal radiation

The conduction in fluids and solids and convection in moving fluids depend on matter, and disappear in the absence of matter. The third and final mode of heat transfer is thermal radiation. Different from conduction and convection, this mode of heat transfer is hindered by matter and in a vacuum is at its best, besides conductive and convective heat transfer rates are linearly proportional to the temperature differences, it is proportional to the differences of the individual absolute temperatures of the bodies. Hence, it is obvious that the existence of radiation becomes intensified at high absolute temperature levels. Thus, thermal radiation contributes largely in combustion applications such as: concrete at high temperatures or concrete subjected to fire [Arp, Gho].

Some aspects of this thermal mode can be explained in terms of electromagnetic waves. Other aspects of this thermal radiation, being a manifestation of the many forms of particle interaction, can be explained in terms of radiation quanta (photons). Based on a theoretical (electromagnetic or quantum) and/or experimental facts an ideal black surface at absolute temperature T is emitting thermal radiation energy E_b according to the Stefan-Boltzmann law (Figure 2.22a).

$$E_b = \sigma \cdot T^4 \tag{2.14}$$

Where E_b in W/m^2 is called the black-body emissive power, and $\sigma = 5.67 \cdot 10^{-8}$ $W/(m^2 \cdot K^4)$ is Stefan-Boltzmann constant. Black-body emissive power represents the maximum amount of heat that can be radiated by a body with a temperature T. The emmisivity of a surface of concrete at $T = 300\ K$ is about 0.94 $W/(m^2 \cdot K^4)$ [Arp].

Let us assume two bodies each with a flat black surface at absolute temperatures T_1 and T_2 separated by a distance l apart in a vacuum, as shown in Figure 2.22b. Surface one has emissive power E_{b1} and surface two has emissive power E_{b2}, then the radiation energy transfer between these bodies can be given as:

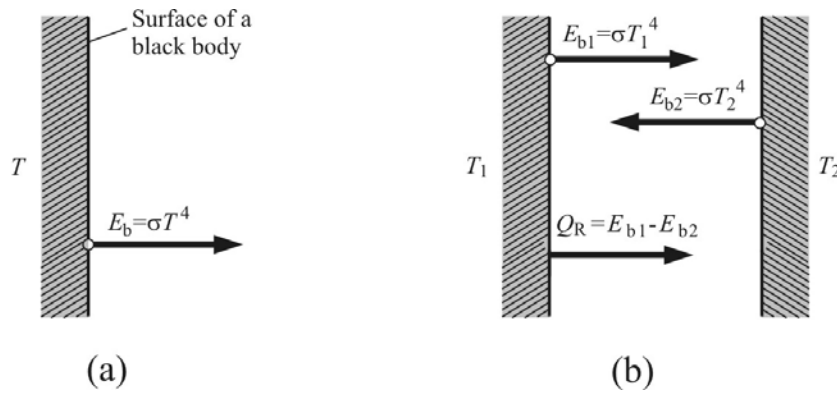$$q_R = E_{b1} - E_{b2} \tag{2.15}$$

Figure 2.22 (a) The Stefan-Boltzmann Law
              (b) Radiation heat transfer between two parallel black surfaces [Arb]

When there is a transparent medium between two bodies, equation (2.14) continues to apply, but the total heat transfer q_T now includes the effects of conduction and convection as well as radiation.

In the current study the thermal radiation will be ignored, because of the small amount of the thermal gradient and its small surface area compared to all segment area.

2.3.4   Thermal expansion of concrete α_T

Concrete exhibits thermal expansion as do all solids, which is a normal strain resulted from temperature change. As a result that concrete is considered as isotropic material, the thermal strain is the same in all directions, in other words the tensor of thermal strain is volumetric. Since it is typically non-uniform throughout the structure due to temperature non-uniformity stresses arise, this often leads to cracking and large-scale spalling.

Due to the composite nature of concrete differences between the thermal expansions of aggregate and hardened cement paste must also taken under consideration. When these variations are significant, heating causes micro stresses and micro cracking that can disrupt the concrete microstructure.

The coefficient of thermal expansion for concrete at normal temperatures is influenced by many factors. As listed in Table 2.11 and shown in Figure 2.23, there is an almost linear relationship between the thermal expansion coefficients of common aggregates and concrete made from them [Baz].

It has been reported that concretes made with siliceous aggregate have the highest expansion coefficients, while concretes with calcareous aggregate have the lowest, those with igneous aggregate have coefficients that are in between [Bon].

It is investigated that hardened Portland cement paste, at normal temperatures, has a higher thermal expansion coefficient than aggregates generally used in concrete. It is expected that the thermal expansion coefficient for concrete will increase as the proportion of cement increases.

Table 2.11   Coefficient of thermal expansion (α_T) for different rocks and concretes at normal temperatures [Br7]

| Rock group	Typical silica content by weight %	Coefficient of thermal expansion α_T (10^{-6} per $^\circ C$)			
		Rock		Concrete	
		Range	Average	Range	Average
Chert	94	7.4 ÷ 13.0	11.8	11.4 ÷ 12.2	13.2
Quartzite	94	7.0 ÷ 13.2	10.3	11.7 ÷ 14.6	12.1
Sandstone	84	4.3 ÷ 12.1	9.3	9.2 ÷ 13.3	11.4
Marble	negligible	2.2 ÷ 16.0	8.3	4.1 ÷ 17.4	10.7
Siliceous Limestone	45	3.6 ÷ 9.7	8.3	8.1 ÷ 11.0	10.7
Granite	66	1.8 ÷ 11.9	6.8	8.1 ÷ 10.3	9.6
Dolerite	50	4.5 ÷ 8.5	6.8	-	9.6
Basalt	51	4.0 ÷ 9.7	6.4	7.9 ÷ 10.4	9.3
Limestone	negligible	1.8 ÷ 11.7	5.5	4.3 ÷ 10.3	8.6
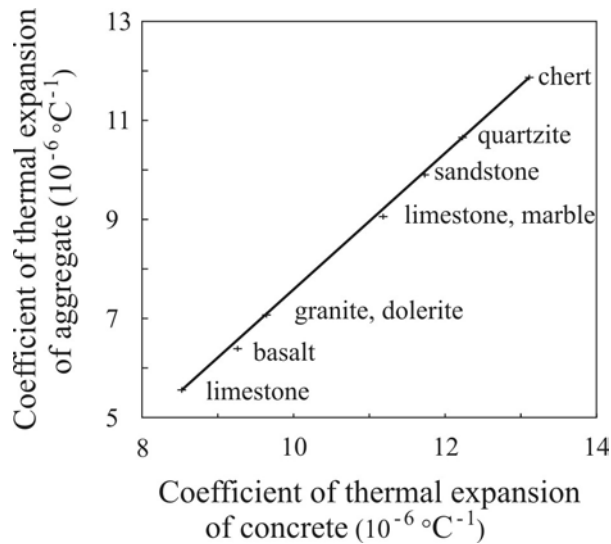
Figure 2.23 Correlation between the coefficient of thermal expansion α_T of aggregate and of concrete [Baz]

The age of concrete also affects the value of thermal expansion coefficient showing a minor decrease with an increase in age; the first week of concrete shows the highest value through its whole life [Tac, Nol, Zei]. Figure 2.24 shows the development of the coefficient of thermal expansion of concrete α_T. In match-cast method, the old of the match-cast segment in the vast majority of cases is one day [Br3, Jea], and then a high value of thermal expansion coefficient α_T is expected. In the current study a constant value of $\alpha_T = 12 \cdot 10^{-6} K^{-1}$ according to Zeitler is used [Zei]. The thermal expansion of fresh concrete is not relevant.
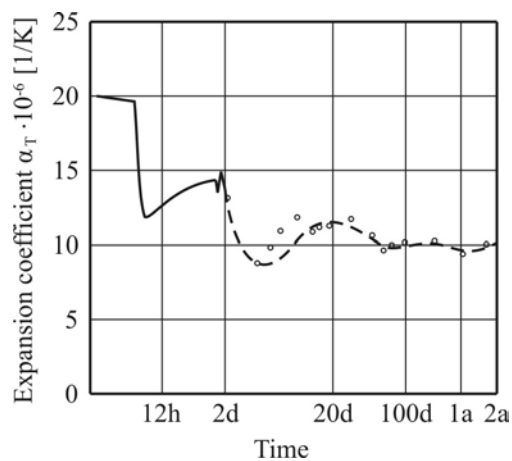
Figure 2.24 Development of coefficient of thermal expansion of concrete α_T versus time [Nol]

2.3.5   Boundary conditions

The flow of heat at the surface of a continuum depends on the heat transfer properties of the boundary layer between the surface and the surrounding area. Many factors to be considered are the type and thickness of the formwork, the time of formwork removal, the curing method, wind velocity, using insulation materials, the ambient temperature and solar radiation.

If the formwork covers the fresh concrete, [We1, War, Rec], the convection coefficient k may be calculated from:

$$k = \frac{1}{\dfrac{1}{\alpha_k} + \dfrac{h}{\lambda_f}} \qquad (2.16)$$

where: α_k is the convection coefficient computed according to equations (2.11) and (2.12)

h is the thickness of the used formwork (m)

λ_f is the thermal conductivity coefficient of a particular formwork material,

for wood it equals 0.14 $W/(m\ ^{\circ}C)$ according to DIN 4108 [Di1].

For a multi layer material equation 2.16 can be written as:

$$k = \frac{1}{\dfrac{1}{\alpha_k + \alpha_r} + \Sigma \dfrac{h_i}{\lambda_{fi}}} \qquad (2.17)$$

in which α_r the coefficient of heat transfer which allows for the effect of radiation $W/(m^2 \cdot {^{\circ}C})$, h_i the thickness of formwork or insulation in layer i and λ_{fi} the thermal conductivity of formwork or insulating material in layer i [Sp4].

Solar radiation can cause a quite significant increase in the maximum temperature obtained during hydration, especially when using a steel formwork. An example of the effect of solar radiation on concrete temperatures is shown in Figure 2.25. The curves a and b represent the concrete temperature at the surface of a wall made of an ordinary Portland cement-based concrete mix. The comparison between the curves a and b shows a variation in peak

temperatures at 18 *h* of about 6 *°C*. Upon cooling this could give rise to higher tensile stresses and enhance the risk of cracking.
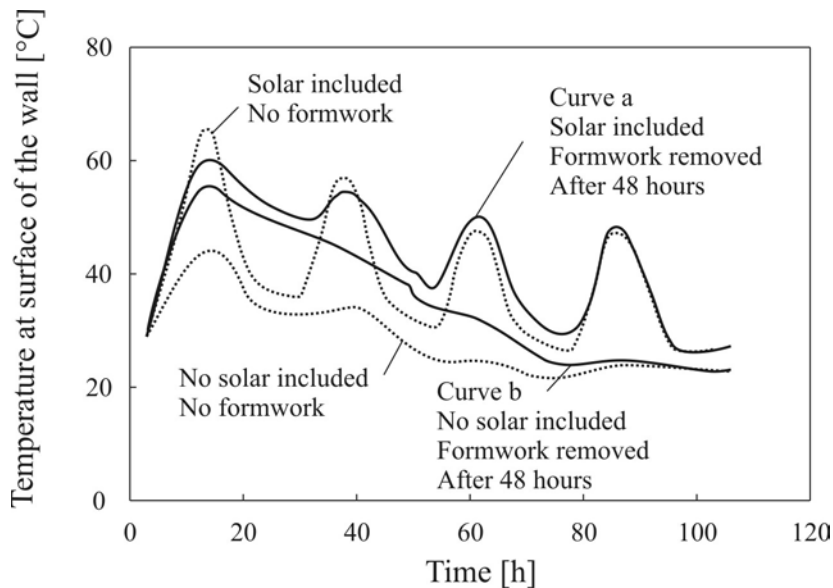

Figure 2.25 Effect of solar radiation on temperatures in hardening concrete structures. Ambient temperature variable [Sp4] – numerical analysis

Maybe the effect of wind is even more traitorous and detrimental than solar radiation. An indication of the effect of wind velocity on temperature development at the surface and in the centre of a 0.7 *m* thick concrete wall is shown in Figure 2.26.
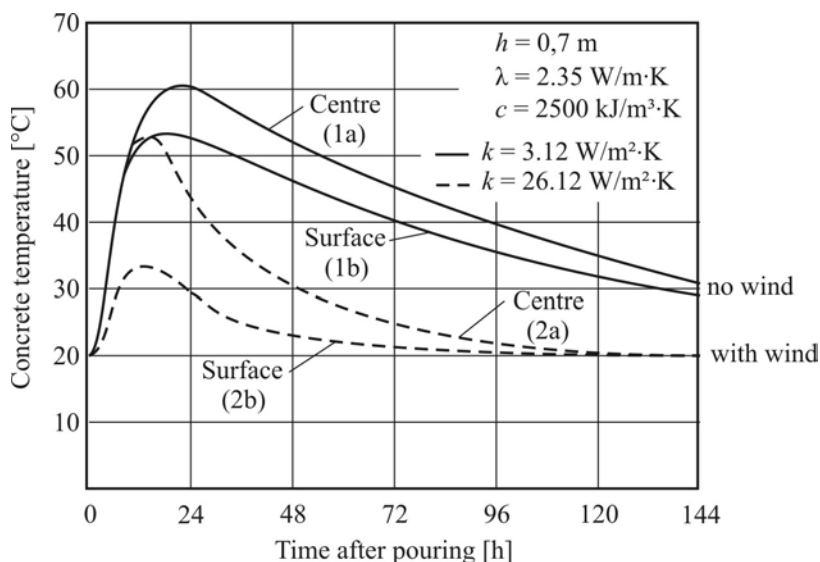
Figure 2.26 Effect of convection coefficient on temperature development in a 0.70 *m* thick wall using finite element model [Ham]

Curves 1*a* and 1*b* are estimated using a convection coefficient *k* of 3.12 *W/(m² °C)* with no wind, whereas curves 2*a* and 2*b* with *k* of 26.3 *W/(m² °C)* with wind velocity 5 *m/s*. In the first day the centre of the wall reached more than 60 °C (curve 1a) while the surface decreased 8 °C due to the convection (curve 1b). With wind the same wall experienced lower temperatures in the first twelve hours, the temperature reached about 52 °C in the centre of the wall (curve 2a) but it decreased to about 33 °C at the surface (curve 2b). Thereafter, the temperature decreased sharply compared to the no-wind case.

It is evident that the role of wind effects can largely influence the development of concrete temperature. Moreover the wind can create a severe thermal gradient between the surface and the centre of the wall. Thus, in the match-cast segment the negative gradient increased due to the wind velocity, which plays a role in bowing of the segment beside the thermal gradient resulted from the heat of hydration. One should bare in mind that the heat convection coefficient α_k is expected to be higher due to the free surface and no use of formwork around the old segment. Hence, the effect of the wind can be more severe.

Weigler and Nicolay [We1] studied the temperature and thermal stresses in normal and lightweight concrete due to development of heat of hydration. Concrete samples used with different thickness *h* = 0.4 *m*, *h* = 0.7 *m* and *h* = 1.0 *m* and covered with wood formwork with 2.5 *cm* thickness and isolation materials have been tested for more than five months to conduct the difference between the core temperature and the edge temperatures. The test samples can be seen in Figure 2.27.
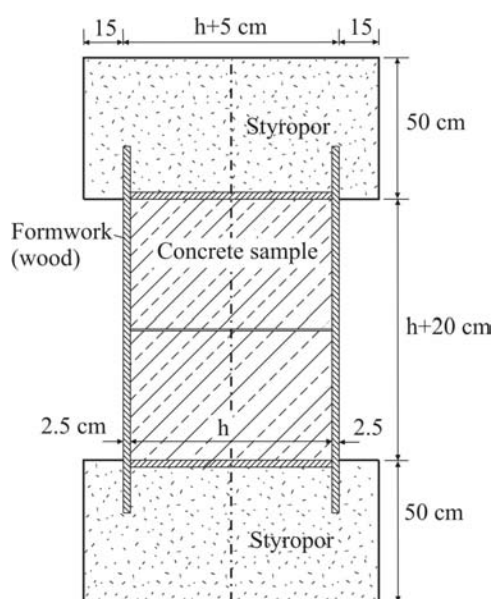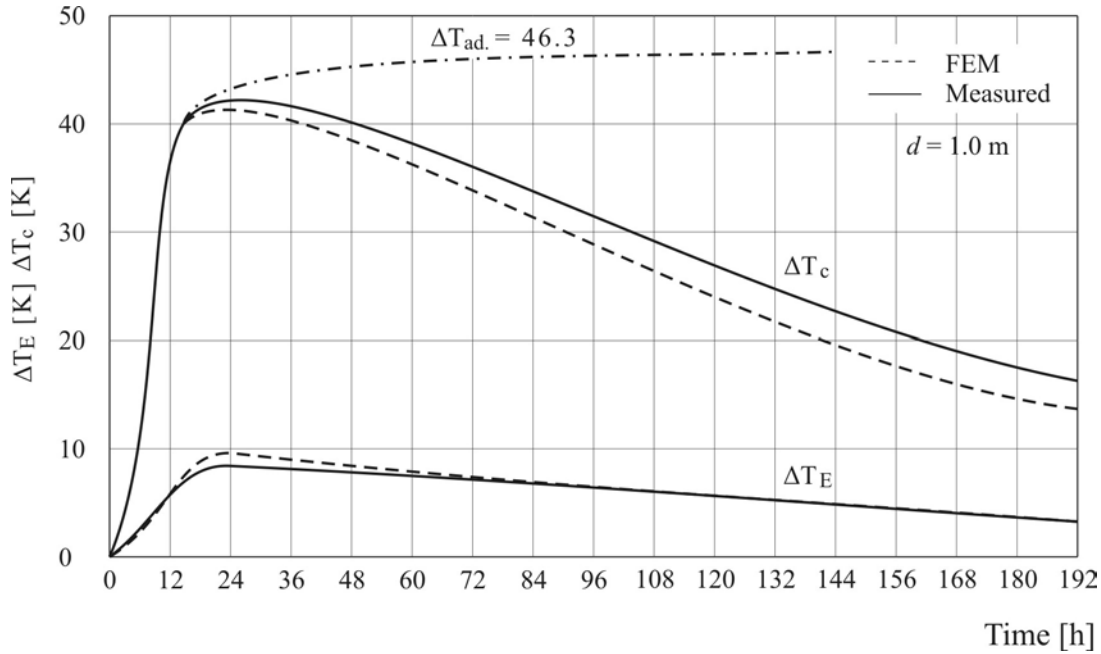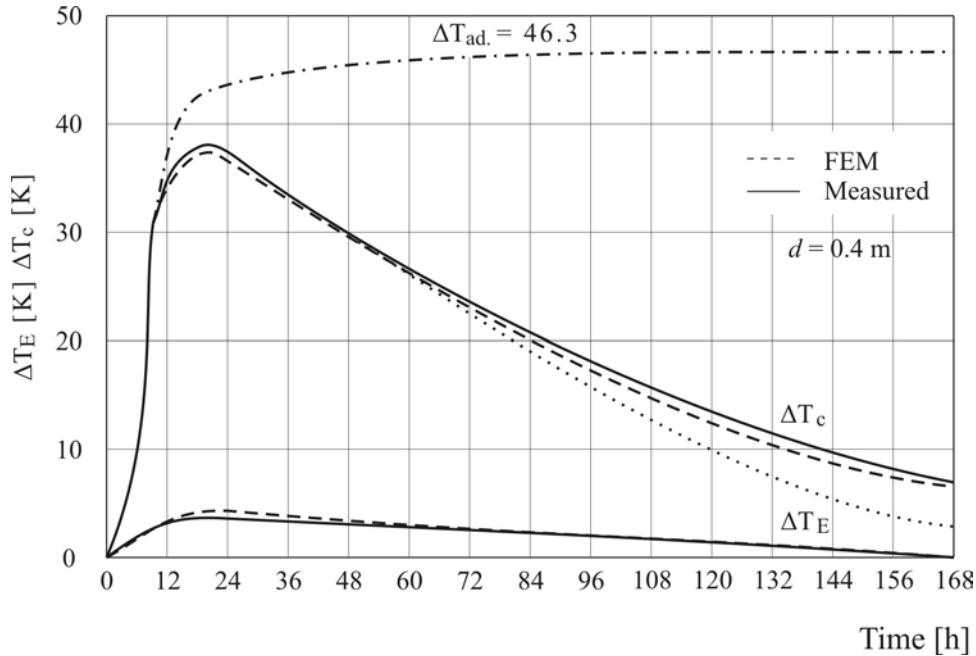

Figure 2.27 Concrete sample [We1]

The results showed that the more the thickness of concrete the higher the temperature as can be seen in Figure 2.28.

(a) $h = 1.0$ m

(b) $h = 0.40$ m

Figure 2.28   The development of temperature at the core ΔT_c and edge of the sample ΔT_E with $h = 1$ m (a) and with $h = 0.4$ m (b) [We1]

A good agreement between the experimental data and the numerical analysis can be observed. This demonstrates that the used concrete model is able to model reality.

In the match-cast segments higher temperatures are expected in the flange-web connections where more thickness of concrete is found.

2.3.6   Setting of concrete

The temperature gradient due to the heat of hydration causes a bowing of the match-cast segment. The fresh concrete will follow this deformation until it reaches enough strength. Thus, the setting of concrete is very important for the maximum value of bowing.

Setting refers to a change from a fluid to a rigid state. The terms initial set and final set are used in practice to describe arbitrarily chosen stages of setting. The setting time of concrete is a different property from the setting time of cement, and it can also be determined. ASTM Standard C403- 77 lays down a procedure, which uses a Proctor penetration needle applied to mortar sieved from the desired concrete. The setting time is arbitrary as there is no sudden advent of setting in practice [Ne1]. It is convenient in match-cast method to search for the setting which refers to the gain of enough strength of a set concrete to stop the concrete from flowing in the direction of the space produced from the bowing match-cast segment.

Figure 2.29 shows the development of strength versus time and the effect of the contribution of every chemical pure compound of cement in the stiffening process [Lea, Odl]. Moreover, C_3S and C_2S play an important role in the strength development, especially C_3S in the first few hours, which may accelerate the setting time of concrete.
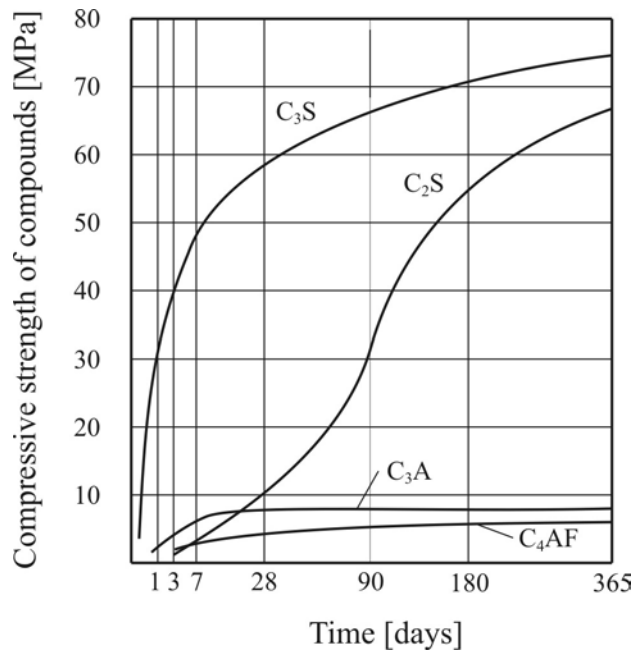
Figure 2.29 The effect of the pure compound of cement on the development
                 of strength of concrete [Lea, Odl]

Cervera *et al.* [Cer] studied the hydration process, the associated temperature rises, the
evolution of concrete strength and stiffness as well as the development of tensile stresses
and the possibility of cracking during the construction process.

Two models were proposed in a format suitable for its implementation in the general
framework of the finite element method to conduct the evolution of the chemical reaction of
concrete hydration as well as the heat generated during the process was thermo-chemical
model and to describe the evolution of the mechanical properties of the material during the
hydration process was aging model.

The aging model is introduced to account for the effect of the curing temperature in the
evolution of the relevant mechanical properties. Figure 2.30 shows the compressive strength
versus time curves obtained for the curing temperature $T_\circ$ = 12.5, 20, 35, and $50^\circ C$,
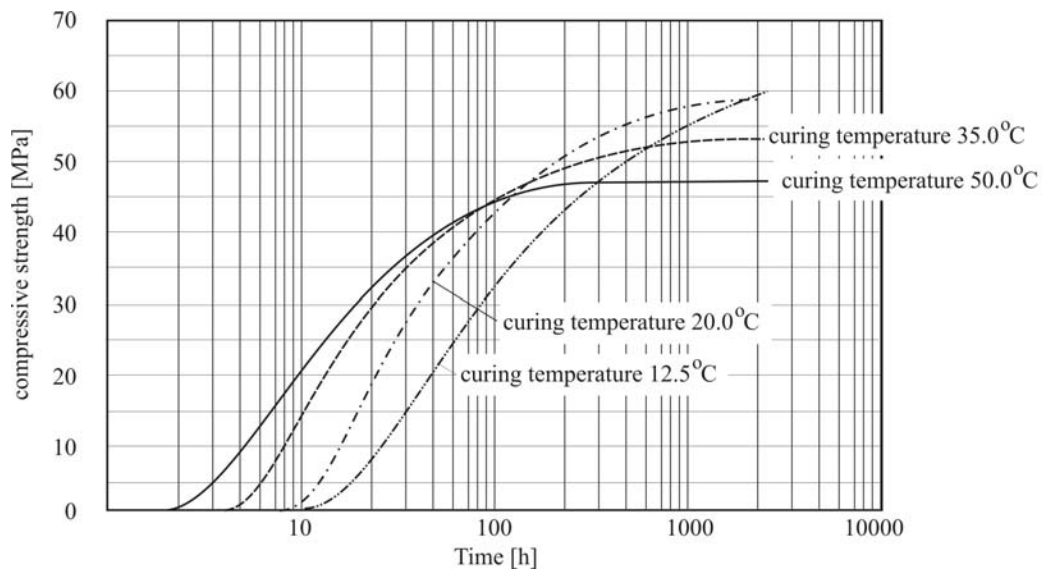respectively (test specimen: cylinder).

Figure 2.30 Compressive strength evolution at different curing temperatures [Cer]

Weigler and Karl [We2] conducted the behaviour of young concrete. The development of the strength of concrete under different conditions was studied. Concrete cylinders with 12 *cm* diameter and 25 *cm* length were tested at 8, 10, 12, 16, 24, 32 *hour*, 3 *days* till 14 *days* to investigate the development of the tensile strength. Figure 2.31 shows the tensile strength of concrete at different ages.
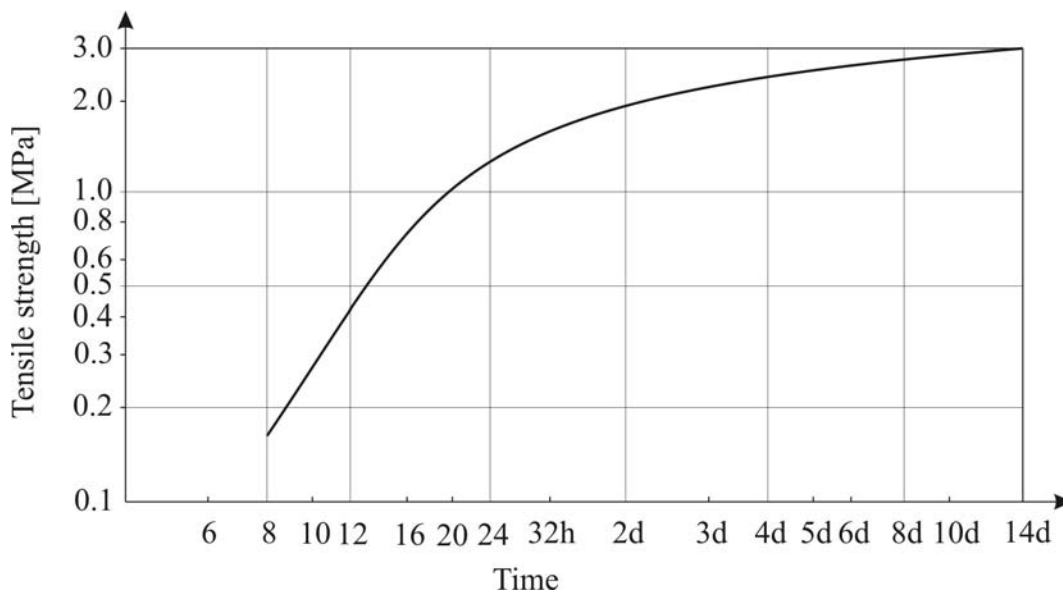

Figure 2.31 Development of tensile strength (*MPa*) versus time [We2]

Many investigations of the development of the mechanical properties of concrete made [Br8, Des, Man, Sp3] showed that the mechanical properties are developing rapidly and differently as can be seen in Figure 2.32.
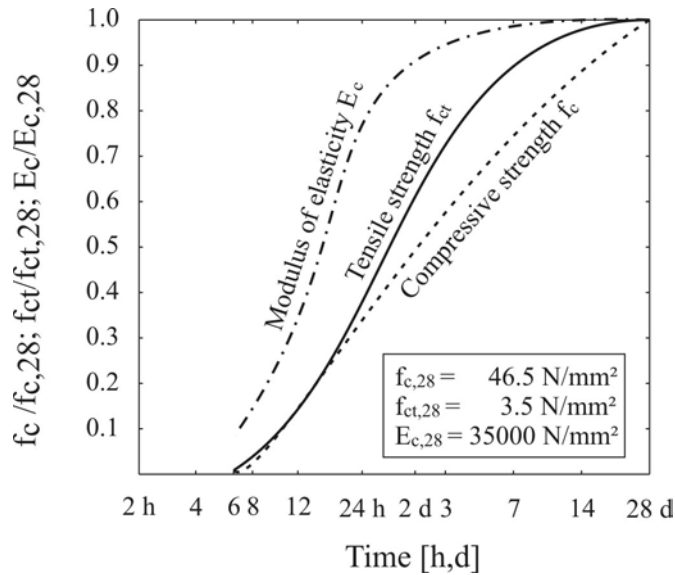
Figure 2.32   Development of compressive strength, tensile strength and modulus of elasticity versus time [Gut]

ACI committee [Ac1] conducted the development of the different strengths of concrete with respect to time as illustrated in Figure 2.33. The figure shows that almost 20 percent of the different strengths were developed in the first day.
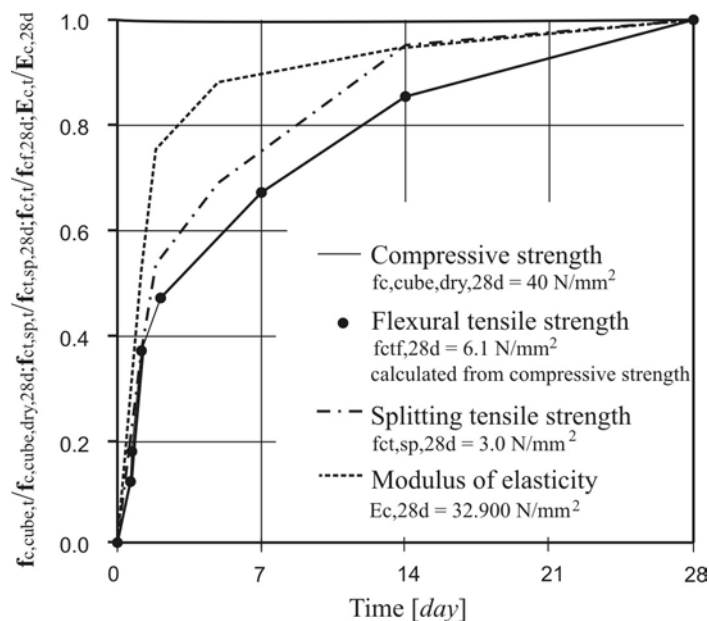
Figure 2.33 Temporal development of compressive strength, flexural tensile strength and splitting tensile strength as well as modulus of elasticity [Ac1, Ruc]

The Eurocode 2 part 1 [EC2] gives equations to estimate the development of concrete strength, tensile strength and elastic modulus versus time.

According to EC2 the compressive strength f_{cm} at a given time could be calculated from the average compressive strength f_{cm} at 28 days by:

$$f_{cm}(t) = \beta_{cc} \times f_{cm} \qquad \text{with } \beta_{cc}(t) = \exp\left[s \cdot \left(1 - \sqrt{28/t}\right)\right] \tag{2.18}$$

where: f_{cm} is the mean compressive strength after 28 days which can be obtained by experimental tests or can be expressed in term of the characteristic strength f_{ck} as: $f_{cm} = f_{ck} + 8 \ MPa$

   s is a coefficient depending on the type of cement
   = 0.20 for CEM 42,5 R, CEM 52,5 N and CEM 52,R N (class R)
   = 0.25 for CEM 32,5 R, CEM 42,5 N (class N)
   = 0.38 for CEM 32,5 N (class S)

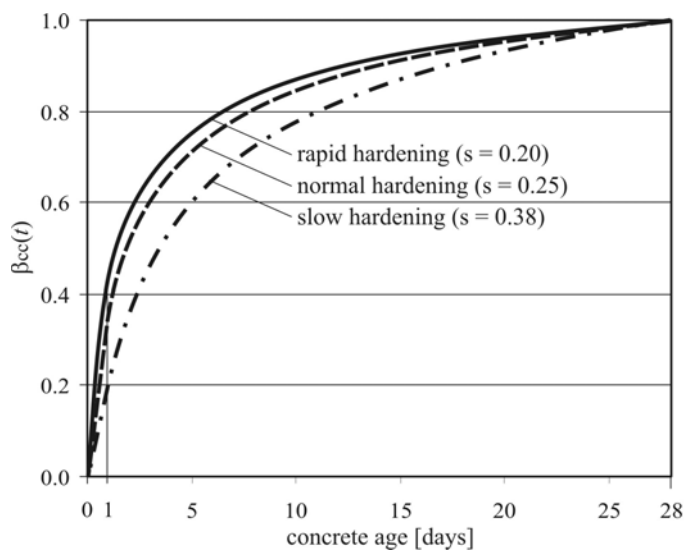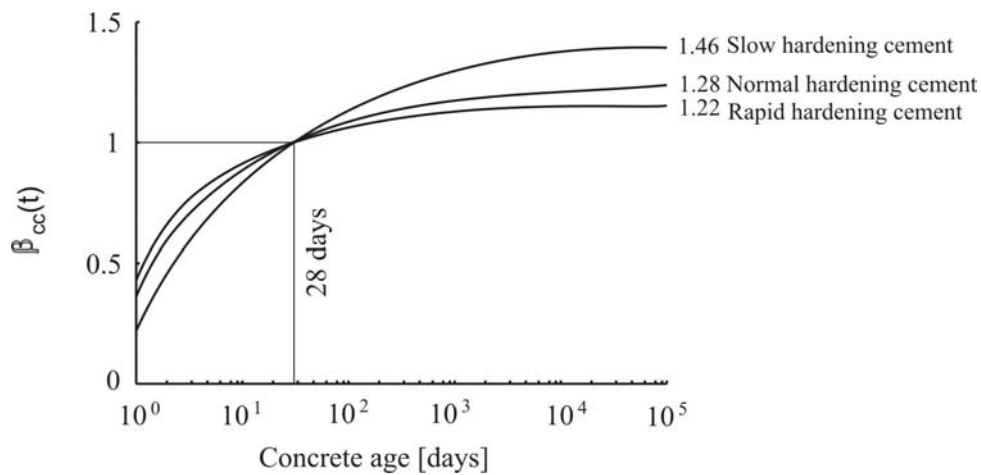 t age of concrete in days

Figure 2.34 Coefficient $\beta_{cc}(t)$ versus concrete age according to EC2

According to Eurocode 2 [Ec2] and German DIN 1045-1 [Di3] the mean tensile strength f_{ctm} as well as the elastic modulus of concrete E_c is related to the characteristic compressive strength.

$$f_{ctm} = 0.3 \cdot f_{ck}^{2/3} \qquad\qquad \text{for } f_{ck} \leq 50 \text{ MPa} \qquad\qquad (2.19a)$$

$$f_{ctm} = 2.12 \cdot \ln\left[1 + \frac{f_{cm}}{10}\right] \qquad \text{for } f_{ck} > 50 \text{ MPa} \qquad\qquad (2.19b)$$

The dimensions of a structural member, curing and drying conditions influence strongly the development of tensile strength of the concrete. The tensile strength can be expressed according to EC 2 [EC2] as:

$$f_{ctm}(t) = [\beta_{cc}(t)]^{\alpha} \cdot f_{ctm} \qquad\qquad (2.20)$$

where: $\alpha = 1$ for $t < 28$ days and $\alpha = 2/3$ for $t \geq 28$ days. For rapid, normal and slow hardening cement, the ultimate multiplication factors are 1.14, 1.17 and 1.28 respectively as t is approaching infinity (∞).

The secant modulus of elasticity can be expressed according to EC2 and DIN as:

$$E_{cm} = 2200 \cdot (f_{cm}/10)^{0.3} \quad \text{[MPa]} \qquad\qquad (2.21)$$

while the variation of the secant modulus of elasticity with time according to EC2 is:

$$E_{cm}(t) = \beta_{cc}(t)^{0.3} \cdot E_{cm} \qquad\qquad (2.22)$$
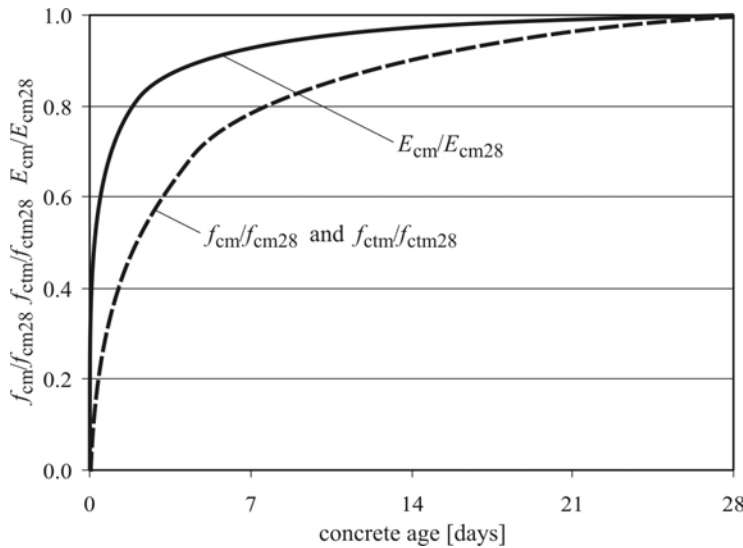

Figure 2.35 Temporal development of compressive strength, flexural tensile strength and splitting tensile strength as well as modulus of elasticity [EC2]

2.3.7   Thermal stress development

The studying of thermal stress development is important in a vast range of industrial and commercial applications [Po2, Spr4, Wis, Cer, Sch]. The physical explanation for the phenomenon is basically related to the simple fact that as the temperature of a material changes, the material expands or contracts. The well-known coefficient of thermal expansion is used to relate the two processes. The thermal expansion coefficient itself is determined from experiments on samples of the material free to expand or contract in an unrestrained manner. However, problems can arise when temperature changes occur in more complex structures because of the fact that in these cases thermal expansion is restrained. Accordingly, stresses are developed that are a potential threat to the integrity of the overall system.

Wischers [Wis] conducted a study of the development of temperature and variable thermal stresses in concrete due to the heat of hydration which could cause cracks especially if the difference is high between the thermal compressive stresses in the core of the structure and the tensile stresses in the edges due to the heating inside and cooling outside, as shown in Figure 2.36.
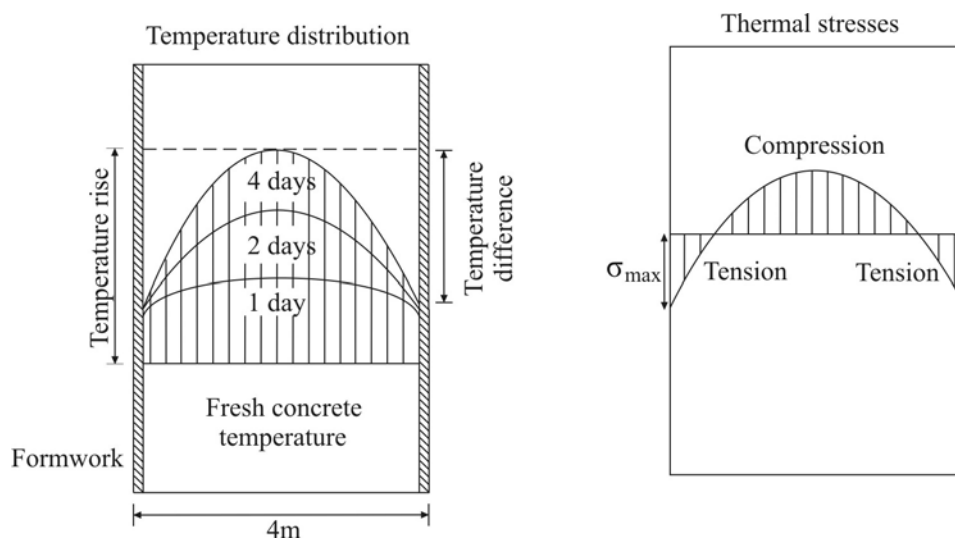

Figure 2.36 Typical temperature distribution and thermal stresses in a plate sample [Wis]

The numerical analysis of the problem is performed to follow the physical stress development as closely as possible. In the first step the unrestrained deformation that may take place in each element of the domain is calculated. This can be computed by multiplying the change in element temperature over a particular time interval by the relevant coefficient

of thermal expansion. These unrestrained deformations can be converted to strains and stresses using standard finite element methods. Again using standard finite element techniques the stresses can then be converted to equivalent nodal forces.

Since it is the structure's inability to allow unrestrained deformation that is the source of stress development in the material, these equivalent nodal forces are applied to the problem to restore its deformations to its original position. Thereafter these equivalent nodal forces act as real loading terms in the problem, and deformations as well as stresses from this loading can be estimated by means of a suitable finite element stress analysis. These deformations and stresses represent the real deformations and stresses that would take place in the problem under consideration. This approach is known as the initial strain method.

2.3.8   Method of calculating deformations (gap) in match-cast segment

The temperature recorded in the match-cast segment in the measurements taken in San Antonio segmental bridge and in Prescon's report (Br3) indicates a temperature gradient similar to that shown in Figure 2.37.
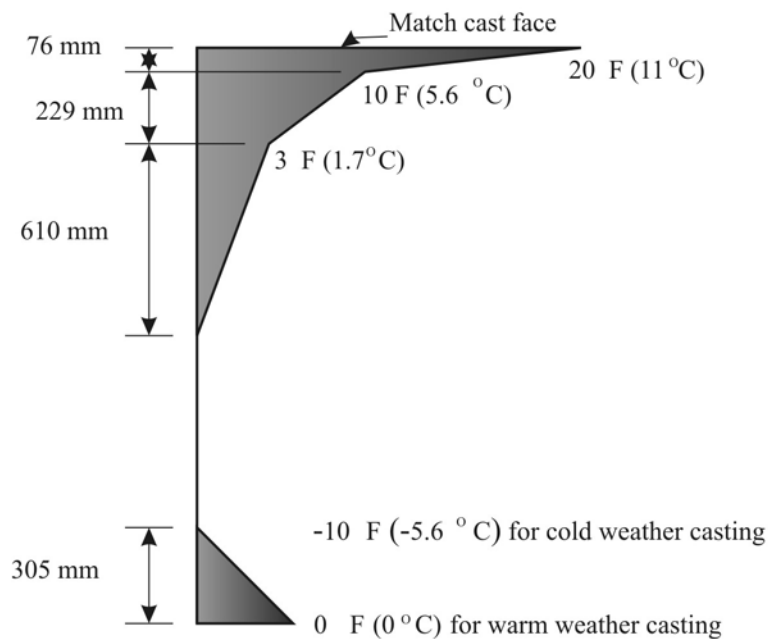

Figure 2.37 Design thermal gradient of segment [Br3]

Based on these values the maximum deflection can be calculated by first determining the equivalent moment, $M_{\Delta T}$, induced by the thermal gradient [Br3, Br4]:

$$\sigma_{temp} = E_c \cdot \alpha_T \cdot T(y) \tag{2.23}$$

The axial force, F_a, is calculated as:

$$F_a = \int \sigma_{temp} \cdot h(y)\, dy = \int E_c \cdot \alpha_T \cdot T(y) \cdot h(y)\, dy \tag{2.24}$$

The equivalent moment, $M_{\Delta T}$, is calculated as:

$$M_{\Delta T} = E_c \cdot \alpha_T \int T(y) \cdot h(y) \cdot y\, dy \tag{2.25}$$

where

T temperature difference between a point at a distance y from the centroid of the section and the centroid, ($^\circ C$)

h thickness of the section at a distance y from the centroid of the section, (mm) (see Figure 2.38)

α_T coefficient of thermal expansion of concrete ($\approx 12 \times 10^{-6}/^\circ C$)

y distance from centroid of section, (mm)

E_c modulus of elasticity of the concrete, (MPa)

b width of the segment in (mm)

The curvature of the elastic segmental deck can then be calculated as:

$$\phi = M_{\Delta T}/(E_c \cdot I_c) \tag{2.26}$$
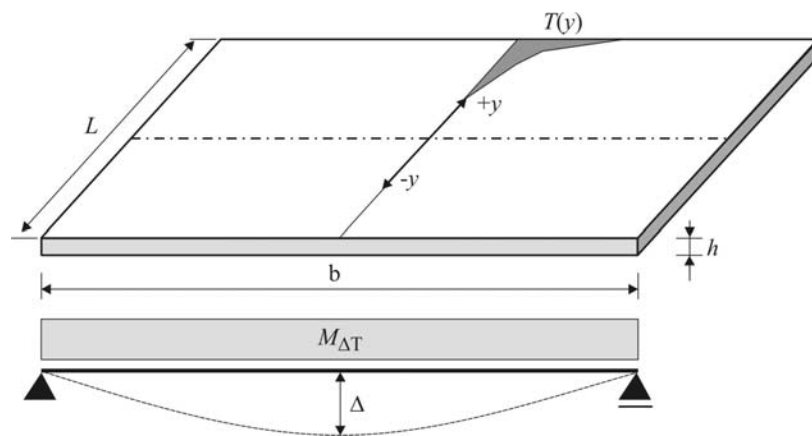
where: $M_{\Delta T}$ the calculated moment

             I_c moment of inertia of the section (slab), (mm^4).

Finally, the maximum deflection of the segment (gap) in (mm) is:

$$\Delta = \frac{\phi \cdot b^2}{8} = \frac{M_{\Delta T} \cdot b^2}{8 \cdot E_c \cdot I_c} \tag{2.27}$$

The above equations are only valid for slender slabs, where the shear deformation is not relevant. It is further assumed that the temperature is constant in transverse direction.
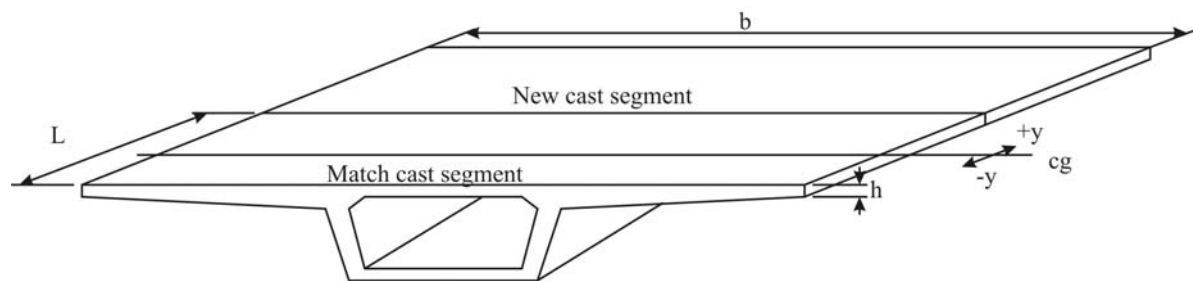
assumed equivalent structural system

Figure 2.37 Variables in segment dimensions

In chapter 3.3.2 this method of calculating the gap will be compared with experimental data of the San Antonio bridge, the Bang Na Expressway and numerical values.

Please note that the thermal gradient of the match-cast segment must be known for the analytical estimation of the gap. The gradient is hardly dependant from many parameters like geometry of the segment, type of concrete, curing and ambient temperature. Thus, measurements on site or thermal finite element analysis as presented in chapter 3 are required to use this simple method.

2.4   Effective flange width and shear lag

The stress distribution in the deck of a hollow box girder segmental bridge must be known to check the permissible compressive strength of concrete and to check the minimum compressive stresses joint. The bowing of a segment will change the longitudinal stresses in the top slab. Therefore the non uniform stress distribution in the slab of a T-beam or hollow box girder due to bending will be discussed in the following.

For a beam or box subjected to bending the cross-section is assumed to remain planer with a linear variation in stress over the section depth and a constant stress at any one level. When flanged beams are subjected to high shear, such as adjacent to supports, the bending in the section can result in a non-uniform distribution of longitudinal stresses across the flanges.
The axial stresses resulted due to bending moments in the box-girder bridges develop initially in webs, a large shear is transmitted from the vertical webs into the horizontal flanges, which can cause longitudinal shear deformations in the flanges. This behaviour leads to higher longitudinal deformations near the wingtips of the flanges and near the centreline of the top and bottom slabs, as illustrated in Figure 2.39. This phenomenon, which results in a non-linear distribution of stresses across the flanges, whereas the beam theory conducts a uniform stress, known as shear lag or stress diffusion. In wide sections the shear lag may be more significant and could affect the maximum stresses in a segmental box-girder bridge and it should not be neglected.
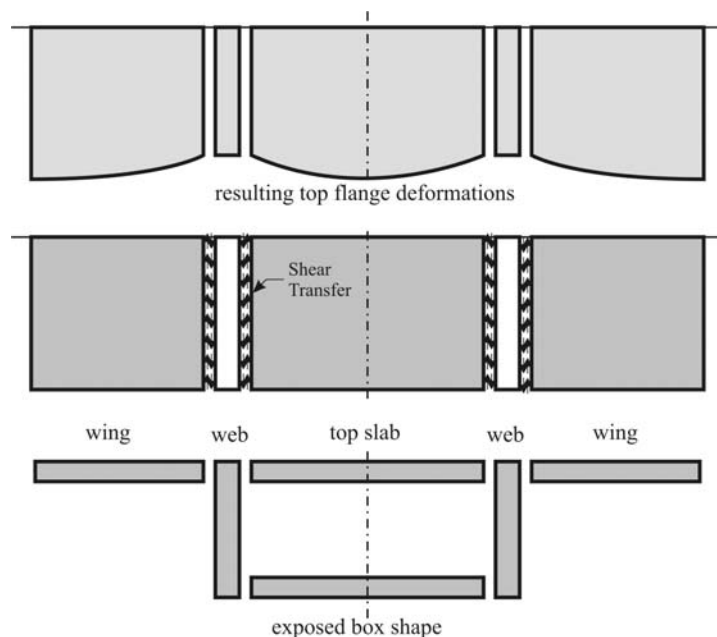

Figure 2.39 Shear lag [Br3]

In spite of the actual longitudinal compression varies because of this effect, it is convenient in design to make use of an effective flange width, which may be smaller than the actual flange width but is considered to be uniformly stressed at the maximum value, as can be seen in Figure 2.40.

This effective width b_{eff} has been found to depend on the effective span length l_0, on the relative thickness h_{eff} of the slab and the type of loading (uniform load, single load). The effective flange width is then defined as that width which can resist a longitudinal force equal to the actual force in the flange, if the longitudinal stresses across the flange were constant and equal to the actual maximum stress.
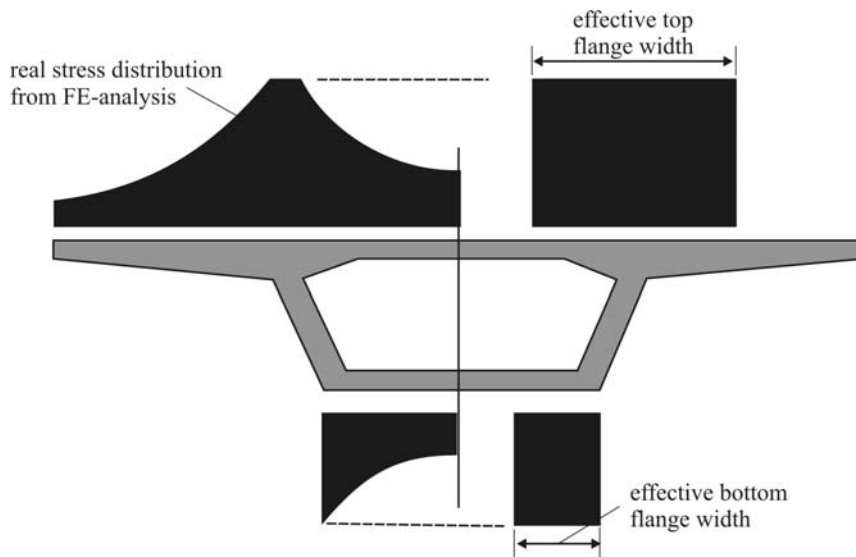

Figure 2.40 Effective flange width [Br3]

According to German Code specification procedure [Di2] for the determination of internal force variables a constant effective width of the flanges over each span can be assumed for simplicity considering the value at mid-span of the analyzed span. The bearing capacity of cross-sections in the final state has to be considered by evaluating the different effective widths for field, support and cantilever ranges according to effective span lengths. The procedure requires firstly an effective span length l_0 be determined. The effective span length l_0 can be taken equal to the distance between the two zero moment points, for a simple span the effective span length is taken equal to the actual span length (l_{eff}). For end

spans in continuous girders, it is taken as 0.85 l_{eff} and for interior spans it is taken as 0.7 l_{eff}. Figure 2.41 shows the effective span length determination.
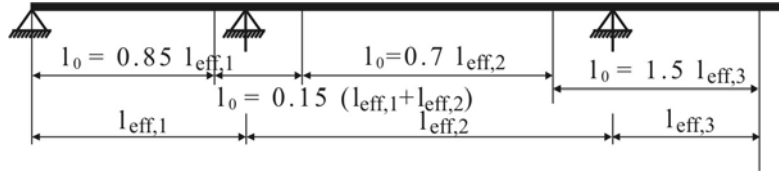

Figure 2.41 Determination of effective span lengths [Di2]

Once the effective span length is determined, each effective flange width can be calculated as:

$$b_{eff} = \sum b_{eff,i} + b_w \tag{2.28}$$

$$b_{eff,i} = 0.2b_i + 0.1 \cdot l_o \leq 0.2l_o \tag{2.29}$$

and $b_{eff,i} \leq b_i$

where: l_o the effective span length

b_i the real flange width

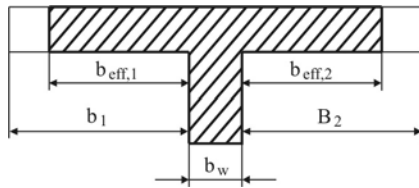b_w the width of the web, as can be seen in Figure 2.42, 2.43

Figure 2.42 Details of the effective flange width [Di2]

In flanges with variable thickness, the web width b_w in previous equation could be increased according to Figure 2.43. The web width is taken equal to ($b_w + b_v$).
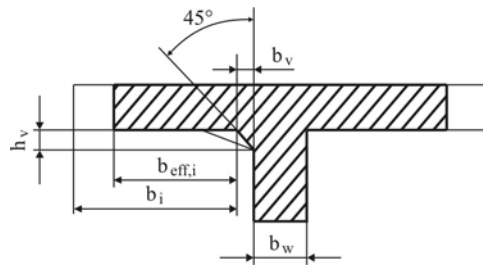
Figure 2.43 Flange with variable thickness [Di2]

The DIN-specification also supplies information on determining cross-sectional properties to be used in estimating normal stresses. Simple beam theory assumes a uniform distribution of the post-tensioning forces immediately ahead of the anchors, but in fact, it needs a distance along the length of the bridge for the post-tensioning forces to diffuse across the section. Figure 2.44 shows the recommended $35°$ angle of diffusion of the post-tensioning forces.
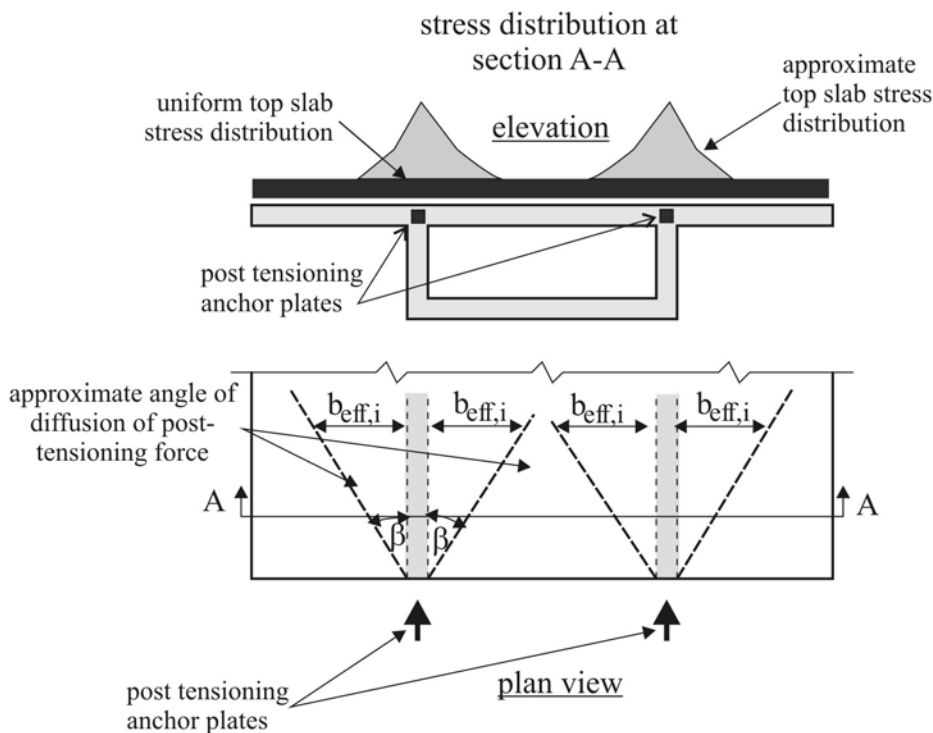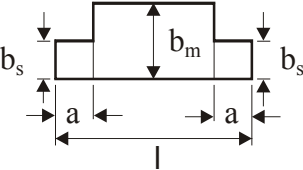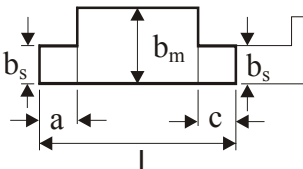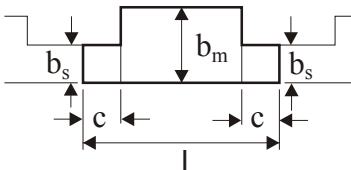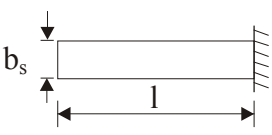

Figure 2.44 Diffusion of concentrated post-tensioning anchor forces [Di2]

The AASHTO approach for determining effective flange widths for bending is nearly the same as that in the German Code specifications, as seen in Figure 2.45.

System	Pattern of Effective Flange Widths	Effective Span Length
Single-Span Girder		$l_i = 1$
End Span of Continous Girder		$l_i = 0.8\, l$
Inner Span of Continous Girder		$l_i = 0.6\, l$
Cantilever Arm		$l_i = 1.5\, l$

a = largest b, but not exceeding 0.25 l
c = 0.1 l

Figure 2.45 Determination of effective span lengths l_i [Aa1]

In general the stress distributions across the width of the flanges are the sum of three load effects. The shear lag related to uniformly distributed dead and live loads causes stress distribution at the mid-span as can be seen in Figure 2.46, meanwhile we can see the stress pattern caused by the transverse diffusion of post-tensioning anchorage loads in Figure 2.47. When the load is applied, the dead and live loads moments and post-tensioning moments may balance each other. Because of the fact that the moments are balanced, the peak stresses caused by shear lag maybe smaller. Thus, the stress distribution is dominated by the diffusion of post-tensioning forces from the anchorages.
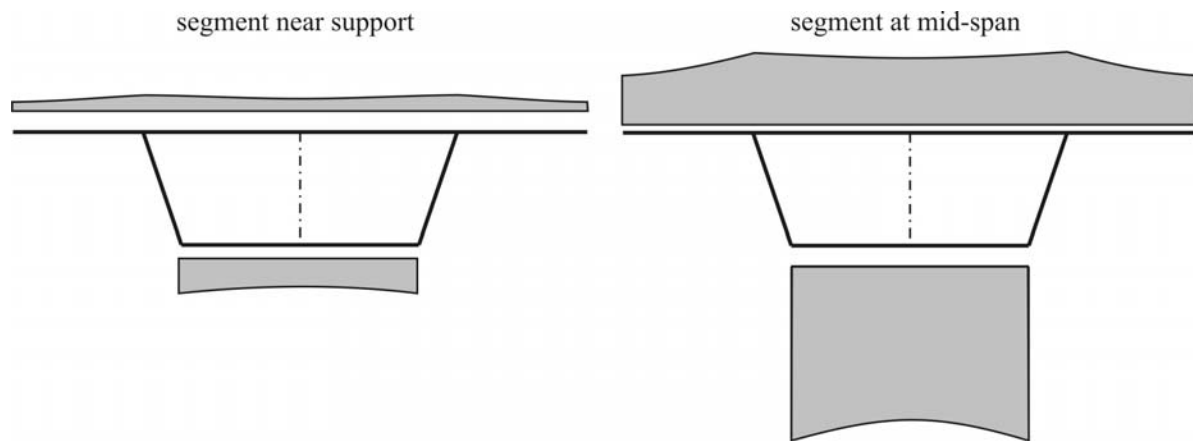
Figure 2.46   Stress distribution due to dead and live loads in a perfect fitted segment [Br3, Fig. 5.23]
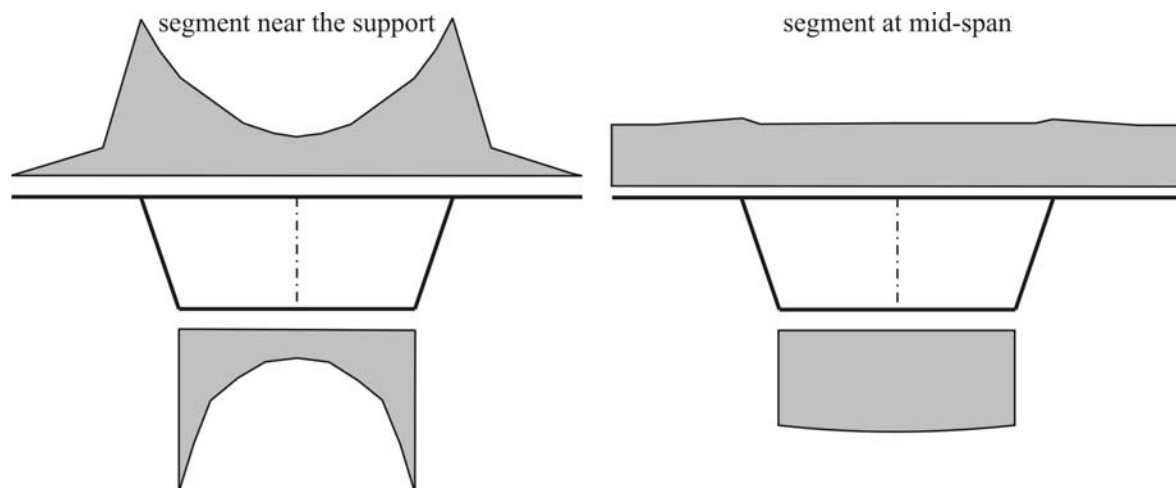

Figure 2.47   Stress distribution due to post-tensioning axial load in a perfectly fitted segment [Br3, Fig. 5.23]

In order to study the problem of shear lag and transverse diffusion of post-tensioning forces, three spans of the San Antonio Project were instrumented by Breen et al [Br3] with five locations of concrete mechanical strain gages. In addition, tendon forces and deflections were also measured.

The results computed from the actual measured strains were then compared with results estimated from three analysis methods:

   1- Simple beam theory.

   2- AASHTO Guide Specification.

   3- A simple computer program called SHLAG (not finite element method!).

The comparison between the calculated and measured stresses indicated that there was no good agreement between them. However, the SHLAG program gave closer results to the measured peak stresses than the beam theory or the AASHTO effective flange width method. SHLAG predicted on average 84% of the measured peak stresses. Simple beam theory gave a constant distribution of the stresses, which it indicates that it cannot be applied in such problems.

The most important factor in the whole life design of reinforced and prestressed concrete bridges is the Serviceability Limit State. Prestressed concrete bridges are very sensitive to long-term increase of deflections. Large bridges (more than 100 m span) built by cantilever method exhibit in many cases a gradual increase of deflections during a very long time of service life. This phenomenon has paramount importance for serviceability, durability and long-time reliability of such bridges. This is why a reliable prediction of deformations of bridges during their construction as well as during their service life is extremely important. Longitudinal stresses in prestressed concrete deck change at each stage of construction and throughout the structure's design life. The stress in the concrete must be kept within allowable limits for both compression and tension.

The stress levels along the length of a deck are checked at all the critical stages in the structure's life. This would normally include [Nig]:
    (a) At transfer of the prestress to the concrete
    (b) During each stage of construction, with temporary loads applied
    (c) At bridge opening, with/without full live load
    (d) After long-term losses in the prestress and full creep redistribution of moments have occurred

According to DIN the factored nominal forces in the tendons, $r_{inf} \cdot P_{m,c+s+r}$ and $r_{sup} \cdot P_{m,c+s+r}$ are considered at specific times, and used when carrying out the serviceability limit state checks. When external tendons are used, the design of the deck should be checked for the case that if any of the two tendons are removed, it should be necessary to replace them in the future. In this case a reduced live load is normally considered to reflect traffic management systems that may be implemented.

In precast segmental construction with match-cast joints the longitudinal reinforcement is not continuous, and it is normal to ensure that the joints remain in compression under almost all loading conditions both during construction and in the permanent structure.

For precast construction, with elements connected using unreinforced concrete or mortar infill, the complete area of the connection is kept in compression to ensure that the joint is held together [Nig, Aa1, BMV].

Deflections of the concrete deck occur due to self-weight and prestress, and from the weight of the quasi-permanently applied loads. Additional movements occur due to long-term creep of the concrete and losses in prestress. The deflections due to the prestress are often greater than, and in the opposite direction to, the dead-load deflections. This results in the deck deflecting (camber) upwards upon application of the prestress and removal of the formwork. Subsequent application of the superimposed dead load and long-term losses in the prestress force reduce this upwards deflection or can result in a net sag deflection.

Creep of concrete can cause the deck to change its profile over its design life and it is usually aiming to achieve the proposed alignment at the time of bridge opening or at time infinity, although the changes in deflections should be checked along time to ensure that they are not excessive.

The adjustment made to the profile during casting to achieve the desired shape is called the pre-camber, and it is achieved by the overall design, the construction process and the concrete properties.

The balance between the dead loads and prestress normally results in small upwards deflections. Deflections are usually not important for normally proportioned prestressed decks designed with stresses within the allowable limits and they do not need to be checked, but in case to confirm the pre-camber values. It is desirable form a visual viewpoint for a span to appear to be hopping rather than sagging. In order to ensure hopping on straight decks small upwards profile is often built into the deck along each span by adjusting the pre-camber. The upward profile used is normally few centimeters at mid-span.

A numerical model is needed to simulate the behaviour of box-girder bridges especially if there are gaps between two adjacent segments, which effect significantly the distribution of the longitudinal stresses. Hence, at the beginning the compressive stresses may concentrate at the tip regions of the flange, then, due to elastic deformations and long-term factors the

gaps begin to close with time. The stresses redistribute as the joints close gradually depending on the amount of longitudinal stresses and value of gaps between the joints.

As a result of this unavoidable phenomenon many problems can arise:

1. It is important to consider the distribution of normal stresses over the actual section to ensure the full width of every joint is within allowable stress limits especially at the beginning of loading.

2. The design of segmental bridges states that all joints must be completely under compression, the AASHTO [Aa3] and German specifications [Bmv] state 1.4 MN/m^2 and 2 MN/m^2 minimum compressive stresses respectively under certain load combinations. The existence of spaces in dry joints could detrimentally affect the durability of the structure. In the case of applying epoxy between the joints, a minimum amount of compression stresses using temporary pre-stressing should be considered.

3. The transverse diffusion of post-tensioning forces must be considered when laying out post-tensioning anchors to ensure adequate compression across all joints.

4. As the gaps between the joints are closing with time, more post-tensioning losses in the longitudinal tendons are expected.

5. During designing a pre-stressed bridge, a camber (upward deflection) in the span is desired to achieve the correct alignment at time infinity. As a result of the gaps between the joints the value of camber decreases and may result in downward deflection.

3   Experimental investigations and numerical simulation of match casting

In this chapter the approaches and measurements made to conduct the bowing effect as well as to estimate the temperatures and deformations during the match-cast process of San Antonio and Bang Na segmental bridges will be presented. Thereafter, a numerical simulation of the match-cast process and the transient thermo-mechanical process will be introduced. The purpose of the numerical model is to estimate the mechanical deformations caused by the thermal stresses and the deformations developed due to heat of hydration and ambient temperature changes. Dead and service loads are ignored in this study.

In order to verify the thermo-mechanical model, the numerical results will be compared with measurements taken in San Antonio and Bang Na bridges. The numerical model will also be compared to an analytical approach based on the equivalent moment formula. An example will be presented. A simple method for practice to estimate the temperature gradient in the match cast segment will be given which can avoid the need of complex finite element analysis.

The influences of the geometry width to length ratio (w/L) and the boundary conditions, such as: the ambient temperatures, wind speed and age of the old and fresh concrete on the bowing effect will be discussed in details.

3.1   The San Antonio "*Y*" Project

The name of the San Antonio Segmental Bridge "*Y* Project" comes from the shape of the intersection of interstate highways. More than three lanes of new highway for both inbound and outbound traffic are provided in the final project [Br3]. The whole project was separated into many phases, six of which included segmental bridge construction as can be seen in Figure 3.1. The plans for the various phases were let at intervals beginning with Project *IA*. The six phases have had a wide variety of box shapes and tendon layouts. The most changed variables were the width of the bottom of the box, from 1.83 *m* to 6.4 *m,* and the width of the wingspan, from 7.92 *m* to 18.28 *m* (Fig 3.2).
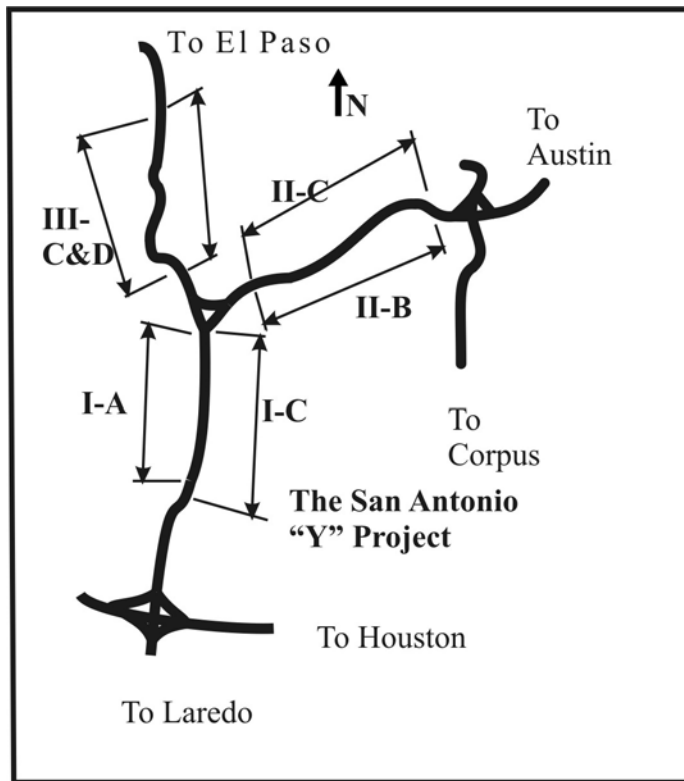
Figure 3.1 Phasing of the San Antonio "*Y*" Project [Br3]

a) Type *I segment* (*w/L* = 3)

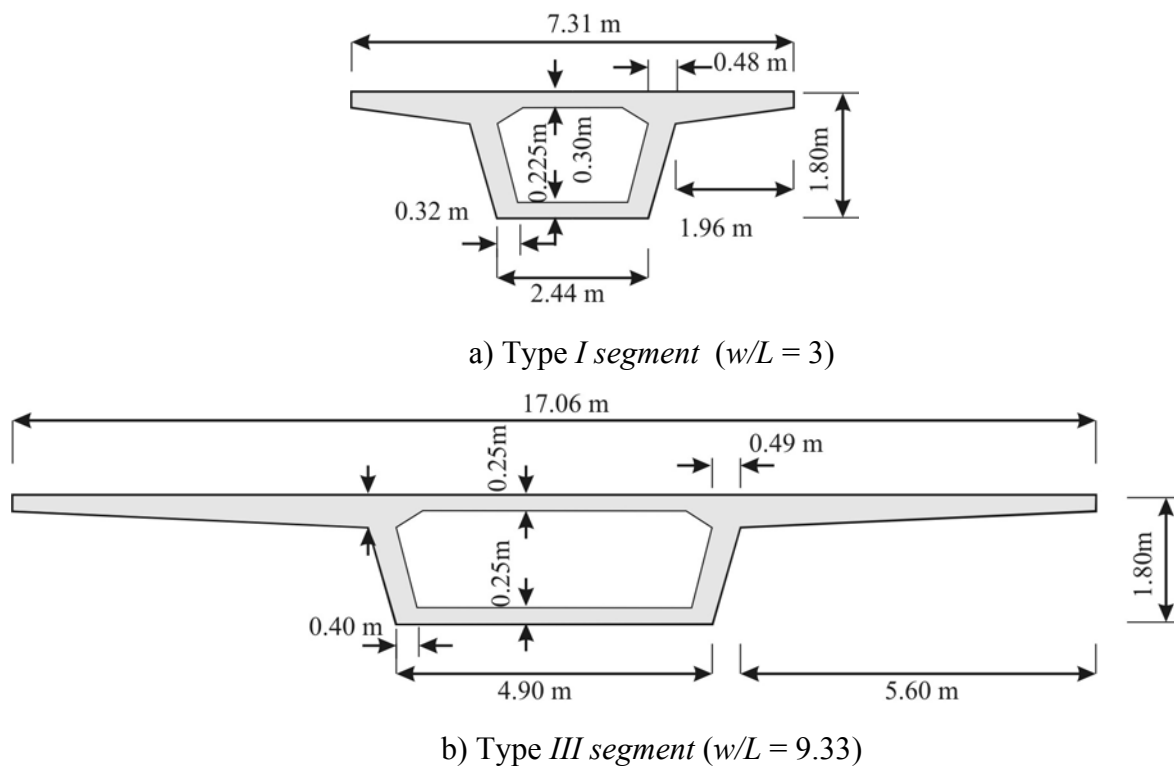b) Type *III segment* (*w/L* = 9.33)

Figure 3.2 Standard segments and dimensions

3.1.1   Description of measurement program

Four pairs of segments of the San Antonio *"Y"* Project *IIC* were instrumented with thermocouples and deformation measurement systems. The cross-sections and details of the two pairs of segments, *IIC*-4 and 5 and *IIC*-8 and 9, shown in Figure 3.2 (a) were type *I* segments with 7.3 *m* width and 2.4 *m* length (*w/L* = 3). Whereas the other two pairs, *44A*-5 and 6 and 44*A*-14 and 15, were *type III* segments with 17.1 *m* width and 1.8 *m* length (*w/L* = 9.33) are shown in Figure 3.2 (b).

Two series of eight thermocouples were placed in each pair of segments as can be seen in Figure 3.3. One array ran through the wing, whereas the other ran through the thickened top slab-web-wing juncture where the temperature was expected to be the highest.

Figure 3.4 shows the deformation measurement system including brackets at each wing tip to which a piano wire was connected. A ratcheted spool was provided with one bracket, which would pull and hold the piano wire very firm. Rulers and small mirrors were placed in the match-cast segment. The wire ran about 12 *mm* above the embedded rulers. The mirrors were used to ensure repeatable readings; measurements were taken at 1-hour intervals starting directly after the completion of the casting of concrete process. The reading of the concrete temperatures in the new and match-cast segments was taken at hourly intervals similarly.

At the time of casting the match-cast segment was approximately 24 hours old. The temperature of the fresh concrete was between 29 to 32 $^{\circ}C$ and it started to increase up to about 60 $^{\circ}C$.

The ambient temperature can strongly affect the heat of hydration. The measurements of the San Antonio segments showed that the concrete closest to the old segment warms faster than the more distant new concrete, because the other parts were subjected to convection and had lower ambient temperature (Fig. 3.5). Please note that the measurements of the BBBE segments showed a different time dependant behaviour. In Thailand, the ambient temperature was around $32^{\circ}C$ and nearly constant of the whole time. Thus the temperature was greater in the middle of the deck than at the joint (Fig. 3.11).
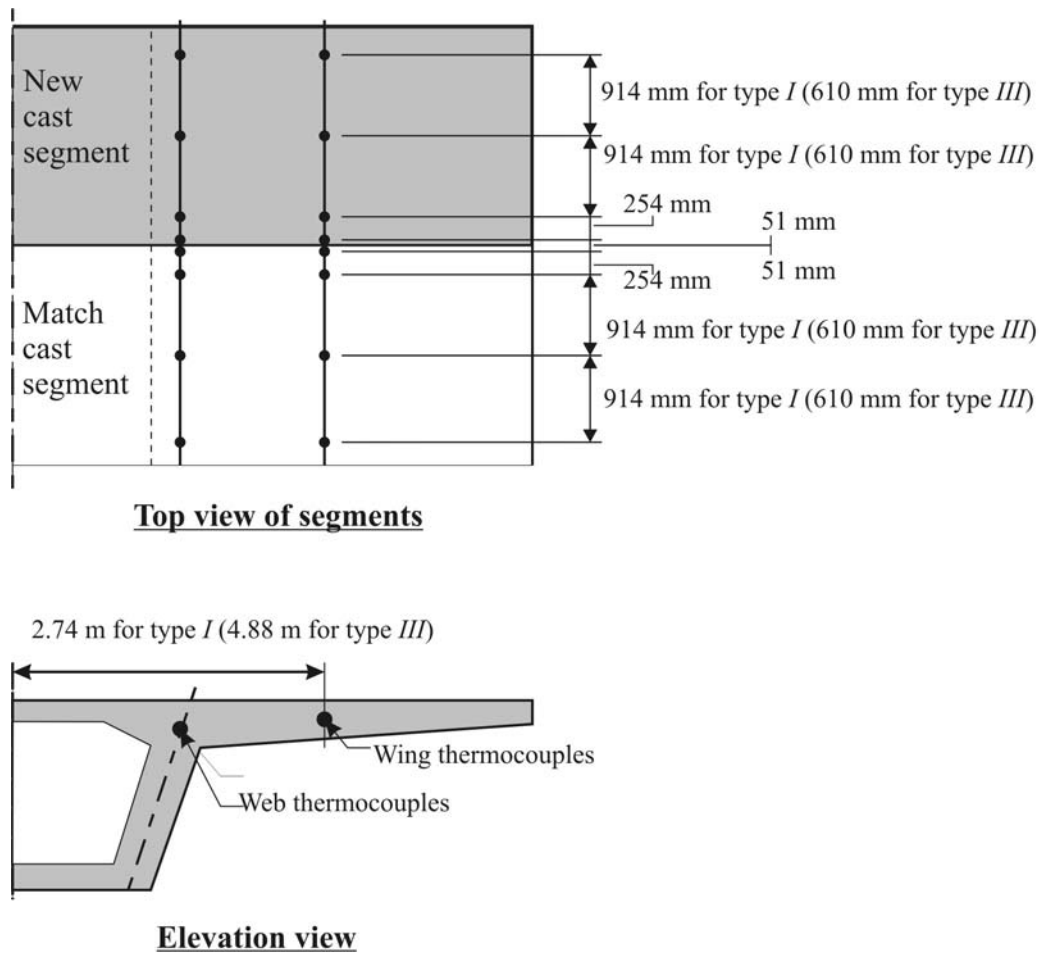
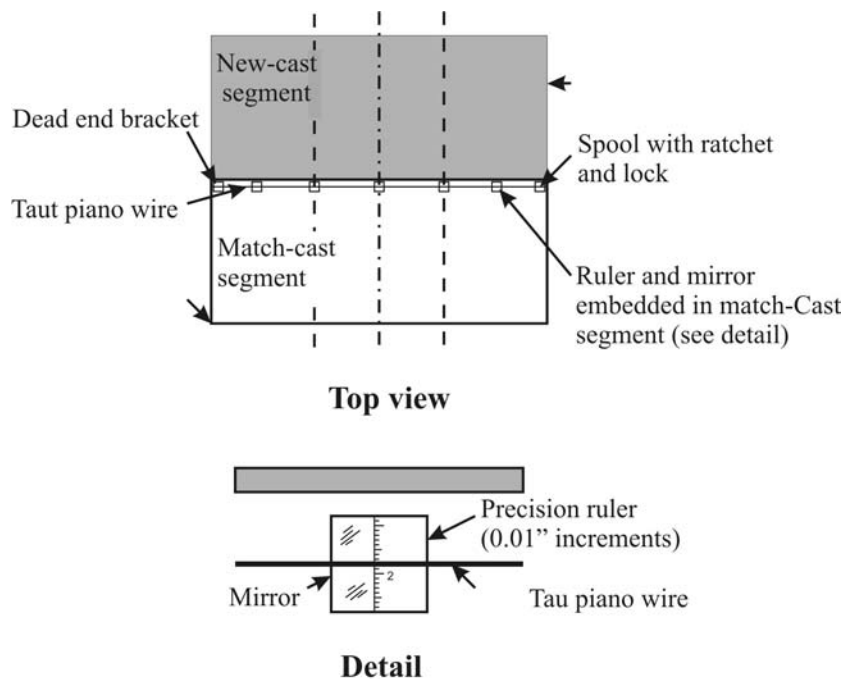**Figure 3.3** Typical thermocouple layout in segments [Br3]

Figure 3.4 Deformation measurement system of new and match cast segments [Br3]

Figures 3.5 and 3.6 show typical plots of temperatures in the new and match-cast segments and the deformations at different periods resulted in the decks for type *I* and type *III* segments respectively. The temperatures recorded by the measurement stations after the completion of casting are used as reference between the subsequent and the initial recordings. This difference is called thermal gradient, which can be positive and/or negative. The total differences in temperatures between time of cast and around 8 hours later were remarkable, but on the free face the temperature started to cool due to the decreasing in the ambient temperatures.

The horizontal deformed shapes estimated by the wire system showed significant deflections in segment (type *III)* with higher (*w/L*) compared to segment (type *I*). Because of a low precision of the rulers (± 25 *mm*) the different curves could not be well distinguished.
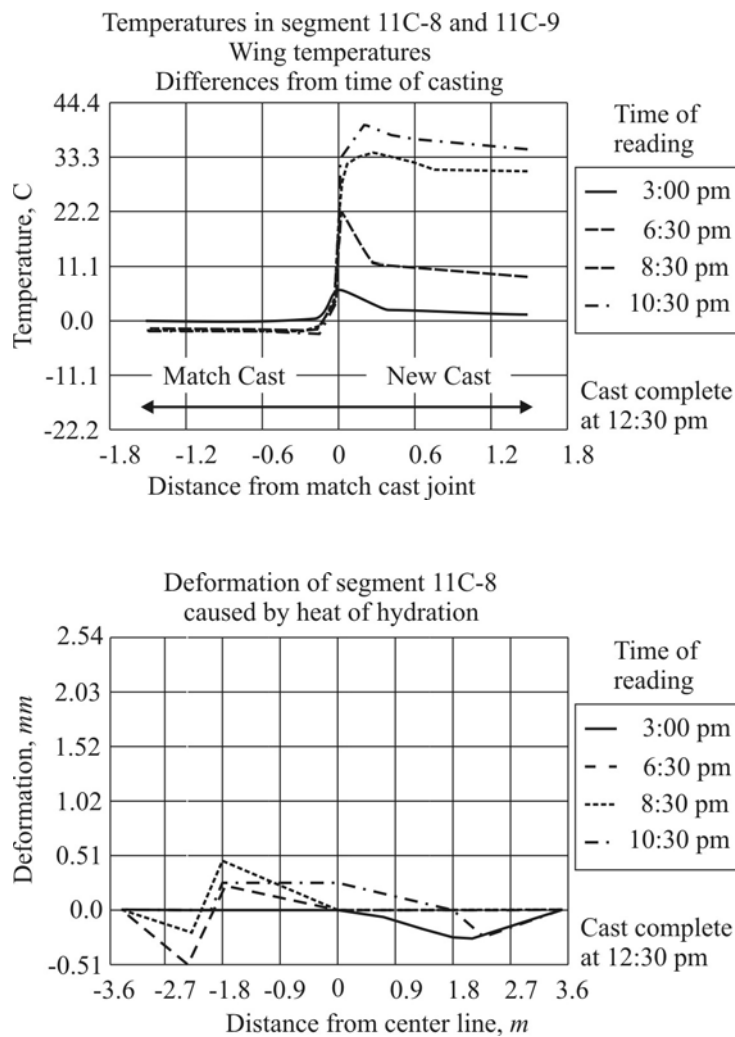

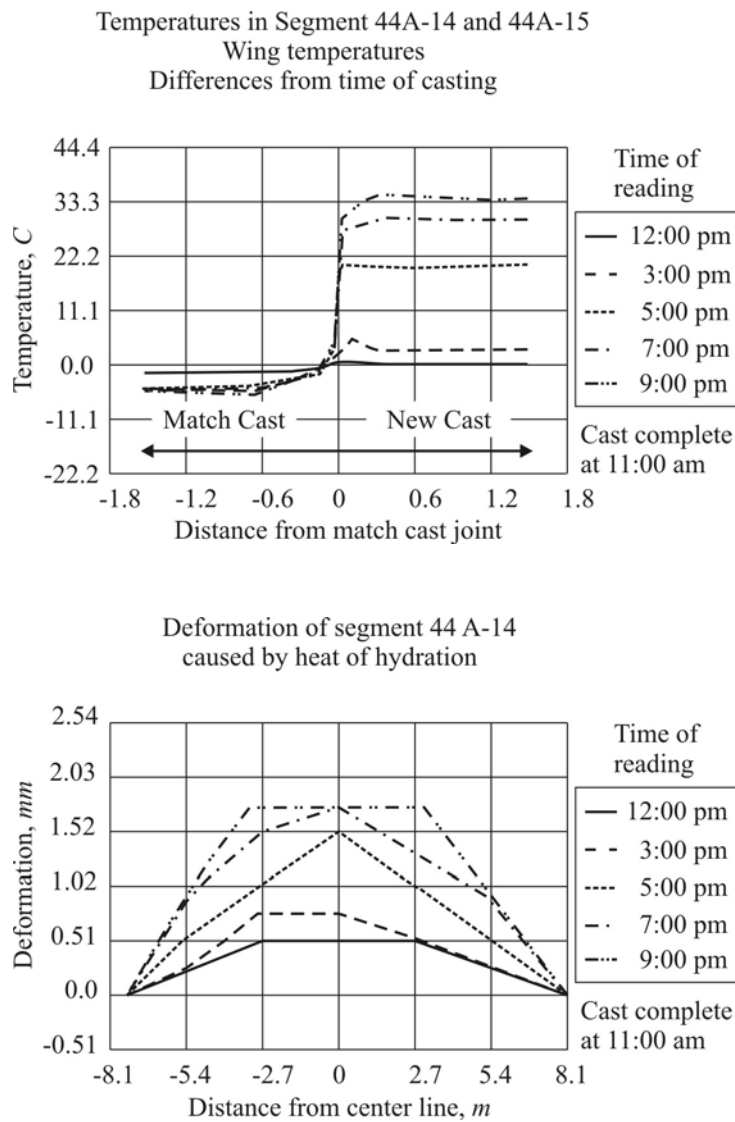**Figure 3.5** Measurements taken in segment type *I* [Br3]

Figure 3.6 Measurements taken in segment type *III* [Br3]

3.2 The Bang Na Expressway, Bangkok.

The Bang Na - Bang Pli - Bang Pakong Expressway (BBBE) in Thailand is a 55 *km* long mainline extremely slender type of externally post-tensioned segmental bridge. The BBBE has 18 segments per span with 27.20 *m* width and 2.55 *m* length (*w/L* = 10.7) for standard segments and 1.25 *m* length (*w/L* = 21.8) for pier segments which accommodates all traffic lanes. A standard segment of the Bang Na bridge can be seen in Figure 3.7.
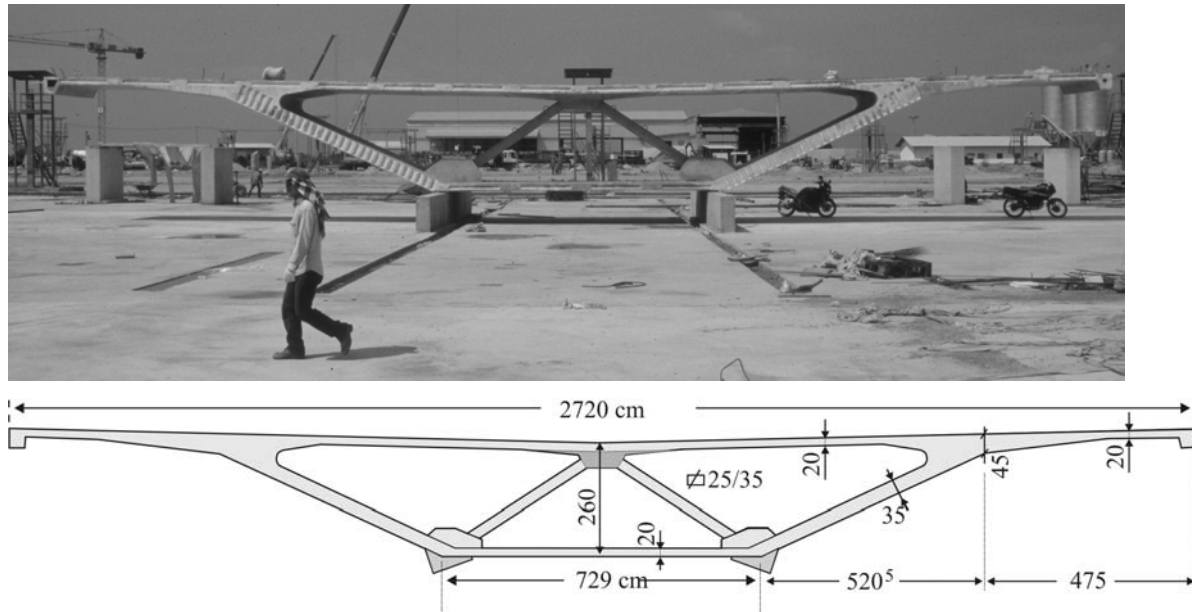
width of segment $w = 2.55\ m$

Figure 3.7 Standard segment of Bang Na segmental bridge [Ro4]

Description of measurement program

Measurements were made on different match-cast segments to predict the temperature gradients and the bowing deformations of segments during match casting operation. There were two conditions of the experiments: the first by casting without heat transfer protection, and the second was casting with heat transfer protection using plastic sheets on both match-cast segments.

The temperature readings for match-cast segments were taken by means of electrical thermometer and steel pipes filled with oil embedded in the concrete at various places in the segments. The readings were taken at 1-hour interval for a period of 10 hours to 24 hours. Figure 3.8 shows the steel pipe locations used to measure the temperature in the match-cast segments.
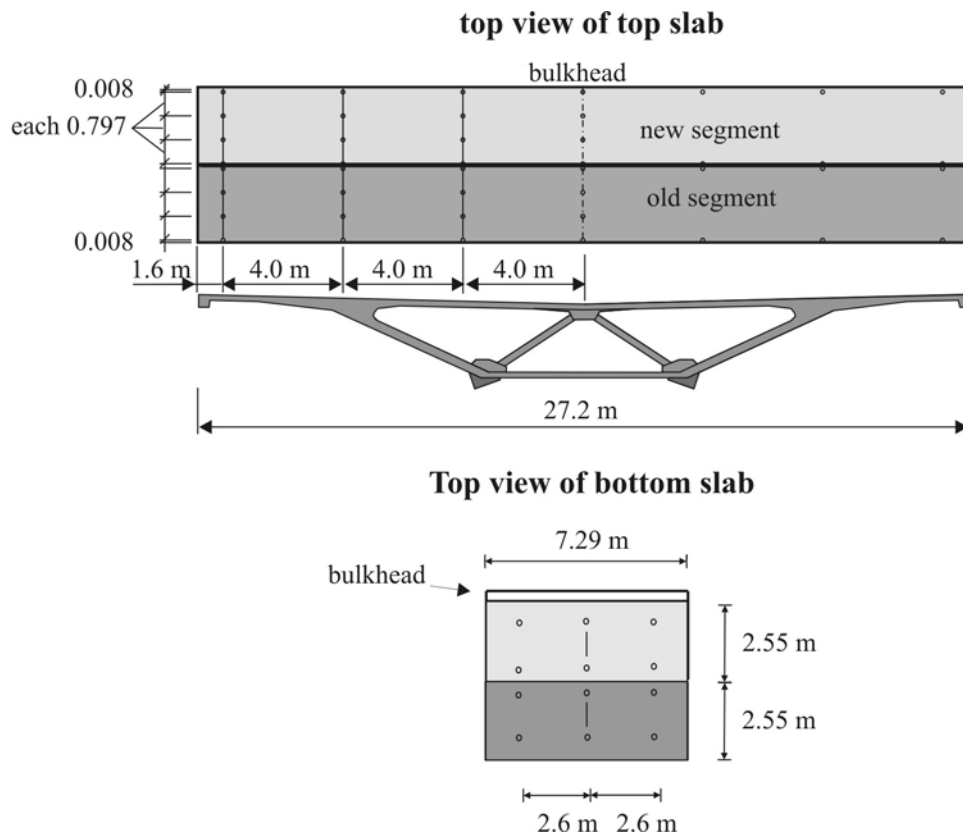
Figure 3.8 Steel pipe locations for temperature readings [Jea]

Results

Figure 3.9 shows a typical temperature distribution in the decks of the match-cast segments after ten hours of casting of concrete. The shapes of temperatures curves versus time were close for the different segments. The maximum average temperature recorded was 71.5 ℃. It can be seen clearly that the temperature rise is higher at the flange-web junction, which can be related to less effects of boundary conditions by the convection on the developed heat of hydration than in thinner sections.

The heat transfer in the joint is pure conductive and the speed of heat transfer to the match-cast segment depends particularly on the coefficient of conductivity of concrete λ. The magnitude of temperature rise in the match-cast segment depends on the specific heat of the concrete c.
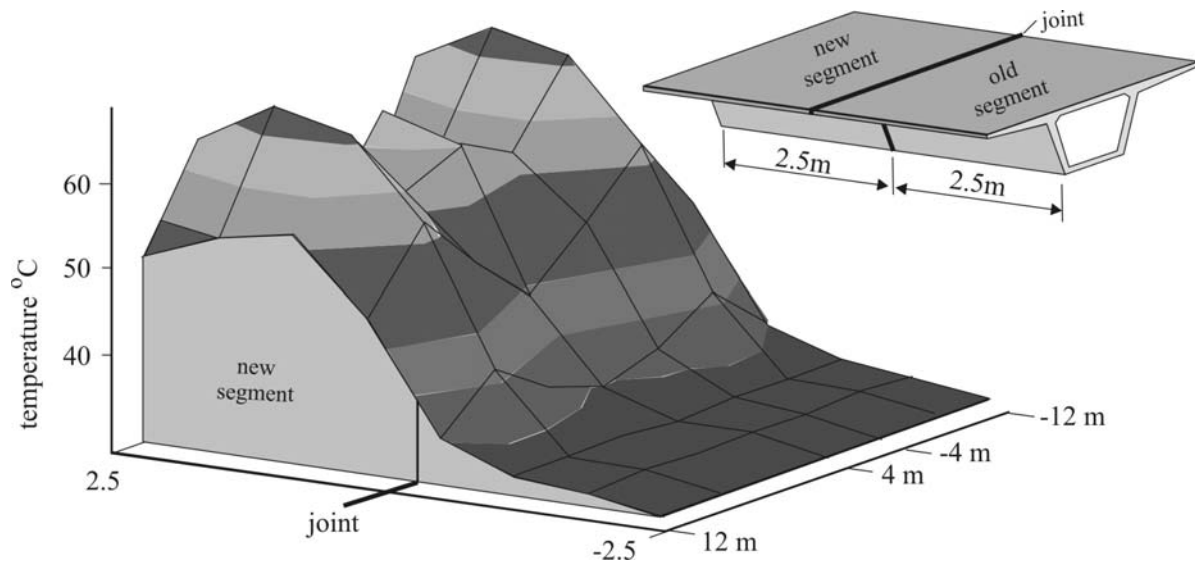
Figure 3.9 Typical temperature distribution in the decks of the match-cast segments after ten hours of concrete casting. [Jea]

Figure 3.10 shows the temperature development of different segments as appointed in the flange-web juncture, where the temperatures recorded by the steel pipes after the completion of casting are used as reference between the subsequent and the initial measurements. The slight differences between curves can be mainly related to the different times of match-cast processes for the given segments, which result in different ambient temperatures during the day.

Figure 3.11 shows different curves representing the distribution of temperature across the middle of decks in the match-cast segments during the process of match casting. The resulting shape of the thermal gradient in the old match-cast segment controls basically the amount of bowing. The higher the descent of the curve in the opposite direction of the joint the larger is the bowing of the segment.
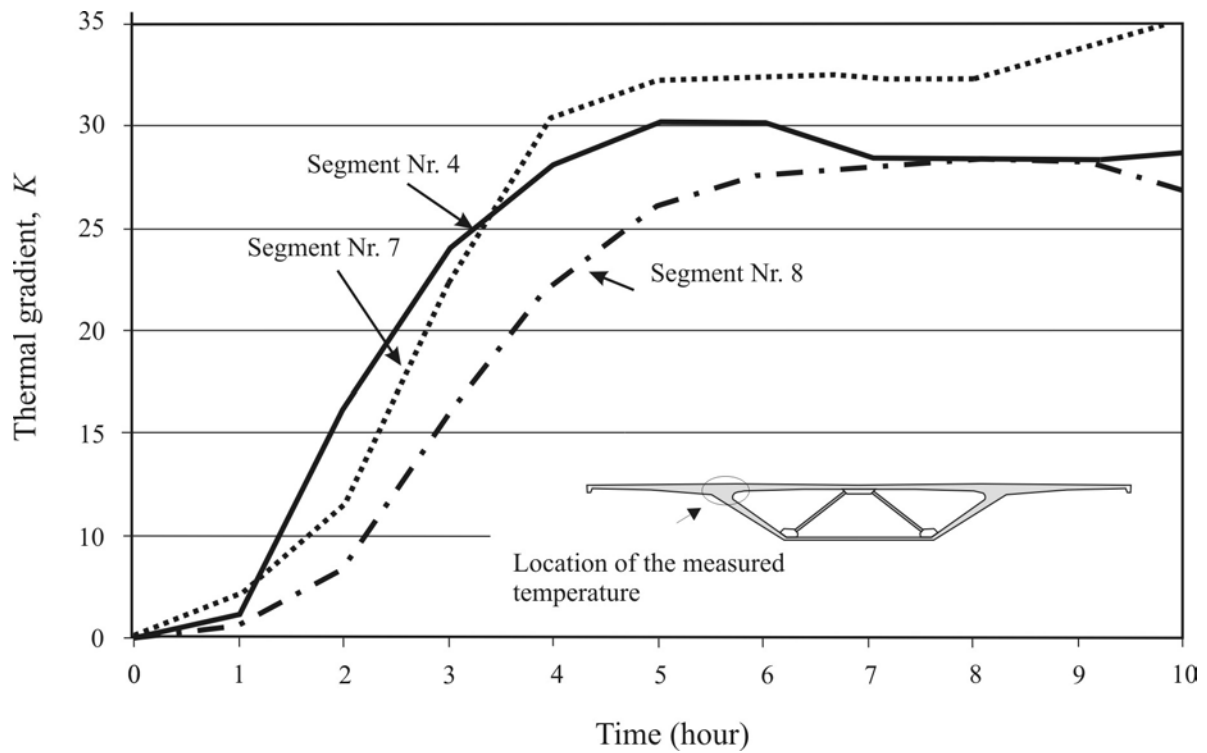
Figure 3.10 Development of temperature in segments 4, 7, and 8 at the flange-web junction [Jea]
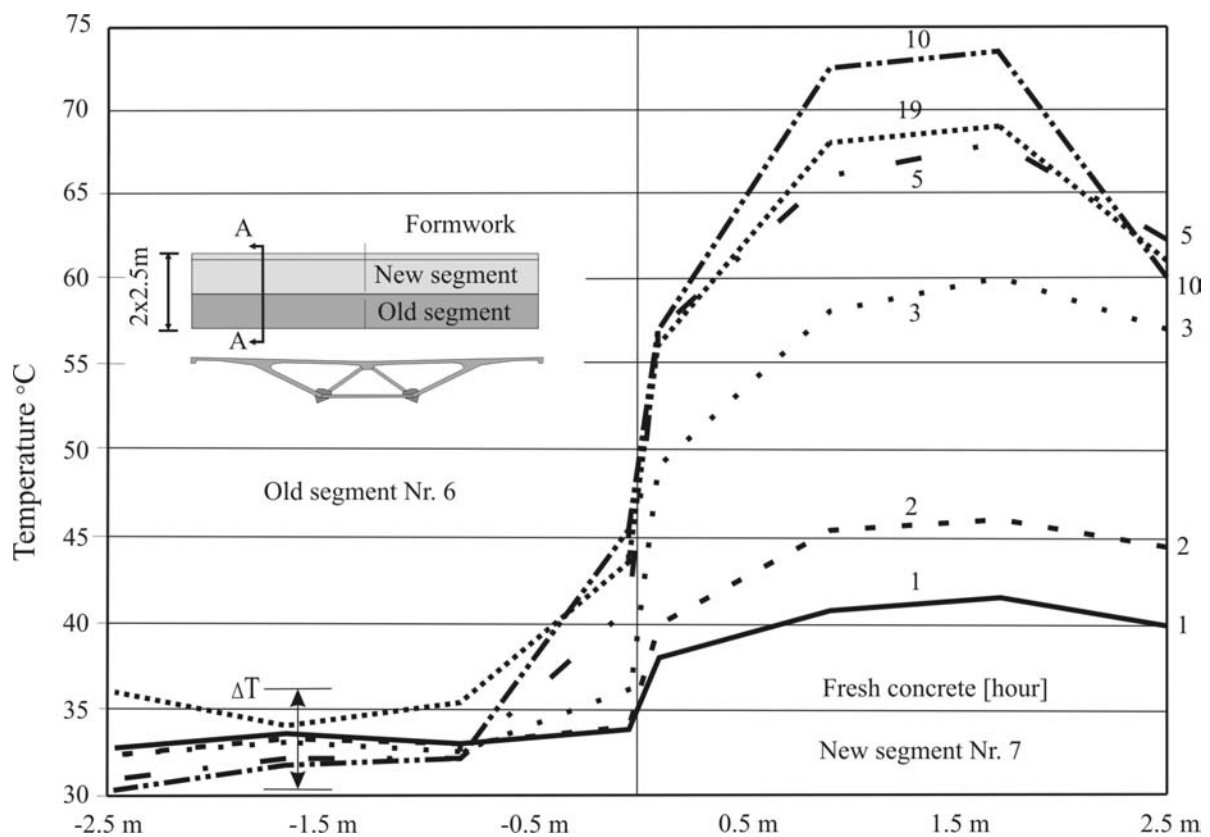

Figure 3.11 Temperature distribution in section A-A [Jea]

Bowing deformation measurement

Steel beams spanning between the bulkhead and the joint between the new cast segment and the match cast segment were used, beside digital dial gauges fixed at the end of the steel beams to measure the deformations resulted from the heat of hydration developed during the match-cast process. The readings of the dial gauges were taken immediately with the readings of temperatures after the casting of concrete. Figure 3.12 shows the steel beams locations used to measure the deformations in the match-cast segments.
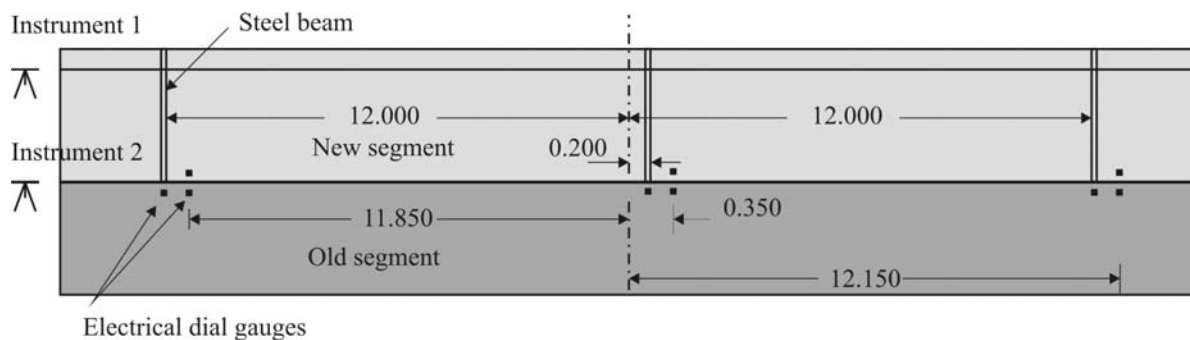

Figure 3.12 Monitoring of bowing effect for segment no. 8 [Jea]

The match-cast segment starts to bow immediately as the thermal gradient due to the heat of hydration and the boundary conditions develop. The measurements of the deformations in some match-cast segments without plastic sheets are shown in Figures 3.13 through 3.15. Figure 3.16 shows bowing of match-cast segment covered with a plastic sheet, which deflected less than those segments without plastic sheets. The plastic cover leads to a significant reduction of the bowing effect.

It should be noted, that the bowing deformation is not symmetric to the elastic neutral axis of the segment. In all cases the deformation on the left edge of the deck is greater than on the right. This un-symmetry may be caused by the pouring procedure.

The match-cast segment can keep bowing even after setting of the new segment, then the old segment returns to its original shape as it cools with time to the ambient temperature. For the current study, only the resulted gap due to bowing at the setting time of concrete is considered.

Figure 3.13 Deformation of the match-cast segment in the vicinity of the joint of segment no. 4 - *no plastic cover* [Jea]

Figure 3.14 Deformation of the match-cast segment in the vicinity of the joint of segment no. 6 - *no plastic cover* [Jea]
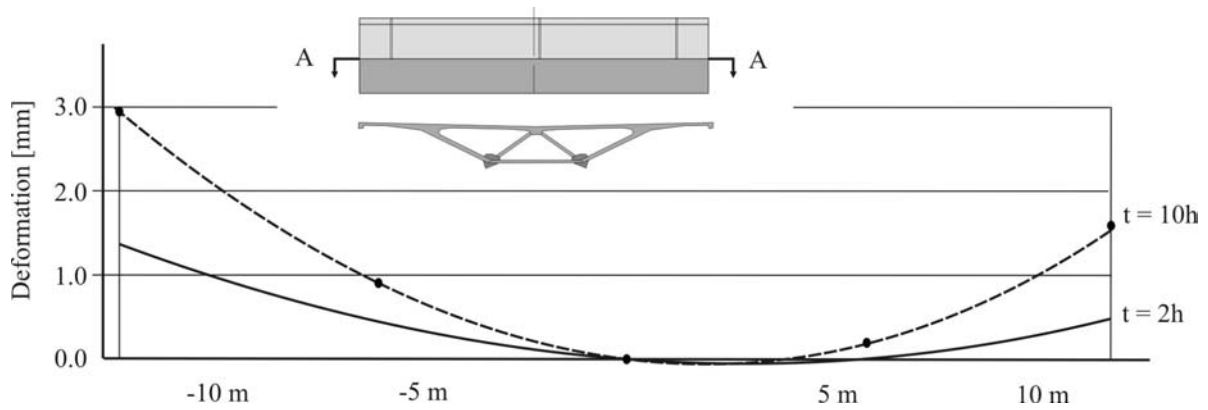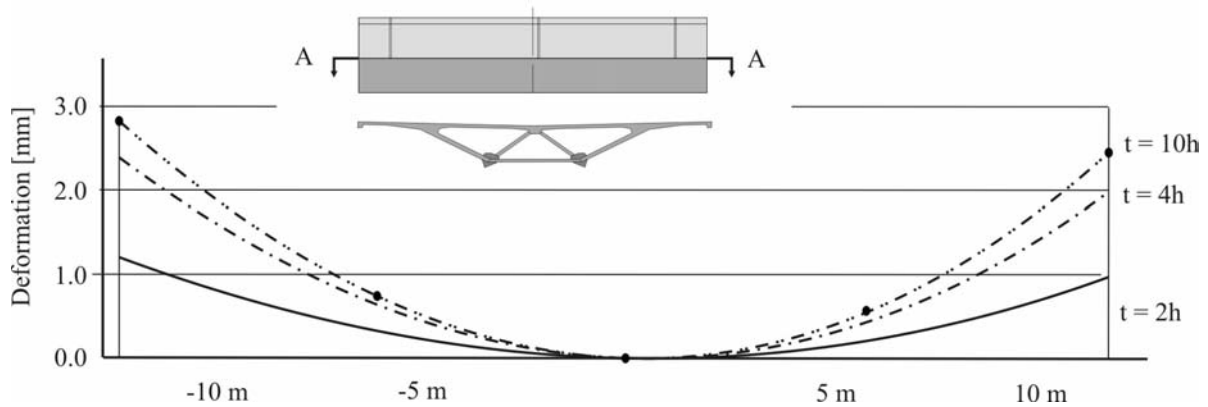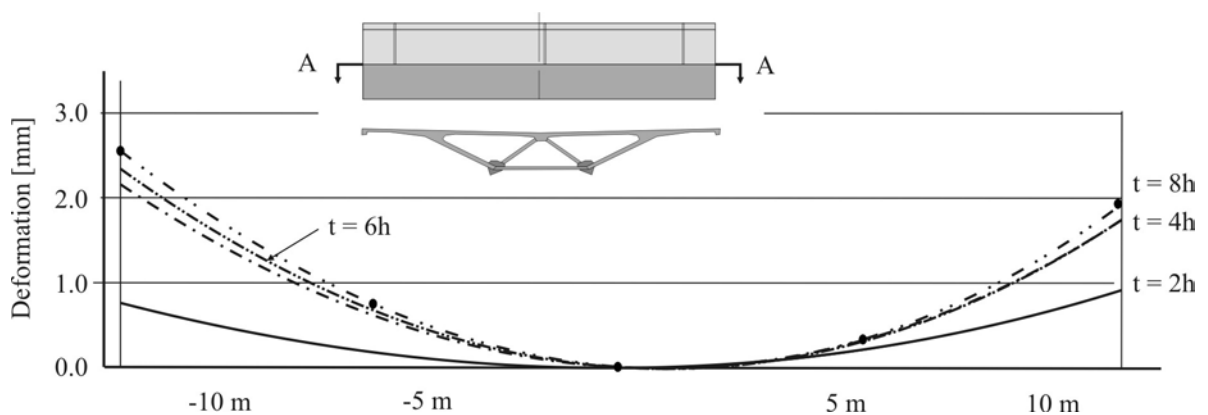

Figure 3.15 Deformation of the match-cast segment in the vicinity of the joint of segment no. 7 - *no plastic cover* [Jea]
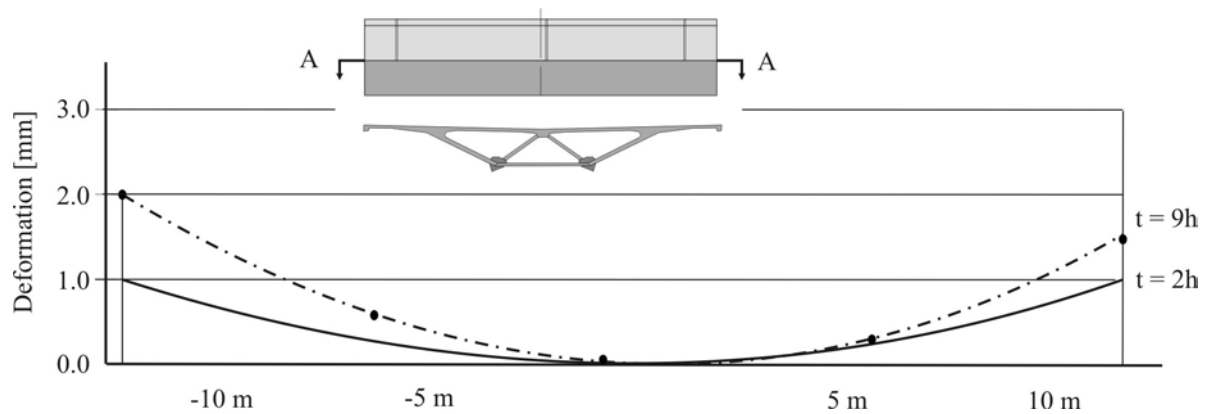
Figure 3.16 Deformation of the match-cast segment *with plastic sheet* in the vicinity of the joint of segment no. 10 [Jea]

3.3   Numerical model of match-cast segments

Three-dimensional thermo-mechanical transient finite element models were developed to predict the response of match-cast segments. The analysis was performed using the general-purpose finite element program ANSYS. Detailed finite element models were developed to represent almost all the factors and boundary conditions that may take apart in the match-casting process.

The concrete in the new match-cast segment was modelled by three-dimensional eight-node thermal solid brick elements which are able to simulate the heat development process in fresh concrete, whereas the concrete in the old match-cast segment was modelled by three-dimensional eight-node thermal and structural field capability solid brick elements to simulate the thermo-mechanical behaviour of solid concrete. The struts and the thicker part where the struts meet the deck are neglected in the analysis of the BBBE bridge.

To represent the heat transfer between both segments across the joint, double node link elements were used to model the transfer and to allow free movement of the structural solid brick elements. The element types used in the current study are shown in Figure 3.17.
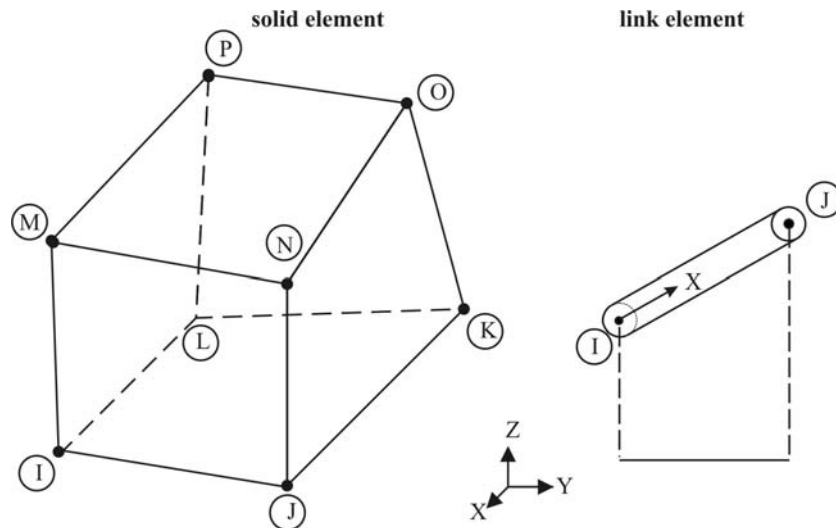
Figure 3.17 Element types used in the thermo-mechanical finite element model [Ans]

This model simulates the unsteady development of heat of hydration of concrete and conducts the heat flux vectors of conduction and convection within the medium and among the adjacent media respectively.

3.3.1   Verification

The numerical models were verified by comparison of the results of the FE-analysis with the measurements obtained in San Antonio and Bang Na segmental bridges. The standard segments used in the San Antonio segmental bridge, type *I* and type *III* and segments no. 4 and 7 of the Bang Na bridge were modelled. Figure 3.18 and Figure 3.19 show the meshing of segment type *III* and the standard segment used in Bang Na bridge respectively.
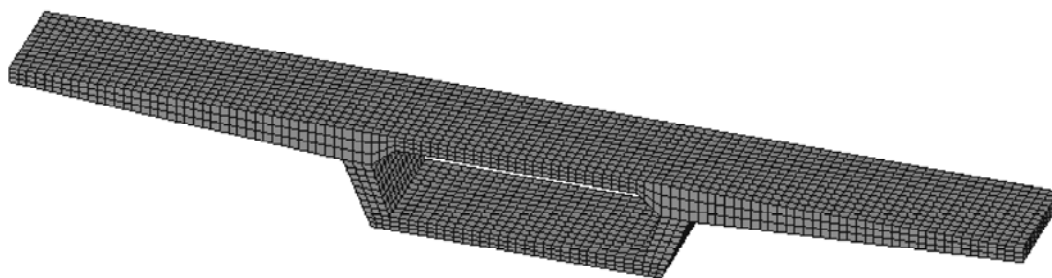
Figure 3.18   Finite element model of San Antonio type *III* match-cast segment
(~ 6000 brick elements)

Figure 3.19   Finite element model of a standard segment of Bang Na bridge

(~ 9300 brick elements)

The models predicted the development of the heat of hydration in new fresh concrete and heat flux vectors which resulted in thermal gradients. These unsteady gradients caused thermal stresses which produced the bowing in the old match-cast segments. The heat of hydration was estimated by applying the heat transfer equations and using the measurements of temperatures taken in San Antonio and Bang Na segmental bridges [Br3, Jea] as no concrete mix details are given for the real bridges. This approach used the developed temperature in the fresh concrete to estimate the heat of hydration. An example of the approach is illustrated in Table 3.1.

Table 3.1 Estimation of heat of hydration from the developed concrete temperature (Bang Na, segment no. 7)

T	Developed temperature ΔT (see Fig. 3.10)	dT	dt	$\Delta_i = \dfrac{c \cdot \rho \cdot dT}{dt}$	Heat of hydration $q_t = \dfrac{\Delta_i + \Delta_{i+1}}{2}$
[h]	[K]	[K]	[h]	[W/m³]	[W/m³]
1	6.2	4.5	1.0	4544.6	3921.6
2	10.7	13.6	1.0	3298.5	6633.7
3	24.3	6.2	1.0	9968.8	7256.7
4	30.5	2	1.0	4544.6	
5	32.5				
.	.	.	.	.	.
.	.	.	.	.	.
.	.	.	.	.	.

The specific heat c and the thermal conductivity coefficient λ used in the model were taken from the work of Weigler [We1] and Eibl [Ei2]. The convection coefficient α_k was calculated according to [Rec, Vdi]. When the formwork covered the fresh concrete α_k is calculated according to [We1, War, Rec]. Details have been given in chapter 2. Temporal development of modulus of elasticity in the old match-cast segment was used according to [Ac1] and assumed to be 20 % of the modulus of elasticity (28 day-strength) as an end value. All the heat transfer coefficients used in the model and listed in Table 3.2 were time and temperature independent. The compressive strength of concrete f_{ck} is not needed in the analysis.

Table 3.2 Heat transfer coefficients

Thermal Conductivity Coefficient	$\lambda =$	2.65	$\left[W /(m \ ^oC) \right]$
Specific Heat	$c =$	1128	$\left[W \ s /(kg \ ^oC) \right]$
Convection Coefficient	$\alpha_k =$	5.8	$\left[W /(m^2 \ ^oC) \right]$
Concrete Density	$\rho =$	2,340	$\left[kg / m^3 \right]$
Modulus of Elasticity (28 day-strength)	$E_c =$	34,000	$\left[MPa \right]$
Thermal Expansion Coefficient	$\alpha_T =$	$12 \cdot 10^{-6}$	$\left[1/^o C \right]$

Figure 3.20 shows the finite element mesh of San Antonio standard match-cast segments (type *III*) and Bang Na standard match-cast segments as well as the resulted deformations.
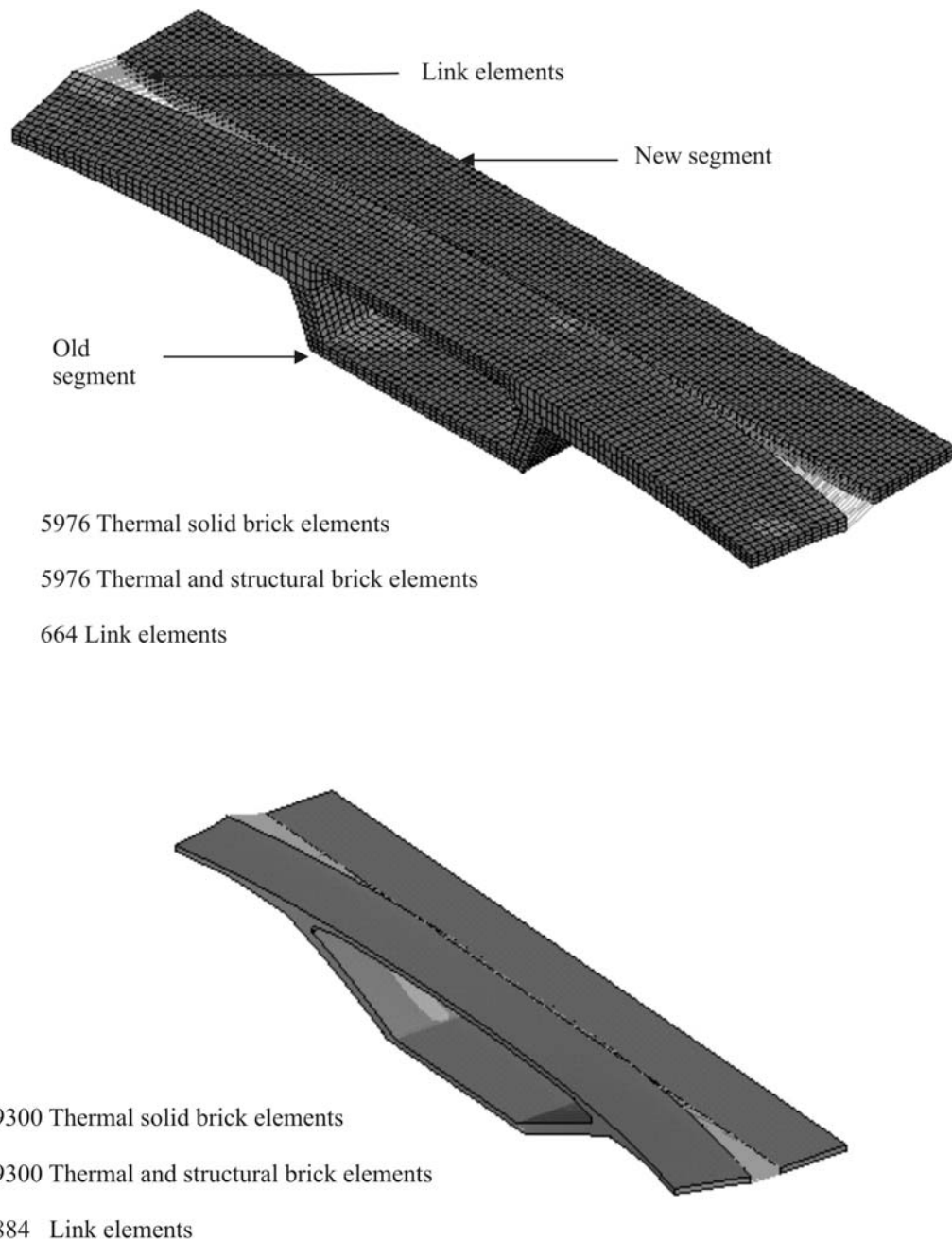
Figure 3.20   Numerical model of the match-cast segments and the deformed shape
(top: San Antonio, bottom: BBBE)

Figure 3.21 shows the measured and calculated temperature gradient in the segment type *III*. Please note that only one measurement line is plotted. Different test results were published for segment type *III* of the San Antonio bridge [Bre]. The measurements showed a faster increase of the temperature than the Finite Element analysis. This discrepancy has little influence on the bowing effect. The temperatures in the fresh concrete at the time of setting (10 *h*) are nearly the same.
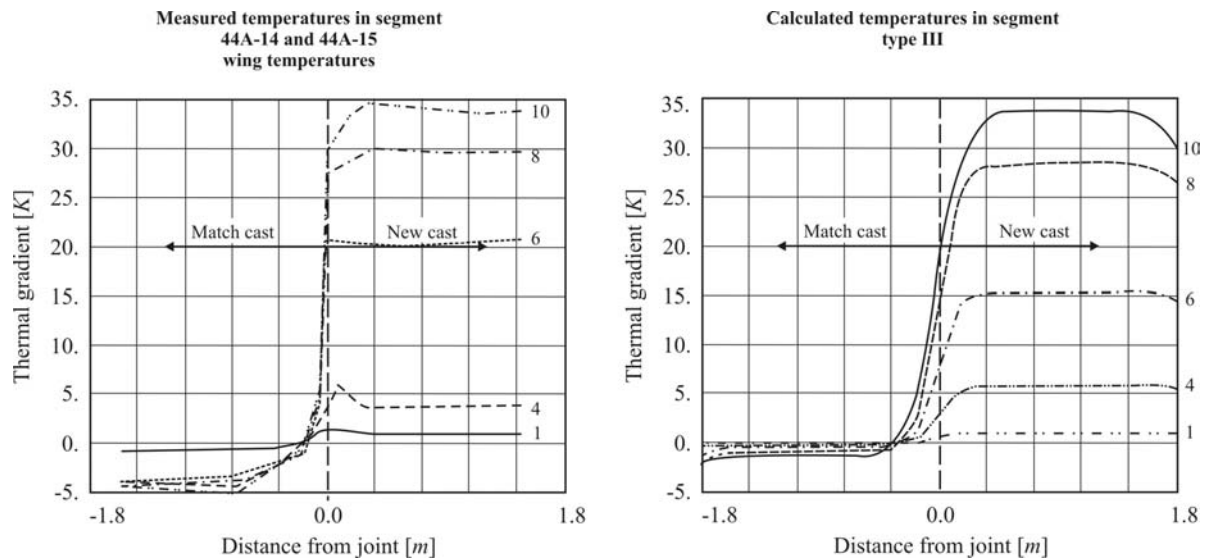
Figure 3.21 Temperature distributions for various times in the centreline of the deck

One of the deflection measurements conducted in old segment type *III* in the San Antonio project across the width of the upper slab in the vicinity of the joint and the numerical results obtained from the finite element model can be seen in Figure 3.21. The total deflection or resulting gap was 1.78 *mm* after ten hours of casting concrete [Br3]. The numerical analysis gives Δ = 1.80 *mm*. The comparison between the numerical model and the measurements gives a very good agreement.
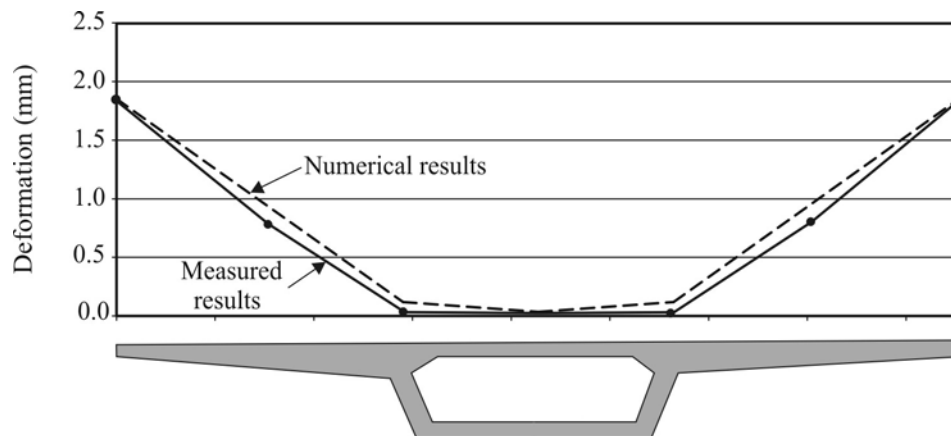
Figure 3.21 Measured and numerical deformations at the upper edge of old segment type *III* after ten hours of match-cast process

The numerical results of the deformed segment and the resulted thermal stresses σ_x are shown in Figure 3.22 and Figure 3.23. The tensile stresses started in the vicinity of the joint due to the expansion of concrete. The maximum estimated value in the upper slab was 0.36 *MPa*. The tensile stresses decreased till they vanished at about 0.3 *m* from the free face

of the old segment. The small tensile stresses in the concrete which are smaller than the tensile strength allows the usage of an elastic material behaviour.
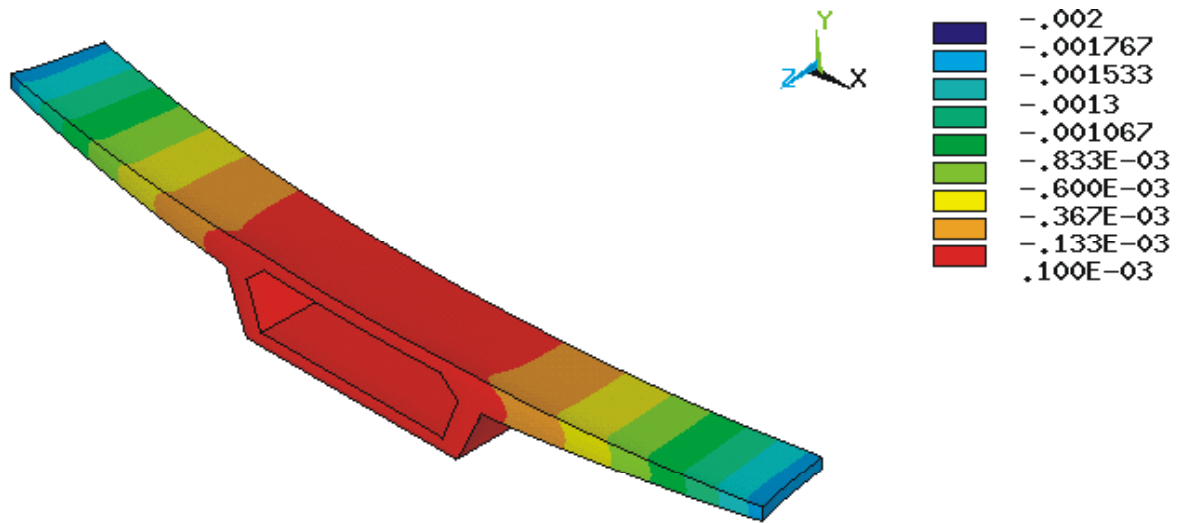
Figure 3.22   Deformation [*m*] in z-axis direction and bowing of the type *III* match-cast segment after ten hours of casting of concrete (Δ_{max} = 1.8 *mm*)
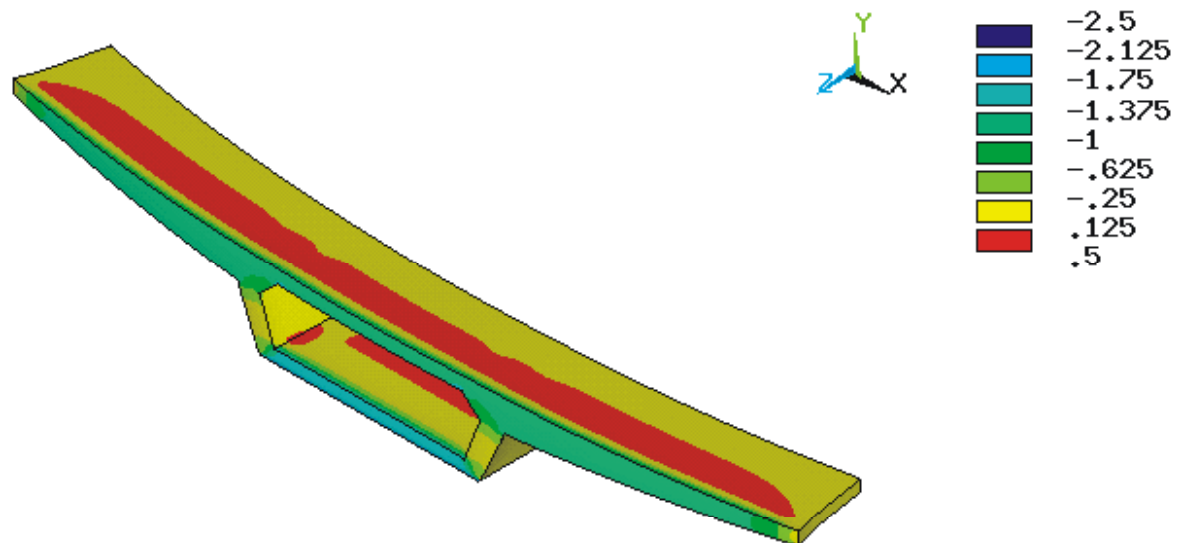
Figure 3.23   Stress distribution σ_x [*MPa*] in the old match-cast segment after ten hours of casting of concrete ($\sigma_{c,t\ max}$ = +0.36 *MPa*)

It should be noted that the old segment will keep deforming even after the initial setting of fresh concrete during the whole heat of hydration process in the new segment and even with decreasing of temperature in the other face of the contact joint i.e. negative thermal gradient. Hence, the thermal tensile stresses in the concrete can keep increasing and the risk of

cracking may increase. The early age of the concrete and the developed modulus of elasticity play an important role in the value of the thermal stresses and stress induced cracks in the young concrete. The propagation of cracking in the segments during the match-cast process is out of the scope of this work.

A comparison between the measurements and the numerical results of segments 4 and 7 of the Bang Na bridge is shown in Figures 3.24 and 3.25. The geometry of both segments is the same. Only the ambient temperature during casting is different. The total deflection at the edge of the top slab was about 3.20 *mm* and 2.5 *mm* after ten hours of casting concrete [Jea], while the numerical analysis gives 3.17 *mm* and 2.60 *mm* in segment 4 and segment 7 respectively. In spite of the same geometries and materials used, differences in measurements between both segments maybe related to the boundary conditions especially the time of the day at which match-cast process took place and possible changes in ambient temperatures which can influence the thermal gradient shape.

The measurements of deformations in the match-cast segments showed some un-symmetry in both flanges which maybe mainly caused by inaccurate placing the steel pipes used to measure the deformations and keeping its alignment during the casting process. Using taut wire as applied in the San Antonio project could be more practical in match-cast method.
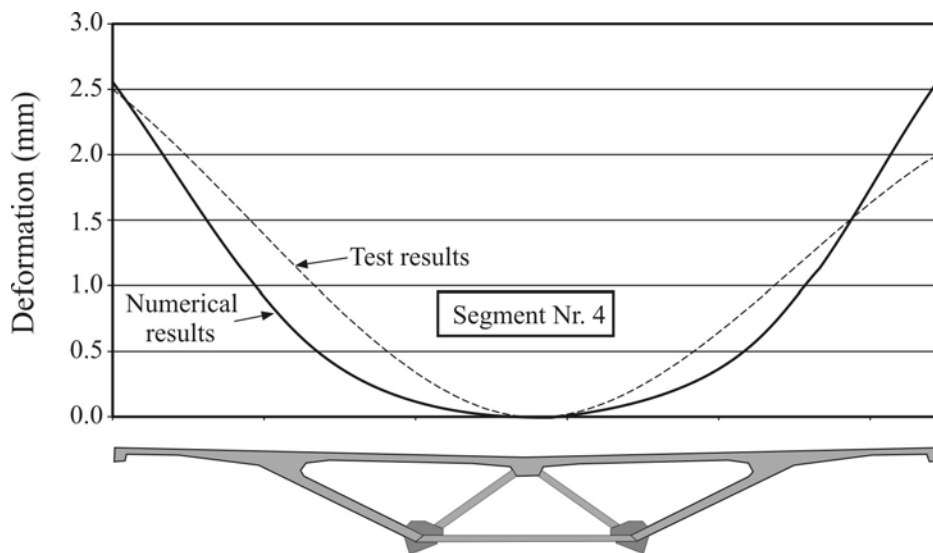
Figure 3.24 Comparison between measured and numerical results of segment no. 4 of the Bang Na bridge ($\Delta_{max, FE} = 2.5$ *mm*)
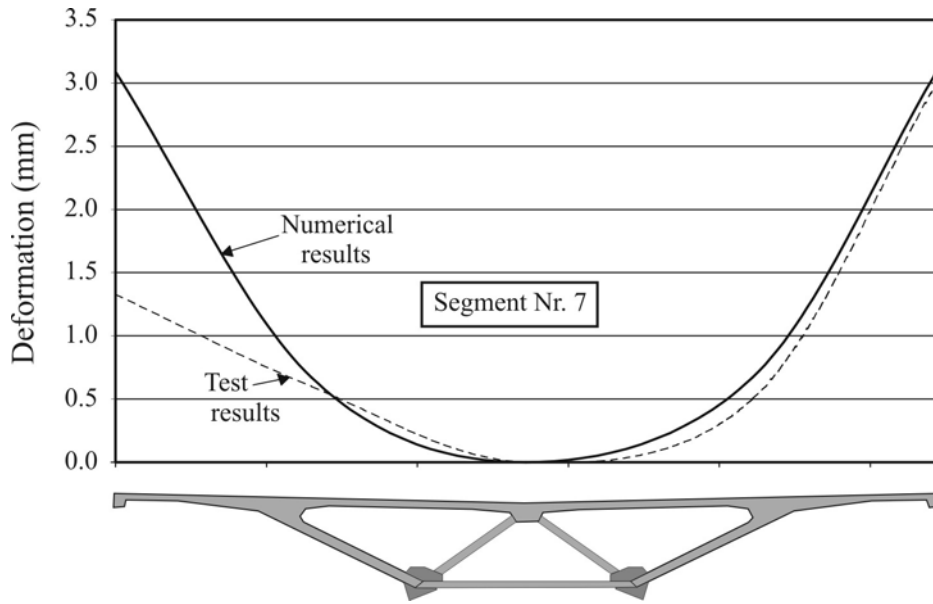
Figure 3.25 Comparison between measured and numerical results of segment no. 7 of the
Bang Na bridge ($\Delta_{max, FE}$ = 3.2 *mm*)

The development of the temperature in the fresh concrete of segment 4 and 7 is shown in
Figure 3.26. A very good agreement between the measured (see Figure 3.10) and the
calculated values can be observed. Thus the time dependant behaviour of the concrete and
the development of the heat of hydration are modelled with a high accuracy.
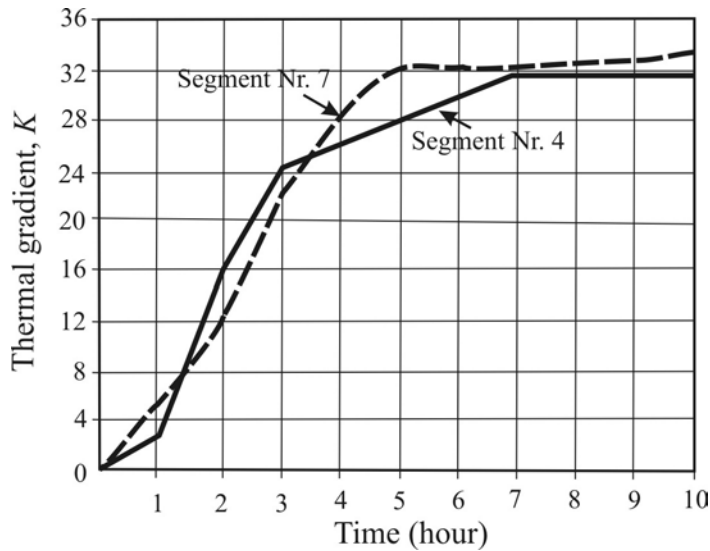
Figure 3.26 Numerical results of temperature development in segments 4 and 7

The numerical results of the deformed segment and the resulted thermal stresses σ_x of both
segments of the Bang Na bridge are shown in Figure 3.27 through Figure 3.30. The

comparisons shown in the figures indicate that there was a good agreement between the measured and thermo-mechanical finite element model results.
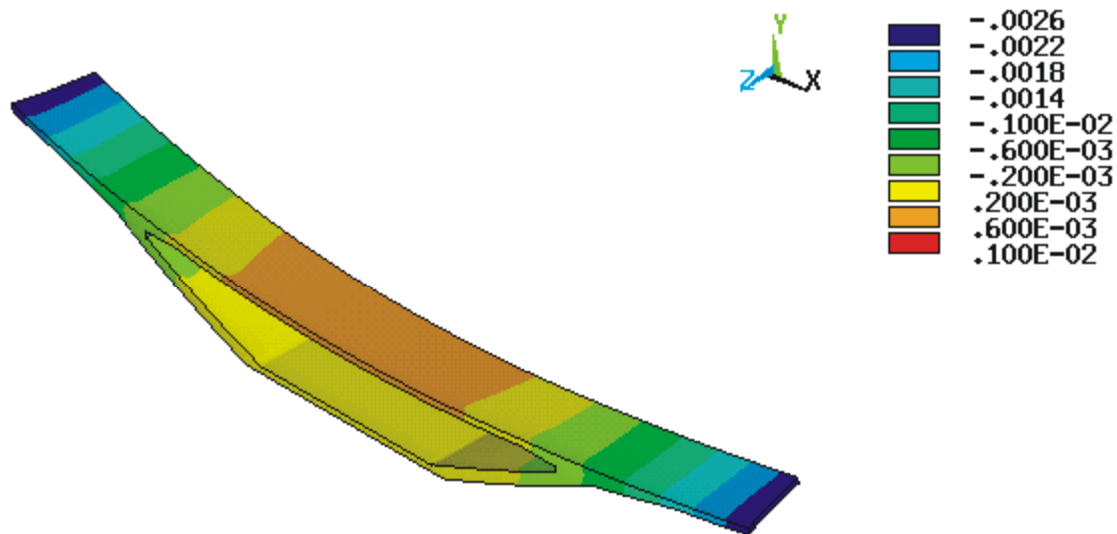
Figure 3.27   Deformation [*m*] in z-axis direction and bowing of the old match-cast segment **no. 4** after ten hours of casting of concrete.
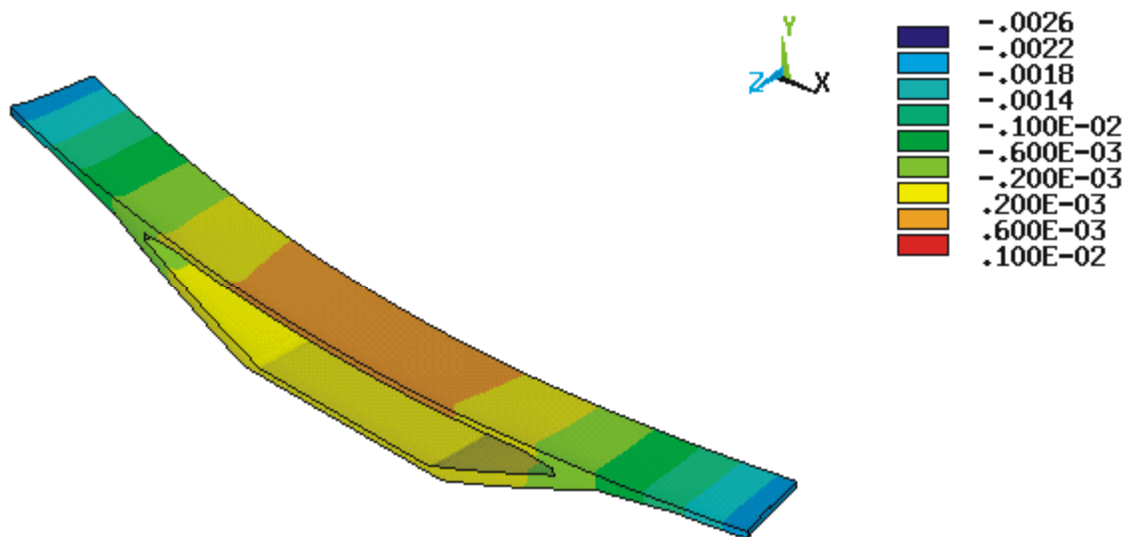
Figure 3.28   Deformation [*m*] in z-axis direction and bowing of the old match-cast segment **no. 7** after ten hours of casting of concrete.

The maximum estimated tensile stress in the upper slab of segment no. 4 was 0.41 *MPa* in the vicinity of the joint and it vanished at about 0.5 *m* from the free face of the old segment, whereas the maximum estimated in the upper slab of segment no. 7 was 0.34 *MPa* and it vanished at about 0.5 *m* from the free face.
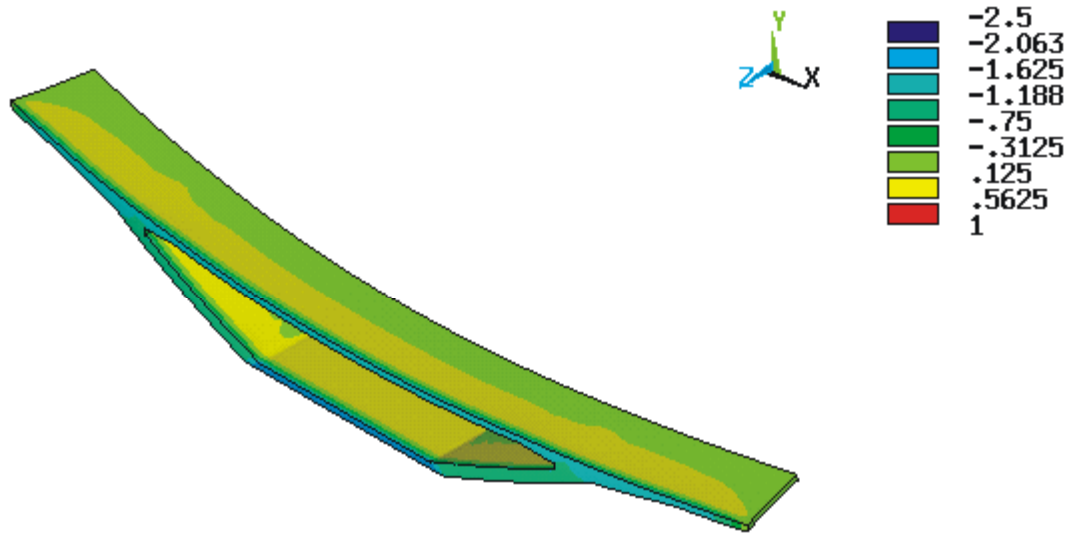
Figure 3.29   Stress distribution σ_x [MPa] in the old match-cast segment 4 after ten hours of casting of concrete ($\sigma_{c,t\,max}$ = +0.41 MPa).
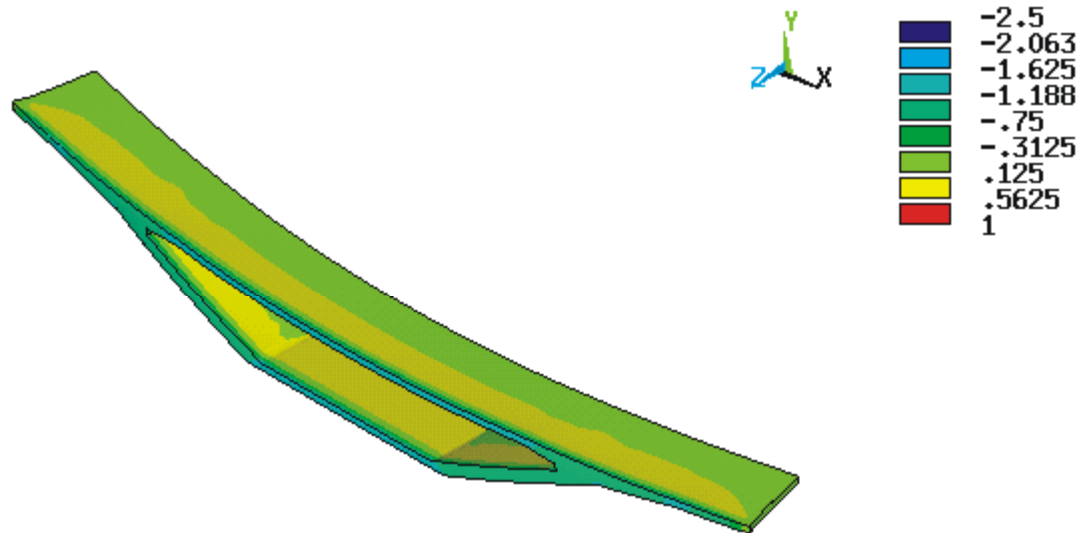
Figure 3.30   Stress distribution σ_x [MPa] in the old match-cast segment 7 after ten hours of casting of concrete ($\sigma_{c,t\,max}$ = +0.34 MPa)

3.3.2   Example of using equivalent moment approach

A simple analytical approach proposed by Breen *et al*. [Bre] based on a certain thermal gradient is used in the following to estimate the resulting gap and to compare the results with the numerical analysis. Details of this model are given in chapter 2.3.8. This approach can be useful if the thermal gradient is estimated at expected setting time of concrete. An example is given to show the analysis and procedure to estimate thermal deformations and the resulting gap in match-cast segments. A comparison between the finite element model and the analytical approach can be seen as well.

The segment type *III* used in the San Antonio bridge with the concrete properties of the mixture one proposed by Zeitler (see Fig. 2.16) is used in the analytical approach. In order to simplify the analysis we assume that the boundary conditions are constant, in other words the surrounding temperature does not change with time.

Due to the variable thickness in a cross-section of the segment, small differences in temperature distributions along the segment are expected which result in different thermal gradient curves. A numerical analysis was used to show thermal gradient curves obtained after ten hours across the old segment at many nodes as shown in the Figure 3.31.
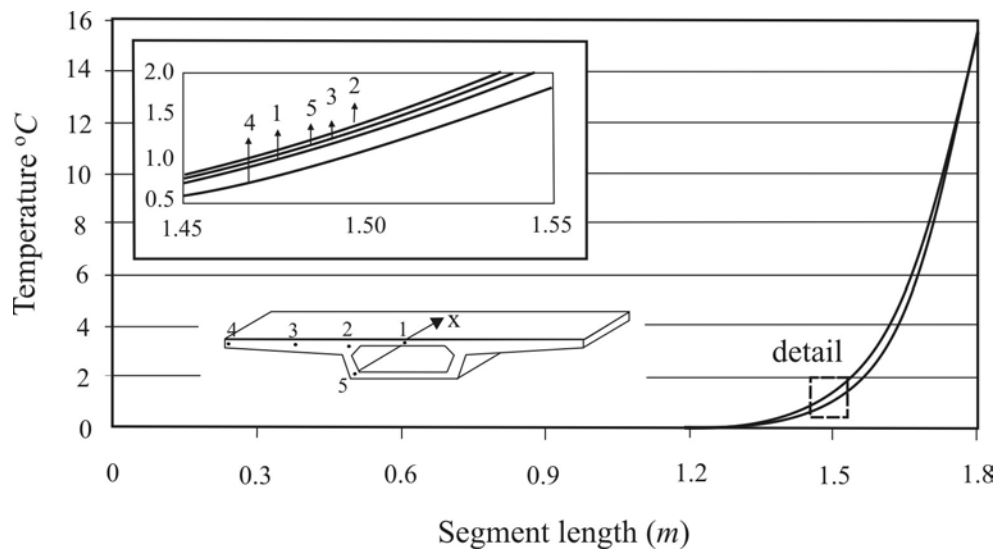
Figure 3.31 Thermal gradient curves at different nodes across the type *III* old segment after 10 h obtained using the numerical model

In the following the thermal gradient curve at node 1, 10 *h* after concreting, which represents almost the average values of the thermal gradient curves is used to estimate the bowing. However, the changes in these thermal gradient curves have little influences on the thermal deformations.

Figure 3.32 shows many thermal gradient curves obtained at node 1 across the old segment after different hours of the beginning of match-casting processess used to make a comparison between the analytical approach and thermo-mechanical finite element model.

In the following the thermal gradient curve at node 1 as seen in Figure 3.33 across the old segment which represents the thermal gradient after 10 hours of mixing concrete is used. It is supposed that the concrete starts hardening at that time. The equivalent moment equation 2.25 can be applied.
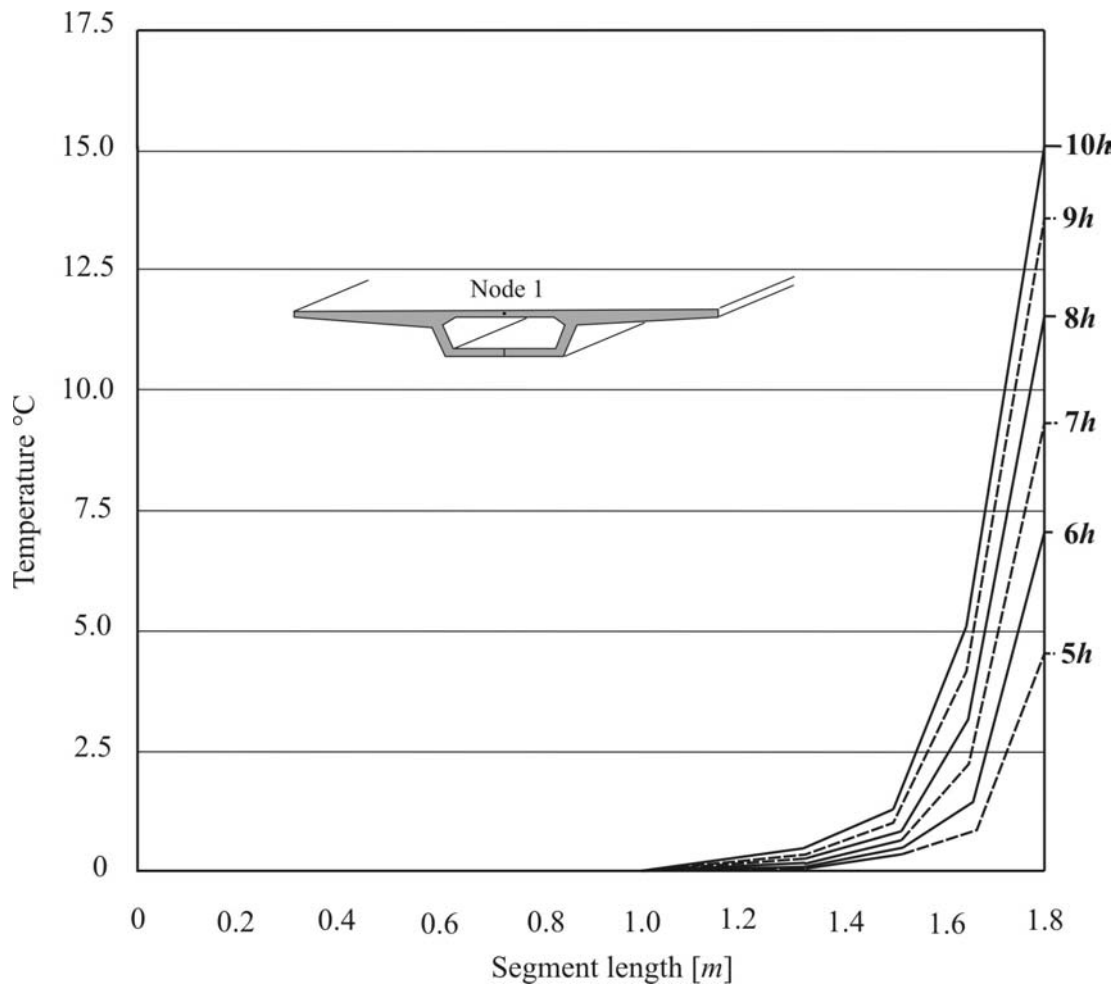
Figure 3.32   Thermal gradient curves after 5, 6, 7, 8, 9 and 10 hours at node1 across the old segment obtained using the numerical model
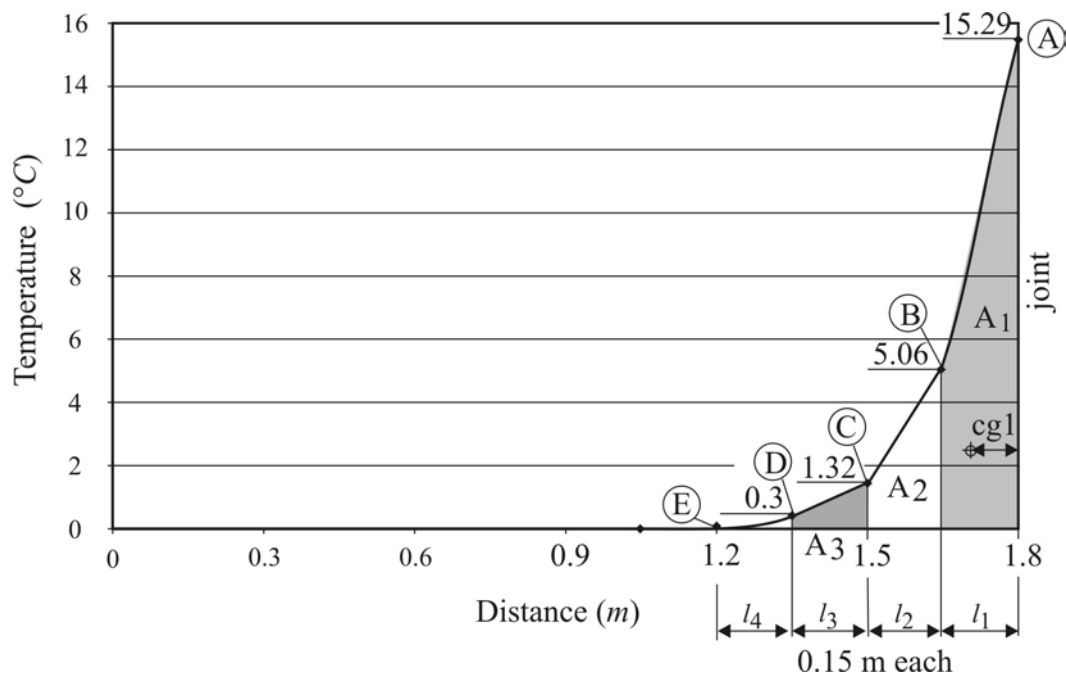

Figure 3.33 Thermal gradient curve after 10 hours at node1 across the old segment

The equivalent moment applied to the section is given by:

$$M_{\Delta T} = \alpha_T \cdot E_c \int T(y) \cdot h(y) \cdot y \, dy = \alpha_T \cdot A_{T1} \cdot h \cdot E_c \cdot \left(\frac{L}{2} - cg_1 \right) \tag{3.1}$$

Numerical integration of the temperature curve shown in Figure 3.32 over the distance gives:

$$A_{T1} = A_1 + A_2 + A_3 + A_4 \tag{3.2}$$

$$A_{T1} = \left[\left(\frac{15.29 + 5.06}{2} \right) \cdot 0.15 \right] + \left[\left(\frac{5.06 + 1.32}{2} \right) \cdot 0.15 \right] + \left[\left(\frac{1.32 + 0.3}{2} \right) \cdot 0.15 \right] + \left[\frac{0.3}{2} \cdot 0.15 \right]$$

$$A_{T1} = 2.149 \ ^oC \cdot m$$

The centre of gravity cg_1 of the total area A_{T1} can be estimated as:

$$cg_1 = \left\{ \left[\frac{(15.29 - 5.06)}{2} \cdot \frac{0.15^2}{3} + 5.06 \cdot \frac{0.15^2}{2} \right] + \left[\frac{(5.06 - 1.32)}{2} \cdot 0.15 \cdot 0.2 + 1.32 \cdot 0.15 \cdot 0.225 \right] + \right.$$

$$\left. + \left[\frac{(1.32 - 0.3)}{2} \cdot 0.15 \cdot 0.35 + 0.3 \cdot 0.15 \cdot 0.375 \right] + \left[\frac{0.3}{2} \cdot 0.15 \cdot 0.50 \right] \right\} / A_{T1} \tag{3.3}$$

$$cg_1 = 0.117 \ m$$

The deflection of the segment can be estimated as:

$$\Delta = \frac{3 \cdot w^2 \cdot \alpha_t}{2 \cdot L^3} \left[A_{T1} \cdot \left(\frac{L}{2} - cg_1 \right) \right] \tag{3.4}$$

where: w is the width of the segment

       L is the length of the segment

$$\Delta = \frac{3 \cdot 17.07^2 \cdot 12 \cdot 10^{-6}}{2 \cdot 1.8^3} \left[2.149 \cdot \left(\frac{1.8}{2} - 0.117 \right) \right]$$

$$\Delta = 1.51 \ mm$$

The deflection obtained by the finite element model is 1.44 *mm* which agrees very well to the equivalent moment approach. Please note that the results of the simple model are based on the assumed or given temperature distribution in the deck of the match cast segment. Thus, measurements or Finite Element analysis is anyhow required to estimate the temperatures due to the heat of hydration.

Table 3.3 shows the comparison between the total deflection obtained by the analytical approach and the thermo-mechanical finite element model. A good agreement between the two approaches can be seen. The main differences between the two approaches came from the fact that in the analytical method only one thermal gradient shape was assumed to pass across the section of the old segments as well as the thermal gradient curve was proposed to be linear in order to simplify the calculations. However, the analytical approach can be practical in estimating the gaps.

Table 3.3 Comparison of deflections obtained by the analytical approach and the numerical model (San Antonio *type III* segment)

Time (*hour*)	Deflection Δ (*mm*) (Analytical approach)	Deflection Δ (*mm*) (Finite element model)	Difference %
After 7 hours	0.813	0.762	6.3
After 8 hours	1.044	0.991	5.1
After 9 hours	1.275	1.231	3.5
After 10 hours	1.503	1.443	4.0

3.4 Influences of concrete properties, segment geometry and boundary conditions on the match-cast process

The concrete properties given by Zeitler [Zei] and the segments type *I* and *III* of the San Antonio bridge [Br3] and the standard segments of BBBE will be used to study the effects of the concrete type, segment geometry i.e., width to length ratio (*w/L*) and the boundary conditions such as: ambient temperature, wind speed and using of formworks. The impact of using insulation materials will be also presented.

3.4.1   Effect of width to length ratio (*w/L*)

The influence of width to length ratio (*w/L*) on the total deflection of the match-cast segments was studied by Podolny [Pod], Fig and Muller [Fig] and Prescon Corporation [Br3]. Podolny stated that the effect is particularly significant for segments with width-to-length (*w/L*) ratios exceeding 6. The standard segments used in the San Antonio segmental bridge, type *I* (*w/L* = 3) and type *III* (*w/L* = 9.3) as well as the standard segment of Bang Na bridge (*w/L* = 10.7) with concrete mix 1 according to Zeitler [Zei] (f_{ck} = 50.5 *MPa*) were

used in the study to show the influence of a higher width to length ratio. All other factors i.e. concrete properties and ambient conditions were kept constant for all cases.

Figures 3.34 and 3.35 show the deformations after ten hours of type *I* and type *III* match-cast segments respectively. The resulting deflection of type *I* ($w/L = 3.0$) was $\Delta = 0.31$ *mm*, whereas in type *III* segment ($w/L = 9.3$) it was $\Delta = 1.72$ *mm*. The analysis of the slender standard segment (D6 segment) of the Bang Na bridge ($w/L = 10.7$) gives a total deflection of about $\Delta = 2.38$ *mm* as shown in Figure 3.36. Thus, it can be seen that the width to length ratio (w/L) has a great effect on the amount of the deflection of the old segment and the resulting gap in the new segment.

Table 3.4 lists the three used standard segments of San Antonio and Bang Na segmental bridges having different w/L and the resulting gaps using the same concrete properties under similar boundary conditions.
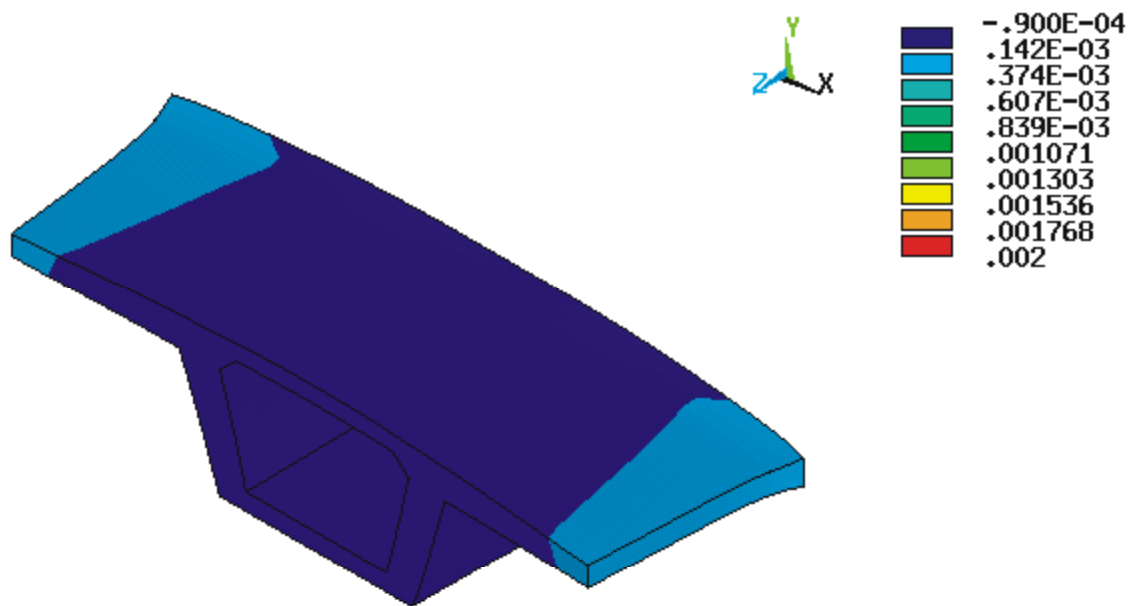
Figure 3.34   Deformations (*m*) in the z-axis direction obtained in the type *I* old segment after 10 hours ($\Delta_{max, FE} = 0.31$ *mm*)
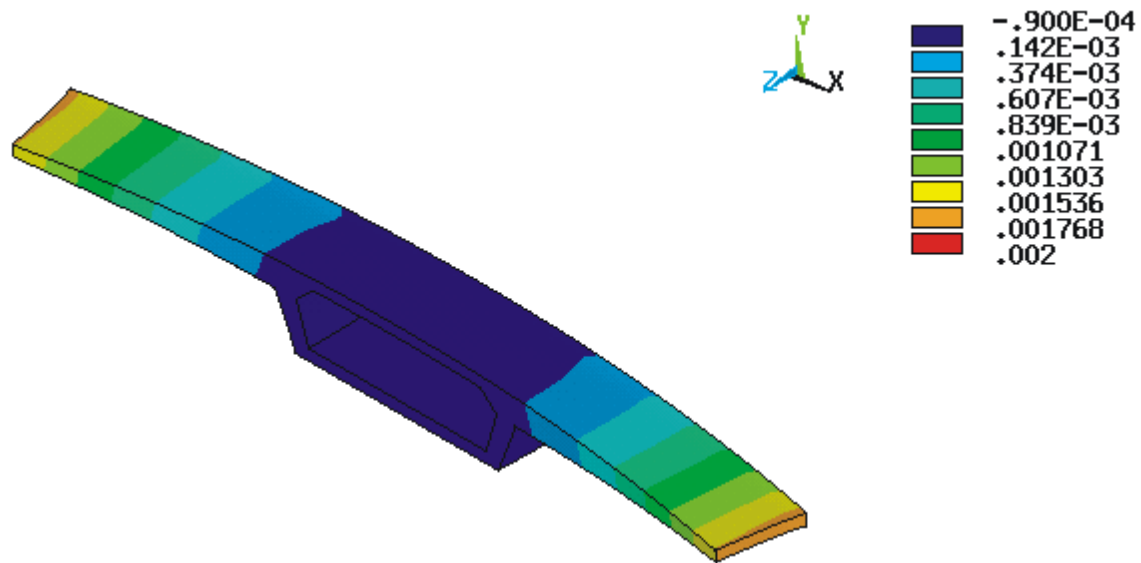
Figure 3.35   Deformations (*m*) in the z-axis direction obtained in the type *III* old segment after 10 hours ($\Delta_{max,\,FE} = 1.72\ mm$)

Figure 3.36   Deformations (*m*) in the z-axis direction obtained in the Bang Na standard segment after 10 hours ($\Delta_{max,\,FE} = 2.38\ mm$)

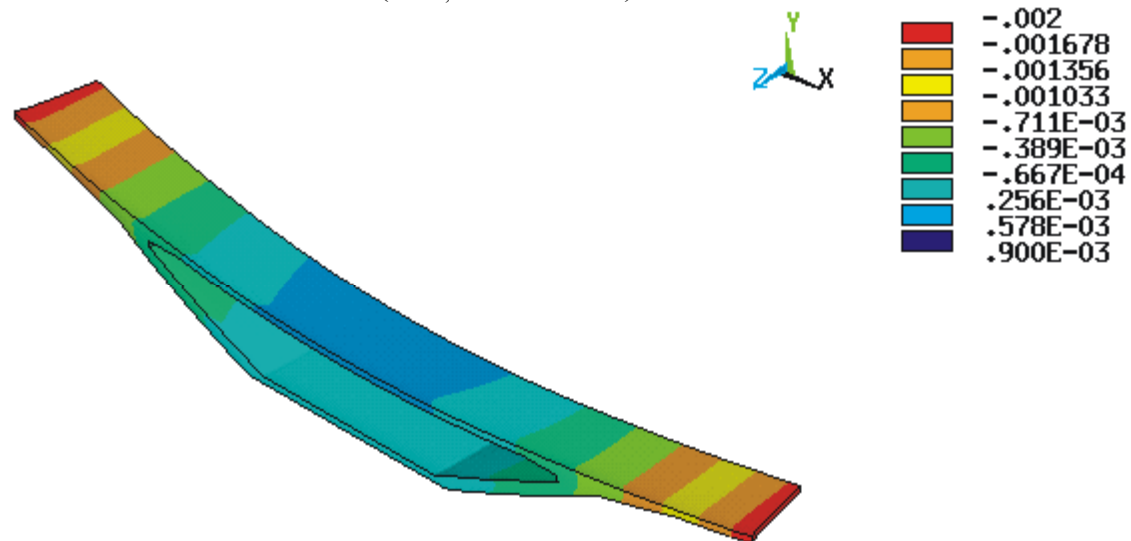**Table 3.4** Comparison among segments having different width to length ratio *w/L*

Segment	*w/L*	Gap (*mm*)
Type *I*	3.0	0.31
Type *III*	9.3	1.72
D6 standard segment	10.7	2.38

Figure 3.37 shows the relation between the width length ratio (w/L) and the resulting gap. It can be clearly seen that the size of the gap increases nonlinearly as the (w/L) increases. The value of the gap is hardly influenced by many parameters as has been stated already. Thus, Figure 3.37 should give a rough impression of the slenderness on the bowing effect only.
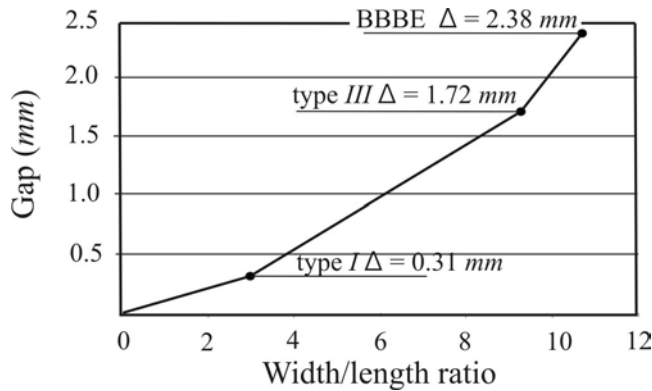
Figure 3.37 Gap (*mm*) versus the width to length ratio (*w/L*)

3.4.2   Effect of concrete type

The different adiabatic temperature curves of the five concrete mixes specified by Zeitler [Zei] indicated that the amount of the heat of hydration depended particularly on the material contents of a mixture; such as: cement content and aggregate types. Figure 3.38 shows the deformed segment using high strength concrete (concrete mix 1, f_{ck} = 50.5 *MPa*, see Table 2.5 and Figure 2.15), where the total deflection was Δ = 1.72 *mm*, whereas Figure 3.39 shows the deformed segment when using low-heat concrete (concrete mix 5 with f_{ck} = 35 *MPa*), where the total deflection decreased about 1.10 *mm* to reach Δ = 0.62 *mm*. In precast segmental bridge construction the high strength concrete is mostly used, as usually a compressive strength of more than f_{ck} = 40 *MPa* is required due to high compressive stresses during the serviceability conditions and to get a fast production. Hence, concrete mixes like concrete 1 is more likely used in practice.
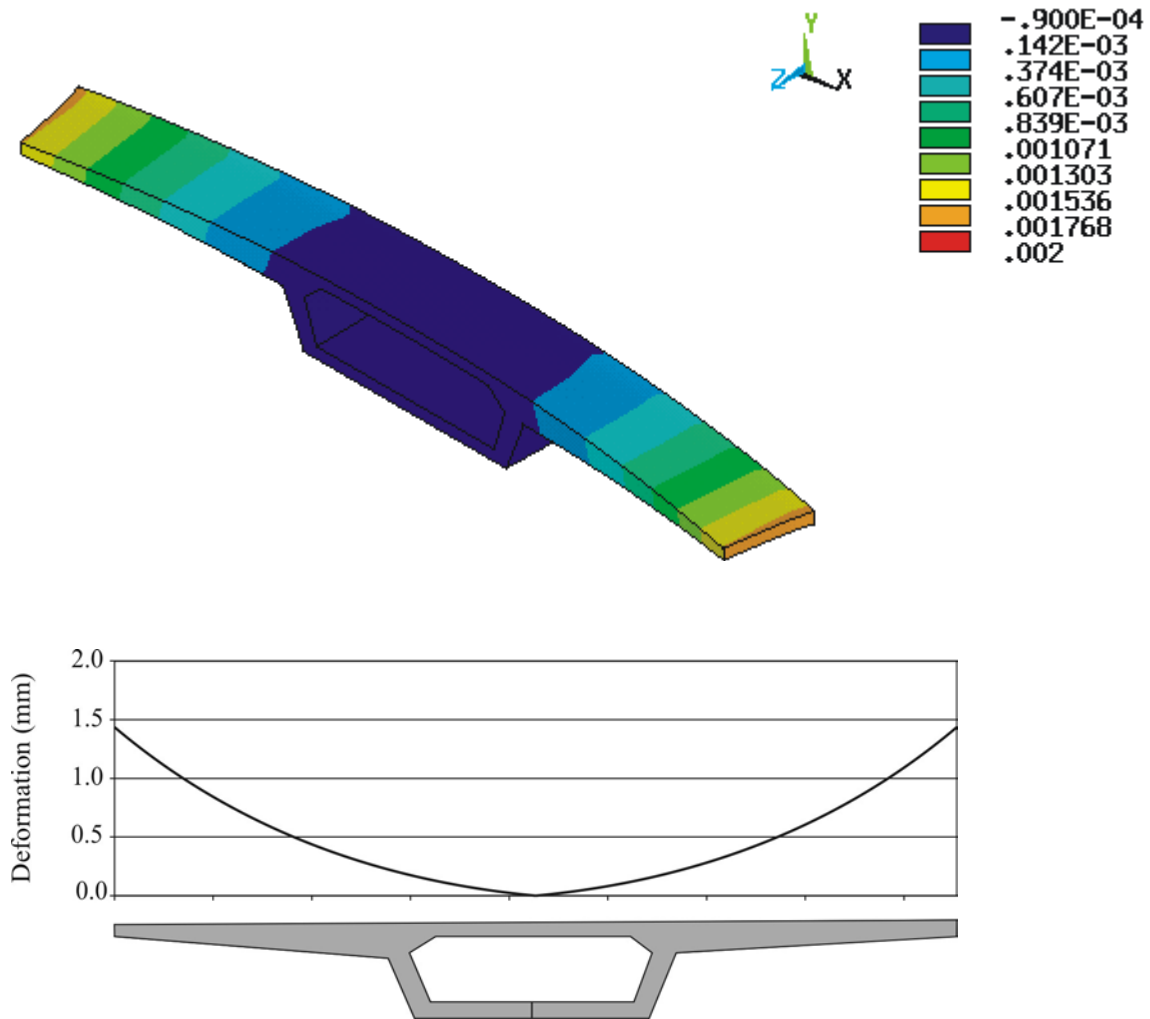
Figure 3.38   Deformations (*m*) in the z-axis direction after 10 hours in the type *III* old
segment using concrete mix 1 (high strength concrete) ($\Delta_{max, FE}$ = 1.72 *mm*)
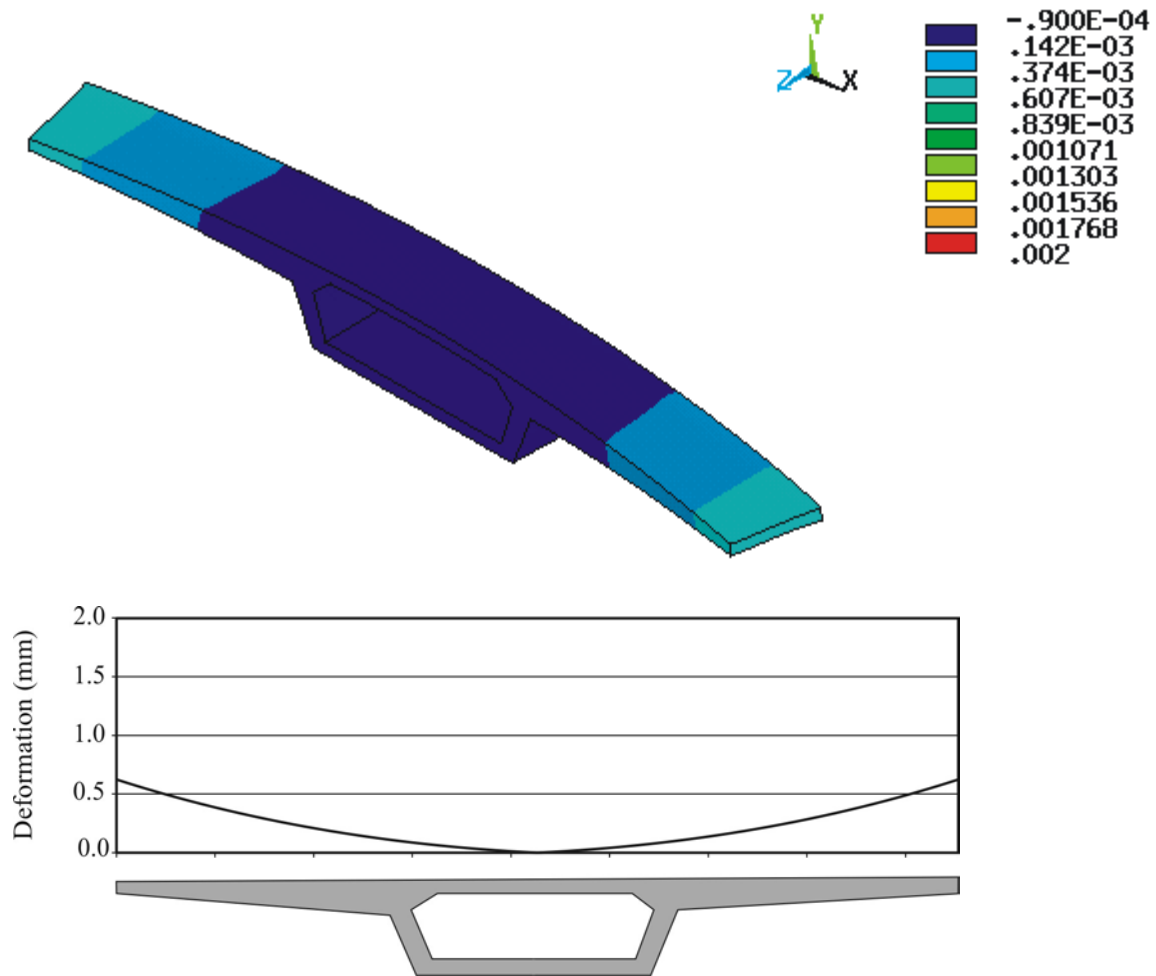
Figure 3.39   Deformations (*m*) in the z-axis direction after 10 hours in the type *III* old
segment using concrete mix 5 (low-heat concrete) ($\Delta_{max,\ FE} = 0.62$ *mm*)

3.4.3   Change of the ambient conditions

The heat flow at the surface of the segments depends on the heat transfer properties of the
boundary layer between the surface and the surrounding area. The factors to be considered
are the change of the ambient temperature, wind velocity, type and thickness of the
formwork. The effect of the thermal radiation in the match-cast process is relatively small
and is therefore ignored in the numerical model.

a)   Change of the ambient temperature.

The process of match-cast method can last more than one day. The change of ambient
temperature from day to night can result in a difference in concrete temperatures that may
lead to or increase the negative values in the thermal gradient of the old segment. Thus,
more bowing can occur in the match-cast segment. To study this effect the thermal gradient
and the bowing of a slender segment (*type III,* concrete mix 1) with and without a drop of

ambient temperature of 6 K have been analyzed. The following convection coefficients have been used:

$$\alpha_k = 5.8\,W\,/(m^2 \cdot^o C) \qquad \text{(wind velocity w = 0 }m/\text{sec)} \qquad \text{acc. equation 2.11}$$

$$k = \cfrac{1}{\cfrac{1}{\alpha_k} + \cfrac{h}{\lambda_f}} = \cfrac{1}{\cfrac{1}{5.8} + \cfrac{0.03}{0.14}} = 2.59\,W\,/(m^2 \cdot^o C). \qquad \text{acc. to equation 2.16}$$

Formwork made of wood plates with a thickness of $h = 3\,cm$

It is assumed that the hardening of the fresh concrete is not affected by the change of temperature. Figure 3.40 and Figure 3.41 show the results of this study. The maximum gap increased from 1.44 mm to 1.72 mm ($\Delta = 20\,\%$) due to the decrease of the ambient temperature. In some regions the difference in temperature between day and night could be much greater. Therefore choosing the time of the beginning of a match-cast process should be taken into consideration to decrease the bowing as much as possible. The best time to start pouring the concrete is the time when the ambient temperature increases.
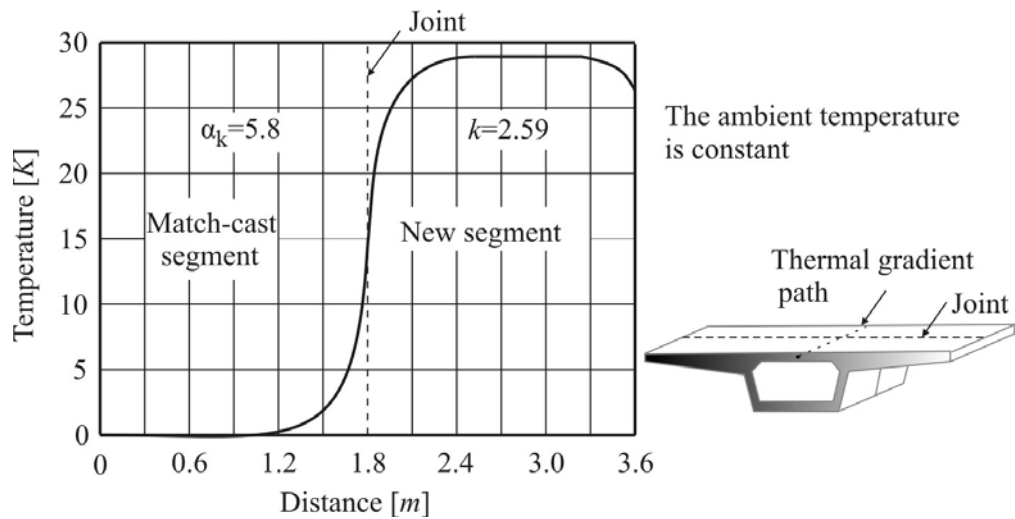
(a) Thermal gradient along the centreline of the deck
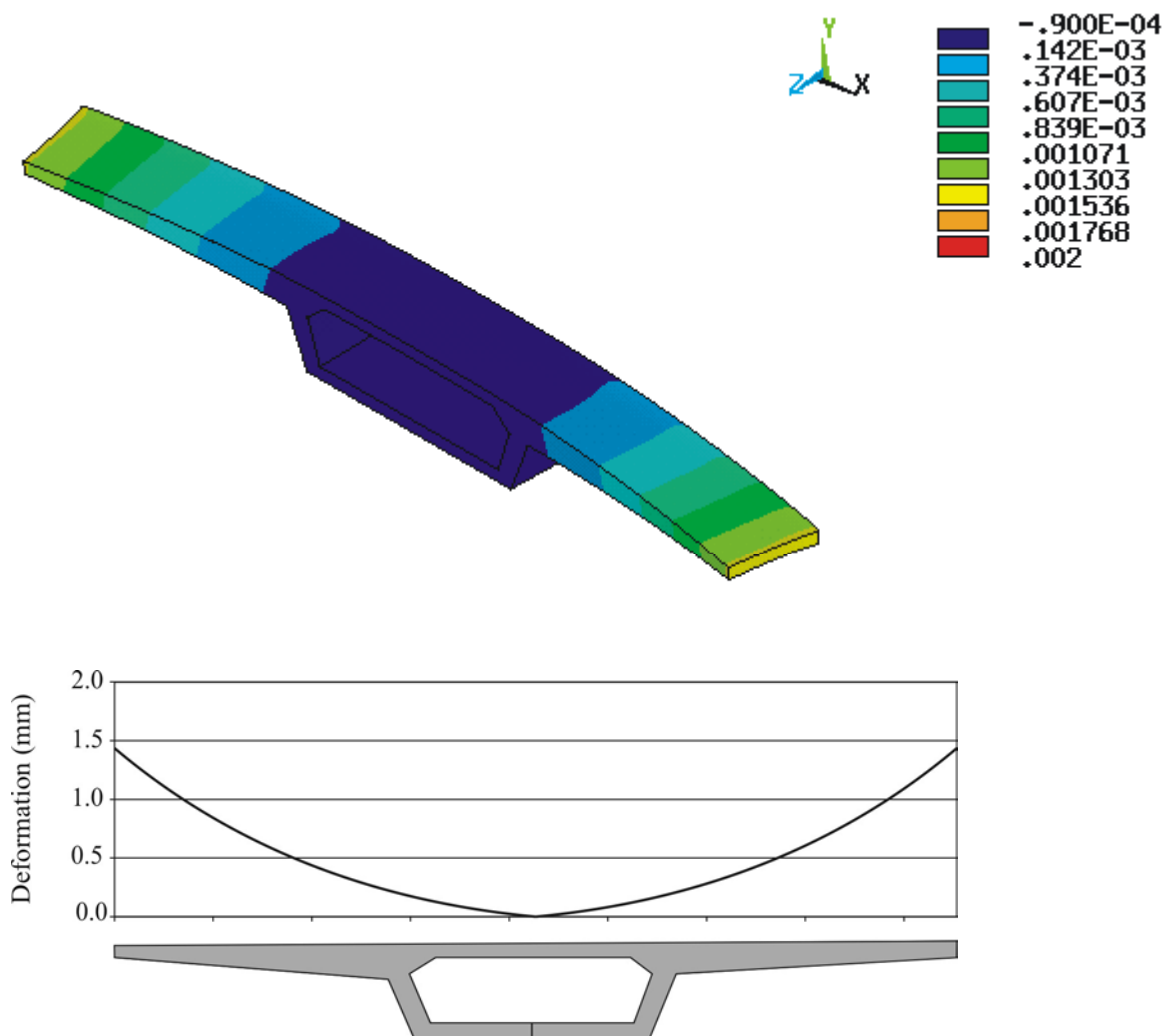
(b) Deformations (*m*) in the z-axis direction obtained (type *III* old segment, concrete 1)

Figure 3.40   Thermal gradient and deformations <u>without</u> change of ambient temperature after 10 hours
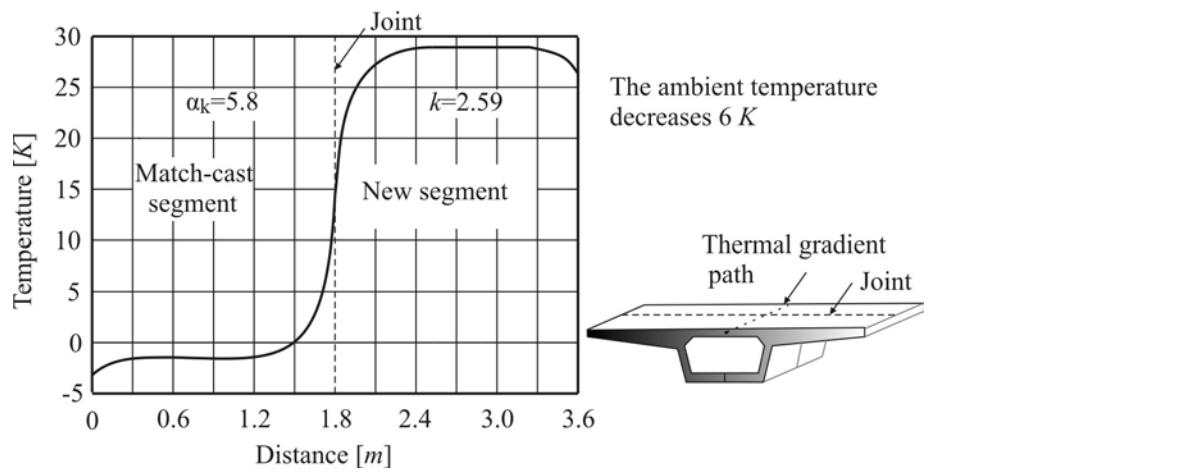
(a) Thermal gradient along the centreline of the deck
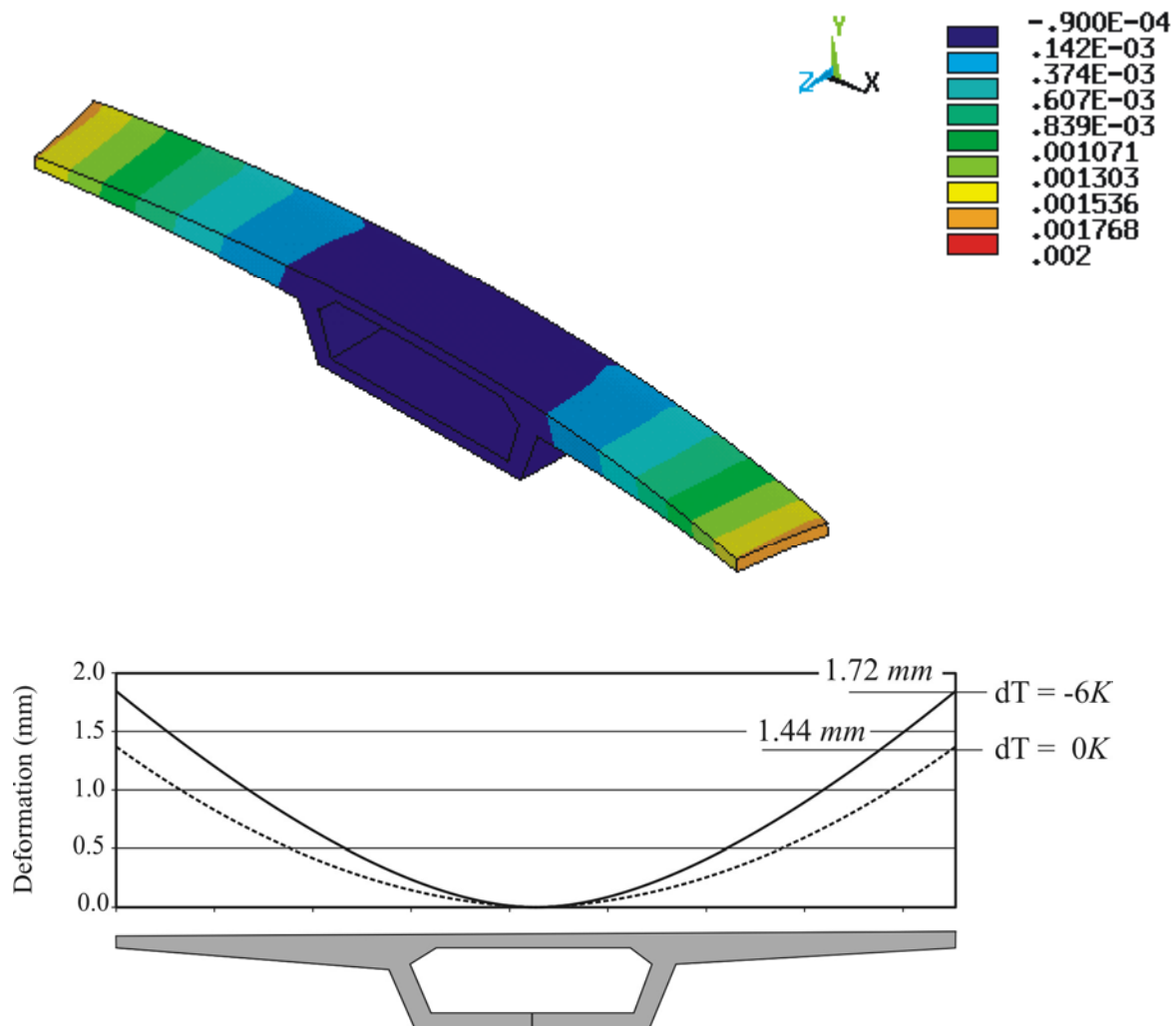
(b) Deformations (*m*) in the z-axis direction obtained (type *III* old segment, concrete 1)

Figure 3.41   Thermal gradient and deformations with a 6 *K* decrease of ambient
temperature after 10 hours

b) The wind velocity

The wind velocity influences the heat transfer coefficient α_k remarkably [Rec, Vdi], which can accelerate the development of the thermal gradient. If the ambient temperature decreases, the wind velocity will lead to more bowing of the match-cast segment. Figure 3.42 shows the effect of a wind velocity of 10 meters per second on the thermal gradient and bowing of match-cast segment in a condition where the ambient temperature decreases by $6\,K$ (convection coefficients $\alpha_k = 7.5 \cdot w^{0.78} = 43.1\,W/(m^2 \cdot {}^o\,C)$ acc. equation 2.12, $k = 4.2\,W/(m^2 \cdot {}^o\,C)$).

The numerical results showed an increase in the maximum gap from 1.72 *mm* to 1.85 *mm* ($\Delta = 8\,\%$) due to wind. If the ambient temperature increases with existence of wind, a decrease in the maximum gap will be resulted.
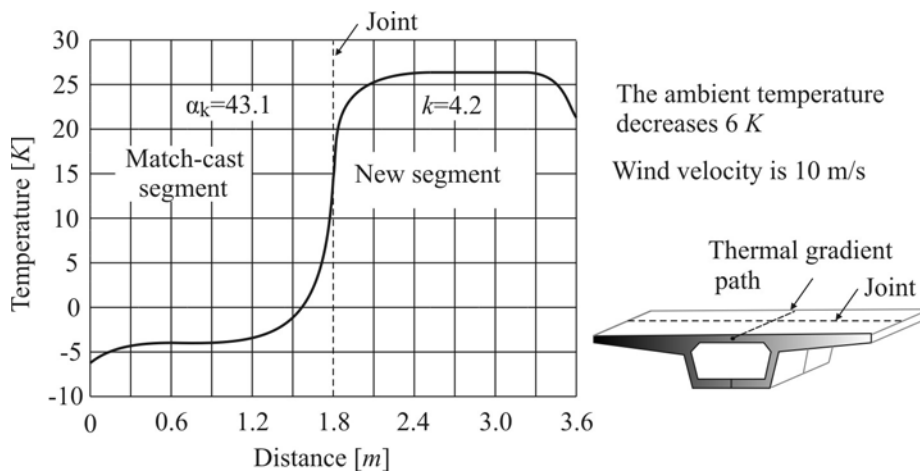
(a) Thermal gradient along the centreline of the deck
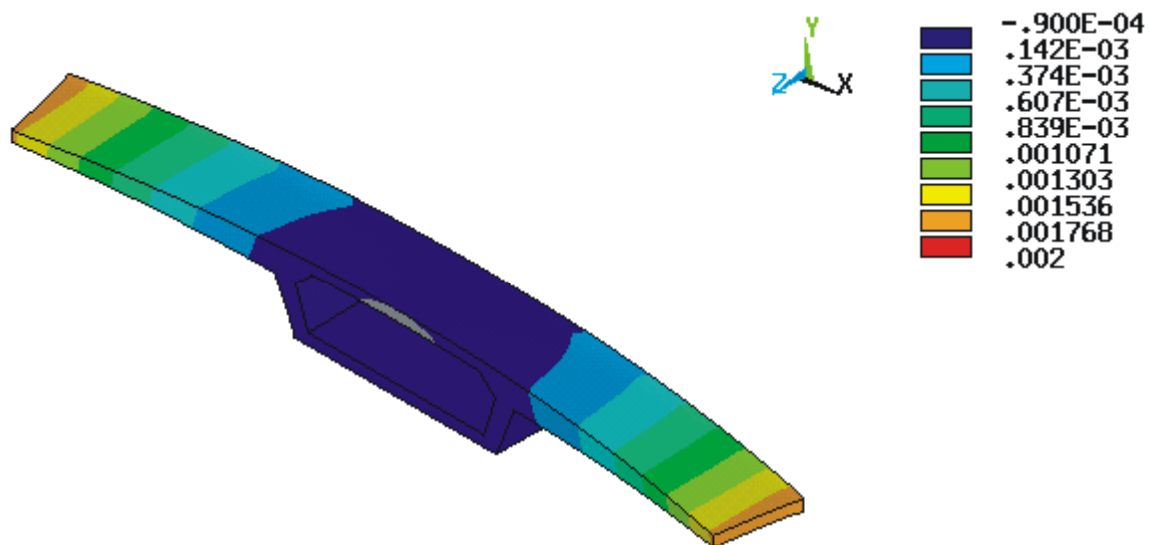
Figure 3.42a Thermal gradient <u>with</u> a 6 *K* decrease of ambient temperature and <u>wind</u> velocity of 10 *m/sec* after 10 hours
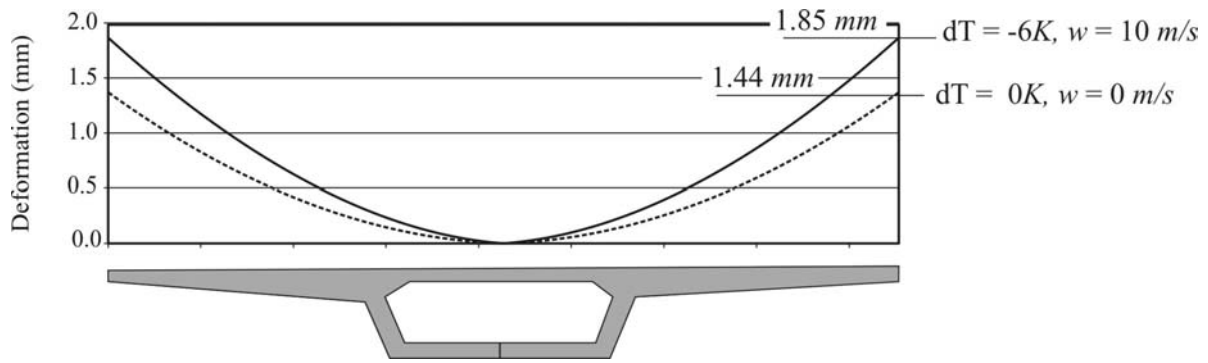
b) Deformations (*m*) in the z-axis direction obtained (type *III* old segment, concrete 1)

Figure 3.42b Deformations with a 6 *K* decrease of ambient temperature and wind velocity of 10 *m/sec* after 10 hours

c) The formwork properties

In the match-cast method the formwork used for the new segment will change the heat transfer or convection coefficient α_k. The convection coefficient of the formwork k can be estimated using equation 2.16.

$$k = \cfrac{1}{\cfrac{1}{\alpha_k} + \cfrac{h}{\lambda_f}}$$

The higher the thickness of the formwork h the less is the convection coefficient k. The thermal conductivity coefficient of formwork material λ_f for wood equals 0.14 $W/(m\ °C)$ according to DIN 4108 [Di1]. For formwork made of wood plates of 3 c*m* thickness k equals 2.59 $W/(m^2\ °C)$, whereas it was 4.1 $W/(m^2\ °C)$ when using 1 *cm* thickness ($\Delta = 60\ \%$). By using the above equation, it is found that the change of the type of formwork has a little influence on the convection coefficient k.

Figure 3.43 shows the deformation of the match-cast segment using formwork of 1 *cm* thickness around the new segment. A maximum gap of $\Delta = 1.43$ *mm* has been estimated. The results show that the properties of the formwork have very little influences on the total deflection of the match-cast segment compared to same conditions but with 3-*cm* formwork thickness as can be seen in Figure 3.40 ($\Delta = 1.44$ *mm*). Accordingly, the influences of the formwork around the new segment used in match-cast method can be ignored.

Figure 3.43 Deformations (*m*) in the *z*-axis direction obtained in the type *III* old segment using concrete mix 1 with 1-*cm* formwork thickness

3.4.4 Use of insulating materials

The insulating materials were used first as a practical measure to decrease the loss of the humidity in concrete at early age in order to avoid shrinkage and temperature induced cracks. In the match-cast process of the Bang Na segmental bridge both matching segments were covered with insulating materials such as plastic sheets to decrease the highly expected bowing. The effectiveness of the use of plastic sheets relies on the low thermal conductivity coefficient λ_f of these materials, which is about 0.03 *W/(m °C)*. A thickness of $h = 1$ *cm* gives a convection coefficient of $k = 1.98$ *W/(m² °C)*.

Figure 3.44 shows a deformed match-cast segment covered with plastic insulating materials The gap is slightly increased to $\Delta = 1.47$ *mm* compared to the match-cast segments without plastic insulating materials as shown in Figure 3.39 ($\Delta = 1.44$ *mm*). This increase in bowing

can be related to the less dissipated heat in the match-cast segment due to the insulation of the plastic materials. If the ambient temperature decreases $6°C$ as shown in Figure 3.45, the total deflection becomes ($\Delta = 1.58$ *mm*) which is less than that of the same conditions but without plastic insulating materials shown in Figure 3.41 ($\Delta = 1.72$ *mm*).

Insulating materials are very efficient when wind velocity of 10 *m/s* beside the $6°C$ decrease in the ambient temperature take place (see Figure 3.46). Thereafter the insulating materials have decreased the total deflection from 1.85 *mm* to 1.59 *mm* ($\Delta = 16$ %). Thus, the numerical results showed that the insulation materials can decrease the amount of total deflection by reducing the deviation in the negative thermal gradient curve. The insulating materials are not practical if there is no change in surrounding temperatures and wind velocity. The new match-cast segment should not be covered with insulating materials which decrease the transferred heat by convection. Hence, a growth in the thermal gradient will be expected.
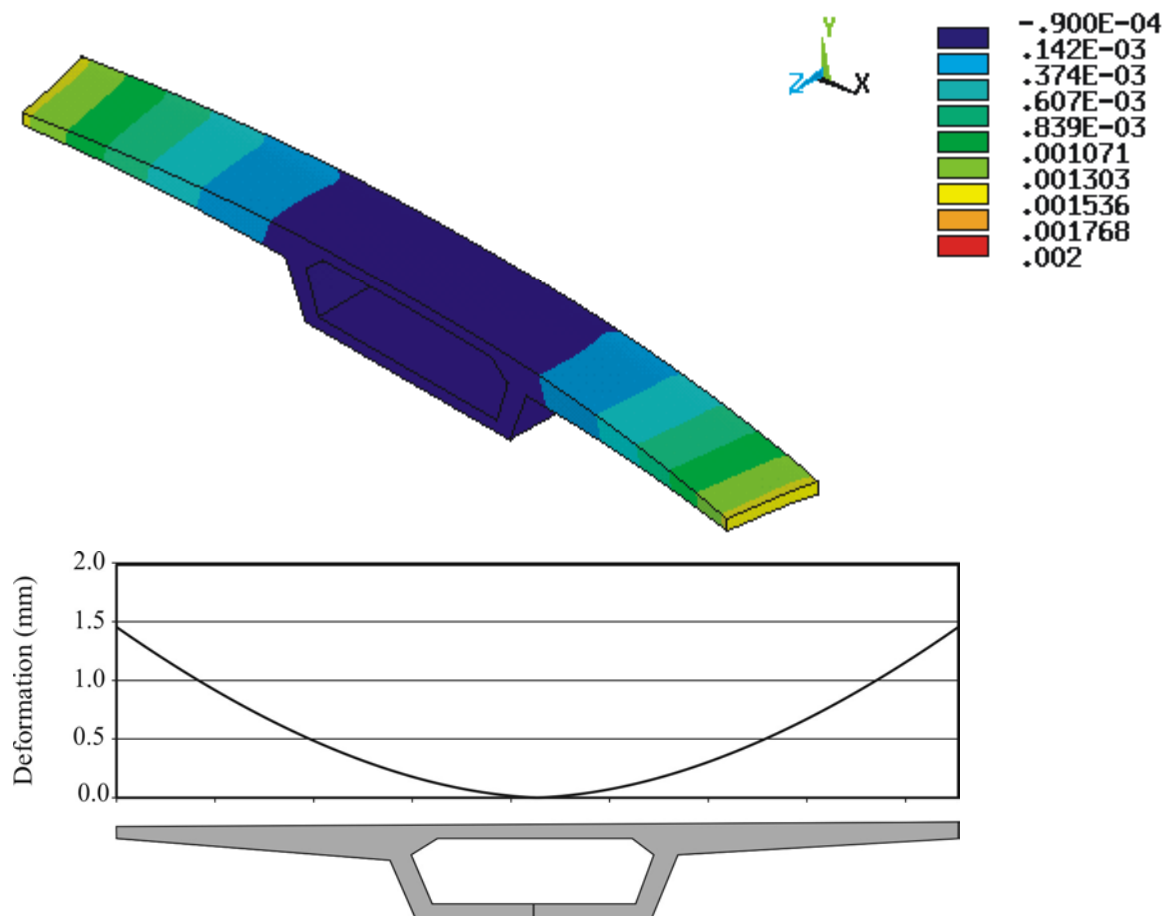
Figure 3.44   Deformations (*m*) in the *z*-axis direction obtained in the type *III* old segment using concrete mix 1 with plastic insulating material
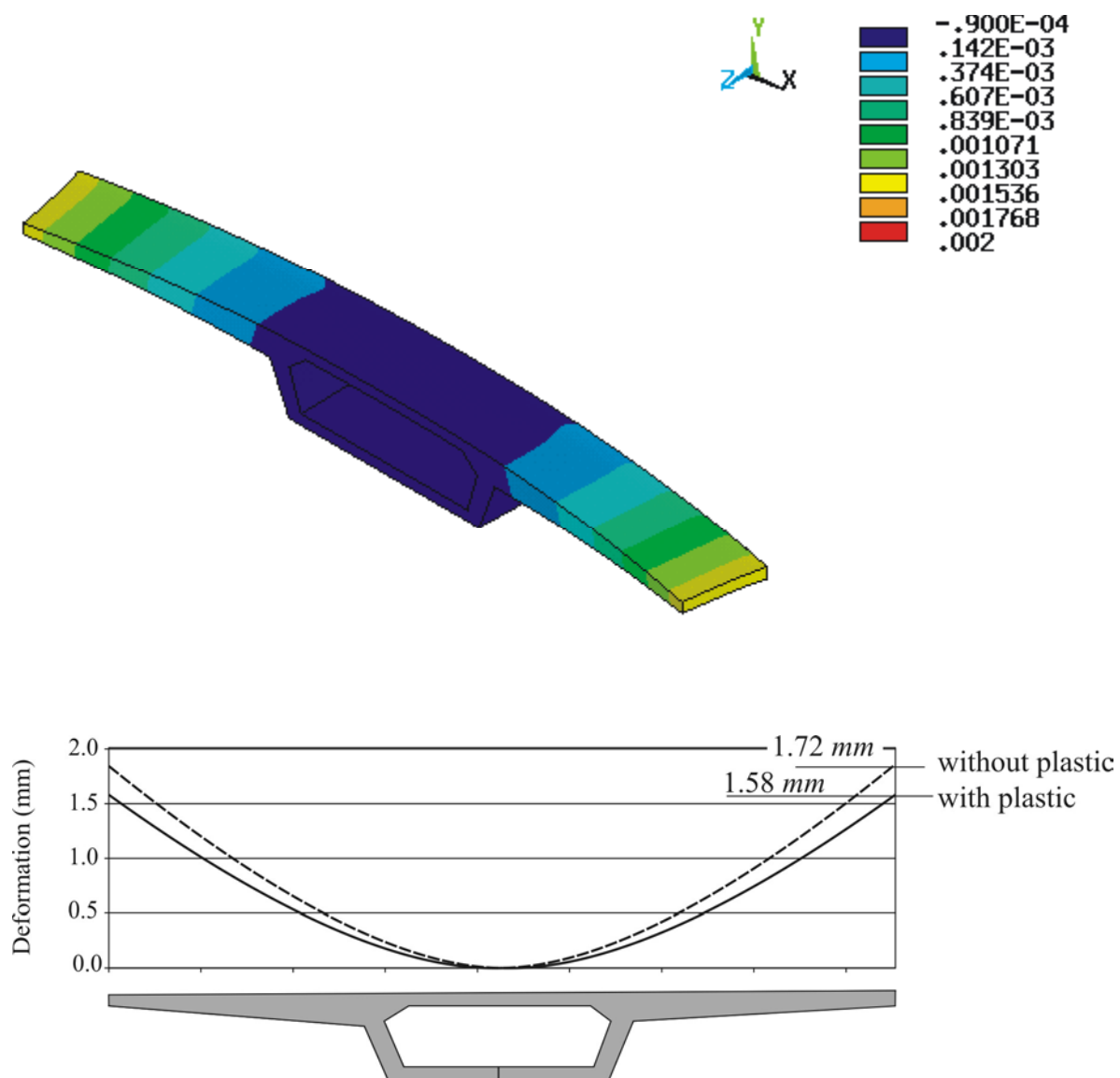
Figure 3.45   Deformations (*m*) in the *z*-axis direction obtained in the type *III* old segment using concrete mix 1 <u>with plastic insulating material with –6 *K* decrease</u> of the ambient temperature
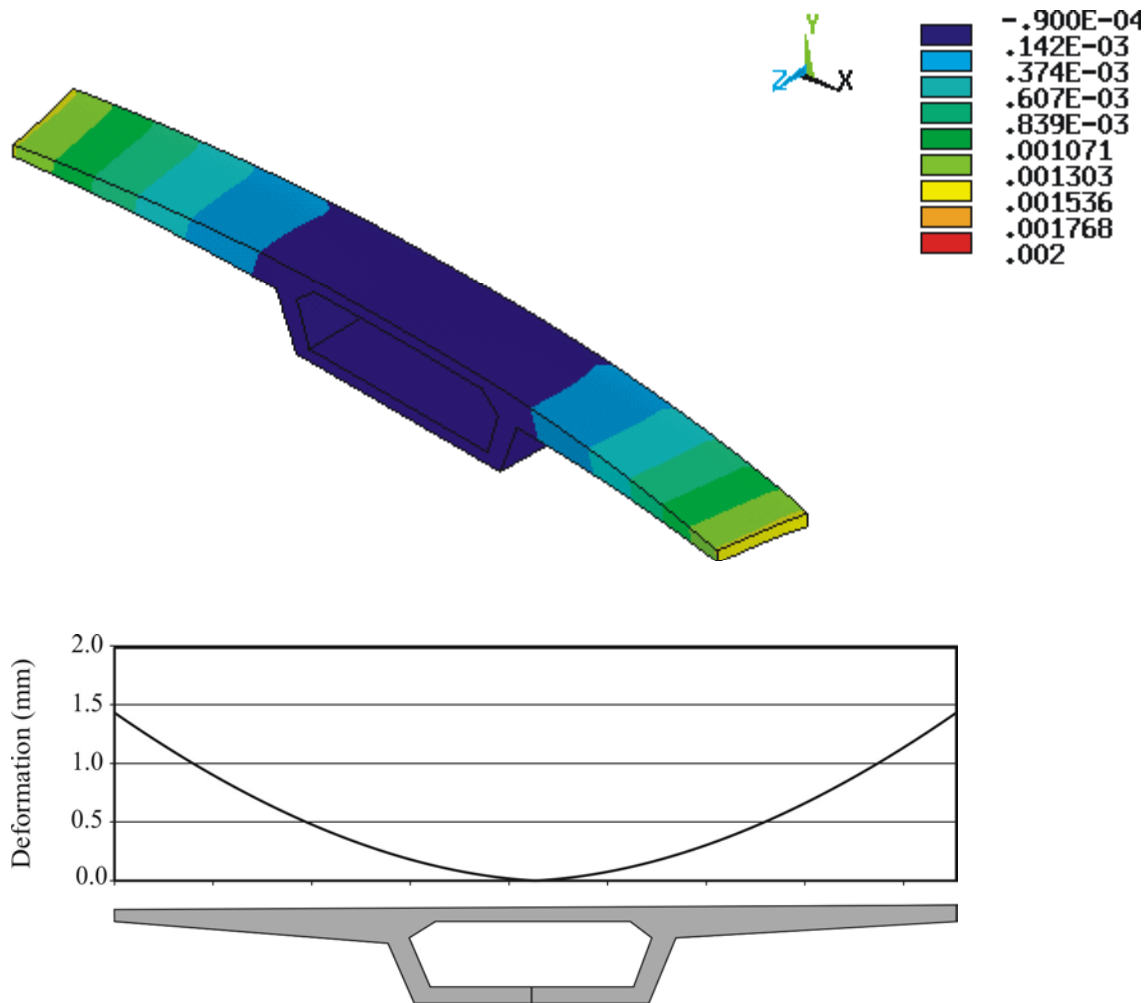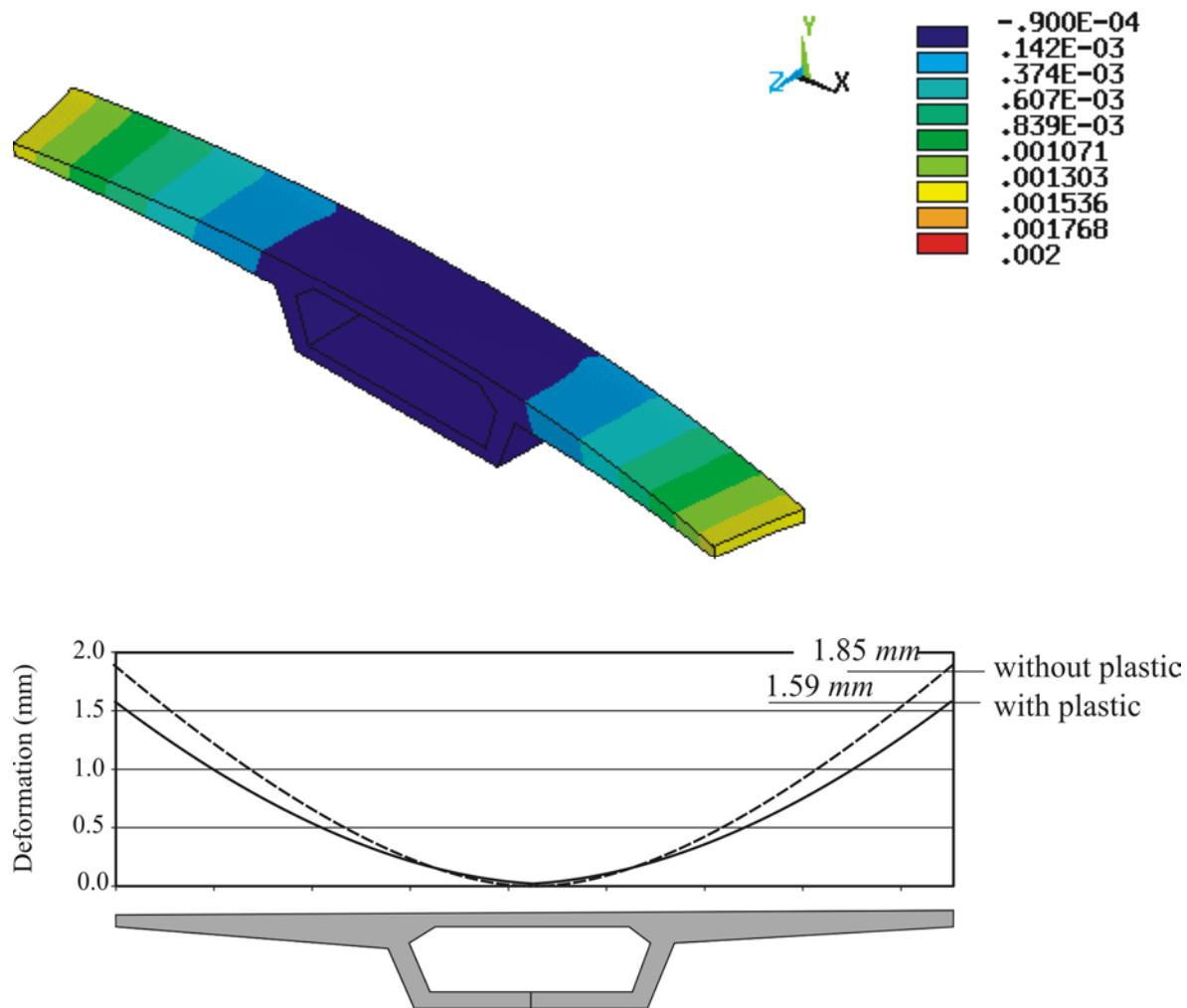
Figure 3.46   Deformations (*m*) in the *z*-axis direction obtained in the type *III* old segment using concrete mix 1 <u>with plastic insulating material with –6 *K* decrease</u> of the ambient temperature and <u>wind velocity of 10 *m/s*</u>

3.5 Summary

With the developed Finite Element model the bowing deformation of segments during match casting can be analyzed with high accuracy as comparisons with measurements on real segments demonstrates.

The parametric study showed that the bowing deformation increases strongly with the slenderness (*w/L*) of the segments. Degrease of ambient temperature and wind will further increase the temperature gradient in the match cast segment and the gap (Fig. 3.47).
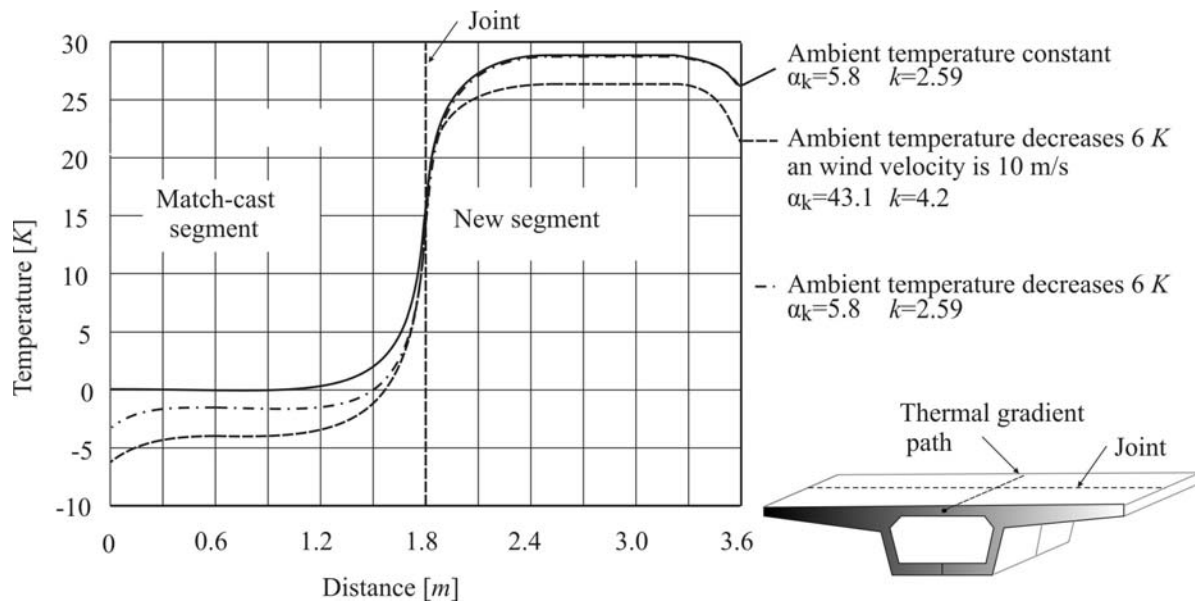
Figure 3.47 Temperature profile for different conditions

The main results of the parametric study are summarized in Table 3.5.

Table 3.5 Bowing deformations of type *III* segment (*w/L* = 9.3)

Concrete mix			1	1	1	5
Covering			no	yes	no	no
Formwork			3 *cm*	3 *cm*	1 *cm*	3 *cm*
	ΔT [K]	Wind speed [*m/sec*]	Gap Δ [*mm*]			
	0	0	1.44	1.47	1.43	0.65
	-6	0	1.72	1.58	-	-
	-6	10	1.85	1.59	-	-

ΔT = change in ambient temperature
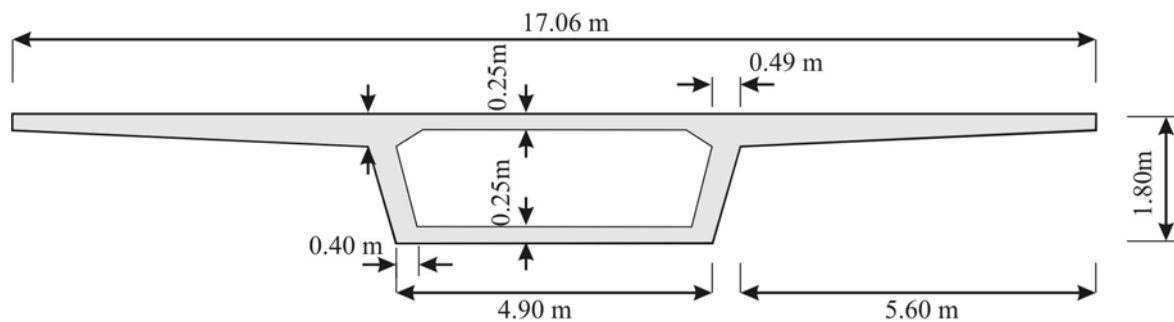
type III segment dimensions

3.6   Simple model to estimate the temperature gradient

By means of a 3-dimensional thermo-mechanical finite element analysis one can estimate the temperature distribution in a segment during match casting and calculate the gap between two adjacent elements with high accuracy for various boundary conditions as has been shown in the previous chapters. The main disadvantage of this method is the time which is needed to model the structure and to carry out and check the analysis. In the following a simple model is presented, which gives reliable results, at least for a preliminary design.

The finite element results have shown that the temperature distribution within the deck slab of a segment is nearly uniform in transverse direction. Thus the 3-dimensional structure can be reduced to a 1-dimensional middle strip of the slab for temperature analysis. (Fig. 3.47).
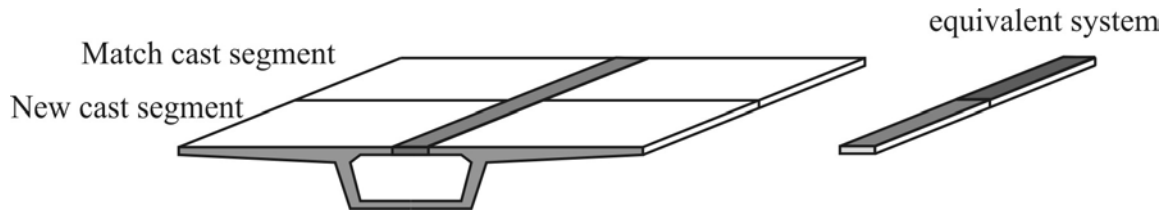
Figure 3.47   Equivalent system

This member can be modelled by simple 1-dimensional finite temperature elements. The basic equations are listed below. More details are given in appendix B.

global equilibrium:
$$\left(\frac{1}{\Delta t}\underline{M}\right)\underline{T}_{i+1} = \left[\frac{1}{\Delta t}\underline{M} - \underline{K}\right]\underline{T}_i + \underline{F}_i \tag{3.5}$$

element matrix:
$$k^{(j)} = \frac{A_c\lambda}{L^{(j)}}\begin{bmatrix} 1 & -1 \\ -1 & 1 \end{bmatrix} + \frac{\alpha_k \mathrm{P} L^{(j)}}{6}\begin{bmatrix} 2 & 1 \\ 1 & 2 \end{bmatrix} + \iint \alpha_k \left[N^{(j)}\right]^T \left[N^{(j)}\right] dS \tag{3.6}$$

specific heat matrix:
$$m = \frac{c\rho A L_i}{6}\begin{bmatrix} 2 & 1 \\ 1 & 2 \end{bmatrix} \tag{3.7}$$

internal heat vector:
$$f = \frac{Q A_c L_i}{2}\begin{Bmatrix} 1 \\ 1 \end{Bmatrix} \tag{3.8}$$

The sparse matrices $\underline{M}$ and $\underline{K}$ in equation 3.5 are constant during the whole analysis. Thus the calculation of the temperatures in the nodes can easily be conducted by means of a spreadsheet or mathematical programme.

In the following the results for a segment with a length of $l = 2.6\ m$ and a deck height of $0.20\ m$ are presented. The ambient temperature is constant. Further details are given in appendix D.

The system is modelled by 6 elements whereby 3 elements represent the new segment and 3 the old match cast segment. The length of the elements has been chosen with regard to the high temperature gradient in the joint region. The finite element analysis and the measurements showed that temperatures in the match cast segment decreased to ambient temperatures over a distance of $\approx 1\ m$ from the joint.

It should be noted that the size of the elements in the joint region should be greater than $10\ cm$ in this example as otherwise numerical instabilities occur (see Fig. 3.49, t_4 and t_5 curves). On the other side, the temperature gradient in the match cast segment is nearly independent of the element size in the joint region as parameter studies have shown (Fig. 3.51).

The fresh concrete is covered on the bottom face of the slab by formwork. Convection takes only place at the top and bottom surfaces of the member and on the left side as the equivalent system is a part of a bigger slab.
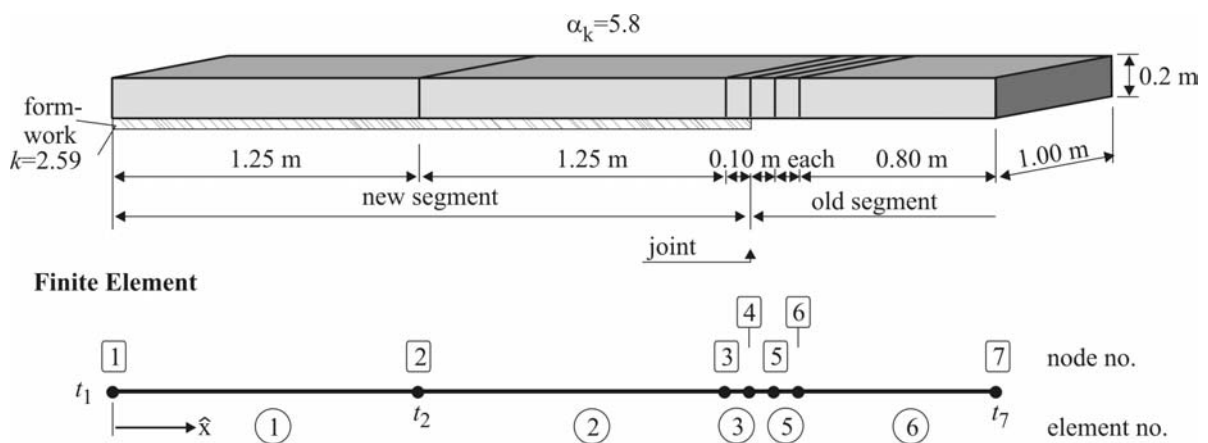
Figure 3.48   System and finite element model

The results of the analysis are shown in the following figures. A good agreement of the temperature gradient between the 3-D finite element analysis and the simple model can be observed (Fig. 3.49). Thus, a one dimensional model is sufficient to estimate the temperature gradient in the match cast segment for ordinary cases when the environmental conditions does not change. The effect of different concrete mixes or insulating sheets can easily be checked by this simple model.
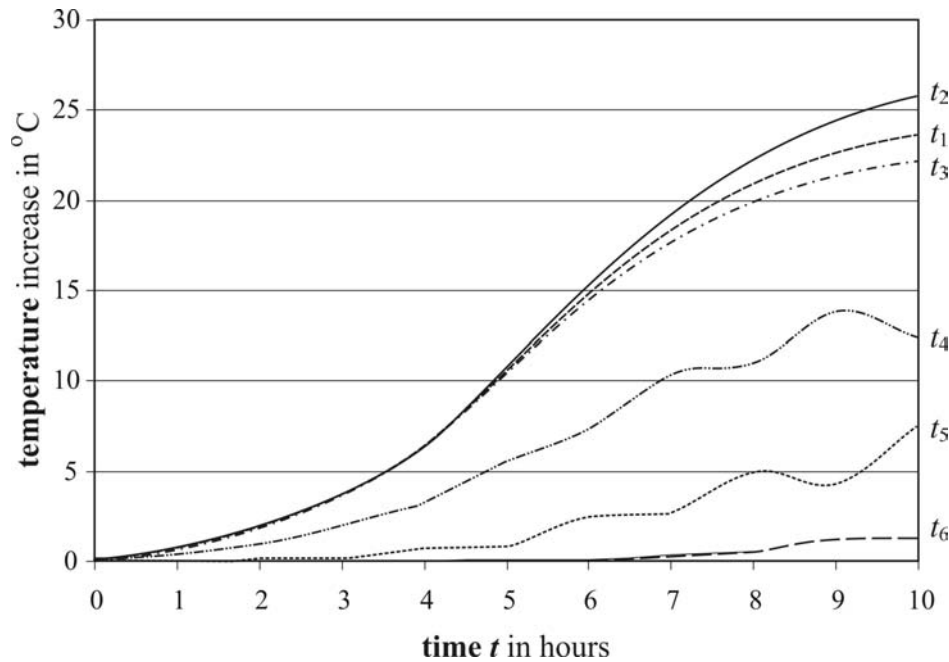
Figure 3.49   Temperature distribution in the nodes over time
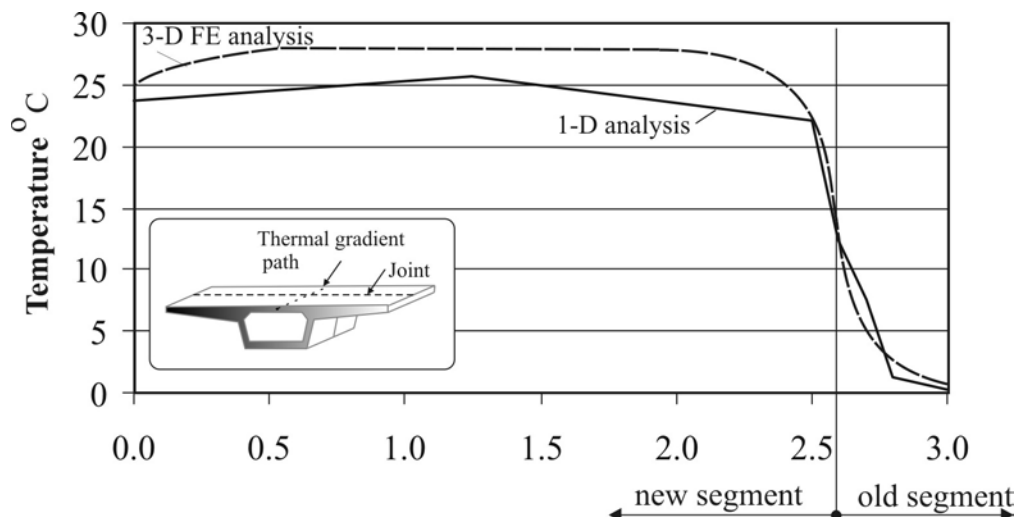
Figure 3.50   Temperature gradient after 10 *h*
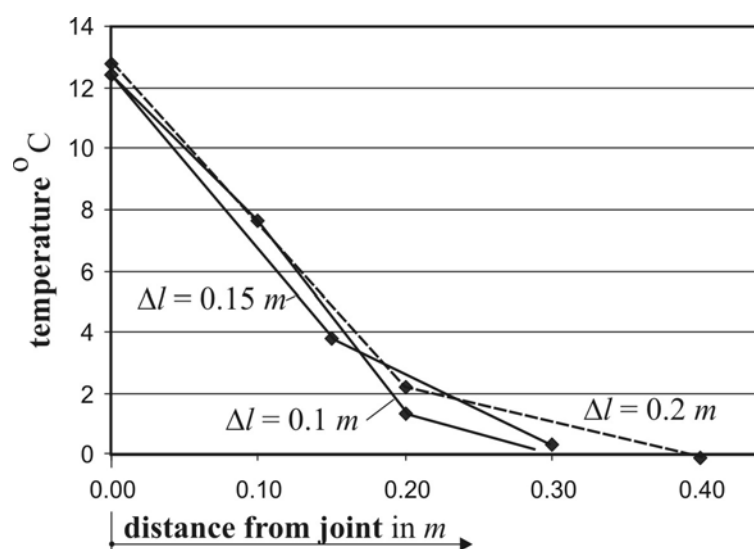
Figure 3.51   Temperature gradient after 10 *h* for different element lengths

4   Behaviour of segmental bridges with bow shaped elements

In this chapter the influence of imperfect bowed segments on the behaviour of two real segmental bridges will be studied. First, complex finite element models of the real structures will be presented and will be verified by test results taken from the SES bridge in Bangkok. Then this numerical model will be extended to imperfect segments with gaps caused by match casting. The influence of the gaps on the serviceability and load bearing capacity of the whole structure under short term and long term loading is studied including the time dependant behaviour of concrete (creep and shrinkage). The same investigations will be conducted for the Bang Na bridge which consists of very slender segments.

4.1   Test span of the segmental bridge of the Second Stage Expressway System

The Second Stage Expressway System (SES) consists of approximately 32 *km* of elevated roads in Bangkok [Ro1]. In 1993 the first phase of the SES was completed. More than 14,500 segments were cast and more than 1000 simply supported spans of precast segmental decks ranging in span length from 24.9 *m* to 48.7 *m* were erected [Ta1]. The standard span of the Second Stage Expressway System in Bangkok is shown in Figure 4.1. It has a length of 45.25 *m* and consists of 14 segments (2 pier -, 3 deviator – and 9 standard segments). Dry joints were used only.

A full-scale test of a 45 *m* long span, a prototype of the segmental decks in the SES, has been carried out in the year 1991. The used segments had a width of 10.2 *m* and a length of 3.4 *m* (w/L = 3.0), whereas the pier segment had a length of 1.225 *m* (w/L = 8.3). The bridge was prestressed by external tendons only which were formed from 12 k15 or 19 k15 strands (St 1660/1860, P_0 = 2440 *kN* and P_0 = 3864 *kN*) protected by high-density polyethylene ducts and cement grouted. Figures 4.2 and 4.3 show the bridge details and the tendon layout. The details of the used segments and shear keys can be seen in Figure 2.2.

Figure 4.1 Span of the Second Stage Expressway segmental bridge in Bangkok [Ro1]
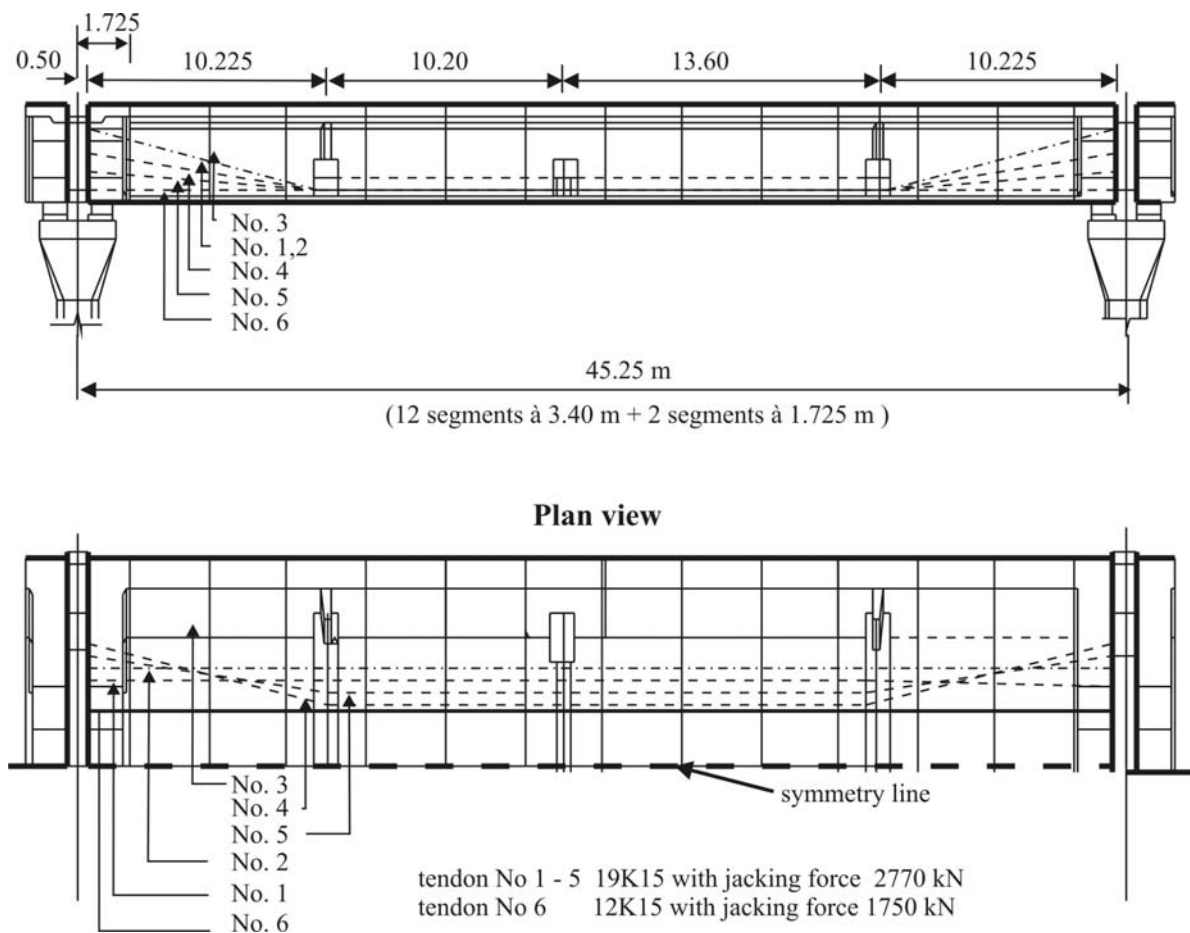
Figure 4.2 Tendon layout of a standard span [Ro1]
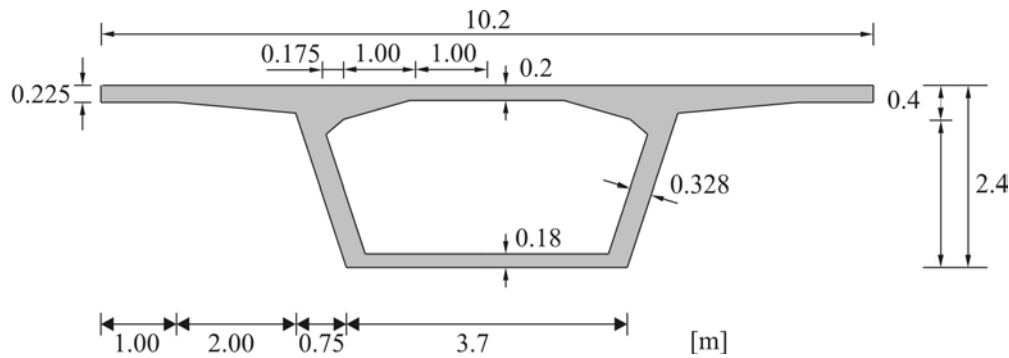
Figure 4.3 Cross section of test span [Ta1]

Instrumentation of test span

In order to monitor the strains in the concrete and tendons at various locations 66 strain gauges were set up in the test span. Joint opening and joint slip was monitored using 24 dial gauges set horizontally for joint opening while those for joint slip were vertical. To monitor the deflection of the span, vertical scales attached to the web of the segments were set up at 56 locations [Ta1].

Loading

Steel billets were stacked up in two load areas as the imposed load for the test, as can be seen in Figure 4.4. Each billet was 347 *kg*. The loading process took five days, during the nighttimes no loading operation was made but strain gauge readings were measured at hourly intervals. Readings were gained at every 120 billets (408.50 *kN*) loading cycle up to a load of 1560 billets (5,310.30 *kN*) relevant a bit before the supposed decompression load. Thereafter readings were acquired at every 20 billet-loading cycle (68.08 *kN*) until collapse. To make sure that no stability problem can occur during the night, 70 billets (238.28 *kN*) were removed from a total load of 2470 (8,408.05 *kN*) at the end of the fourth day. The failure occurred in the fifth day at a load of 2620 billets (8,918.66 *kN*). Table 4.1 lists the loading operation.
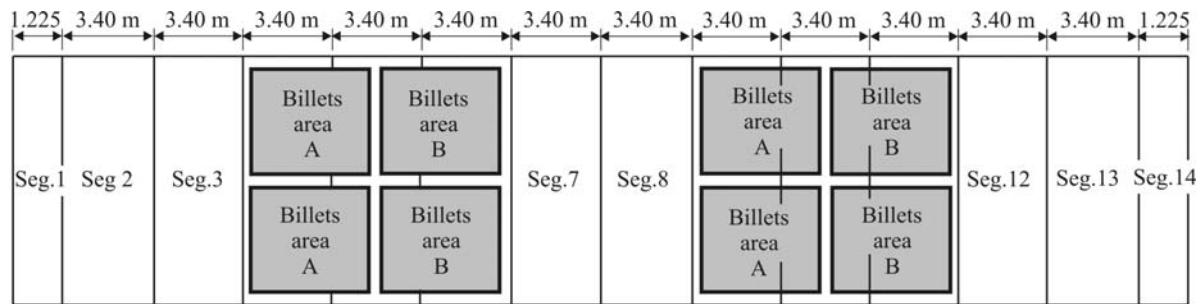
Figure 4.4 Arrangements of steel billets areas on the deck of the SES bridge [Ta1]

Table 4.1 Loading operations during the five days of loading [Ta1]

Day	Load stage	No. of billets and load	Applied mid-span moment [kNm]
1	No load	0	0
	Trial Load	120 (408.5 KN)	3,200
	No load	0	0
	Overnight load	360 (1,225.5 KN)	8,600
2	Design service load	1080 (3,676.4 KN)	24,600
	Overnight load	1320 (4,493.4 KN)	30,000
3	Observed decompression load at joint 8- 9	1620 (5,514.6 KN)	36,500
	Observed decompression load at joint 7- 8	1660 (5,650.8 KN)	37,250
	Design ultimate load (overnight load)	1980 (6,740.1 KN)	44,600
4	Load to 2470 billets	2470 (8,408.1 KN)	54,900
	Unload 70 billets for safety (overnight load)	2400 (8,169.8 KN)	53,600
5	Design ultimate load / Φ	2600 (8,850.6 KN)	57,700
	Failure load	2620 (8,918.7 KN)	58,200

Beside the billets load, the structure was subjected to other loadings such as: temperature, wind, rain, etc. In the finite element analysis of the SES segmental bridge only the imposed load of the billets and the dead load will be considered.

The test span was loaded to its design limits for two years in order to investigate the behaviour under long-term loadings. The deflection and deformation characteristics were monitored continuously; the changes in mid-span deflection and length of span are listed in Table 4.2. Figure 4.5 shows the deflection of mid-span of SES segmental bridge during two years of loading.

Table 4.2 Change in mid-span deflection and span length during two years of loading [Ta1]

Date	Deflection at joint 7- 8 in *mm*	Span length in *m*
29 May 1991	0.0	44.237
05 June 1991	2.7	44.239
12 June 1991	4.0	44.231
19 June 1991	5.0	-
26 June 1991	7.3	-
26 July 1991	13.2	44.234
26 Aug. 1991	10.0	-
26 Sep. 1991	15.3	-
26 Oct. 1991	15.2	-
26 Dec. 1991	15.8	-
05 Feb. 1992	18.8	-
06 Apr. 1992	20.3	-
05 June 1992	21.6	-
05 Aug. 1992	22.9	-
05 Oct. 1992	24.3	-
11 Nov. 1992	25.2	-
10 May 1993	25.8	44.230
11 May 1993	25.2	-
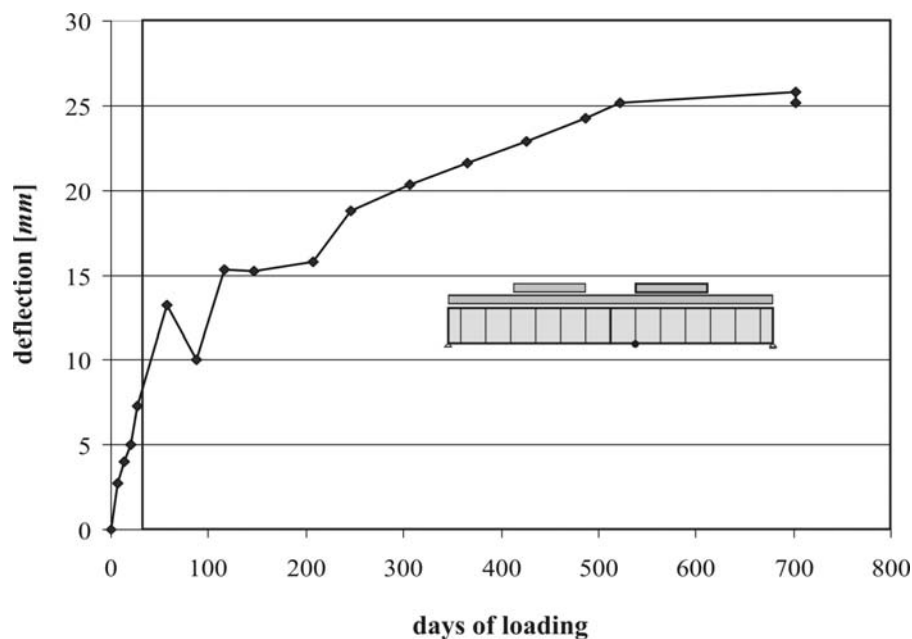
Figure 4.5 Change in mid-span deflection during two years of loading the SES bridge [Ta1]

4.2 Numerical simulation of SES segmental bridge

4.2.1 The numerical model

The finite element program ANSYS is used to analyze a three-dimensional non-linear model of a segmental bridge including dry joints between the segments. The hollow box girder is modelled by four-node thin shell elements; the tendons by truss elements, and contact elements are used to replace the shear keys in order to transfer compression and friction forces across the joints. The friction losses of the tendons in the deviators are ignored in the model. Figure 4.6 shows the SES bridge finite element model.
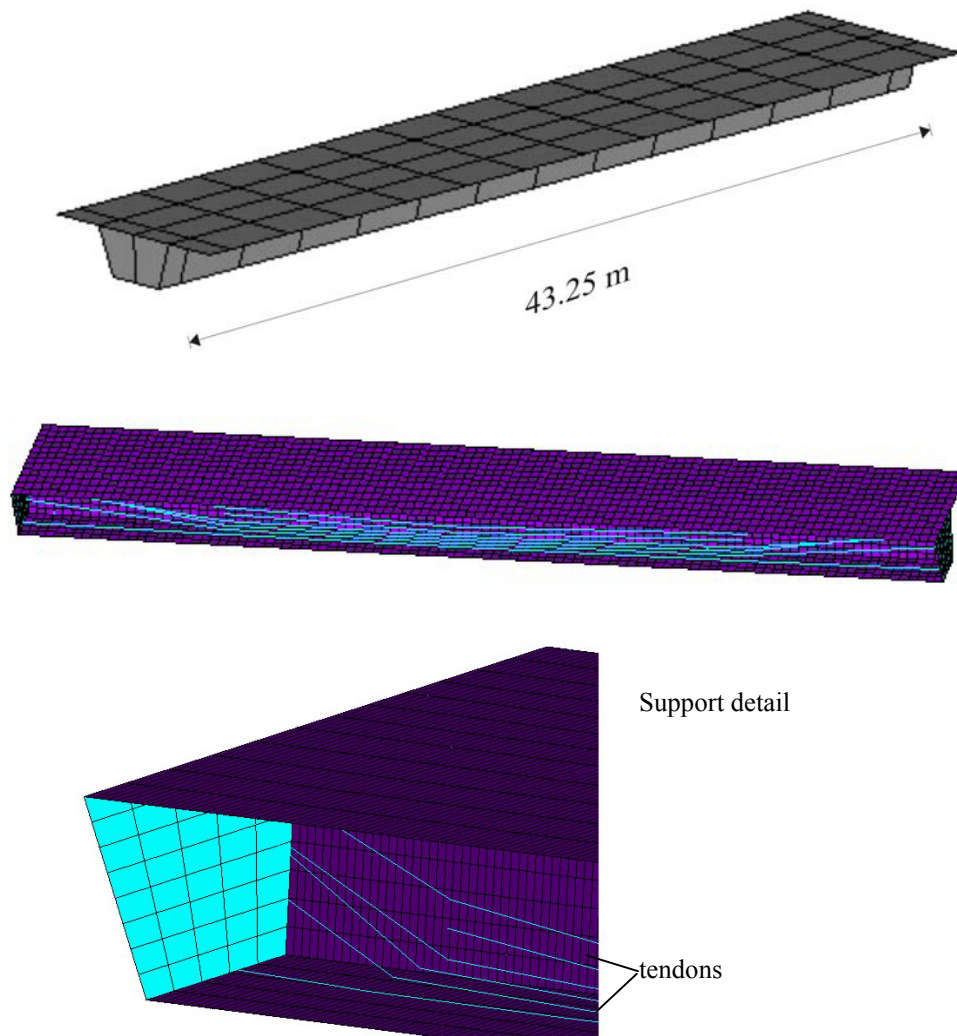
Figure 4.6 SES bridge finite element model

4.2.2 Material properties used in the FE model

Concrete

All the tests carried out on the segmental bridges showed that the deformation and bearing capacity of these structures are controlled by the behaviour of the joints. Thus, a simple non-linear stress-strain relationship of the concrete according to the German Code [Di2] was used herein as can be seen in Figure 4.7.
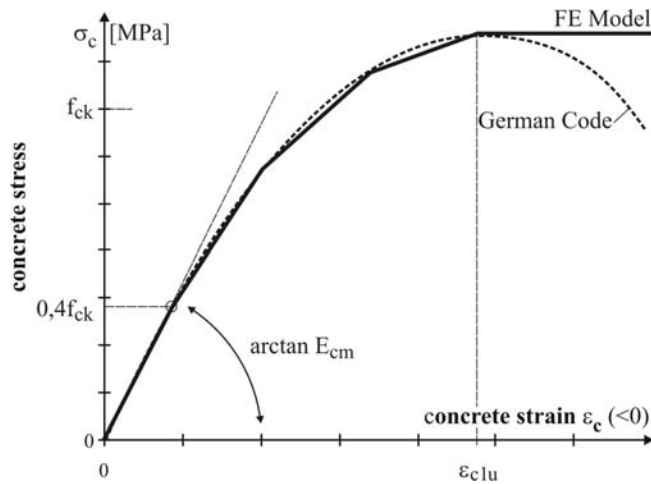
Figure 4.7 Stress-strain relationship of concrete [Di3]

Tendons

In most concrete structures the design aims to let the steel yield before the crushing of the concrete in the compressive zone. Hence, ideal elastic – ideal plastic relationship is used for the tendons to enable the model to describe the failure mechanism. Figure 4.8 shows the stress-strain relationship of the prestressing steel according to German Code (Di2).
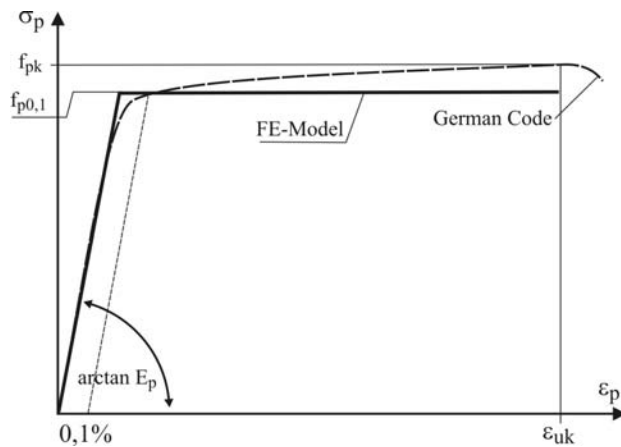
Figure 4.8 Stress-strain relationship of prestressing steel [Di2]

Because external prestressing without bond was used, the tendons are only connected to the structure at the piers and the deviator segments.

Contact elements

The contact elements used in the model to describe the behaviour of the joints support only the compression and shear forces. They do not work as long as there is a gap between the two adjacent segments. The contact elements have the ability to work again as the gap closes with time. Sliding can occur once the maximum shear force is exceeded which never happened during the analysis. Thus shear keys can be neglected in the model. Figure 4.9 shows the force-deflection relationship of the contact element which can be separated into normal and tangential direction.
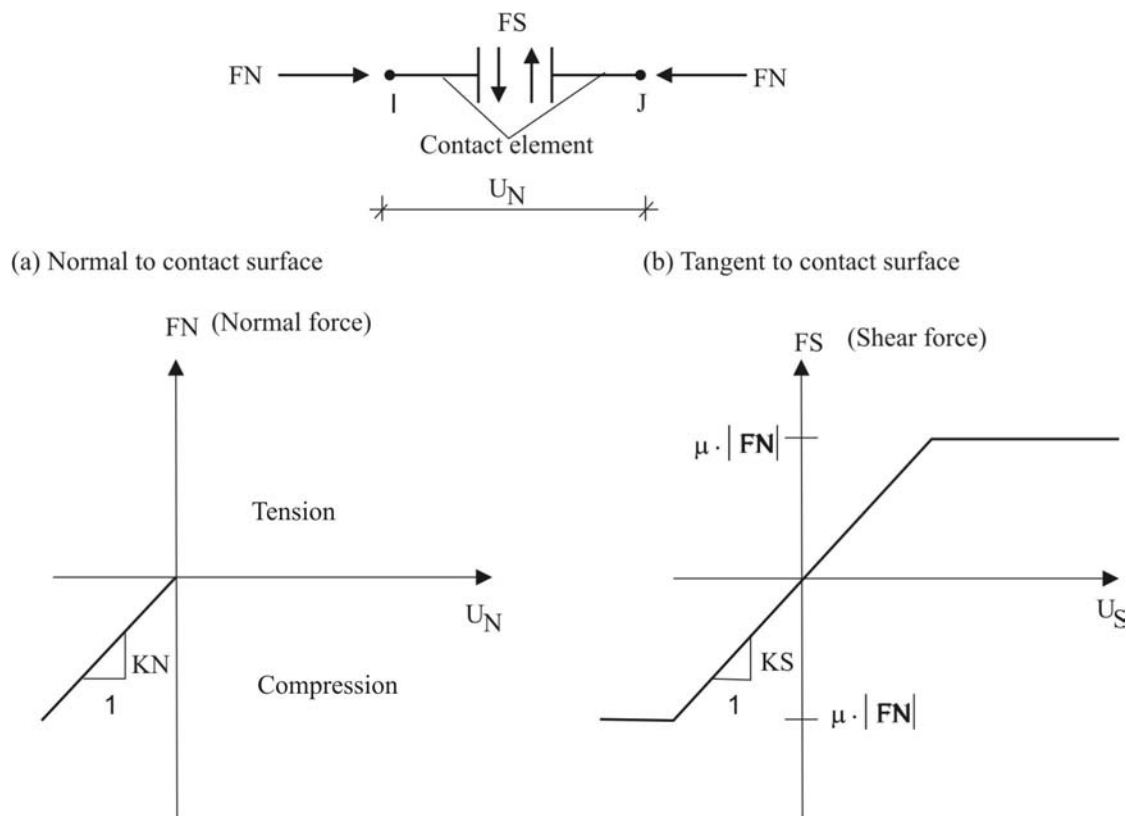
Figure 4.9 Force-deflection relationship of contact element "Contact52" [Ans]

The friction coefficient μ which represents the maximum possible shear force transferred by the contact element equals 0.7 as given by Specker [Sp2] for rough concrete surfaces. The shear coefficient *KS* based on the test results of Kupfer [Ku1] equals 15,000 *N/mm*.

4.2.3   Verification

The numerical model is verified by simulating the full-scale tests of the SES segmental bridge, where the behaviour of a precast segmental bridge with external tendons and dry joints was investigated [Ta1, Ta2]. The concrete and tendon properties used in the numerical model of SES segmental bridge are listed in Table 4.3. Figure 4.4 and 4.10 shows the arrangement of the live loads (billets) on the deck used in the numerical model.

Table 4.3 Material properties used in the numerical model of SES segmental bridge [Ta1]

Material	Properties item	Average value
Concrete	Compressive strength, f_{ck}	58.0 MPa
	Modulus of elasticity, E_c	43,000 MPa
	Poisson's ratio, v	0.2
Tendons	Modulus of elasticity, E_s	193,000 MPa
	Yield strength, f_{yk}	1,530 MPa
	Breaking strength, f_{pk}	1,920 MPa
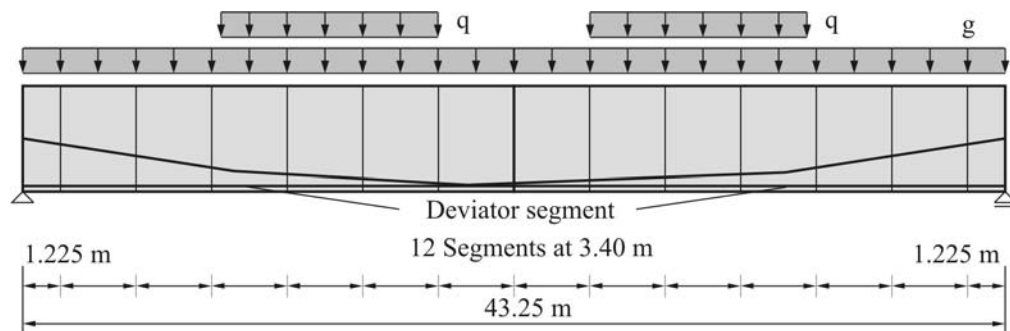
Figure 4.10 Load arrangement used in the finite element model

Figure 4.11 shows the longitudinal compressive stresses σ_x (*MPa*) and deflection of the SES segmental bridge due to a combination of dead load and tendons forces, thereafter due to full loading at the fifth day. First the bridge deforms upwards due to the high prestressing.

(a) $M_q = 0$ *MNm* (dead load only)

(b) $M_q = 58.2$ *MNm* (failure load)
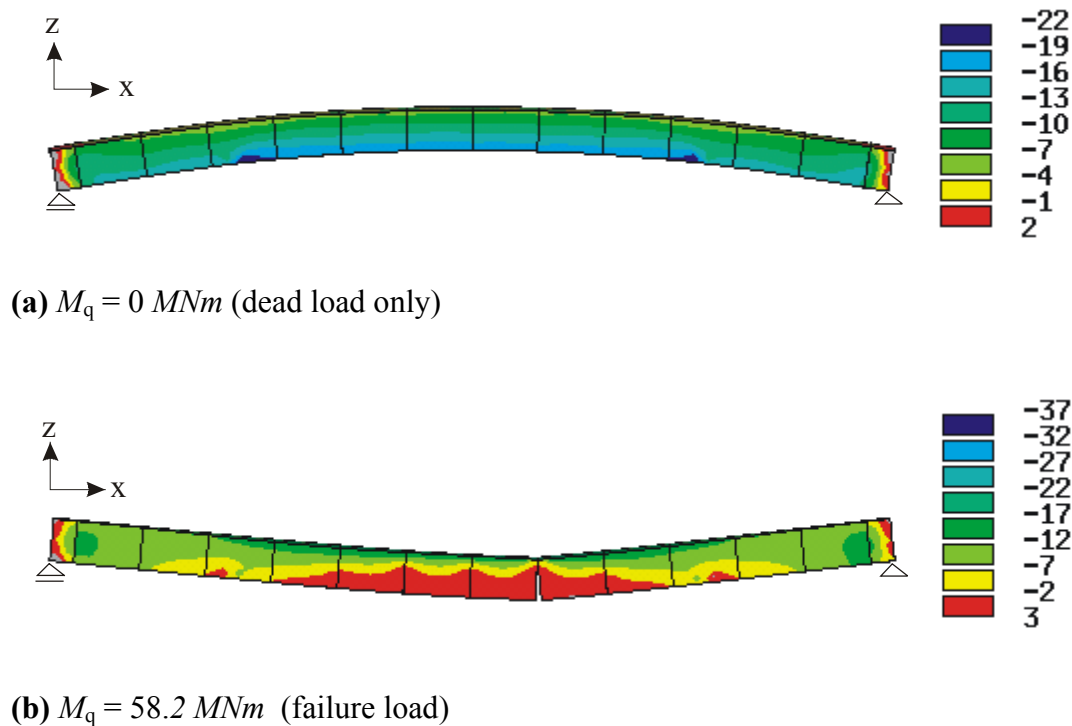
Figure 4.11 Longitudinal stress σ_x (*MPa*) and deflection in the SES segmental bridge

If the live load is increased the structure behaves elastic until the first joint close to midspan opens. Then the stiffness of the structure is significantly reduced.

The deflections versus the applied live load bending moment of the numerical analysis were compared to the measured results obtained by the five-day-collapse test as can be seen in Figure 4.12. The structure behaves fully elastic until the joint between segment 7 and segment 8 starts to open. This behaviour was also observed in the test. The measured value of the joint opening after applying a live load bending moment of 58.2 *MNm* was about 35 *mm*, whereas the numerical value was about 33 *mm*. The comparison between both the numerical and measured results is plotted in Figure 4.13.

The measured deflections of the two-year-tested span resulted in a final deflection of about 25 *mm* (see Figure 4.14), while the numerical model considering creep and shrinkage effects according to German Code [Di2] showed a maximum deflection of about 24 *mm*. A good agreement between the measured and numerical results can be seen in Figure 4.14. This demonstrates that the developed numerical model can be used to analyze the behaviour of segmental bridges under short and/or long-term loading.
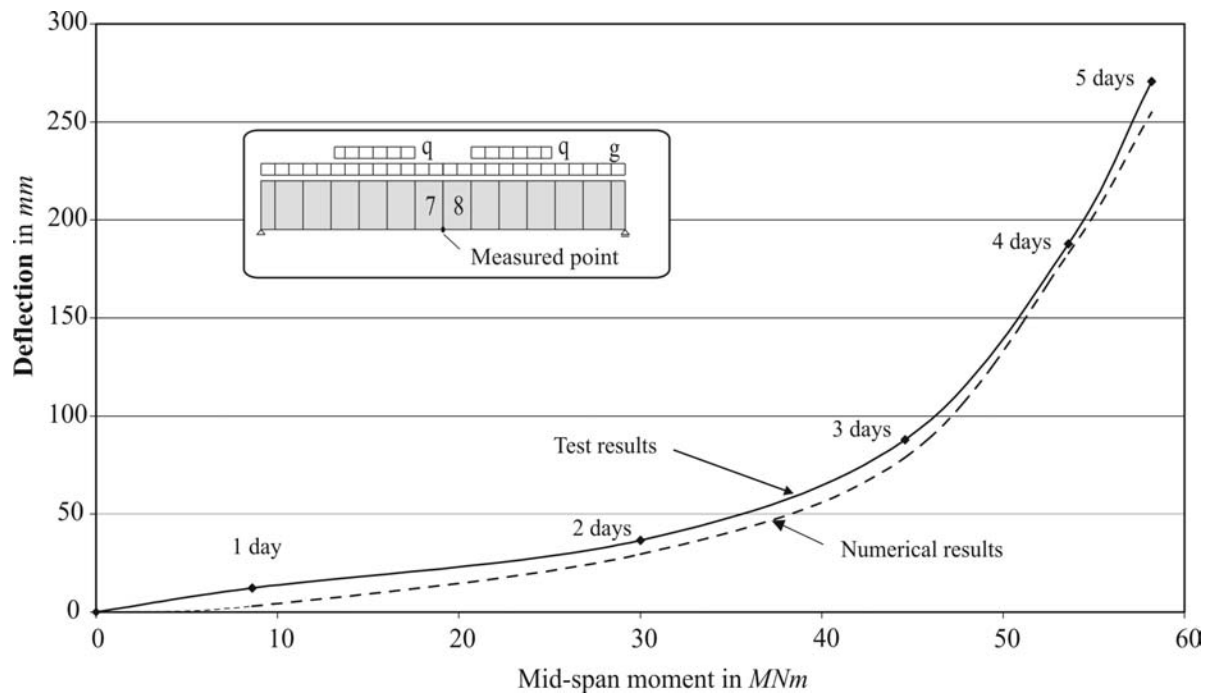
Figure 4.12 Measured and numerical estimated deflections of the SES segmental bridge
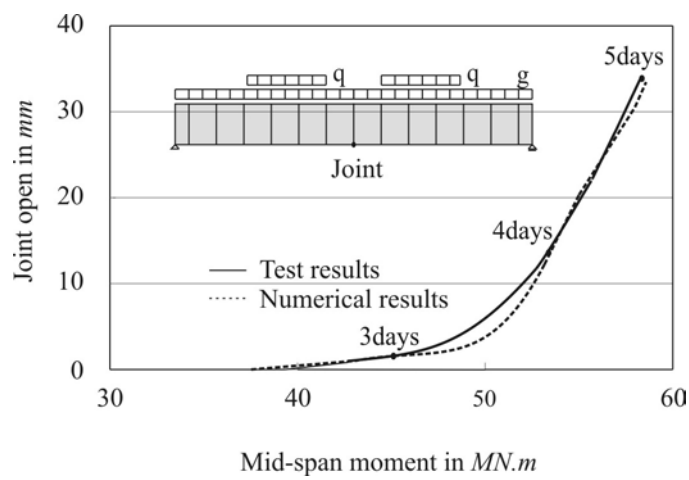
Figure 4.13 Joint opening
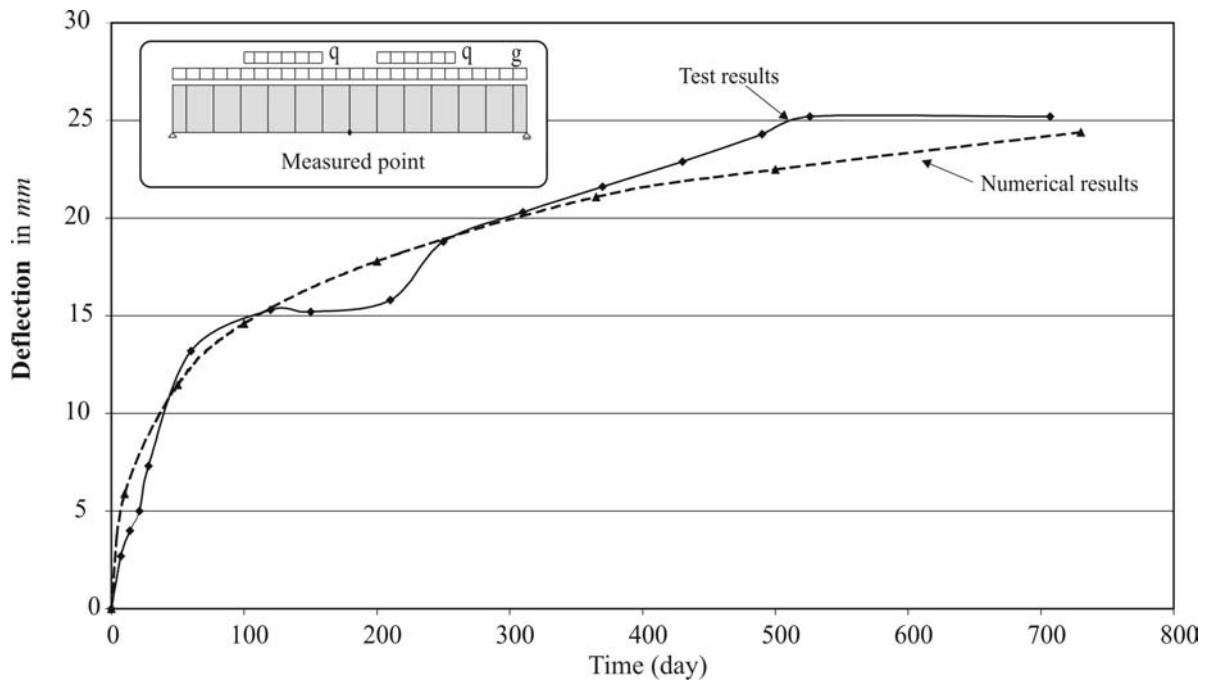
Figure 4.14 SES bridge deflection versus time (creep coefficient φ_∞ is 2.5)

4.3   Bowing effect on the behaviour of segmental bridges

Imperfect bow shaped segments caused by the temperature induced deformation during match casting can affect obviously the serviceability and load bearing capacity of a segmental bridge in short and/or long terms. The SES and Bang Na segmental bridges are modelled to consider various segment geometries with different gap values and to show whether the phenomenon is detrimental to take some appropriate measures to minimize the risks or whether it has little influences on the structure. The load combinations in short and long term considering creep and shrinkage according to German Code DIN 1045-1 [Di3] are applied in the numerical analysis to study the phenomenon.

Deflections, longitudinal compressive stresses, shears lag redistribution and losses of tendon forces versus time will be the main objectives of the study.

4.3.1   Bridge loads and load arrangement

The load combination used to analyze segmental bridges consists of permanent, traffic live loads and prestressing. The permanent loads (G) are referred in some specifications to the following weights:

- Dead load of the structure
- Utility ducts or casting and contents
- Traffic signs

- Concrete barriers

- Wearing surface and/or potential deck overlays

- Other elements deemed permanent loads by the design engineer and owner

In the current study for simplicity the dead load of the box girder segments are assumed to represent the total permanent loads.

The design traffic live load is a combination of two design trucks with four wheels each and a design of lanes with constant loading. The width of notional lane w in the carriageway is generally 3 m and the possible number of lanes n_1 is given according to German and European Code in Table 4.4.

The German code design truck (Q_{ik}) consists of two 300 and 200 KN axles at the first and second lanes respectively spaced at 1.2 m in driving direction. The uniformly distributed load (q_{ik}) on the first lane is 9.0 KN/m^2 and on the rest area 2.5 KN/m^2 respectively as listed in Table 4.5. Figure 4.15 shows the arrangement of the live load on the deck of a bridge.

Table 4.4 Number of lanes n_1 and width of lanes w [Di2]

Carriageway width w	Number of notional lanes	Width of a notional lane	Width of remaining Area
$w < 5.4\ m$	$n_1 = 1$	$3\ m$	$w - 3\ m$
$5.4\ m \leq w < 6\ m$	$n_1 = 2$	$w/2$	0
$6\ m \leq w$	$n_1 = Int\left(w/3\right)$	$3\ m$	$w - 3 \cdot n_1$

Figure 4.15 German Code truck design load details [Di2]
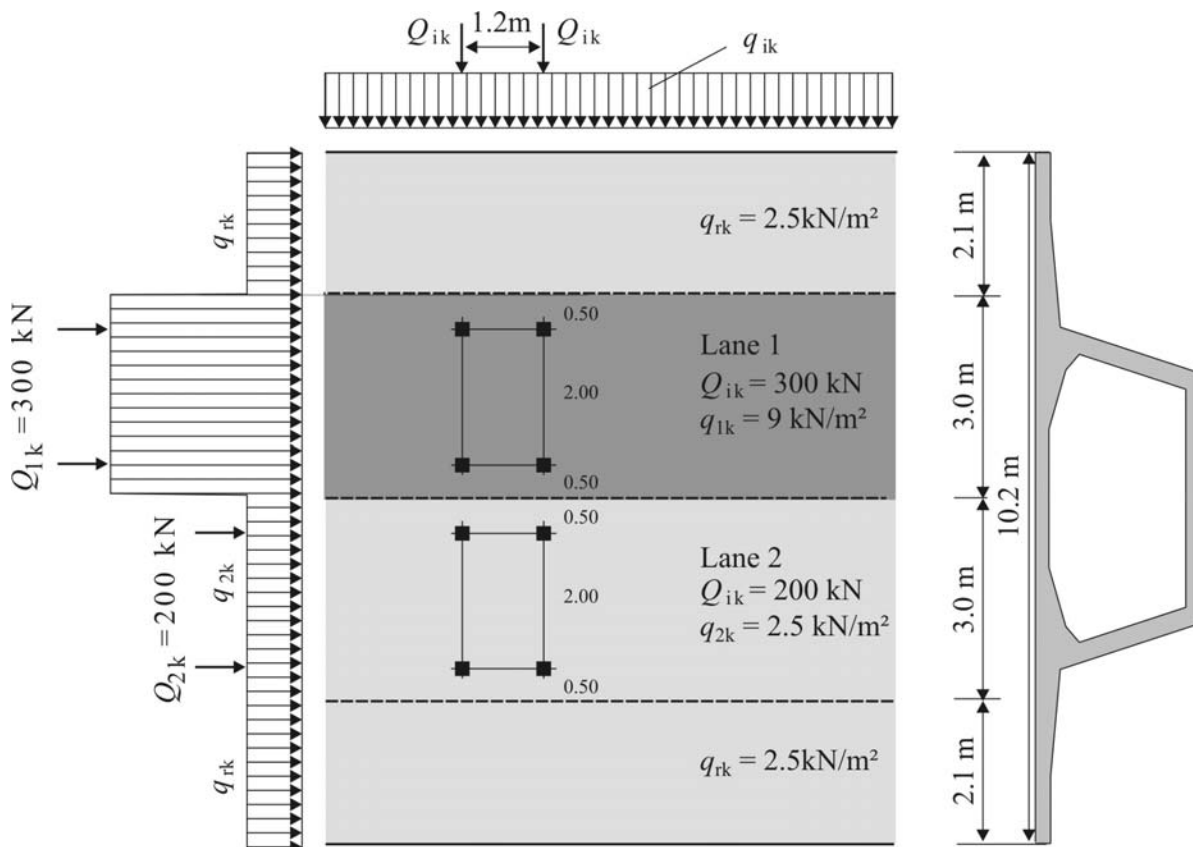
The load combination given by the German Code DIN 1045-100 or 'DIN-Fachbericht 102' [Di2, Di3] is written as:

Ultimate limit state (permanent conditions):

$$\sum_{j \geq 1} \gamma_{G,j} \cdot G_{k,j} \oplus \gamma_p \cdot P_k \oplus \gamma_{Q,1} \cdot Q_{k,1} \oplus \sum_{i>1} \gamma_{Q,i} \cdot \psi_{0,i} \cdot Q_{k,i} \qquad (4.1)$$

where $\oplus$ means „in combination with "

Serviceability limit state:

rare combination:

$$\sum_{j \geq 1} G_{k,j} \oplus P_k \oplus Q_{k,1} \oplus \sum_{i>1} \psi_{0,i} \cdot Q_{k,i} \qquad (4.2)$$

frequent combination:

$$\sum_{j \geq 1} G_{k,j} \oplus P_k \oplus \psi_{1,1} \cdot Q_{k,1} \oplus \sum_{i>1} \psi_{2,i} \cdot Q_{k,i} \qquad (4.3)$$

non-frequent combination:

$$\sum_{j \geq 1} G_{k,j} \oplus P_k \oplus \psi'_{1,1} \cdot Q_{k,1} \oplus \sum_{i>1} \psi_{1,i} \cdot Q_{k,i} \qquad (4.4)$$

quasi-permanent combination:

$$\boxed{\sum_{j \geq 1} G_{k,j} \oplus P_k \oplus \sum_{i>1} \psi_{2,i} \cdot Q_{k,i}} \qquad (4.5)$$

For the following analysis of an external prestressed bridge with internal transverse prestressing the quasi-permanent load combination is used for long term analysis whereas the rare load combination is used for short term.

The load combination factors ψ for the live load according to [Di4], Tab. C.2 are:

	ψ_0	ψ_1	ψ_2	ψ_1'
TS	0.75	0.75	0.20	0.80
UDL	0.40	0.40	0.20	0.80

The used load combinations can be written as follows:

quasi-permanent: $\Sigma G_k + P_k + 0.2 \cdot Q_{ik} + 0.2 \cdot q_{ik}$ - long term loading   (4.6a)

rare combination: $\sum G_k + P_k + Q_{ik} + q_{ik}$ - short term loading   (4.6b)

In Germany the traffic loads have to be multiplied by a factor α which is equal to $\alpha_{Qi} = 0.8$ for axle loading and $\alpha_{qi} = 1.0$ for uniform loading.

Table 4.5 shows the basic values for the short-term load combination according to German Code. Figure 4.16 shows the dead and live load arrangement used in the finite element model. The axle loads are transferred to a uniformly distributed load for simplicity.

Table 4.5 Basic values of Q_{ik} and q_{ik} for load model 1 [Di2]

Position	Double axle Q_{ik} (kN)	α_{Qi}	$\alpha_{Qi} \cdot Q_{ik}$ (kN)	Uniformly distributed load $\alpha_{qi} \cdot q_{ik}$ (kN/m^2)
Lane 1	300	0.8	**240**	**9.0**
Lane 2	200	0.8	**160**	**2.5**
Lane 3	0	-	**0**	**2.5**
Another lane	0	-	**0**	**2.5**
Remaining area	0	-	**0**	**2.5**
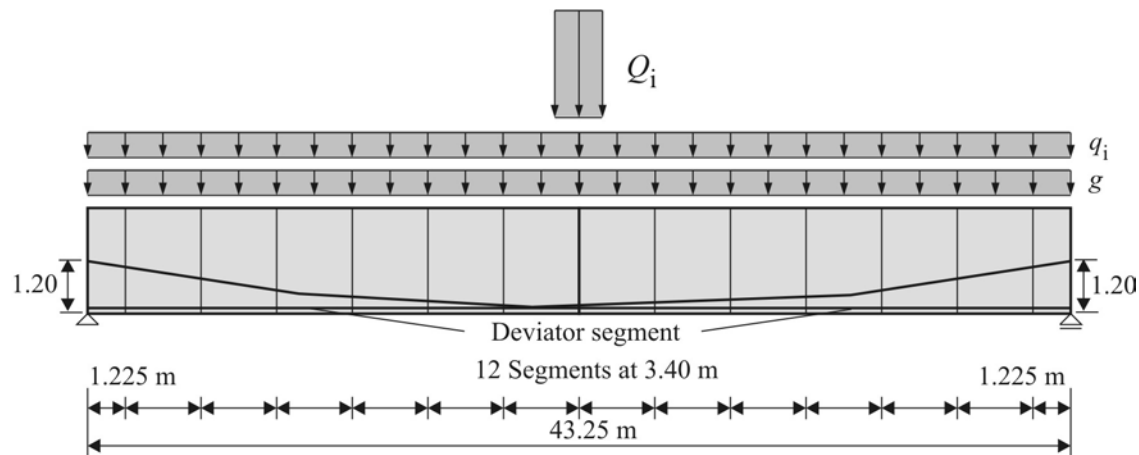
Figure 4.16 Loading distribution used in the finite element model

In this study all loads were considered to be symmetric in transverse direction in order to show the influence of gaps in the segments on the whole structure more clearly. Thus torsion effects are neglected. The wheel loads were transferred to an equivalent uniform distributed load having a width of 1.2 *m* in longitudinal direction and a length of 10.2 *m* in transverse direction of the bridge.

Because of the creep and shrinkage strains in concrete, effective prestressing *P* can only be achieved by using high-strength steels in the range of f_{pk} = 1,860 *N/mm²* or more. The magnitude of normal prestress losses can be expected to be in the range of 241 to 414 *N/mm²* according to Nawy [Naw]. A more detailed analysis will be carried out later. According to the recommendations of the "Deutschen Beton-Vereins" [Deu], the tendon forces layout should provide a compressive stress in the joints not less than 2.0 *N/mm²* to ensure that the joints are held together in serviceability conditions.

In addition the construction stages have to be considered. Some segmental bridges are erected using epoxy joints. After a segment has been erected, permanent cantilever post-tensioning is applied at each end of the cantilever. Therefore, during the placing of the first segment at one end, the element has to be attached to the cantilever by means of temporary post-tensioning. The temporary post-tensioning must provide a compression of not less than 0.35 *N/mm²* across the joints to ensure that the joints are properly closed and that the excess epoxy is squeezed out. It is recommended that the uniformly distributed compressive stress is applied across the joints to avoid small differences in the thickness of the epoxy joint which could affect the structure's geometry. It should be noticed that the first joint would be

affected more with diffusion of the tendon forces, which can result in non-uniformly distributed compressive stress across the joint.

4.3.2   Long-term loads

The construction of segmental bridges started more than 50 years ago. Since then, the effect of creep and shrinkage on segmental precast and cast-in-place bridges has been under constant debate. Many design engineers, are still unsure what effect creep and shrinkage has on the final stresses and deflection of a structure.

Realistic prediction of concrete creep and shrinkage is a basic requirement for achieving appropriate prediction of deflection variations in concrete bridges. Such an analysis is obviously able to take into account all changes of the structural system during the construction process. Concrete creep and shrinkage are very complex phenomena involving several interacting physical mechanisms on various scales of the microstructure, which are influenced by many variable factors. Therefore, a relatively high degree of sophistication in a realistic prediction model is inevitable. Moreover, a creep and shrinkage prediction model should have several principal parameters in the basis of short-time tests carried out on the given concrete to be used. The updating task which is essential for the modern design of large span bridges can be successful only if the creep and shrinkage curves of the model have suitable shapes not only for long time periods but also for short time periods. By updating the model, significant improvements of long-term prediction can be achieved.

The most important factor in the whole life design of reinforced and prestressed concrete bridges is the Serviceability Limit State. Prestressed concrete bridges are very sensitive to long-term increase of deflections. Large bridges (more than 100 m span) exhibit in many cases a gradual increase of deflections during a very long time of service life. This phenomenon has paramount importance for serviceability, durability and long-time reliability of such bridges. This is why a reliable prediction of deformations and stresses of bridges during their construction as well as during their service life is extremely important. The stress in the concrete must be kept within allowable limits for both compression and tension.

The stress levels along the length of a deck are checked at all the critical stages in the structure's life. This would normally include:

- At transfer of the prestress to the concrete

- During each stage of construction, with temporary loads applied
- At bridge opening, with full live load
- After long-term losses in the prestress and full creep redistribution of moments have occurred

4.3.2.1 Creep of concrete

There could be three stages of concrete creep; at the time of load applying an instantaneous strain can result in. Thereafter, the rate of creep decreases with respect to time which can be called the primary range. The secondary creep describes the range of steady state creep; the straight-line relation represents the limits of secondary creep. Thereafter, if there is an increase in stresses a tertiary creep can occur. The three stages of concrete creep are shown in Figure 4.16.

The tertiary creep can or can not occur; this may happen in concrete as a result of an increase in creep due to microcracking at stresses larger than the typical level of working stress, which is approximately 40 percent of the short-term strength.

In normal levels of concrete working stress, primary creep is hard to be distinguished from the secondary creep. The tertiary creep does not occur.

The resultant strain due to creep under sustained constant stress at a time t (shrinkage and temperature effect are ignored) is:

$$\varepsilon_c(t) = \varepsilon_c(t_0) + \varphi(t,t_0) \cdot \varepsilon_c(t_0) \quad \text{(constant stress)} \tag{4.7}$$

where: $\varphi(t,t_0)$ creep coefficient

t time

t_0 time of loading

The dimensionless coefficient φ represents the ratio of creep strain to the instantaneous strain. The mathematical approach to estimate the creep coefficient according to German Code is given in Appendix C.
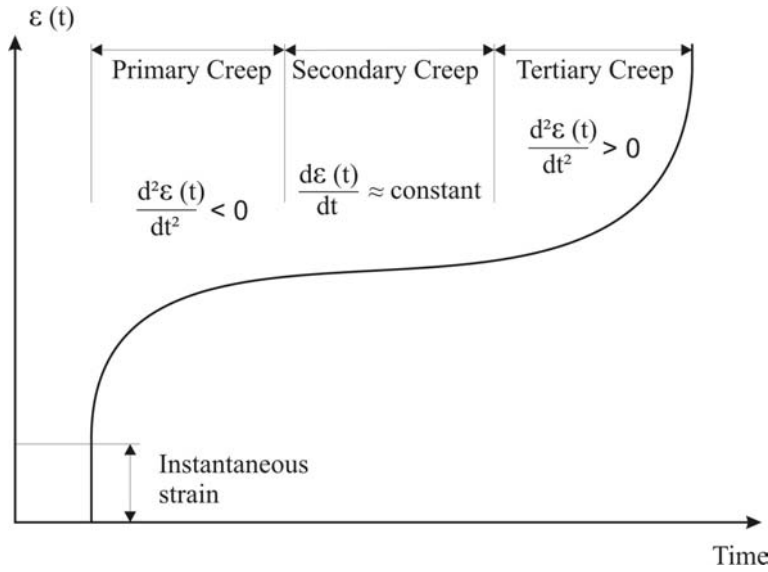
Figure 4.17 General form of the strain time curve for a concrete subjected to creep

4.3.2.2   Shrinkage of concrete

Shrinkage is the volume reduction of unloaded concrete at constant temperature. It is a consequence of the chemical reaction and the drying process, which starts directly after the stopping of concrete curing. General behaviour of shrinkage strains through a thickness of an unloaded and an unrestrained plain concrete slab as shown in the Figure 4.18. The difference of concrete strain over the height of the section $\Delta\varepsilon_{c,s}$ causes internal stresses to restore the compatibility of the cross section. These self-equilibrium internal stresses occur in all concrete structures and they are compressive in the interior part of the section and tensile at the drying surfaces. These tensile stresses can overcome the tensile strength of the plain concrete and result in surface cracking. In case the drying is the same on the whole section, then the total strain is uniform and equals to the mean shrinkage strain $\Delta\varepsilon_{c,s}$, and this assumption is used in the current study.
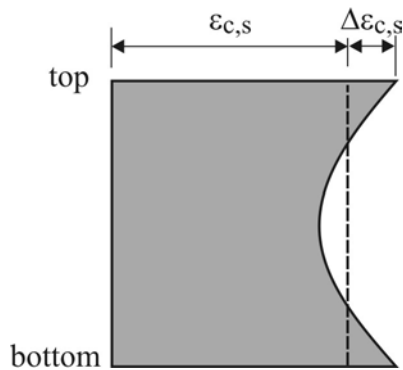
Figure 4.18 Shrinkage strains in plain concrete slab

The German Code stated that the total shrinkage strain $\varepsilon_{c,s}$ is composed of two parts, the drying shrinkage ε_{cds} strain and the autogenous shrinkage strain ε_{cas}. The drying shrinkage strain is a function of transfer of water through the hardened concrete. The autogenous shrinkage develops during the hardening of the concrete. The shrinkage strain estimation according to German Code is given in Appendix C.

Shrinkage – besides the axial shortening of the bridge beams – can also affect the box girder deflections due to non-uniform development of shrinkage resulting from different thickness of flanges.

It is well known that the time evolution of shrinkage and the drying-induced part of creep in box girder bridges is considerably affected by the thickness of flanges and webs as well as by environmental conditions [Kri]. In the negative moment regions over the internal (intermediate) support of continuous box girders, the shrinkage and creep strains evolve rather differently, on one hand in the thin top flanges and on the other hand in the thick bottom flange plates. Generally, the thin parts of the cross section tend to shrink and creep faster than the thicker parts.

The different time evolutions of shrinkage and drying creep in the individual parts of the cross section are a phenomenon that may significantly affect the long-term performance. Particularly the long-term bridge deflections. The reason is that the differences in strains in the individual parts of the cross section induce an additional curvature of the deflection curve of the bridge girder. A minor curvature appears also in box girder segments having both flanges of the same thickness, but different widths because of differences in the volume- surface ratio. Figure 4.19 shows the effect of creep and differential shrinkage on the deflection.
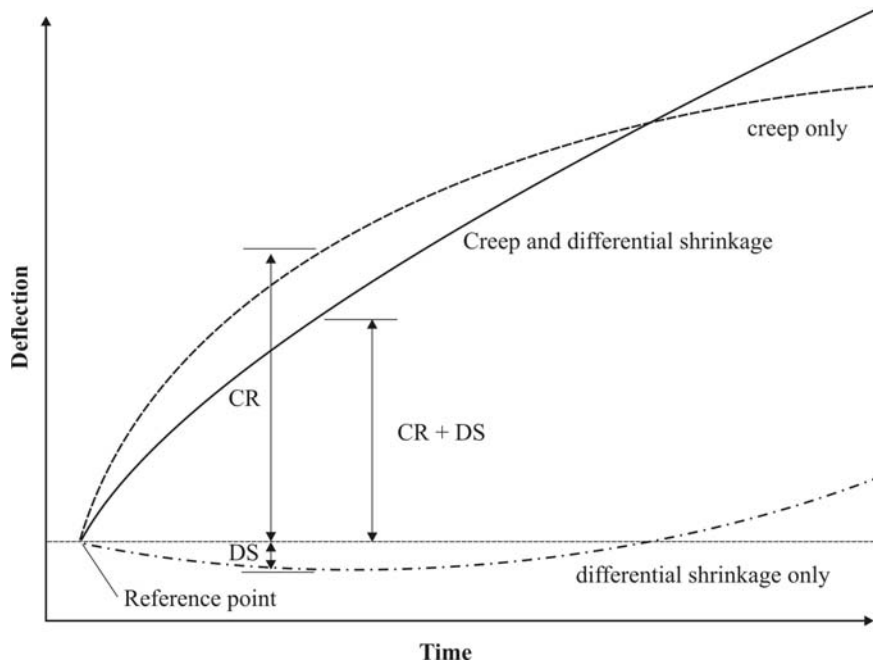
Figure 4.19 Effect of creep and differential shrinkage on deflections [Kri]

To avoid using complicated equations (see Appendix C), Euro and German Codes give simplified figures to estimate the coefficients of creep φ and shrinkage strain $\varepsilon_{c,s}$. The creep coefficient φ depends on the age of concrete t_0 at which the loading begins (see Figures 4.20 and C1 to C4 in Appendix C), the relative humidity *RH*, the concrete strength f_{ck}. For example, the creep coefficient for $t_o = 3$ *days* is about 25 % more than that for $t_o = 9$ *days*. Furthermore the value of creep depends on the cross-section area in relation to the perimeter, which is expressed by:

$$h_\circ = \frac{2A_c}{u} \tag{4.8}$$

where A_c is the cross section area of a concrete member.

      u is the perimeter around the constant cross-sectional area.

The sum of the outer and inner perimeter has to be used in the above equation, as usually segments are stored several days on the precast yard before erection. For the SES segments this results in $h_0 \approx 282$ mm. The value for the Bang Na elements is $h_0 \approx 268$ mm.
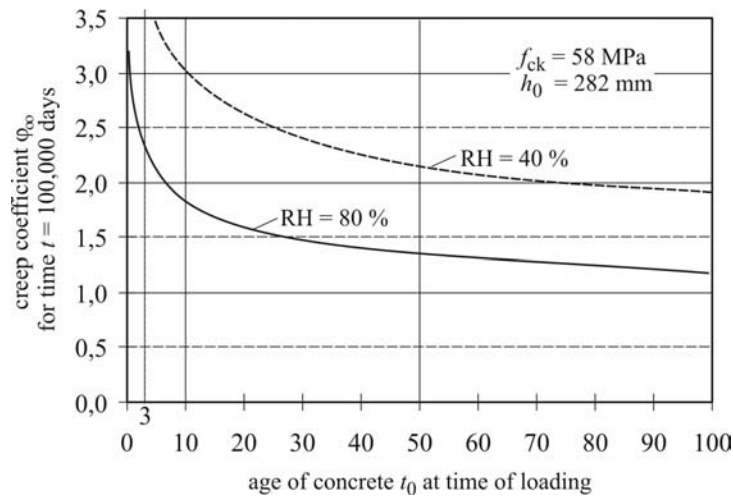
Figure 4.20 Creep coefficient φ_∞ for different times t_0 of initial loading

Further information is given in appendix C. Figures C5 to C7 show the creep coefficient and shrinkage strain of the concrete at different ages.

4.3.2.3 Extension of the ANSYS creep

The before mentioned creep formulae have to be modelled by one of the various creep models given in ANSYS to analyse the segmental bridges. The numerical approach represents the creep behaviour of arbitrary materials, which is usually described by analytical formulas with a number of free coefficients. The creep strain increment is given by:

$$\Delta \varepsilon_{c,c} = C_1 \sigma^{C_2} \varepsilon^{C_3} e^{\frac{-C_4}{T}} \Delta t \qquad (4.9)$$

where: ε equivalent strain (based on modified total strain)

σ equivalent stress

T temperature (absolute)

t time at end of substep

e natural logarithm base

The coefficients (C_1 to C_4) are used to adapt the creep laws to creep test results performed at constant load and temperature [Alt]. In practice it is hard to achieve a satisfying adjustment for a wide range of temperatures and stresses using only one set of coefficients. Instead it seems that the coefficients itself are dependent on the temperature or on the stress level. Thus, a supplementary tool is developed which permits to show the creep behaviour of a material for different stress and temperature levels independently. This can be useful if

strong stress and / or temperature gradients are present and if both primary and secondary creep are to be considered in the analysis.

In the current study, only steady stress level was used and temperature effects are neglected. Thus the coefficients C_2 to C_4 are taken as 0.0. This leads to the following equation to estimated the creep strain increment:

$$\Delta\varepsilon_{c,c} = \frac{\sigma_c(t_0)}{E_{c,0}} \cdot \Delta\varphi(t,t_0)$$ (4.10)

where: $\sigma_c(t_0)$ concrete compressive stress at time of initial loading

            $E_{c,0}$ modulus of elasticity at time of initial loading

            $\varphi(t, t_0)$ creep coefficient at time t

The formulae for the creep coefficient φ are taken from the German Code DIN 1045-1 (see appendix C). Figure 4.21 shows a simple example which is used to verify the ANSYS creep model. A very good agreement between numerical and German Code results is obtained. Further details are given in Appendix C.
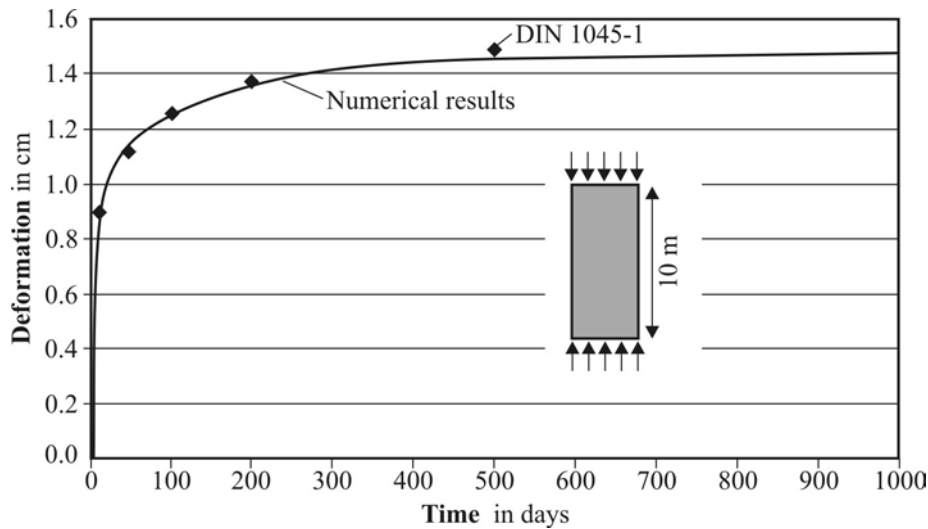
Figure 4.21 Creep deformation - ANSYS results versus German Code

4.3.3 Numerical results

4.3.3.1 SES bridge

It is obvious that the stress distribution in the joint of two adjacent elements will hardly change if bow shaped segments instead of perfect segments are used. Furthermore an increase of the deflection of the whole structure is expected. Information about these effects is still missing. Therefore a numerical study has been conducted. Figure 4.22 shows the anticipated shape of the gap (1.5 *mm*) in a segment used in the finite element model of the SES segmental bridge. For simplicity a polygonal shape instead of a smooth curve (see chapter 3.4) has been used for the gap shape.
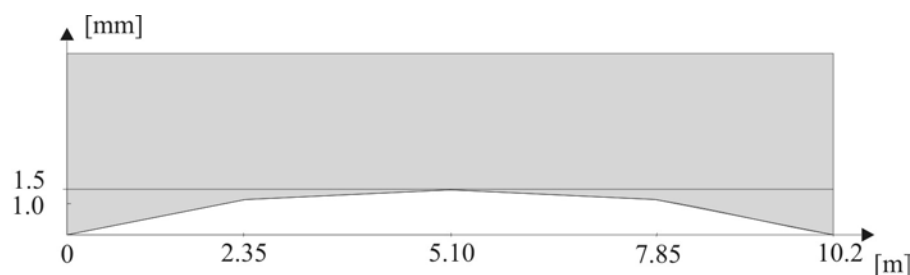
Figure 4.22 Gap shape used in the Finite Element analysis

Initial deformations and deflections increase significantly if loads are sustained over a long period of time due to the effects of shrinkage and creep. These two effects are usually combined in structural analysis. A creep coefficient of $\varphi_{\infty} = 2.5$ and shrinkage strain of $\varepsilon_{c,c,\infty} = -23.75e-5$ were used to study the long-term behaviour of the structures. Equations and figures given in Appendix C were used to obtain the creep and shrinkage coefficients for different times. The tendon losses are ignored herein to show the influences of the bowing-effect on the whole structure.

Figure 4.23 shows the longitudinal stress distribution (σ_x) in the deck slab of the SES segmental bridge due to short-term loading given by the German Code (Equation 4.5). The compressive stresses in the joint at mid-span are shown beneath. The maximum compressive stresses can be clearly seen in the regions above the webs at mid-span due to the shear lag effect. The stresses appear to be fairly uniform across the bottom slab, where the influence of the end diaphragms is evident.

The regions directly in front of the diaphragms show high stresses, which would indicate that the majority of the post tensioning forces have not diffused. This behaviour of the post

tensioning forces can lead to joint opening and tensile stresses near the pier segment (see [Cha]). The deflection was estimated to be about +11.0 *mm* upward (camber). A positive sign indicates the upward deflection. The deflections due to the prestressing are more than, and in the opposite direction to, the dead-load deflections. This results in the bridge deflecting upwards upon application of the prestressing and removal of the erection trusses. Subsequent application of the superimposed dead load and long-term losses in the prestress forces reduce this upwards deflection or can lead to a net sag deflection.
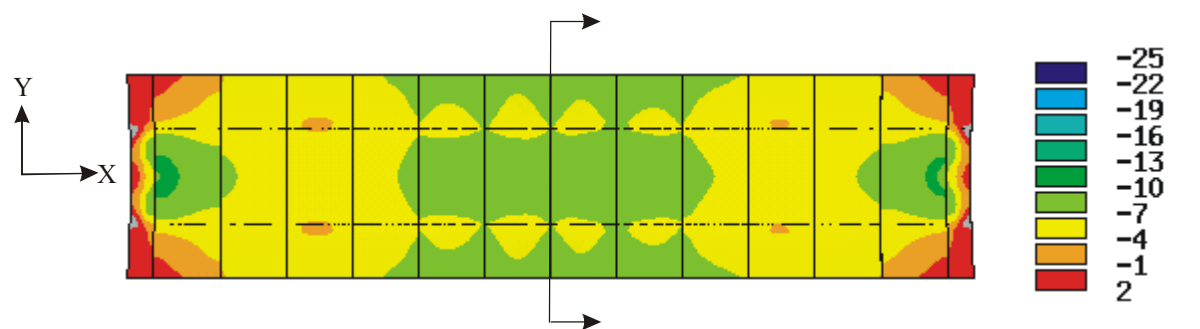
(a) deck slab
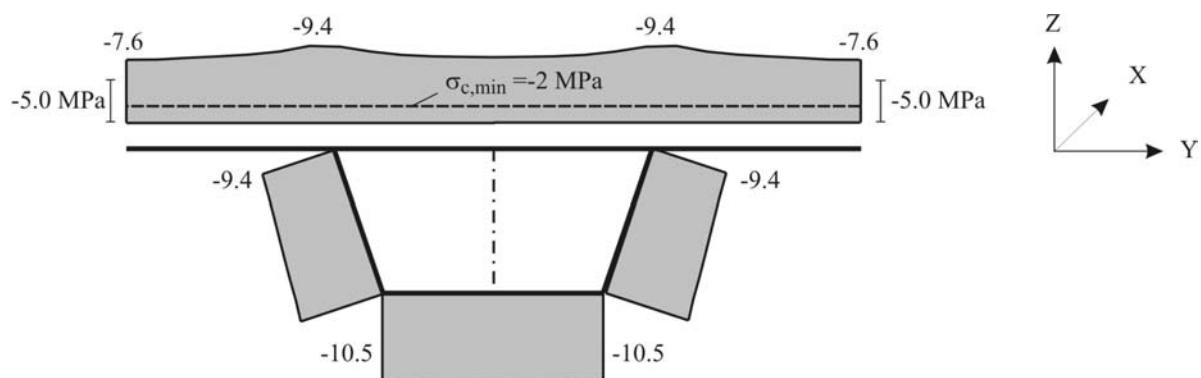
(b) joint at mid-span

Figure 4.23 Longitudinal stress distribution σ_x (*MPa*) with perfectly fitted segments under short-term loading

The numerical model was also very adequate to predict those tensile stresses that can develop at the wingtips of segments near supports, meanwhile the beam theory is inadequate to calculate peak compressive stresses and does not predict those tensile stresses.

The transverse diffusion of post-tensioning forces close to the end diaphragms is a critical issue, which comes from two standpoints. The first is the over-compression of the regions near the piers. The second is the required compression stresses across the full width of the

joints. Hence, adequate post-tensioning details must be developed to consider the transverse diffusion of post-tensioning forces.

The numerical results using segments with gap or bow shaped segments showed different compressive stress distribution and deflection. A maximum gap of 1.5 *mm* was used in the analysis in every standard segment, but in reality smaller gap is expected in such segments (see chapter 3.4). As can be seen in Figure 4.24 the use of bow shaped segments in the superstructure has led to areas of reduced compression in the segment's centerline, whereas stress peaks occurred at the tips of the segment's cantilever slab. A maximum deflection of −16.0 *mm* (downwards) was estimated.

(a) deck slab

(b) joint at midspan

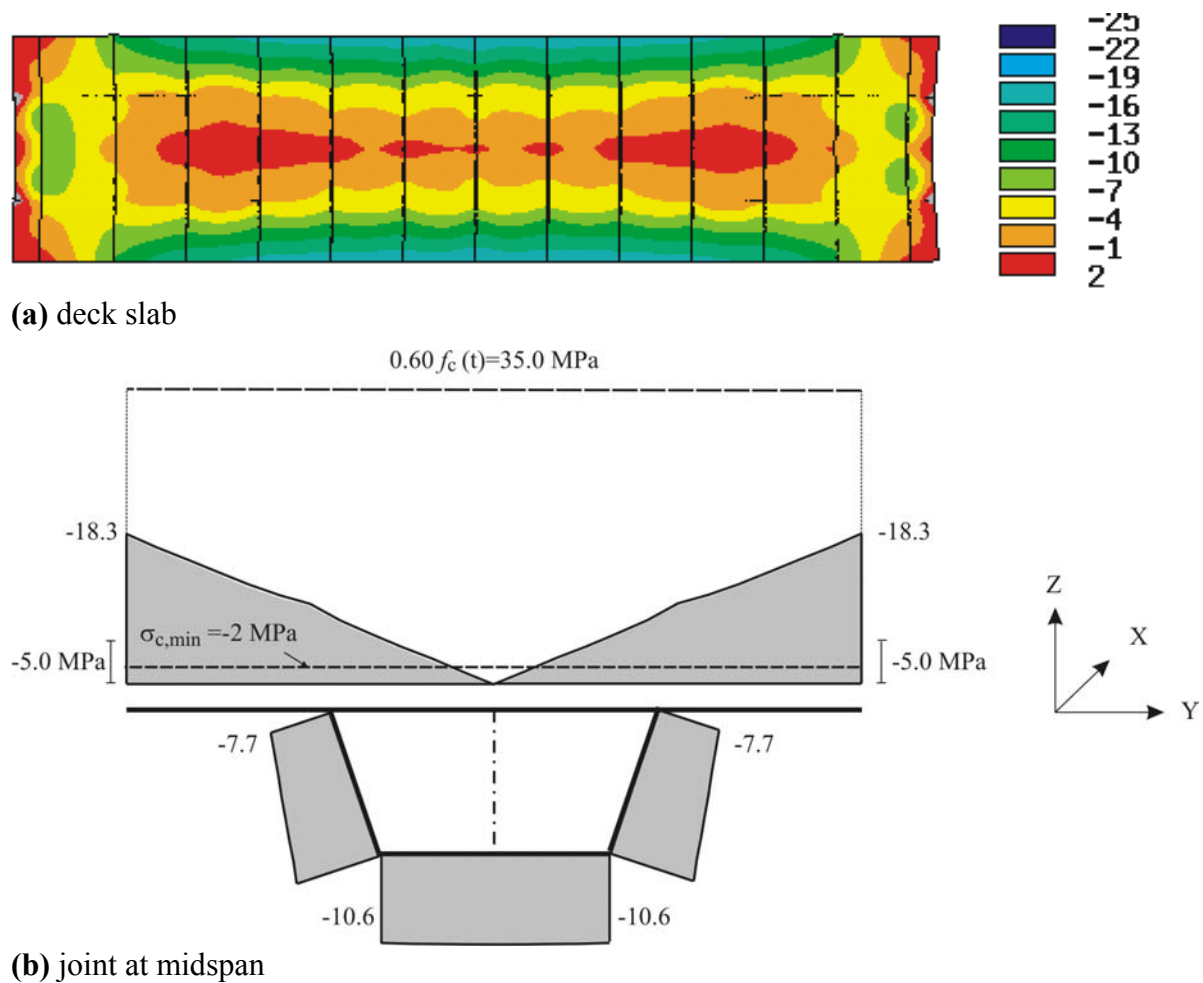**Figure 4.24**   Longitudinal stress distribution σ_x (*MPa*) with bow shaped segments under short-term loading

The concrete stresses should be checked to ensure that they would keep under the maximum allowable stress limits given by the standards and the specifications. The measurements of tests made on concrete have shown that concrete loaded constantly to $0.8 f_{ck}$ can eventually

creep to failure or show longitudinal cracks [Br3]. Thus, high compression stresses could cause problems. The German Code [Di2] allows for a maximum compressive stress of $0.6 f_{ck}$ under permanent loading if non-linear creep models are used.

The numerical results showed that there were almost no compressive stresses in the deck slab's centerline region. Compressive stresses of at least 2.0 *MPa* should be applied across the dry joints according to serviceability requirements given in the German regulations. If epoxy resin is used in the joints, the temporary prestressing should stress the joints adequately during the hardening of the epoxy material.

The pattern of stress distribution is intended in general to determine design moments, shear forces and deflections. However, it is required to consider the distribution of normal stresses over the actual section to ensure that the full width of every segmental joint is within allowable stress limits. The effective flange width b_{eff} is generally used in structures for analysis and for calculation of section capacity and stresses and for ensuring that they all are effective in resisting bending stresses. The procedures provided by the different standards and specifications to determine the effective flange width do not include the redistribution of stresses nor the influences of bow shaped segments.

When bow shaped segments are used, the stress pattern can be affected since the adjacent segments do not have full contact at the joints. Thus, peak stresses may initially take place at the cantilever slabs with almost zero compressive stresses in the centreline regions of the top slabs before the post-tensioning axial loads change the stress pattern with time.

In the following analysis the creep and shrinkage of concrete is considered. Figure 4.25 shows the longitudinal compressive stress distribution (σ_x) in the upper slabs of perfectly fitted segments at time of loading ($t = 0$) according to loading case of the long-term state (see equ. 4.6a) given by the German Code. The cross-sectional compressive stresses in the joint at the mid-span are shown beneath. The maximum deflection at time 0 was about +30.0 *mm*. At time infinity ($t = \infty$) the results showed an increase of the deflection to about +69.0 *mm*, due to creep and shrinkage whereas a small change in the stress redistribution was noticed in the whole structure as can be seen in Figure 4.26. It was considered that the more highly stressed regions of the slabs above and below the webs would experience more changes than the wings. Concrete creep can cause the deck to change its profile over its

design life and it is a usual aim to achieve the desired alignment at the end of construction or at the time of the bridge opening, although the long-term changes in deflections should be checked to ensure that they are not excessive.

(a) deck slab

(b) joint at midspan

Figure 4.25 Longitudinal stress distribution σ_x (*MPa*) with perfect segments at time $t = 0$ using long-term loading (quasi permanent load combination)

(a) deck slab

(b) joint at midspan

Figure 4.26   Longitudinal stress distribution σ_x (*MPa*) with perfect segments at time infinity $t = \infty$ using long-term loading (quasi permanent load combination)

In Figures 4.27 and 4.28 segmental bridge with bow shaped segments using long-term loading at time ($t = 0$) and at time infinity ($t = \infty$) can be seen respectively. The stresses redistributed to reach the same distribution almost as the perfectly fitted segments with time as well as the gaps have been closed completely. The deflection at time t $\to \infty$ is +40.0 *mm*, which is still less than the deflection of the perfectly fitted segments.

Figure 4.29 shows a comparison of the longitudinal stresses at midspan between perfectly fitted segments and segments with gap at time of loading. The shrinkage plays a significant role in decreasing the total deflection of the structure. The numerical results showed that the bridge with gap in segments deflected to +48.0 *mm* at time infinity when considering only creep, whereas it was only +40.0 *mm* when both creep and shrinkage were considered in the analysis.

(a) deck slab

(b) joint at midspan
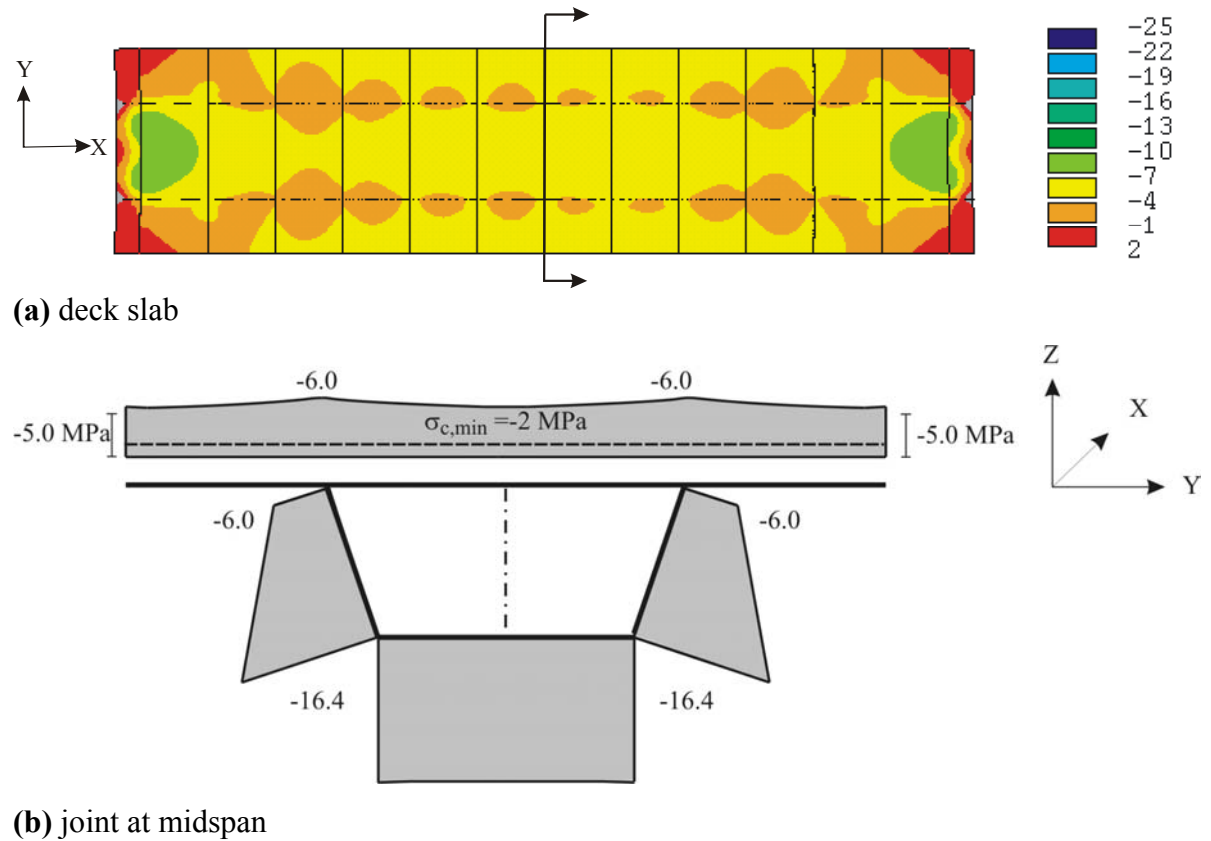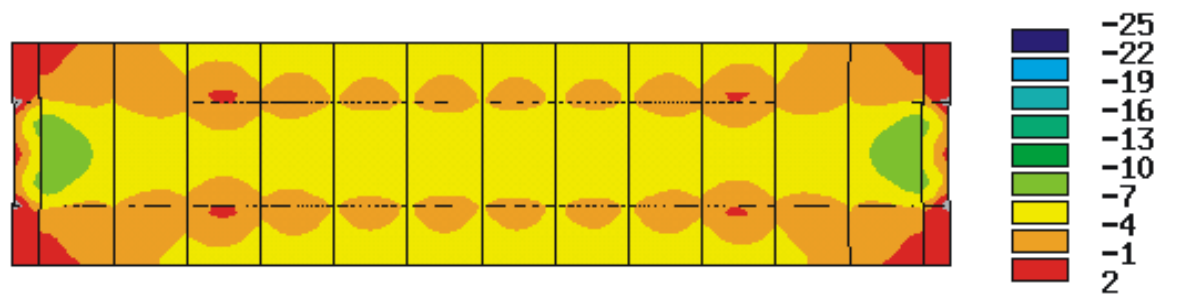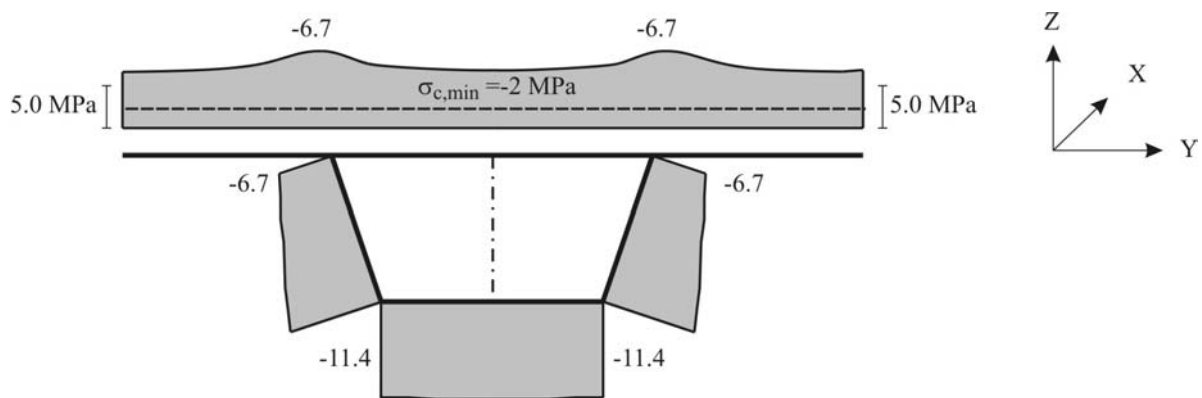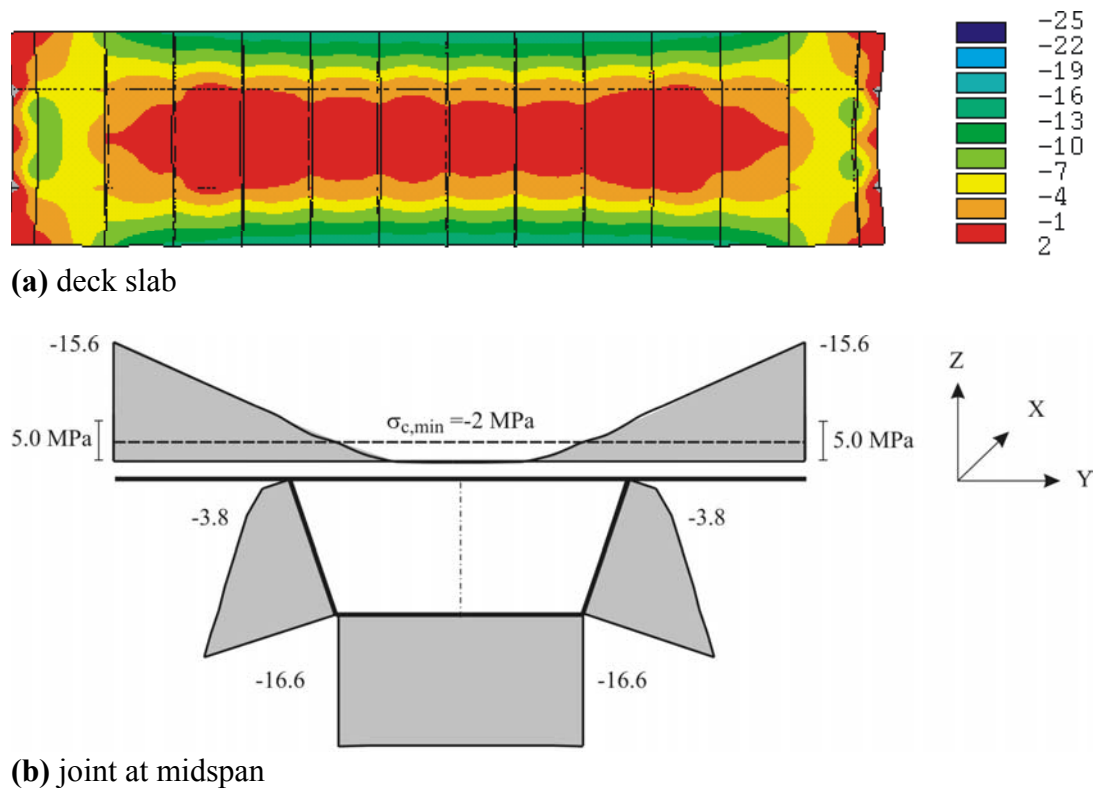
Figure 4.27   Longitudinal stress distribution σ_x (*MPa*) with bow shaped segments at time $t = 0$ using long-term loading (quasi permanent load combination)

(a) deck slab

(b) joint at midspan
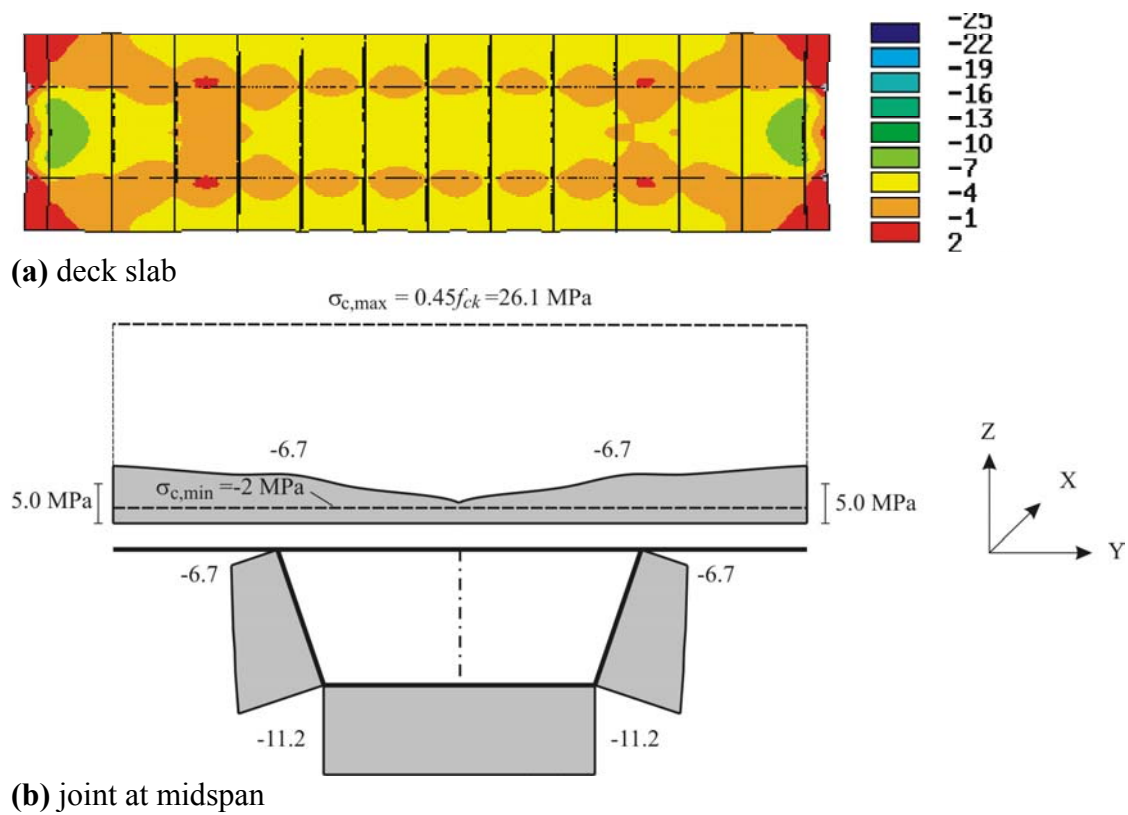
Figure 4.28   Longitudinal stress distribution σ_x (*MPa*) with bow shaped segments at time infinity using long term loading (quasi permanent load combination)
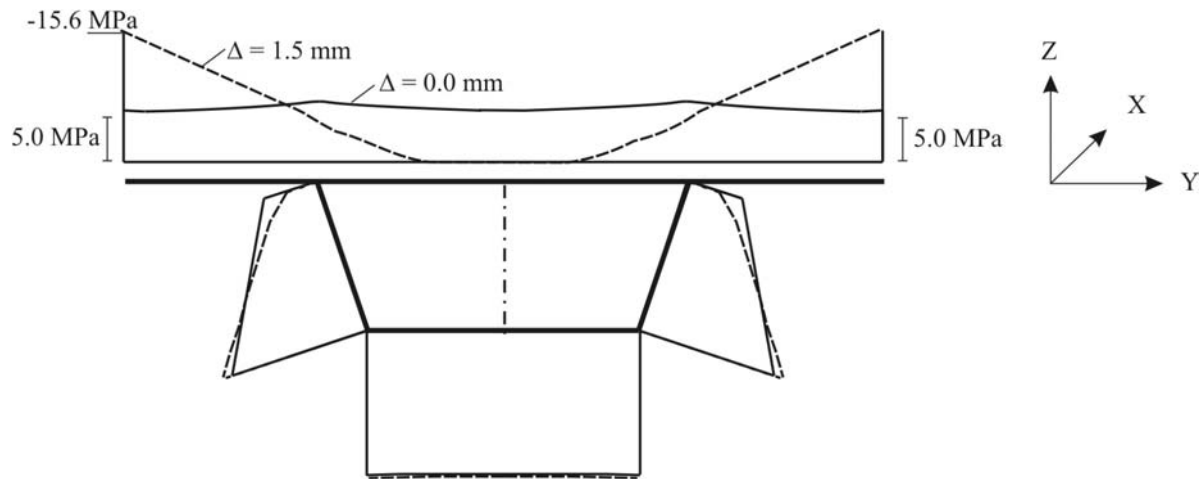
Figure 4.29 Comparison of longitudinal stress distributions σ_x (*MPa*) at midspan between fitted and bow shaped segments at time $t = 0$ using long-term loading

Because of the small amount of the gaps in such segments, it is expected that the gaps can close faster and in few days the stresses may redistribute as at time infinity. The stress distributions in different time intervals are shown in Figure 4.30.
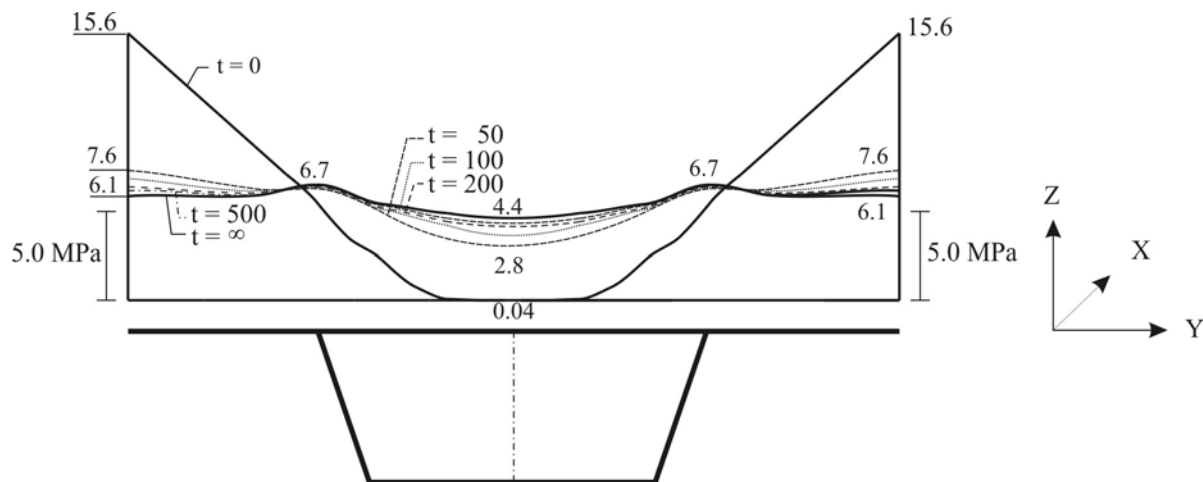
Figure 4.30   Longitudinal stress distribution σ_x (*MPa*) with bow shaped segments at different times t in days using long term loading

The main results of the various analysis are summarized in table 4.6.

Table 4.6 Deflections and concrete stresses

segments	time $t = 0$ - short term loading -			time $t = 0$ - long term loading -			time $t = \infty$ - long term loading -		
	f [mm]	$\sigma_{c,max}$ [MPa]	$\sigma_{c,min}$ [MPa]	f [mm]	$\sigma_{c,max}$ [MPa]	$\sigma_{c,min}$ [MPa]	f [mm]	$\sigma_{c,max}$ [MPa]	$\sigma_{c,min}$ [MPa]
perfect fitted	+11	-9.4	-7.6	+30	-6.0	-5.3	+69	-6.7	-5.2
bow shaped	-16	-18.3	0.0	0.0	-15.6	0.0	+40	-6.7	-4.4

f = midspan deflection

In many cases the transverse prestressing is used in deck slabs of bridges to resist some bending moments and shear forces developed in the transverse direction. Furthermore the deflection of the cantilever can be reduced. The tendon layout of the transverse tendons as used in the SES segmental bridge is shown in Figure 4.31. It is assumed that the tendons profile is not curved but straight for simplicity. This tendon layout was used to predict the influence of transverse prestressing on the stress distribution and gaps.

Transverse tendons in the upper slabs of segments have little effect on the stress distribution and closing of gaps as can be seen in Figure 4.32 if compared to the stress redistributions of the non-transverse prestressing segments shown in Figures 4.33.

Seven transverse tendons, each one is $P_0 = 836$ kN
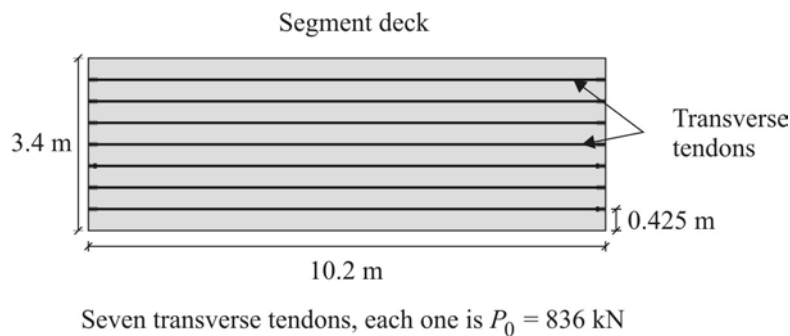
Figure 4.31 Transverse tendons layout
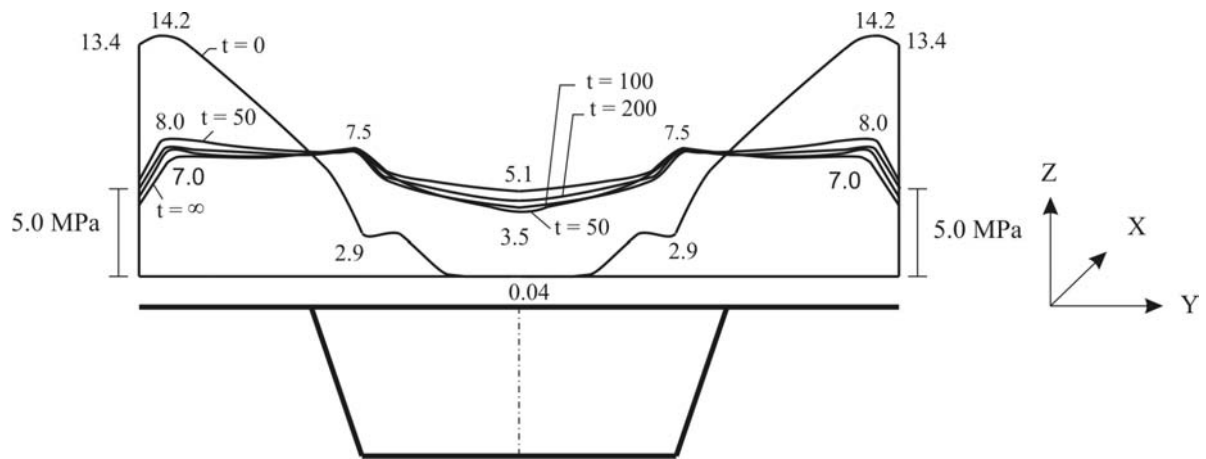
Figure 4.32   Longitudinal stress distribution σ_x (N/mm^2) with bow shaped segments and transverse prestressing at different times t in days
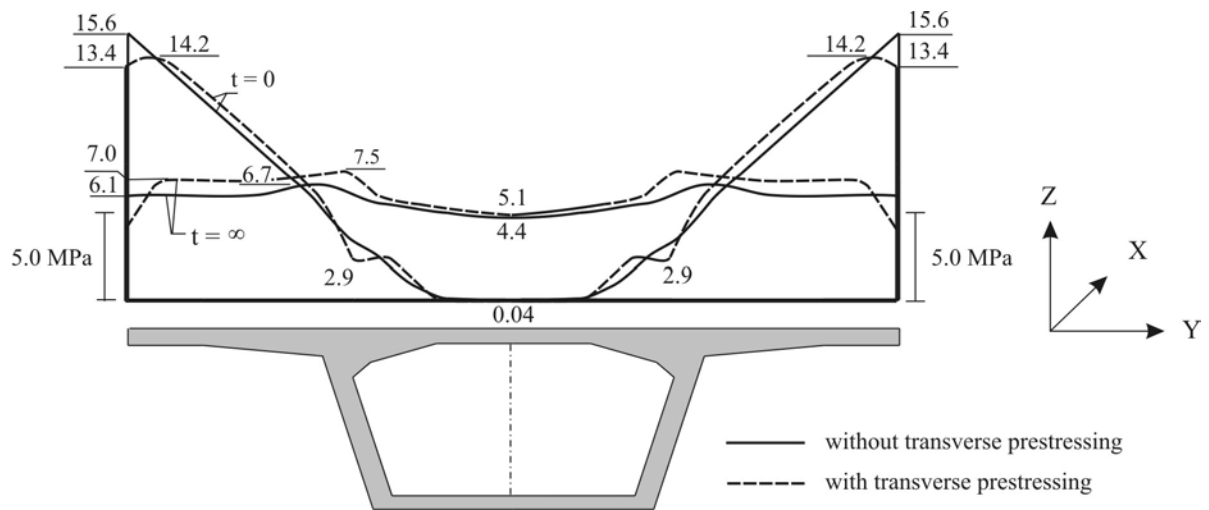
Figure 4.33   Longitudinal stress distribution σ_x (MPa) with bow shaped segments at different times t in days with/without transverse prestressing

4.3.3.2 Bang Na segmental bridge

A simple supported standard span of the Bang Na Pli-Bang Pakong Expressway (BBBE) has a span length of 44.4 *m* and a large width to length ratio ($w/L = 10.7$). A number of sixteen standard and deviator segments as well as two pier segments were numerically simulated. The material properties of the bridge taken from [Fi2] are given in Table 4.7. The bridge details, tendon layout and different segments cross-sections are shown in Figure 4.34.

Table 4.7   Material properties used in the numerical model of Bang Na segmental bridge [Fi2]

Material	Properties item	Average value
Concrete	Compressive strength, f_{ck}	51.8 *MPa*
	Modulus of elasticity, E_c	39,900 *MPa*
	Poisson's ratio, ν	0.2
Tendons	Modulus of elasticity, E_s	195,000 *MPa*
	Yield strength, f_{yk}	1,530 *MPa*
	Ultimate strength, f_{pk}	1,860 *MPa*
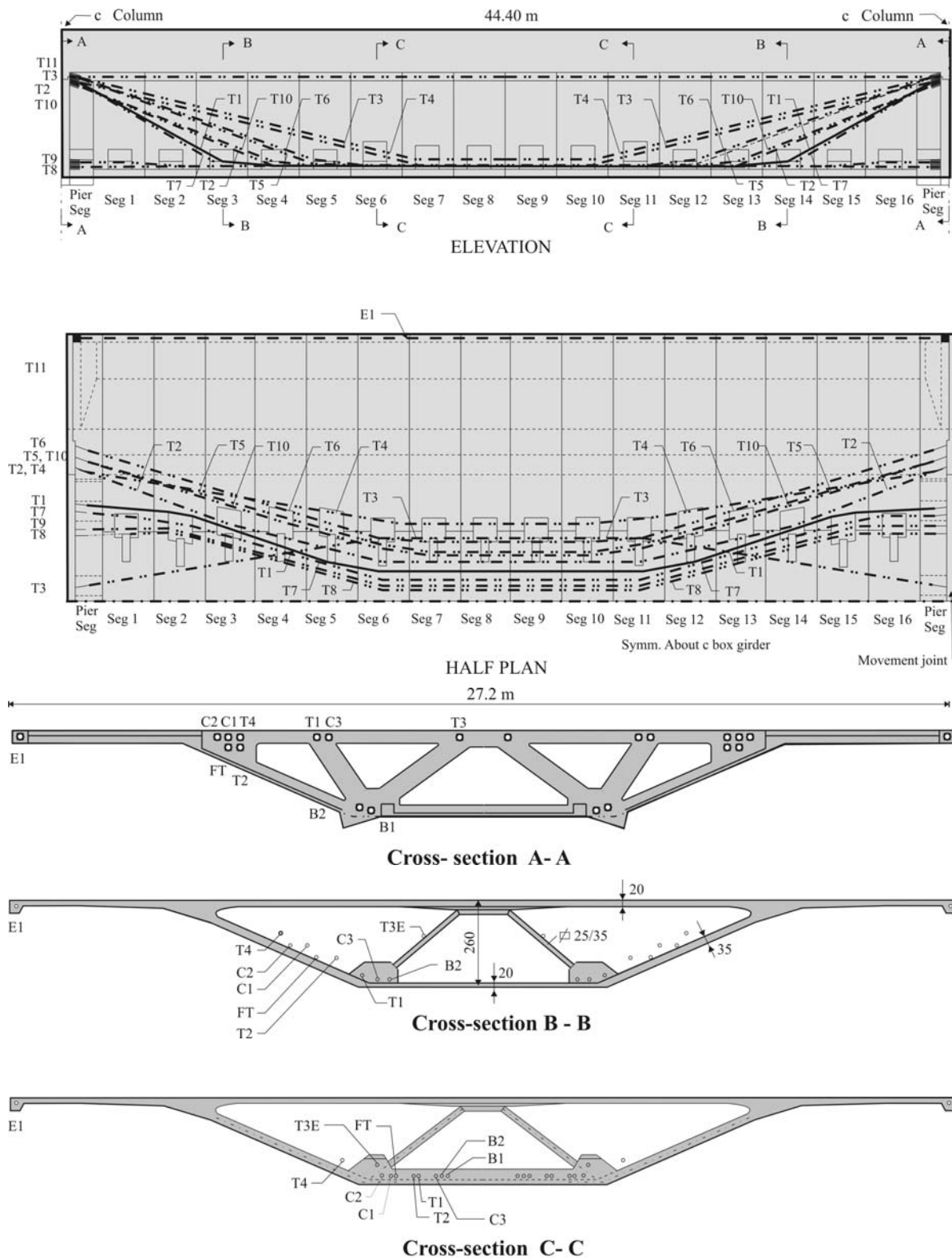
Figure 4.34 Bang Na details and tendon layout [Fi2]

The hollow box girder was modelled by four-node thin shell elements; the tendons by truss elements, and contact elements were used to transfer compression and friction forces across the joints. The loading cases of short and long term used herein were according to the German Code. The transverse tendon layout was considered symmetric across the segments in order to show the influences of the "bowing effect" more clearly. Please note that some of the transverse tendons are running through the webs and the bottom slab (Fig. 4.34). The numerical model of the Bang Na bridge can be seen in Figure 4.35.
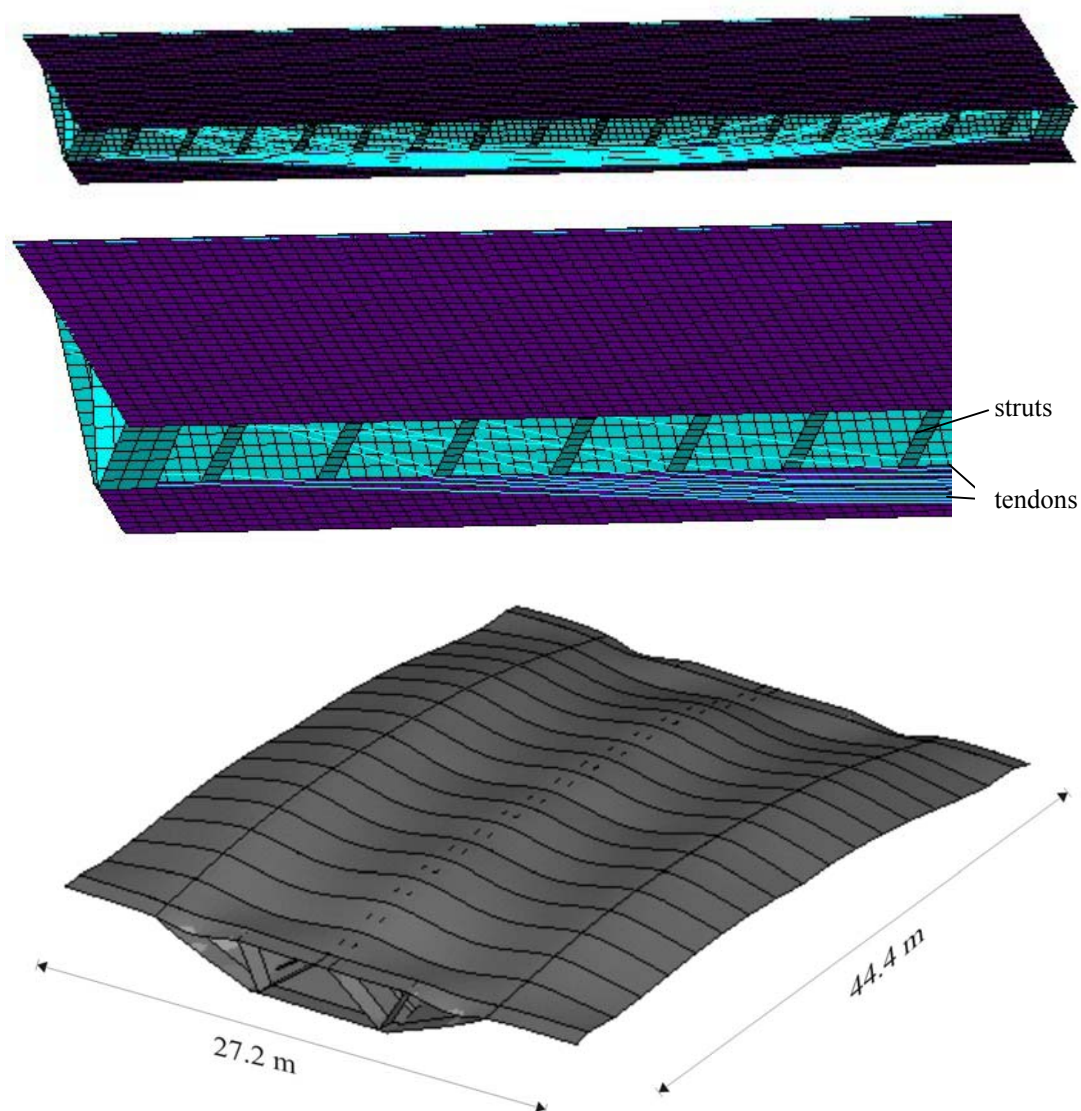
Figure 4.35   Finite element model of the Bang Na Bridge and deformed shape

The Bang Na segmental bridge with its large width to length ratio experienced a large gap in segments due to the "bowing effect" in the match-cast process (see chapter 3.3). To study

the influences of the resulting gaps on the serviceability and bearing capacity of the whole structure a 3 *mm* gap value in segments was used in the numerical simulation. The gap shape as simulated in the numerical model can be seen in Figure 4.36.
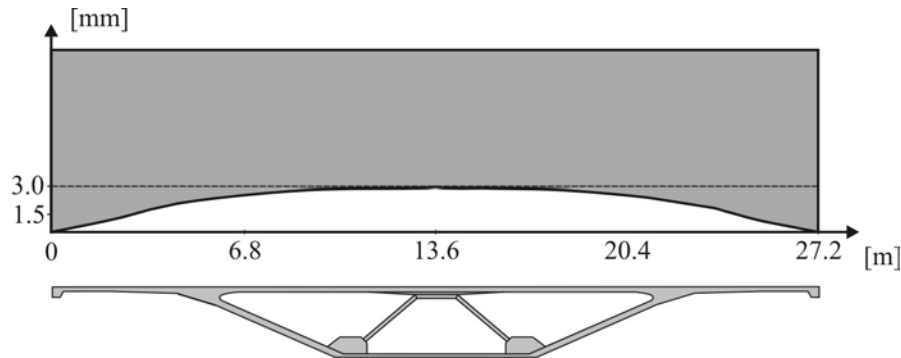
Figure 4.36   Gap shape used in the Finite Element model

Figures 4.37 and 4.38 show the longitudinal compressive stress distributions (σ_x) in the upper slabs of segments with perfectly fitted segments and segments with 3.0 *mm* gap respectively, while the normal compressive stresses (σ_x) in the joint at the mid-span are shown underneath.

The obtained results of the bow shaped segments showed that the longitudinal compressive stress distribution (σ_x) across the joints has changed significantly compared to perfectly fitted segments with apparent increasing of compression stresses in the deck slab wing region. Moreover, when segments with gap have been used, an increase in the total deflection of the whole structure has been estimated. The deflection of the bridge with perfect fitted segments was about +18.0 *mm*, whereas it was about -12.0 *mm* with bow shaped segments.
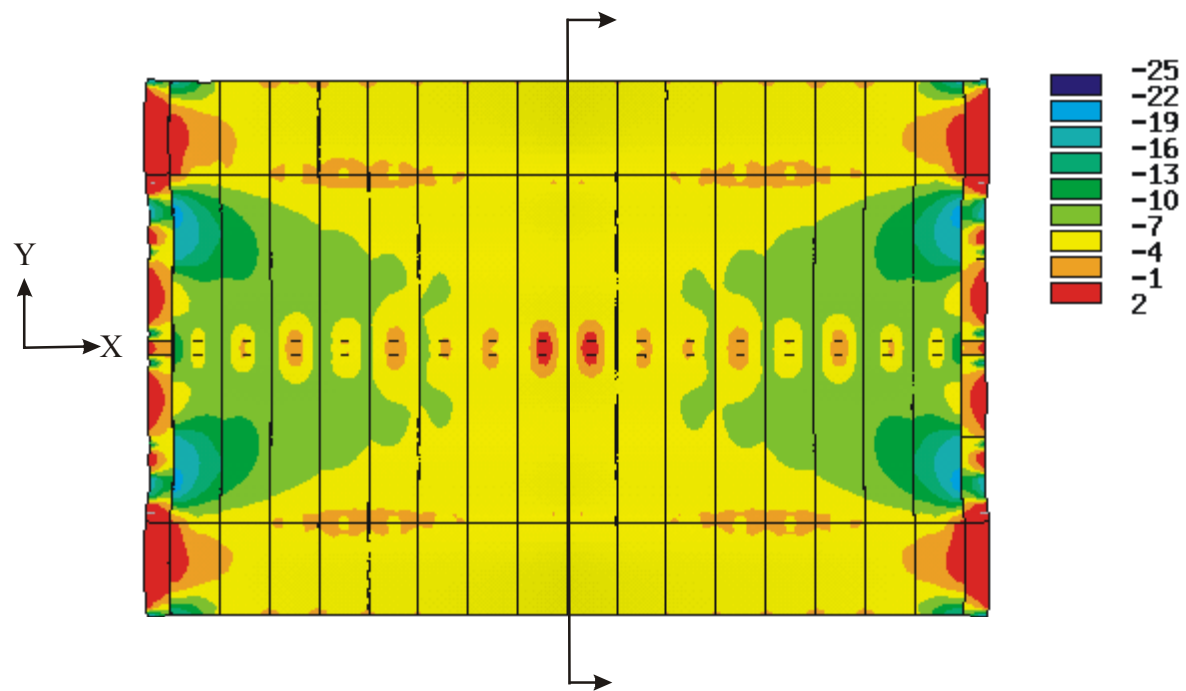
(a) deck slab
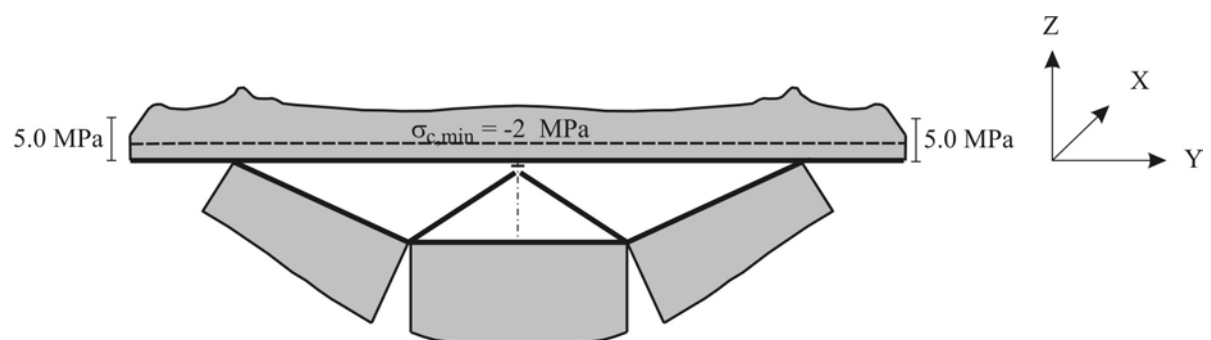
(b) joint at midspan

Figure 4.37   Longitudinal stress distribution σ_x (*MPa*) with perfectly fitted segments under short-term loading
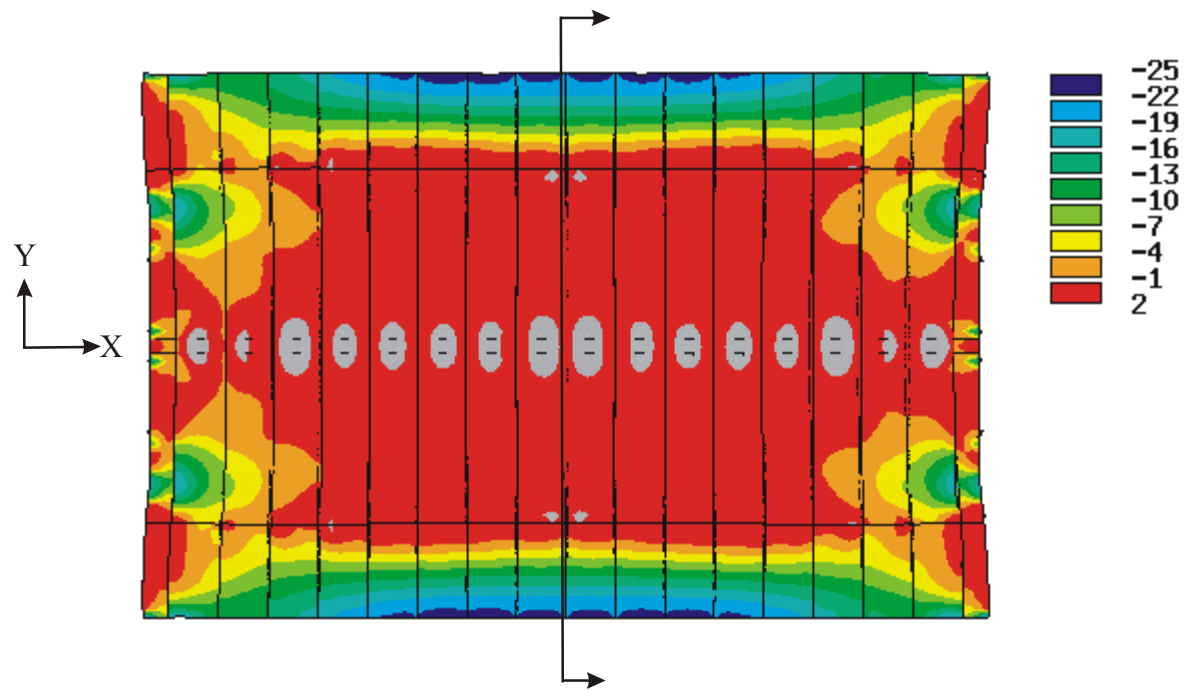
(a) deck slab
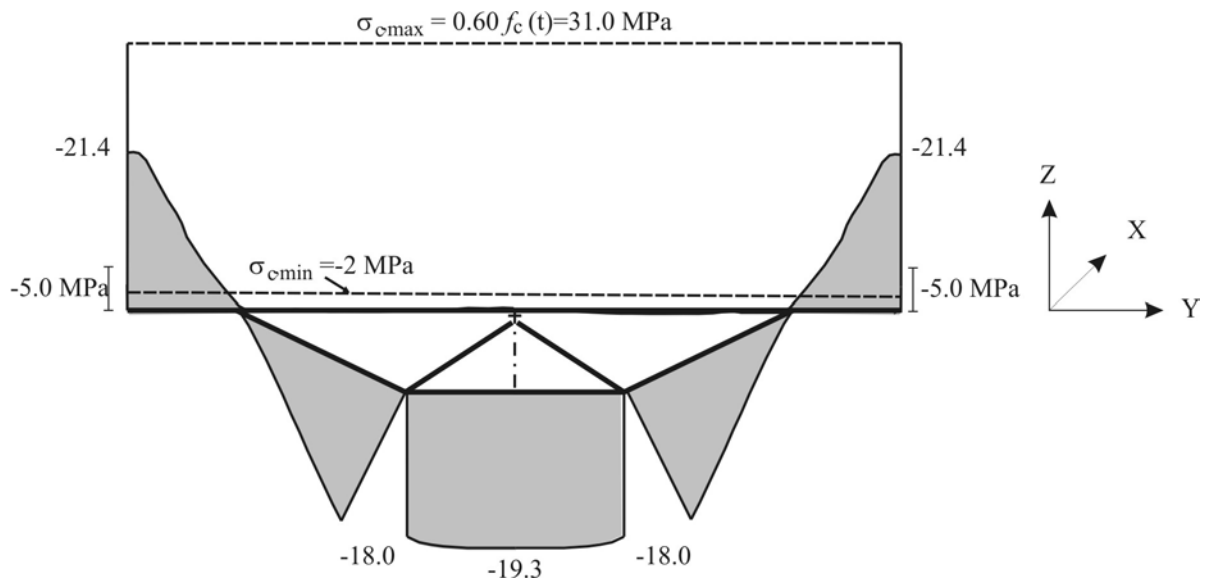
(b) joint at midspan

Figure 4.38 Longitudinal stress distribution σ_x (*MPa*) with bow shaped segments under short-term loading

The imperfect segments with gap cause excessive compressive stresses in the wing tip regions. The prestressing tendon no. *T*11 in the real bridge extended in the wing tips (see Figure 4.34) added even more compressive stresses. Hence, the longitudinal tendons in the

wings of deck slabs can be detrimental on the bearing capacity of the concrete and in the design of tendons that should be taken under consideration.

The existence of gaps in the joints does not only change the distribution of compressive stresses in the top slab but also raises questions about reduction of the bearing capacity of shear and torsion resistance of the shear keys in the upper slabs and in the webs. Thus a minimum compression in the joint must always be guaranteed.

Figures 4.39 shows the longitudinal stress distribution (σ_x) in the deck slabs of perfectly fitted segments at time of loading ($t = 0$) according to loading case of the long-term state (quasi permanent load combination) given by the German Code. The deflection was about +28.0 *mm* at time of loading. At time infinity ($t = \infty$) the results showed an increase of the deflection to about +77.0 *mm*, whereas a small change in the stress redistribution was noticed in the whole structure as can be seen in Figure 4.39.
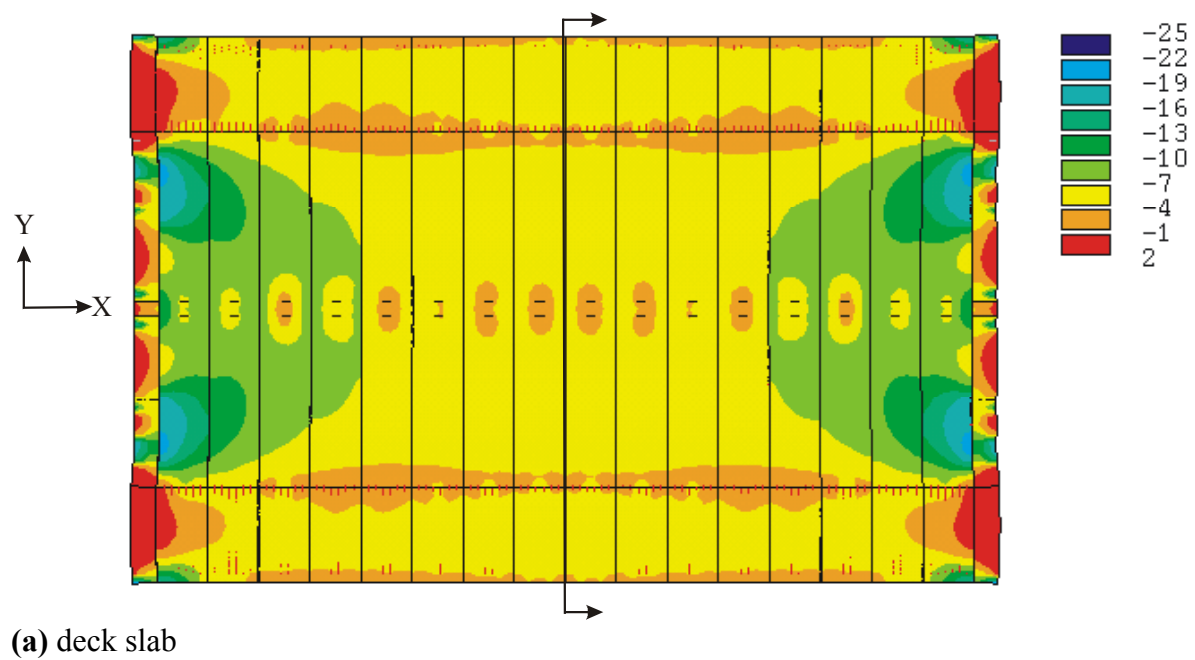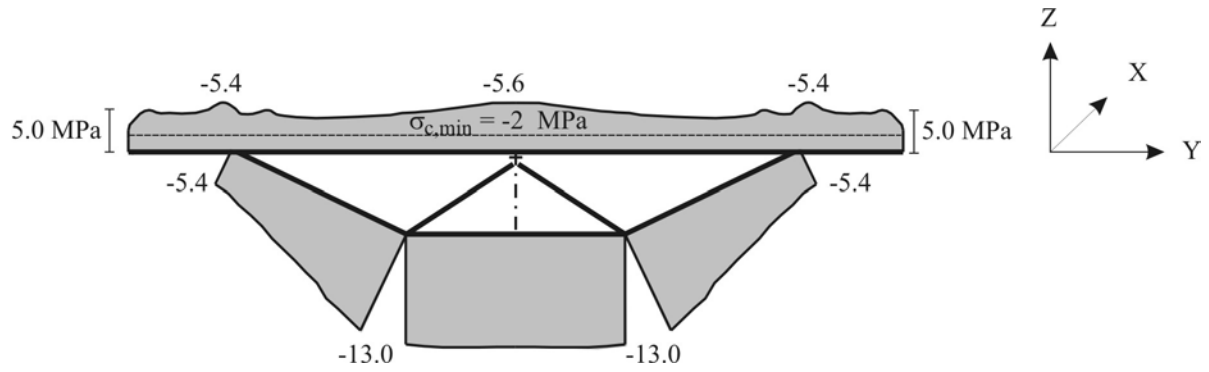
(a) deck slab

(b) joint at midspan

Figure 4.39   Longitudinal stress distribution σ_x (*MPa*) with fitted segments at time $t = 0$ using long-term loading ($\varphi_\infty = 2.5$, quasi permanent load combination)
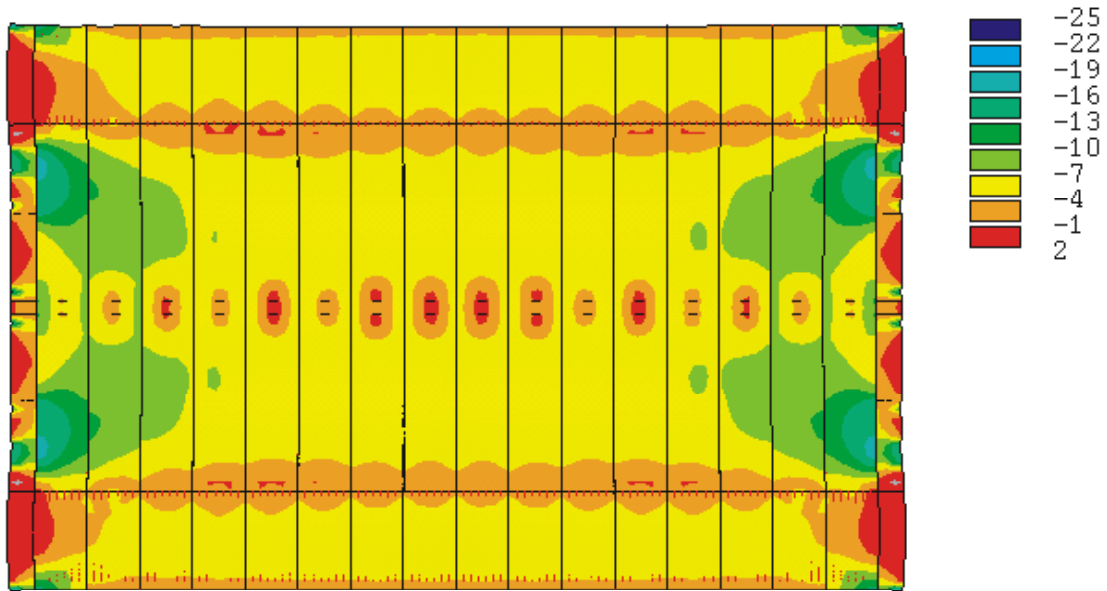
(a) deck slab
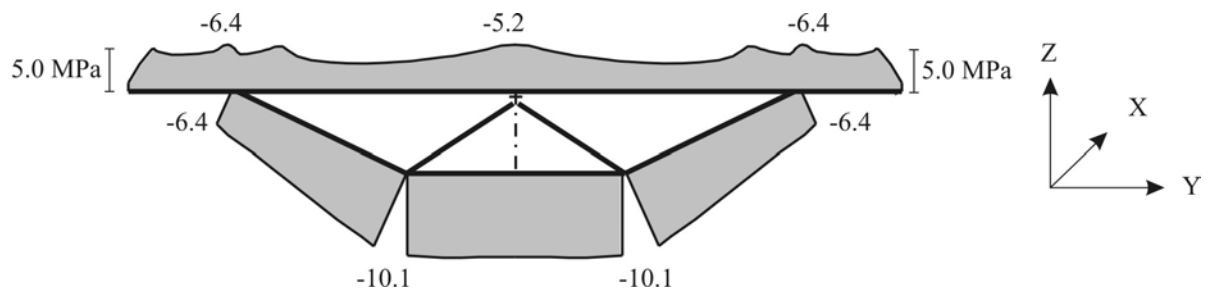
(b) joint at midspan

Figure 4.40 Longitudinal stress distribution σ_x (*MPa*) with fitted segments at time infinity $t = \infty$ using long-term loading ($\varphi_\infty = 2.5$, quasi permanent load combination)

Figures 4.41 and 4.42 show the stress distribution in the segmental bridge using segments with gap at time of loading ($t = 0$) and at time infinity ($t = \infty$) respectively. The stresses

redistributed significantly to reach almost the same distribution of the perfectly fitted segments with time as well as the gaps have been closed completely. The deflection was at first about +3.0 *mm* then it increased at time infinity to +29.0 *mm*, which is less than the deflection of the perfectly fitted segments at that time.

The numerical results showed that the average loss percentage in tendons of segmental bridge with perfectly fitted segments at time infinity was 11.7 %, whereas it increased to 18.8 % when bow shaped segments were used.

(a) deck slab
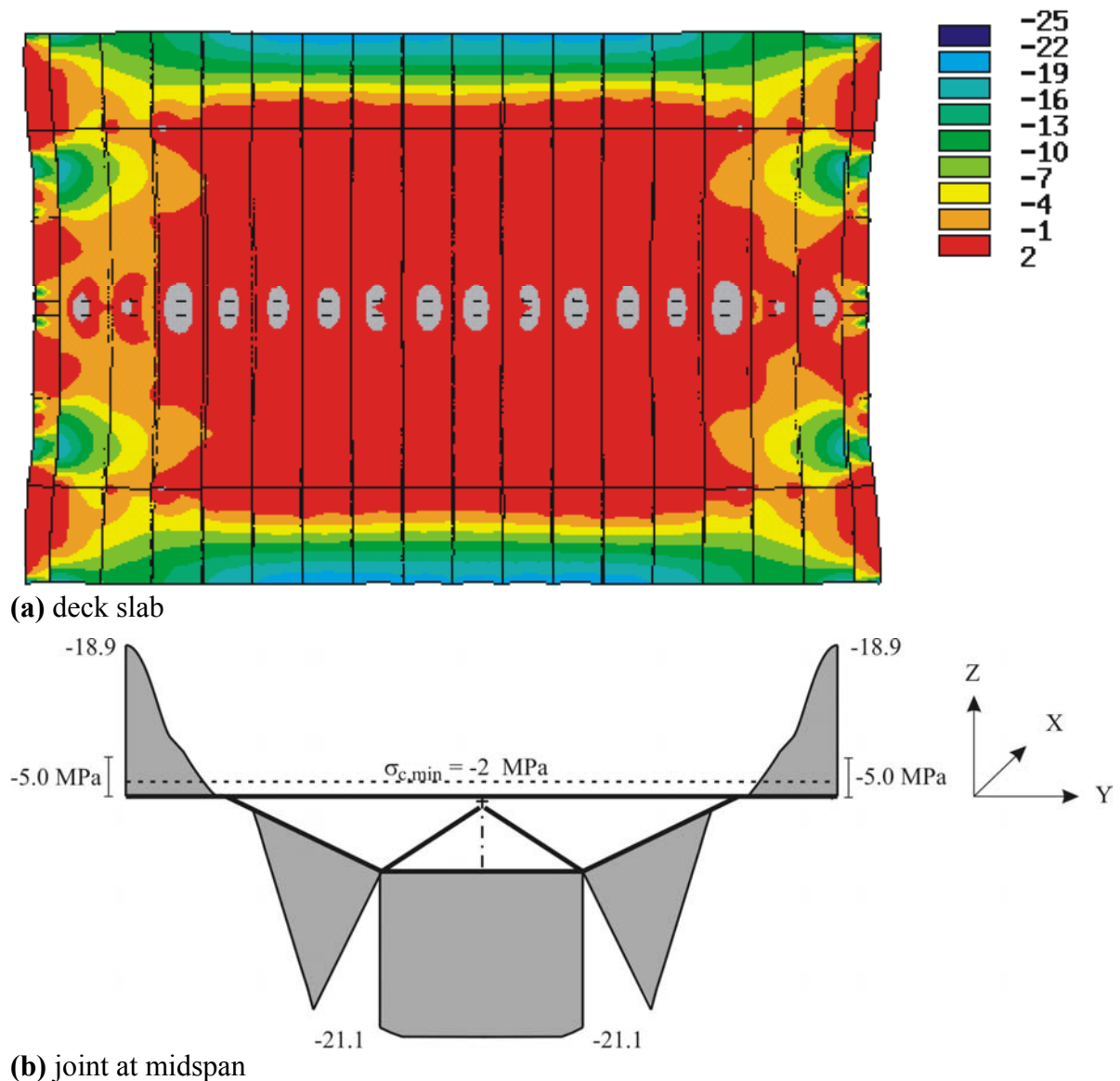
(b) joint at midspan

Figure 4.41 Longitudinal stress distribution σ_x (*MPa*) with bow shaped segments at time $t = 0$ using long-term loading ($\varphi_\infty = 2.5$, quasi permanent load combination)
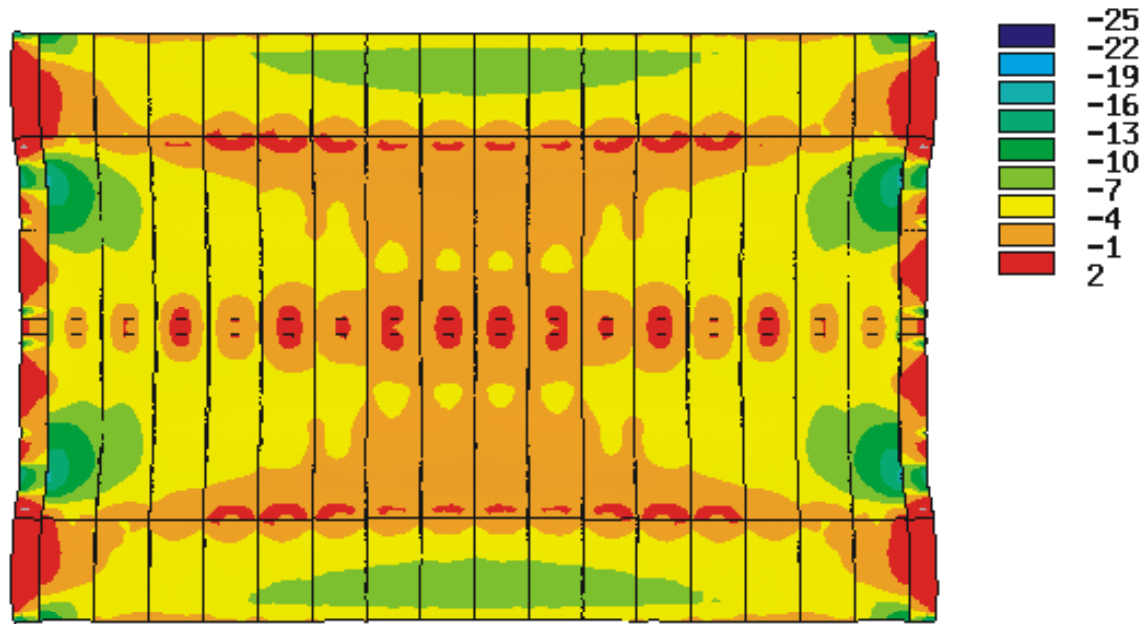
(a) deck slab
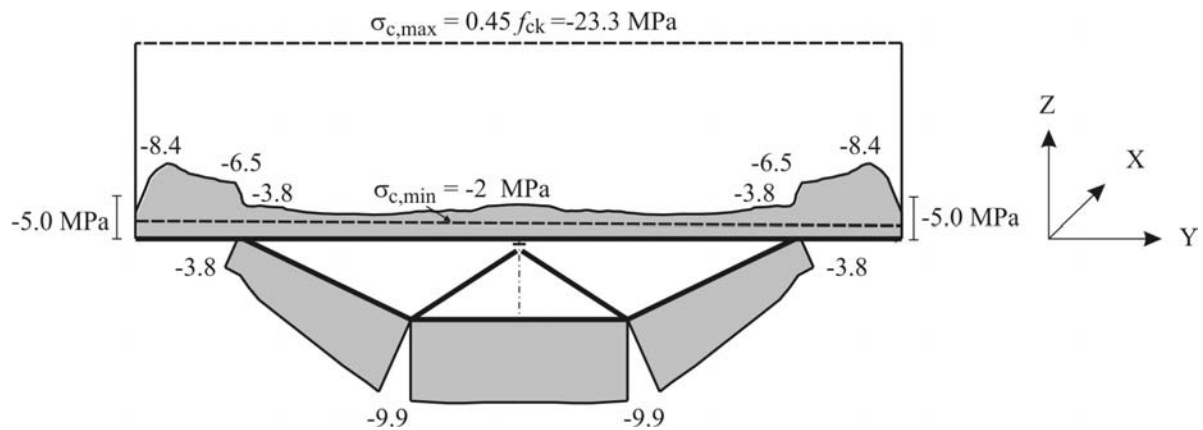
(b) joint at midspan

Figure 4.42 Longitudinal stress distribution σ_x (*MPa*) with bow shaped segments at time infinity using long-term loading ($\varphi_\infty = 2.5$, quasi permanent load combination)

Figure 4.43 shows a comparison of the stress distributions in midspan between perfect fitted segments and segments with gap at time of loading, whereas in Figure 4.44 the stress distributions at time of loading and at infinity of segments with gap are plotted.
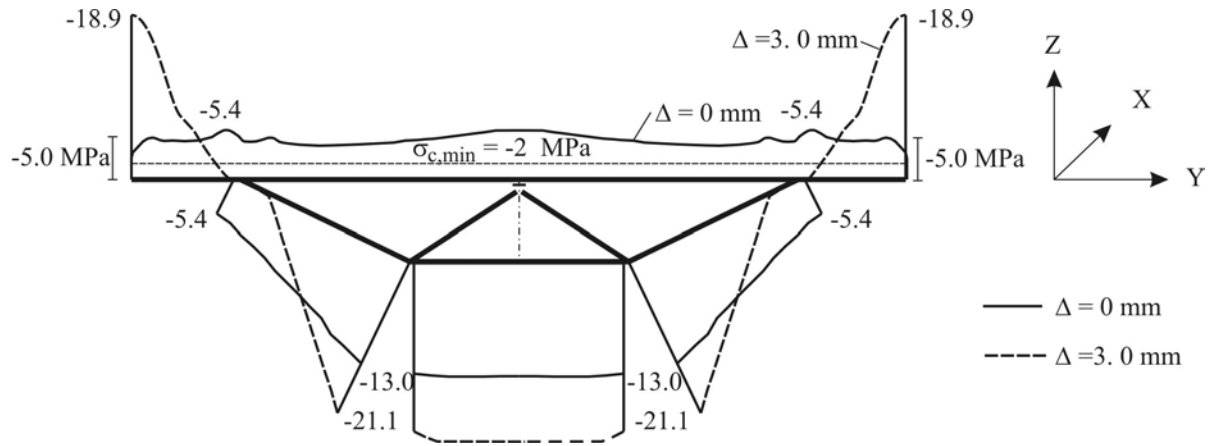
Figure 4.43   Longitudinal stress distribution σ_x (*MPa*) at midspan between fitted and bow shaped segments at time of loading using long-term state
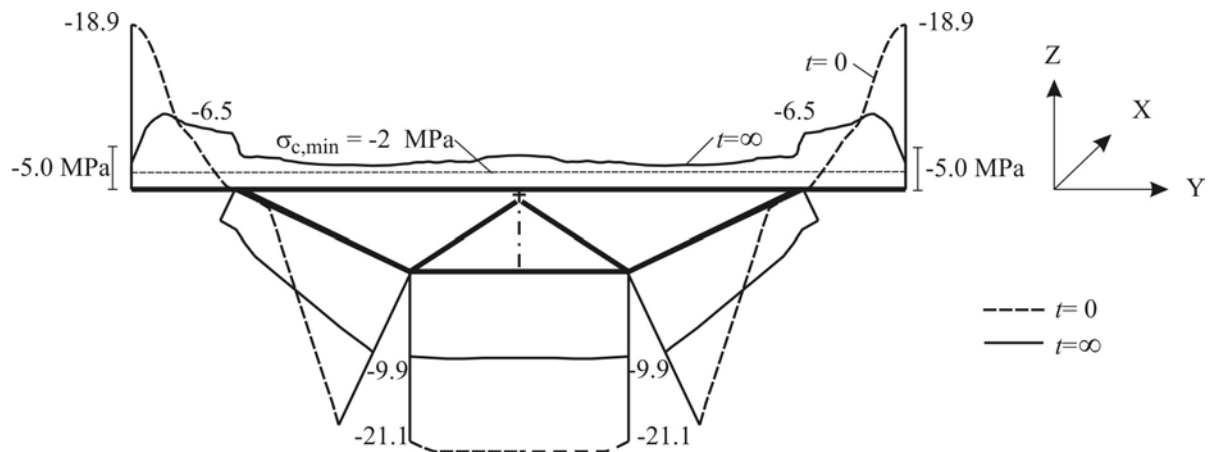
Figure 4.44   Longitudinal stress distributions σ_x (*MPa*) at midspan at time of loading and time infinity using bow shaped segments ($\Delta = 3$ *mm*)

Because of the large amount of the gap in such slender segments, it is expected that gaps will close slowly with time. The stresses redistribute as the gaps start to close. The stress distributions at various time intervals are shown in Figure 4.45.
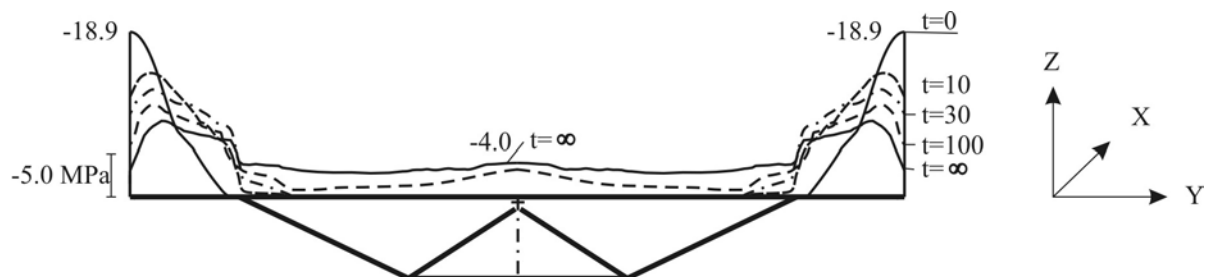
Figure 4.45   Longitudinal stress distribution σ_x (*MPa*) at midspan with bow shaped segments at different times *t* in days ($\Delta = 3$ *mm*) ($\varphi_\infty = 2.5$)

The creep coefficient φ_∞ decreases with the delay in loading time t_0. Thus, a creep coefficient of $\varphi_\infty = 1.8$ is obtained when the loading begins after 100 *days* of match casting process. Such long period between segment production and span erection on site is very likely to happen as the segment production starts with the construction of the substructure long time before the erection. Figures 4.46 and 4.47 show the longitudinal stress distribution σ_x using a creep coefficient of $\varphi_\infty = 1.8$ at time $t = 100$ *days* and time infinity ($t = \infty$) respectively. The results in Figure 4.46 show that the gap is not closed completely if it is compared to the Figure 4.45 at time $t = 100$ *days*. At time infinity the gap is closed but the minimum compressive stresses in the dry joints are less than 2.0 *MPa*, the value which is required according to the DIN standards. Hence, creep plays an important role in closing gaps and a start of loading must be significantly considered in the analysis.

(a) deck slab

(b) joint at midspan
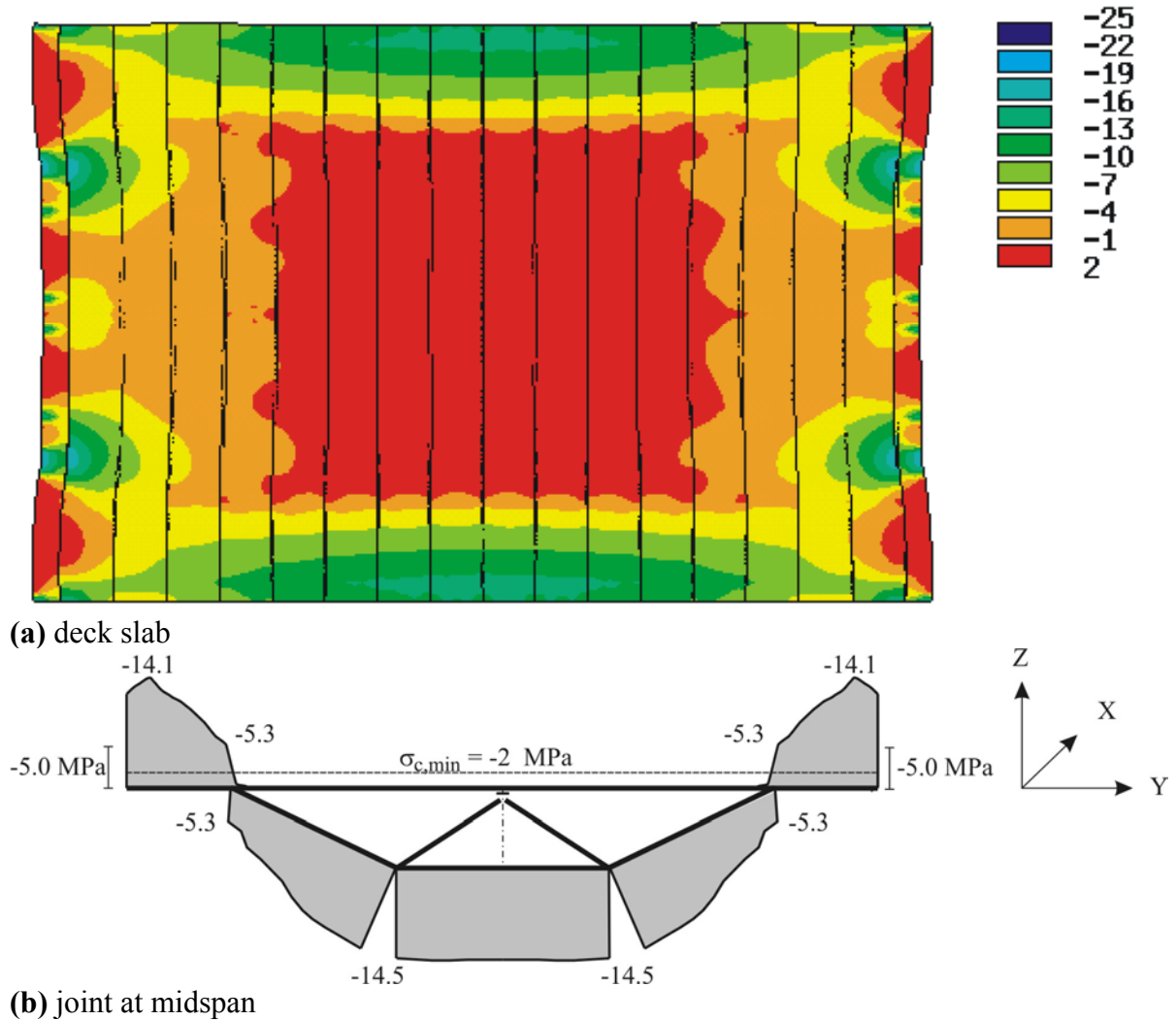
Figure 4.46   Longitudinal stress distribution σ_x (*MPa*) with bow shaped segments at time 100 *days* (loading after 100 *days*) using long-term loading ($\varphi_\infty = 1.8$, quasi permanent load combination)

(a) deck slab

(b) joint at midspan
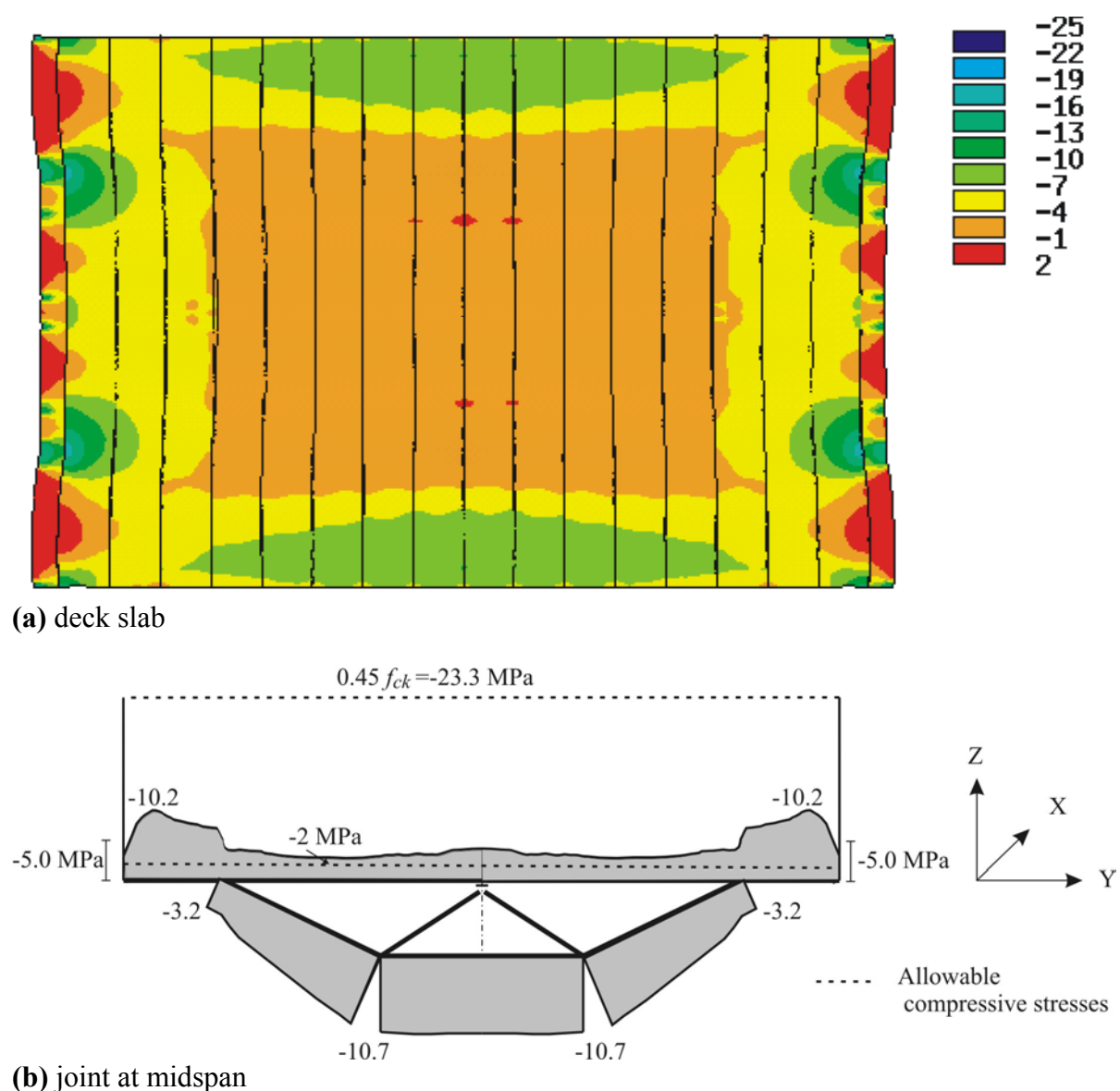
Figure 4.47   Longitudinal stress distribution σ_x (*MPa*) with bow shaped segments at time infinity (loading after 100 *days*) using long-term loading ($\varphi_\infty = 1.8$, quasi permanent load combination)

The main results of the various analysis are summarized in table 4.8.

Table 4.8 Deflections and concrete stresses (f = midspan deflection)

segments	time $t = 0$ - short term loading -			time $t = 0$ - long term loading -			time $t = \infty$ - long term loading -		
	f [*mm*]	$\sigma_{c,max}$ [MPa]	$\sigma_{c,min}$ [MPa]	f [*mm*]	$\sigma_{c,max}$ [MPa]	$\sigma_{c,min}$ [MPa]	f [*mm*]	$\sigma_{c,max}$ [MPa]	$\sigma_{c,min}$ [MPa]
perfect fitted	+18	-7.1	-3.3	+28	-5.6	-2.2	+77	-6.4	-0.8
bow shaped	-12	-21.4	0.0	+3	-18.9	0.0	+29	-8.4	-3.0

4.4   Recommended design and construction approaches

The various analysis have shown that the simple beam theory is very inadequate to predict the peak compressive stresses or the stress distribution; moreover it does not predict the possible tensile stresses that can develop at the cantilever slabs of segments near the supports. The effective flange width approach specified by the German Code used to determine section properties for analysis and for calculation of the peak stresses does not deal with imperfect structures with bow shaped segments. Finite element simulations of segmental bridges give good prediction of stress distributions and describes the behaviour of the structure during the short and long term as has been demonstrated in chapter 4.3. The developed finite element model is capable of conducting the impact of using bow shaped segments on the stress patterns and their redistributions with time, which gives a more rigorous analysis.

The stresses must be checked at different regions of the structure during the critical periods and must be compared to the allowable stresses given by the standards and the specifications. The long-term changes in deflection should be checked to ensure that it is not excessive. The transverse diffusion of post tensioning forces must be considered in the design to ensure adequate compressive stresses across joints near the supports.

It must be checked that the gaps close within a relatively short time if the climate permits and that the full width of every segmental joint is within allowable stress limits. In epoxy joints, the epoxy resin is normally less than 3 *mm* thick. Thus, the gap value must be clearly smaller than that value to ensure minimum compressive stresses obtained from the temporarily prestressing.

The numerical results using bow shaped segments ($\Delta = 1.5$ *mm*) at time infinity showed little influences on the serviceability and the bearing capacity of SES segmental bridges due to the low width to length ratio ($w/L = 3.0$) of the elements. At time $t = 0$ zero stresses in the deck had been observed (see table 4.6). Thus, the bowing effect in such structures cannot be ignored. The Bang Na segmental bridge ($w/L = 10.7$) with bow shaped segments of 3 *mm* gap experienced a mechanical behaviour within the allowable standards at time infinity if the segments are not stored for a long period before the erection. Like the SES segments zero stresses in the deck had been observed (see table 4.8) for time $t = 0$. Thus, 3 *mm* gap is

not considered to be permissible in segments of the structure with the used concrete properties and geometry.

If a rigorous analysis is required the following design and construction approaches are recommended to be applied in order to predict the behaviour of the bow shaped segments in structures:

- The properties of the concrete should be determined and the expected boundary conditions should be applied in the thermo-mechanical finite element model of the match-cast segments.

- The deformations of the old segment are determined after the expected initial time of concrete setting, which represents the bow shape in the new segment.

- The mechanical finite element model of segmental bridges is applied using the bow shaped segments in the short and long terms.

- The stress patterns, deflections and losses in prestressing forces should be determined.

- The peak stresses at the cantilever regions and near the supports must be checked to be within the allowable limits.

- In dry joints, minimum compressive stresses must be provided in the joints, or can be provided due to closing the gaps during the time if serviceability.

If the stresses were found to be excessive or the gaps do not close with time, special procedures and construction approaches should be followed in the match-cast process in order to avoid the risks of using bow shaped segments. If the gap value is more than 3 *mm* and epoxy resin is used in the final structure, then special approaches should be used to decrease the gap value.

The deflected shape of the old match-cast segment depends mainly on the shape of the thermal gradient. The most efficient way to decrease the bowing is by decreasing the severe thermal gradient which can be achieved in many measures:

- The heat of hydration is based on the concrete mixes used. Thus, different batch designs could have a significant effect on the thermal gradient. The use of low heat concrete with appropriate compressive strength can be recommended. This proposal

can be in opposite to construction constraint which requires a fast hardening of the concrete.

- The amount of retarders should be controlled in order to achieve lower setting time of concrete, which produces smaller gap in new match-cast segments.

- The lower the thermal diffusivity D of concrete the smaller the resulting gap in the match-cast method.

- The new match-cast segment should not be insulated or covered with materials, which have a low thermal conductivity coefficient in order to minimize the developed heat of hydration in fresh concrete.

- By keeping the old match-cast segment warm. Steam curing maybe necessary in a cold climate which is very costly. A less expensive alternative is to cover the segment by insulation sheets. The orientation of the casting bed can help by keeping the free face in the direction of the sun.

- Any measures of warming the old match-cast segment may help in reducing the thermal gradient.

- In a cold windy climate, the use of curing blankets and plastic sheeting is recommended since cooler air temperatures create a more severe thermal gradient.

- The higher the age of a match-cast segment the lower the coefficient of thermal expansion of concrete. An older match-cast segment with relatively smaller thermal expansion is recommended for use, which produces less thermal deformations.

- Isothermal enclosure in joints, which can reduce the heat transfer across joins, can be used if they do not alter the joint properties.

- Choosing the correct time of starting the casting process can reduce the thermal gradient. The most adequate time is when the ambient temperature starts to rise which can produce a smaller thermal gradient.

- Transverse prestressing can be used to resist thermal stresses and minimize slightly the bowing of old match-cast segments.

5   Summary and conclusion

Hollow-box girder bridges made of precast segments stressed together by external tendons have become a preferred construction technique for many elevated highway projects in the world. The main difference between this type of bridge and cast-in-place monolithic structures is the lack of mild reinforcement passing through the joints between the elements. Thus, the slices or segments must be stressed together by external tendons. In early bridges constructed using this new technique, the precast segments are connected with thin *in situ* concrete or mortar joints, whereas in recent bridges the segments are match cast in a plant and joined together only with a thin film of epoxy. Many segmental bridges in Asia and the USA have been erected without any epoxy in the joints for economic reasons. Shear keys are used on the surface of the joint to help in the alignment process of segments during erection and to transfer the shear forces between the segments. Hence, the shear keys should fit each other on both sides of two adjacent elements. Therefore, the manufacturing of precast segments has to be done by the match-cast method which provides a nearly perfect fitting of two adjacent elements.

Due to its flexibility, the short line match-cast method is the preferred segment production method for segmental post-tensioned concrete box girder bridges. However, even with this method one can not avoid a gap between two adjacent segments. The bowing effect or banana shape which occurs during match casting is caused by the flow of heat of hydration and can lead to a permanent curvature in new segments, and cause the new segment to have one straight and one curved side. This imperfection may have a significant influence on the load bearing capacity of the bridge and the behavior of the structure under serviceability loads.

During match casting, the bowing effect may affect the tolerances in the manufacturing process, and even be detrimental to the old match segment. The deformation of early age concrete can create tensile stresses which are greater than the actual tensile strength of concrete. This may result in cracking of concrete. Bow shaped segments showed problems during the epoxy and temporary post-tensioning operations during the erection at the site. It may possess problems in closing the joints. The use of bow shaped segments in the final structure will lead to areas of reduced compression in the segment's centerline, sometimes

even zero stresses, whereas stress peaks will occur at the tips of the segment's cantilever slab. The joints should always be closed under serviceability loads and compressive stress under the permissible limit of approximately -2 *MPa* is required to prevent the risk of joint opening. No systematic study about the bowing phenomenon has been carried out so far.

Knowledge of the expected temperature rise during the hydration of cement is important to predict the bowing phenomenon. Tests can hardly be carried out due to the size of the segments and the various boundary conditions. Thus, the finite element method was used to study the heat transfer problem during match casting which allows to estimate the temperature development and distribution within a segment. The transient thermo-mechanical finite element model is based on the principles and laws of thermodynamics for conducting the chemical and physical states, the conservation of energy, the physics of heat conduction, fluid motion for convection and the physics of thermal energy conversion. The software called 'ANSYS' was applied as a numerical solution tool. The model was verified by measurements in the site made for the San Antonio *Y* project and the Bang Na (BBBE) standard segments during match casting. The very good agreement between the measured and predicted results demonstrate that the numerical model is suitable for analyzing the bowing phenomenon. A systematic study of the match cast process has been conducted for segments with different slenderness (*w/L*) and different boundary conditions such as ambient temperature, wind speed, formwork properties and insulating materials. The results showed that the gap increases strongly with the slenderness of a segment. A decrease in ambient temperatures will further increase the temperature gradient and the gap in the match cast segment. Insulating materials over the match cast segment are very efficient to reduce the gap. The new segment should not be covered.

The numerical simulations showed that the simple equivalent moment approach is able to estimate the gap size. The main problem by using this method is that the temperature gradient in the match-cast segment at the time of setting of the fresh concrete has to be known.

No systematic study has been conducted so far about the impact of using imperfect bow shaped segments in segmental bridges. Thus, non-linear finite element models of two real bridges were used to estimate the stresses in the structures having perfect fitted and bow shaped segments. The time dependant behavior of concrete (creep and shrinkage) was included in these investigations. The measurements made at the test span of the Second Stage Expressway System (SES) were used to verify the complex numerical model. The measured and estimated results agreed well. The numerical analysis showed that bow shaped segments have little influences on the serviceability and the bearing capacity of SES segmental bridges due to the low width to length ratio ($w/L = 3.0$) of the segments. The stresses, except at time $t = 0$, are within the permissible limits. Thus, the bowing effect in such structures can only be ignored under the given boundary condition (gap $\Delta = 1.5$ *mm*) at time infinity, $t = \infty$. This problem increased for the slender segments of the Bang Na (BBBE) bridges which have a high width to length ratio ($w/L = 10.7$). The numerical analysis of the bridge with bow shaped segments gives a new compressive stress distribution in the joints with areas of reduced compression in the segment's centerline whereas excessive stress occurred at the tips of the segment's cantilever slab. Moreover, the imperfection had a significant influence on the deflected shape of the whole bridge and resulted in more prestress losses. Thus, the bowing effect should be considered in the design of such slender precast segmental bridges.

The transient study of the structure showed that the compressive stress redistributed with time due to creep and shrinkage effects. The time dependant behavior of concrete plays an important role in closing the gaps. The gap between bow shaped segments ($\Delta = 3$ *mm*) in the Bang Na bridge will close completely and the stresses are within the permissible limits at $t = \infty$, if the structure is loaded shortly after segment production. This is not the case if the bridge construction and the loading starts later which is often the case. After 100 *days* the creep coefficient is reduced from $\varphi_\infty = 2.5$ to $\varphi_\infty = 1.8$. Even with the older segments the gaps closed but the compressive stresses in the inner part of the deck slab are very low and clearly smaller than the permissible value. Thus, measures have to be taken for bridges with such slender segments to reduce the gap size.

If the bow shaped segments were found to be detrimental on the structure, special design and construction approaches should be followed to minimize the magnitude of the resulting

bowed shape in the match-cast process which are explained in detail in chapter 4.4. The most efficient way to reduce the bowing is by decreasing the severe thermal gradient. Batch designs, e.g. low heat concrete, can reduce the gap. The most adequate time for pouring is when the ambient temperature starts to rise which can produce a smaller temperature gradient. Curing blankets and plastic sheeting in the old match-cast segment is more recommended in cold windy climate, since cooler air temperatures create more severe negative thermal gradient. The older match-cast segments with relatively smaller thermal expansion should be used if possible. The orientation of the casting bed can help by keeping the free face in the direction of the sun. Transverse prestressing can be used to reduce the bowing of old match-cast segments by resisting thermal stresses.

References

[Aa1] AASHTO. *Guide Specification for the Design and Construction of Segmental Concrete Bridges.* 1993

[Aa2] AASHTO. *Guide Specification for the Design and Construction of Segmental Concrete Bridges.* 1999

[Aa3] AASHTO. *Standard Specification and Guide Specification for Segmental Concrete Bridges.* 1989 - 1992

[Ab1] Rombach G., Abendeh R., *Temperature Induced Deformation in Match-Cast Segments.* IABSE Symposium "Metropolitan Habitats and Infrastructure", Shanghai, 2004

[Ab2] Abendeh R., Brockmann C., Fischer O., Rombach G., *Temperaturinduzierte, bleibende Verformungen von Brückensegmenten bei der Herstellung im Kontaktverfahren.* Beton- und Stahlbetonbau 3/2005, pp. 207 – 215, 2005

[Ac1] ACI Committee 517: *Accelerated Curing of Concrete at Atmospheric Pressure - State of the Art.* ACI Journal 77, No. 6, 1980, pp. 429-448

[Alt] Altstadt E., Moessner T., *Extension of the ANSYS Creep and Damage Simulation Capabilities.* Report of Forschungszentrum Rossendorf, 2000

[Am1] American Concrete Institute. *Manual of concrete practice.* Part I. ACI-CI 213R-79, ACI 207.1r-70, ACI 207.2R-73, ACI 207.4 R-80, 1987

[Ans] Ansys, *Ansys Elements User's Manual*, Release 5.3. Houston 1994, USA

[Arp] Arpaci V., Kao S. and Selamet A., *Introduction to heat transfer.* Prentice Hall, 1999, USA

[Ba1] Petrov C., *Construction of Bang Na Expressway, Bangkok, Thailand*, First FIB Congress ,Concrete Structures in the 21th Century', Osaka FIB, 2002

[Ba2] Brockmann C., Rogenhofer, H., *Bang Na Expressway, Bangkok, Thailand World's Longest Bridge and Largest Precasting Operation*, PCI Journal, 2000, pp. 26-38

[Ba3] Barker J., *The Cantilevered Precast Segmental Bridge over the Kishaukee River in Illinois (USA),* L'Industria Italiana del Cementro, 1988, pp. 26-33

[Baz] Bazant Z., Kaplan M., *Concrete at High Temperatures, Materials Properties and Mathematical Models.* Longman Group Limited, London 1996

[Bmv] BMV/DBV: *Empfehlungen für Segmentfertigteilbrücken mit externen Spanngliedern.* Fassung 04/89

[Bon] Bonell D., Harber F., *The Thermal Expansion of Concrete.* National Buildings Studies, Technical Paper No. 7. HMSO, London 1951.

[Br1] Kashima S., Breen J., *Construction and Load Tests of a Segmental Precast Box Girder Bridge Model.* Research Report 121-5, Center for Highway Research, The University of Texas, Austin, 1975.

[Br2] Kashima S., Breen J., *Epoxy Resins for Jointing Segmentally Constructed Prestressed Concrete Bridges.* Research Report 121-2, Center for Highway Research, The University of Texas, Austin, 1974

[Br3]   Roberts C., Breen J., Kreger M., *Measurement Based Revisions for Segmental Bridge Design and Construction Criteria.* Texas Department of Transportation, Report no. 1234-3F, 1993, pp. 303-320

[Br4]   Roberts-Wollmann L., Breen, E., Kreger E., *Temperature Induced Deformation in Match Cast Segments.* PCI Journal, Vol.40, No.4, July-August, 1995, pp. 62-70

[Br5]   Brockmann C., Springer S., *Advanced in the External Post-Tensioning of Segmental Bridges.* First FIB Kongress ,Concrete Structures in the 21th Century', Osaka, 2002

[Br6]   Brockmann C., *Aufbau eines Fertigteilwerkes Bang Po in Thailand.* BFT 3/2000 pp. 28-33, 4/2000 pp. 82-91, 5/2000 pp. 66-73

[Br7]   Browne D., *Properties of concrete in reactor vessels.* Proceedings of Conference on prestressed concrete Pressure Vessels, Institute of Civil Engineers, London. Group C, Paper 13, pp. 11-31

[Br8]   Breitenbücher R., *Zwangspannungen und Rissbildung infolge Hydratations-wärme.* Dissertation. TU München, 1989

[Bun]   Bundesministerium für Verkehr, *Empfehlungen für Segmentfertigteilbrücken mit externen Spanngliedern.* Ausgabe 1999

[Ca1]   Carlson R., *A Simple Method for the Computation of Temperatures in Concrete Structures.* ACI-Journal, 34, 1937, pp. 89 - 102

[Ca2]   Carmen P. and Nelson A., *The Thermal Conductivity and Diffusivity of Concrete.* Bulletin No. 122, University of Illinois Engineering Experiment Station, Urbana-Champaign.

[Cam]   Campbell-Allen D., Thorne P., *The Thermal Conductivity of Concrete.* Magazine of Concrete Research, 15(43), pp. 39 - 48

[Cer]   Cervera M., Oliver J., Prato T., *Thermo-Chemo-Mechanical Model for Concrete, I: Hydration and Aging.* Journal of Engineering Mechanics, September 1999, pp. 1018-1027

[Cha]   Chaffo N., *Design of Pier Segment in Segmental Hollow Box Girder Bridges.* Phd-thesis, University of Hamburg-Harburg, 2003

[Da1]   Deutscher Ausschuss für Stahlbeton, *Erläuterungen zu DIN 1045-1.* Deutscher Ausschuss für Stahlbeton, Heft 525, Berlin 2003

[Deu]   Deutscher Betonverein, *Empfehlungen für Segmentfertigteilbrücken mit externen Spanngliedern.* Deutscher Betonverein, Bundesministerium für Verkehr, Ausgabe 1999

[Des]   De Schutter G., Taerwe L., *Degree of hydration-based description of mechanical properties of early age concrete.* Materials and Structures, Vol. 19, pp. 335 - 334, 1996

[Di1]   *DIN 4108 Wärmeschutz im Hochbau.* Deutsches Institut für Normung, Berlin 1969

[Di2]   *DIN-Fachbericht 102: Betonbrücken.* Deutsches Institut für Normung, Berlin 2003

[Di3]   *DIN 1045-1:2001-07: Tragwerke aus Beton, Stahlbeton und Spannbeton – Teil 1: Bemessung und Konstruktion.* DIN Deutsche Institut für Normung, Berlin 2001.

[Di4]   *DIN-Fachbericht 101: Einwirkungen auf Brücken.* DIN Deutsche Institut für Normung, Berlin 2003.

[Ei1]   Eibl, J., *Der Segmentbrückenbau - eine vorteilhafte Bauweise.* Beton- und Stahlbetonbau 95, Heft 2000, pp. 632-637

[Ei2]   Eibl J., Prommersberger G., Bachmann H., *Rechnerische Erfassung des aus Hydratationswärme entstehenden Spannungszustands am Beispiel der Talbrücke Frauenwald.* Beton- und Stahlbetonbau 85 (1990), H.4., pp. 89-90

[EC2]   *Euocode2: Design of concrete structure – part 1-1: general rules and rules for buildings.* Draft Nov. 2004

[Fi1]   Fischer O., Krill A., *The Bang Na Expressway, Bangkok: A Full-Scale Loading Test of A Precast Segmental Box Girder Bridge for Six Lanes of Traffic.* FIP-Symposium 1998, Amsterdam

[Fi2]   Fischer O., *Der Bang Na Expressway, Bangkok.* Beton- und Stahlbetonbau 93(1998), Heft 2. pp. 36-41

[Fi3]   FIB: Proceedings of the First FIB Congress ,Concrete Structures in the 21th Century', Osaka, 2002

[Fig]   Figg and Muller Engineers, *Prestressed Concrete Segmental Bridge Construction Manual.* Bridge Contractors Seminar, Asheville, NC, June 1981

[Gho]   Ghoshdastidar P., *Heat Transfer.* Oxford University Press, 2004, India

[Gut]   Gutsch A., *Stoffeigenschaften jungen Betons - Versuche und Modelle.* Deutscher Ausschuss für Stahlbeton, Heft 495, Berlin, 1999

[Ham]   Hamfler, H., *Berechnung von Temperatur-, Feuchte- und Verschiebungs-feldern in erhärtenden Betonbauteilen nach der Methode der finiten Elemente.* Deutscher Ausschuss für Stahlbeton, no. 395, 1988, Berlin

[Inc]   Incropera F., DeWitt D., *Introduction to Heat Transfer.* Third edition, John Wiley & Sons, 1996, USA

[Jea]   Jean Müller International (Hrsg.), *Bang Na - Bang Pli - Bang Pakong Expressway Project Report on Bowing Deformations in Match-Cast Segments Induced by Temperature Gradient due to Heat of Hydration.* San Diego 1996, Internal report of Bilfinger + Berger Bauaktiengesellschaft, Mannheim

[Kav]   Kaviany M., *Principles of Heat Transfer.* John Wiley & Sons, Inc. 2002, USA

[Kri]   Kristek V., Kohoutkova A., *Serviceability Limit State of Prestressed Concrete Bridges.* First FIB Congress ,Concrete Structures in the 21th Century', Osaka, 2002

[Kor]   Kordina K., Teutsch M., Weber V., *Spannbetonbauteile in Segmentbauart.* Deutscher Ausschuss für Stahlbeton, Heft 350, Berlin, 1984

[Ku1]   Kupfer H., Guckenberger K., Dachner F., *Versuche zum Tragverhalten von segmentären Spannbetonträgern.* Deutscher Ausschuss für Stahlbeton, Heft 335, Berlin, 1982

[Ku2]   Kordina K., *et al.*, *Trag- und Verformungsverhalten von Spannbetonteilen in Segmentbauart mit Vorspannung ohne Verbund.* Abschlußbericht, TU Braunschweig, 1990

[Lal]   Lalande M. L., *L'emploi du béton précontrainte dans la préfabrication des ouvrages d'art.* Travaux, august 1946, pp. 281-298

[Lau]   Laube, M, *Werkstoffmodell zur Berechnung von Temperaturspannungen in massigen Betonbauteilen in jungen Alter.*, Dissertation, TU- Braunschweig

[Lea]   Lea, F., *The Chemistry of Cement and Concrete*. Edward Arnold Ltd., 1970

[Log]   Logan D., *A First Course in the Finite Element Method.* Second edition, PWS-KENT Publishing Company, USA, 1992

[Man]   Mangold M., *Die Entwicklung von Zwang- und Eigenspannungen in Betonbauteilen während der Hydratation.* Berichte aus dem Baustoffinstitut, Baustoffinstitut München, 1994

[Mch]   McHenry, D., *Measured and computed temperatures of concrete at Norris Dam.* ACI-Journal 34/1937, pp. 117-125

[Mil]   Mills H., *Factors influencing cessation of hydration in water cured cement pastes*, ACI-Sp 60. Washington, 1966, pp. 406-424

[Mit]   Mitchell J., *Thermal Properties.* ASTM Special Technical Publication No.169, ASTM, Philadelphia, 1956, pp. 129-35

[Mor]   Moreton A., *Segmental Bridge Construction in Florida - a Review and Perspective.* PCI Journal, 1989, pp. 36-66

[Naw]   Nawy E., *Prestressed Concrete, a Fundamental Approach.* Prentice Hall, USA, Third edition, 2000.

[Ne1]   Neville A., *Properties of Concrete.* Third Edition, Pitman Publishing Inc, England, 1981

[Ne2]   Neville A., Brooks J., *Concrete Technology.* Longman Scientific and Technical, England, 1987, pp. 8-15

[Nig]   Nigel H., *Prestressed Concrete Bridges: Design and Construction.* Thomas Telford Ltd., Great Britain, 2003

[Nol]   Nolting E., *Zur Frage der Entwicklung lastunabhängiger Verformungen und Wärmedehnzahlen junger Beton.* Dissertation, Institut für Baustoffkunde und Materialprüfung der Universität Hannover, Heft 56, 1989

[Odl]   Odler I., *Strength of Cement.* Materials and Structures, Vol. 24, pp. 143-157, 1991

[Pat]   Pate D., The Chesapeake and Delaware Canal Bridge-Design-Construction Highlights. PCI Journal, 1995, pp. 20-30

[Po1]   Podolny W., Muller J.,. *Construction and Design of Prestressed Concrete Segmental Bridges.* John Wiley and Sons, New York, 1982

[Po2]   Podolny W., *The Cause of Cracking in Post-Tensioned Concrete Box.* PCI Journal, V.30, No. 2, USA, 1985, pp. 82-139

[Rec]   Recknagel-Sprenger, *Taschenbuch für Heizung und Klimatechnik.* R. Oldenbourg, München / Wien 1979

[Rho]   Rhodes A., *Thermal Properties.* ASTM Special Technical Publication No.169B, ASTM, Philadelphia, 1978, pp. 242-261

[Ro1]   Rombach, G., *Bangkok Expressway - Segmentbrückenbau contra Verkehrs-chaos,* in: *Aus dem Massivbau and seinem Umfeld* (Hilsdorf, Kobler ed.), Schriftenreihe des Institutes für Massivbau und Baustofftechnologie, University of Karlsruhe, 1995

[Ro2]   Rombach G., Specker A., *Numerical Modelling of Segmental Bridges.* ECCM 1999 Conference, München, 1999

[Ro3]   Rombach G., *Dry Joint Behavior of Hollow Box Girder Segmental Bridges.* FIP Symposium *Segmental Construction in Concrete*, New Delhi 2004

[Ro4]   Rombach G., Specker A., *Segmentbrücken.* Betonkalender 2004

[Rog]   Rogenhofer H., Herold W., *The Bang Na Expressway - Fabrication of Precast Concrete Boxes in the World Longest Segmental Yard*," Proc. of 13th FIP Congress, Amsterdam, 1998, pp. 197-200

[Ros]   Rostasy F., Krauß M., Budelmann H., *Planungswerkzeug zur Kontrolle der frühen Rissbildung in massigen Betonbauteilen, Teil 2: Hydratation und Wärmefreisetzung.* Bautechnik 79, 2002, Heft 8

[Ruc]   Rucker P., Beckhaus K., Wiegrink D. and Schiessl P., *Temperaturspannungen in dicken Betonbauteilen im jungen Alter.* Beton- und Stahlbetonbau, No. 7, 2003, pp. 389-398

[Sch]   Schöppel K., *Entwicklung der Zwangspannungen im Beton während der Hydration.* Dissertation, Universität der Bundeswehr München, 1993

[Sof]   Sofia M., Homsi E., *Fabrication and Erection of Precast Concrete Segmental Boxes for Baldwin Bridge.* PCI Journal, 1994, pp. 36-42

[Sp1]   Specht M., *Dauerhaftigkeit von Massivbrücken.* Technische Universität Berlin, 1983

[Sp2]   Specker A., *Der Einfluss der Fugen auf die Querkraft- und Torsionstragfähig-keit extern vorgespannter Segmentbrücken.* Dissertation, Technische Universität Hamburg-Harburg, 2001

[Sp3]   Springenschmid R., *Thermal Cracking in Concrete at Early Ages.* Technische Universität München, Germany, 1994

[Sp4]   Springenschmid R.," *Prevention of Thermal Cracking in Concrete at Early Ages,*" RILEM Technical Committee 119, Germany, 1994.

[Swe]   Swenson, E., *Weather in relation to winter concreting.* Proc. RILEM Symp. Winter Concreting, 1956, Copenhagen, pp. 122-128

[Ta1]   Takebayashi T., Deeprasertwong K., Leung Y., *A full-scale destructive test of a precast segmental box girder bridge with dry joints and external tendons.* Proceedings of the Institution of a Civil Engineering, August 1994, pp. 297-315

[Ta2]   Takebayashi T., Deeprasertwong K., *Full scale testing of a Precast Concrete Segmental Bridge with External Tendons and Dry Joints.* FIP Symposium 93, Kyoto, Japan, 1993

[Tac]   Tacke R., *Feuchte- und Festigkeitsentwicklung hydratisierenden Betons - Modellierung und numerische Analyse.* Dissertation, Technische Universität Braunschweig, 2002

[Ten]   Fukunaga Y., et al., *Design and Construction of the New Tomei Expressway Tenryugawa Bridge.* First FIB Congress 'Concrete Structures in the 21th Century', Osaka FIB, 2002

[Tet]   Tetmayer, *Deutsche Töpfer- und Ziegler Zeitung.* p. 234, 1883

[Top]   Topaloff B., *Geklebte Betonbrücken in Frankreich.* VDI-Berichte Nr. 122, VDI-Verlag, Düsseldorf 1968, pp. 43-47

[Usb]   US Bureau of Reclamation, *The Thermal Properties of Concrete.* Boulder Canyon Project, Bulletin No. 1 of Final Report, Part 7. US Bureau of Reclamation, Denver, Co., 1971

[Vdi]   *VDI-Handbuch Heizungstechnik. VDI-Richtlinien VDI 2070.* Heizungstechnik. Wärmezustand, Wärmewirkung, Wärmeübertragung, 1961, Beuth-Verlag, Berlin und Köln

[War]   Warncke, F., *Beitrag zur Berechnung der Temperaturen und Temperaturspannungen im Beton infolge Hydratation,"* Dissertation, Technische Universität Berlin 1971

[We1]   Weigler, H. and Nicolay, J., *Temperatur und Zwangsspannung in Konstruktionsleichtbeton infolge Hydratation.* Forschungsberichte der Arbeitgruppe Massivbau der Technischen Hochschule Darmstadt, No. 18, 1974

[We2]   Weigler H., Karl S., *Junger Beton, Beanspruchung-Festigkeit-Verformung,"* Forschungsberichte aus dem Institut für Massivbau der Technischen Hochschule Darmstadt

[Wis]   Wischers, G., *Betontechnische und konstruktive Maßnahmen gegen Temperaturrisse in massigen Bauteilen.* beton 1-64, pp. 22-26 und beton 2-64, pp. 65-73

[Zei]   Zeitler W., *Untersuchungen zu Temperatur- und Spannungszuständen in Betonbauteilen infolge Hydratation.* Dissertation, Technische Hochschule Darmstadt, 1983, pp. 15-40.

[Zol]   Zoldners F., *Thermal properties of concrete and sustained elevated temperatures. In temperature and concrete.* ACI Special Publication No. 25, Paper Sp 25-1. American Concrete Institute, Detroit, pp. 1-31.

Appendix A

Table A.1 Lists of precast segmental bridges

| Land	Bridge	Time	Full length [km]	Width of segment [m]	Length of segment [m]	Width length ratio w/L
USA [Mor]	Sunshine Skyway	1987	-	28.78	3.86	7.5
USA[Ba3]	Kishwaukee Bridge	-	0.331	12.5	2.5	5.0
Japan [Fi3]	Kawagoe Viaduct	2002	1.3	14.64	3	4.9
Laos [Fi3]	The Lao-Nippon Bridge	2000	1.38	11.5-14.3	2.5-3.5	4.6, 4.1
Japan [Fi3]	The Oidaira Viaduct	2005	0.833	17.14	6	2.9
Japan [Fi3]	Yatomi Viaduct	1999	1.5	15.29	3	5.1
Japan [Fi3]	Nishi Hirao Viadict	-	0.426	10.85	1.45-1.9	7.5, 5.7
France[Po1]	Oleron Viaduct	1966	2.86	10.6	3.3	3.2
Switzerland [Po1]	Chillon Viaduct	-	2.21	13	3, 3.2, 2.2	4.3, 4.1, 5.9
Netherland [Po1]	Hartel Bridge	-	0.5845	16	4.8-3.75	3.3, 4.3
Brazil [Po1]	Rio-Niteroi Bridge	1973	8.24	13.2	4.8-2.8	2.8, 4.7
USA [Po1]	JFK Memorial Causeway	1973	1	8.53	3.05	2.8
Canada [Po1]	Bear River Bridge	1972	0.609	12	4.3	2.8
France [Po1]	Saint Cloud Bridge	1975	1.1	20.4	2.25	9.1
Denmark [Po1]	Sallingsund Bridge	-	1.68	16	3.57	4.5
France [Po1]	B-3 South Viaduct	-	2	15.25	2.5-1.5	6.1, 10.2
Australia [Po1]	Captain Cook Bridge	1971	0.555	13.5	2.64	5.1
USA [Po1]	Zilwaukee Bridge	1987	2.46	21.6	2.4 -3.65	9, 5.9
USA [Po1]	Overstreet Bridge	-	0.808	13	3	4.3
USA [Pat]	The Chesapeake and Delaware Land Bridge	1995	1.417	17.88	3	6
USA [Sof]	Baldwin Bridge	1993	0.769	22.8-**26.3**	3.2, 1.9, 2.2	13.8-7.1
USA [Br3]	San Antonio 'Y' Segmental Bridge	1990	-	17.1-7.31	1.8, 2.4	9.3-3.0
Thailand [Ta1]	The Second stage Expressway System (SES)	1993	32.0	10.2	3.4	3
Thailand [Fi1]	The Bang Na Bridge Pli-Bang Pakong Expressway (BBBE)	2001	55.0	27.2	2.55	10.7
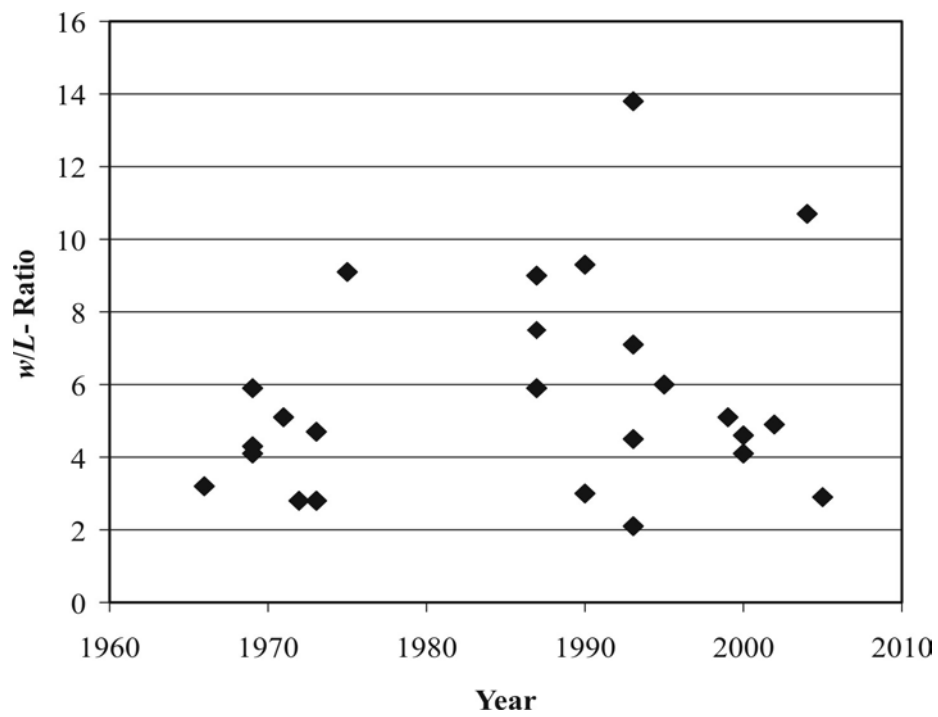
Figure A 1 Slenderness of segments (width to length ratio)

Appendix B

Finite element formulation using a variational method [Log]

By minimization of the following functional (analogous to the potential energy functional)

$$\pi_h = U + \Omega_Q + \Omega_q + \Omega_h \tag{B1}$$

where: $$U = \frac{1}{2}\iiint_v \left[\lambda_{xx}\left(\frac{\partial T}{\partial x}\right)^2 + \lambda_{yy}\left(\frac{\partial T}{\partial y}\right)^2 + \lambda_{zz}\left(\frac{\partial T}{\partial z}\right)^2 \right] dV \tag{B2}$$

$$\Omega_Q = -\iiint_v Q\,T\,dV \qquad \Omega_q = -\iint_{s2} q^*\,T\,dS \qquad \Omega_h = \frac{1}{2}\iint_{s3} \alpha_k (T - T_\infty)^2\,dS \tag{B3}$$

T	temperature
$\lambda_{xx}, \lambda_{yy}, \lambda_{zz}$	thermal conductivities
Q	rate of heat generated per unit volume

$S2$ and $S3$ are separate surfaces areas over which heat flow q^* and convection loss $\alpha_k\ (T-T_\infty)$ are specified.

We define the temperature functions T within each element in terms of the shape functions N_i and the nodal temperatures t_i as:

$$\{T\} = [N] \cdot \{t\} \tag{B4}$$

where $$\{t\}^T = \{t_1\ t_2\ t_3\ t_4 \dots t_i\} \tag{B5}$$

We define the temperature gradient/temperature and heat flux/temperature gradient relationships in a two dimensional space as:

$$\{g\} = \left\{ \begin{array}{c} \dfrac{\partial T}{\partial x} \\[2mm] \dfrac{\partial T}{\partial y} \end{array} \right\} \tag{B6}$$

the heat flux is given by:

$$\left\{ \begin{array}{c} q_x \\ q_y \end{array} \right\} = -[D] \cdot \{g\} \tag{B7}$$

where the material property matrix **D** is

$$[D] = \begin{bmatrix} \lambda_{xx} & 0 \\ 0 & \lambda_{yy} \end{bmatrix} \tag{B8}$$

using equations (B4) - (B8) in eq. (B2) and then using eq. (B1), π_h can be written in matrix form as

$$\pi_h = \frac{1}{2} \iiint_v \left[\{g\}^T [D] \{g\} \right] dV - \iiint_v \{t\}^T [N]^T Q \, dV$$

$$- \iint_{s_2} \{t\}^T [N]^T q^* dS + \frac{1}{2} \iint_{s_3} \alpha_k \cdot \left[\left(\{t\}^T [N]^T - T_\infty \right)^2 \right] \cdot dS \tag{B9}$$

using Eq. (A4) in Eq. (A6), we have

$$\{g\} = \begin{bmatrix} \dfrac{\partial N_1}{\partial x} & \dfrac{\partial N_2}{\partial x} & \cdots & \dfrac{\partial N_i}{\partial x} \\[2mm] \dfrac{\partial N_1}{\partial y} & \dfrac{\partial N_2}{\partial y} & \cdots & \dfrac{\partial N_i}{\partial y} \end{bmatrix} \begin{Bmatrix} t_1 \\ t_2 \\ t_3 \\ \vdots \\ t_i \end{Bmatrix} \tag{B10}$$

rewriting Eq. (A10) in compact matrix form, we have

$$\{g\} = [B]\{t\} \tag{B11}$$

$$\pi_h = \frac{1}{2} \{t\}^T \iiint_V [B]^T [D][B] \, dV \{t\} - \{t\}^T \iiint_V [N]^T Q \, dV - \{t\}^T \iint_{s_2} [N]^T q^* dS$$

$$+ \frac{1}{2} \iint_{s_3} \alpha_k \left[\{t\}^T [N]^T [N]\{t\} - \left(\{t\}^T [N]^T + [N]\{t\} \right) T_\infty + T_\infty^2 \right] dS \tag{B12}$$

on minimizing Eq. (B12) with respect to $\{t\}$, we obtain

$$\frac{\partial \pi_h}{\partial \{t\}} = \iiint_v [B]^T [D][B] \, dV \{t\} - \iiint_v [N]^T Q \, dV - \iint_{s_2} [N]^T q^* dS$$

$$+ \iint_{s_3} \alpha_k [N]^T [N] \, dS \{t\} - \iint_{s_3} [N]^T \alpha_k T_\infty dS = 0 \tag{B13}$$

simplifying Eq. (B13), we obtain

$$\left[\iiint_v [B]^T [D][B] \, dV + \iint_{s_3} \alpha_k [N]^T [N] \, dS \right] \{t\} = \{f_Q\} + \{f_q\} + \{f_h\} \tag{B14}$$

where the force matrices have been defined by

$$\{f_Q\} = \iiint_v [N]^T Q dV \qquad \{f_q\} = \iint_{s_2} [N]^T q^* dS \qquad \{f_h\} = \iint_s [N]^T \alpha_k T_\infty dS \tag{B15}$$

$$[k] = \iiint_v [B]^T [D][B] \, dV + \iint_{s_3} \alpha_k [N]^T [N] \, dS \tag{B16}$$

rewriting equation (B14) in compact matrix form, we have

$$\boxed{[k]\{t\} = \{f\}} \tag{B17}$$

One-Dimensional Finite Element [Log]

In the following the matrices and equations for a simple one-dimensional finite temperature element with 2 nodes will be presented. This element will later be used to estimate the temperature gradient during match casting.
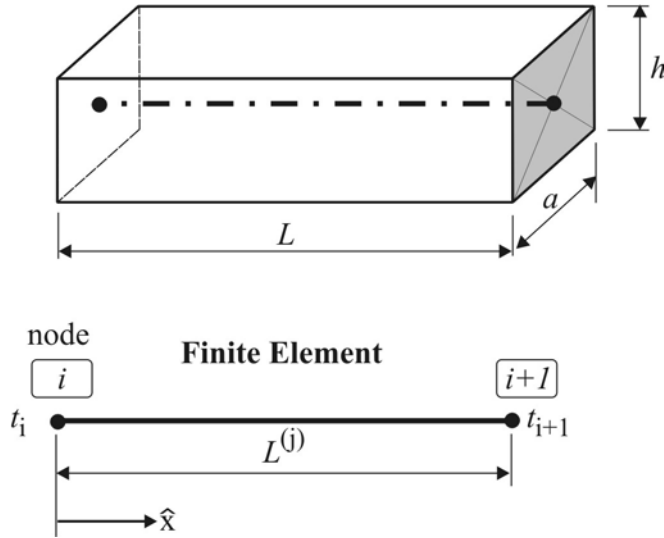

Figure B1 One-dimensional temperature element

The temperature distribution within the element (*j*) is approximated by the form functions.

$$T^{(j)} = N_1^{(j)} \cdot t_i + N_2^{(j)} \cdot t_{i+1} \qquad\qquad \{t\} = \begin{bmatrix} t_i & t_{i+1} \end{bmatrix} \qquad (B18)$$

$$N_1^{(j)} = 1 - \frac{\hat{x}}{L^{(j)}} \qquad\qquad N_2^{(j)} = \frac{\hat{x}}{L^{(j)}} \qquad \Longrightarrow \quad \begin{bmatrix} N^{(j)} \end{bmatrix} = \begin{bmatrix} 1 - \frac{\hat{x}}{L^{(j)}} & \frac{\hat{x}}{L^{(j)}} \end{bmatrix} \qquad (B19)$$

Temperature gradient :

$$\{g^{(j)}\} = \left\{ \frac{dT^{(j)}}{d\hat{x}} \right\} = \begin{bmatrix} B^{(j)} \end{bmatrix} \cdot \{t\} \qquad (B20)$$

$$\begin{bmatrix} B^{(j)} \end{bmatrix} = \left\{ \frac{dN_1^{(j)}}{d\hat{x}} \quad \frac{dN_2^{(j)}}{d\hat{x}} \right\} = \left\{ -\frac{1}{L^{(j)}} \quad \frac{1}{L^{(j)}} \right\} \qquad (B21)$$

Heat flux/temperature gradient:

$$q_x^{(j)} = [D] \cdot \{g^{(j)}\} \qquad \text{with } [D] = [\lambda_{xx}] \qquad (B22)$$

Element conduction matrix:

$$\left[k_c^{(j)}\right] = \iiint_v \left[B^{(j)}\right]^T [D]\left[B^{(j)}\right] dV = \int_0^{L^{(j)}} \begin{Bmatrix} -\dfrac{1}{L^{(j)}} \\ \dfrac{1}{L^{(j)}} \end{Bmatrix} [\lambda_{xx}] \begin{bmatrix} -\dfrac{1}{L^{(j)}} & \dfrac{1}{L^{(j)}} \end{bmatrix} \cdot A_c \, dx \tag{B23}$$

$$\left[k_c^{(j)}\right] = \frac{A_c \cdot \lambda_{xx}}{L^{(j)}} \begin{bmatrix} 1 & -1 \\ -1 & 1 \end{bmatrix} \tag{B24}$$

convection part of the element matrix:

$$\left[k_\alpha^{(j)}\right] = \iint_{s_3} \alpha_k \left[N^{(j)}\right]^T \left[N^{(j)}\right] dS = \alpha_k \cdot P \int_0^{L^{(j)}} \begin{Bmatrix} 1 - \dfrac{\hat{x}}{L^{(j)}} \\ \dfrac{\hat{x}}{L^{(j)}} \end{Bmatrix} \cdot \begin{bmatrix} 1 - \dfrac{\hat{x}}{L^{(j)}} & \dfrac{\hat{x}}{L^{(j)}} \end{bmatrix} d\hat{x} + \alpha_k \cdot A_c \cdot \begin{bmatrix} 1 & 0 \\ 0 & 0 \end{bmatrix} + \alpha_k \cdot A_c \cdot \begin{bmatrix} 0 & 0 \\ 0 & 1 \end{bmatrix} \tag{B25}$$

Please note that the above equation is only valid, if the convection is constant over the whole perimeter of the element. If not, P has to be replaced by the width a and the height h of the member. The last two terms represent the convection on the left and right face of the element. This part has to be neglected if there is no convection e.g. no temperature gradient. The convection coefficient α_T in the above equation has to be substituted by the convection coefficient k if the member is covered by formwork or other insulation materials.

$$\left[k_\alpha^{(j)}\right] = \frac{\alpha_k \cdot P \cdot L^{(j)}}{6} \cdot \begin{bmatrix} 2 & 1 \\ 1 & 2 \end{bmatrix} + \alpha_k \cdot A_c \cdot \begin{bmatrix} 1 & 0 \\ 0 & 0 \end{bmatrix} + \alpha_k \cdot A_c \cdot \begin{bmatrix} 0 & 0 \\ 0 & 1 \end{bmatrix} \tag{B26}$$

The force matrix terms are:

$$\left\{f_Q^{(j)}\right\} = \iiint_v \left[N^{(j)}\right]^T Q^{(j)} \, dV = Q^{(j)} \cdot A_c \int_0^{L^{(j)}} \begin{Bmatrix} 1 - \dfrac{\hat{x}}{L^{(j)}} \\ \dfrac{\hat{x}}{L^{(j)}} \end{Bmatrix} dx = \frac{Q^{(j)} \cdot A_c \cdot L^{(j)}}{2} \cdot \begin{Bmatrix} 1 \\ 1 \end{Bmatrix} \tag{B27}$$

$$\left\{f_q^{(j)}\right\} = \iint_{s_2} [N]^T q^* \, dS = q^* \cdot P \int_0^{L^{(j)}} \begin{Bmatrix} 1 - \dfrac{\hat{x}}{L^{(j)}} \\ \dfrac{\hat{x}}{L^{(j)}} \end{Bmatrix} d\hat{x} = \frac{q^{*(j)} \cdot P \cdot L^{(j)}}{2} \cdot \begin{Bmatrix} 1 \\ 1 \end{Bmatrix} \tag{B28}$$

$$\left\{f_h^{(j)}\right\} = \iint_{s_3} \alpha_k \cdot T_\infty \left[N^{(j)}\right]^T dS = \frac{\alpha_k \cdot T_\infty \cdot P \cdot L^{(j)}}{2} \cdot \begin{Bmatrix} 1 \\ 1 \end{Bmatrix} \tag{B29}$$

$$\left\{f^{(j)}\right\} = 0.5 \cdot L^{(j)} \cdot \left(Q^{(j)} \cdot A_c + q^{*(j)} \cdot P + \alpha_k \cdot T_\infty \cdot P\right) \cdot \begin{Bmatrix} 1 \\ 1 \end{Bmatrix} \tag{B30}$$

Time dependant heat transfer in one dimension [Log]

The governing equations can be derived from equations B1 to B3 if the Q term is replaced by $Q - c \cdot \rho \cdot \dot{T}$ and one dimension is considered only. $\dot{T}$ is the time derivative of the temperature field.

$$\pi_h = \frac{1}{2} \iiint_v \left[\lambda_{xx} \left(\frac{\partial T}{\partial x} \right)^2 - 2 \left(Q - c \cdot \rho \cdot \dot{T} \right) \cdot T \right] dV - \iint_{S_2} q^* T \, dS + \frac{1}{2} \iint_{S_3} \alpha_k (T - T_\infty)^2 \, dS \qquad \text{(B31)}$$

Minimization of the above equation with respect to the nodal temperature results in an additional term $\left[\hat{m} \right]$.

$$\left[\hat{m}^{(j)} \right] = \iiint_v c \cdot \rho \cdot \left[N^{(j)} \right]^T \left[N^{(j)} \right] dV = c \cdot \rho \cdot A_c \int_0^{L^{(j)}} \left\{ \begin{array}{c} 1 - \dfrac{\hat{x}}{L^{(j)}} \\ \dfrac{\hat{x}}{L^{(j)}} \end{array} \right\} \cdot \left[1 - \dfrac{\hat{x}}{L^{(j)}} \quad \dfrac{\hat{x}}{L^{(j)}} \right] d\hat{x} \qquad \text{(B32)}$$

$$\left[\hat{m}^{(j)} \right] = \frac{c \cdot \rho \cdot A_c \cdot L^{(j)}}{6} \cdot \begin{bmatrix} 2 & 1 \\ 1 & 2 \end{bmatrix} \qquad \text{(B33)}$$

The global equilibrium is as:

$$\{F\} = [K]\{T\} + [M]\{\dot{T}\} \qquad \text{(B34)}$$

Substitution the time derivative of the temperature by : $\underline{\dot{T}}_{i+1} = \dfrac{\underline{T}_{i+1} - \underline{T}_i}{\Delta t} \qquad \text{(B35)}$

one gets:

$$\left(\frac{1}{\Delta t} \underline{M} \right) \underline{T}_{i+1} = \left[\frac{1}{\Delta t} \underline{M} - \underline{K} \right] \underline{T}_i + \underline{F}_i \qquad \text{(B36)}$$

Appendix C

Creep and shrinkage according to German Code DIN 1045-1 and [Da1]

$$\varphi(t,t_0) = \varepsilon_{cc}(t,t_0) \cdot \frac{E_{c0}}{\sigma_c(t_0)}$$

a) Creep coefficient

$$\varphi(t,t_0) = \varphi_0 \cdot \beta_c(t-t_0) \tag{C1}$$

where, $\varphi_0 = \varphi_{RH} \cdot \beta(f_{cm}) \cdot \beta(t_0)$ $\tag{C2}$

by considering the relative humidity

$$\varphi_{RH} = \left[1 + \frac{1-(RH/100)}{\sqrt[3]{0.1 \cdot h_0 / h_1}} \cdot \alpha_1\right] \cdot \alpha_2 \tag{C3}$$

by considering the effect of concrete strength

$$\beta(f_{cm}) = \frac{16.8}{\sqrt{f_{cm}}} \tag{C4}$$

with $f_{cm} = f_{ck} + 8 N/mm^2$

by considering the old of the concrete at beginning of loading

$$\beta(t_0) = \frac{1}{0.1 + \left(t_{0,eff}/t_1\right)^{0.2}} \tag{C5}$$

$$t_{0,eff} = t_0 \cdot \left(\frac{9}{2+(t_0/t_1)^{1.2}} + 1\right)^{\alpha} \geq 0.5 \, \text{days}$$

$$\beta_c(t-t_0) = \left(\frac{t-t_0/t_1}{\beta_H + (t-t_1)/t_1}\right)^{0.3} \tag{C6}$$

by considering the cross-sectional area

$$\beta_H = 150 \cdot \left[1 + \left(1.2 \cdot \frac{RH}{100}\right)^{18}\right] \cdot \frac{h_0}{h_1} + 250 \cdot \alpha_3 \leq 1500 \cdot \alpha_3 \tag{C7}$$

with $h_0 = 2 A_c / u$

A_c cross-section

u circumference of cross section

considering the effect of the cement type:

the effect of the cement type on the behavior of the concrete creep will

be considered during the modification of the concrete age t_0

$$t_{0,eff} = t_0 \cdot \left(\frac{9}{2 + (t_0/t_1)^{1.2}} + 1 \right)^{\alpha} \geq 0.5 \, \text{days} \tag{C8}$$

the following factors for considering the concrete strength:

$$\alpha_1 = \left[\frac{35}{f_{cm}} \right]^{0.7} \quad \alpha_2 = \left[\frac{35}{f_{cm}} \right]^{0.2} \quad \alpha_3 = \left[\frac{35}{f_{cm}} \right]^{0.5} \tag{C9}$$

where: t the time of applying load

       t_0 the time of the beginning of loading

       t_1 $= 1 \, day$

       RH humidity

       h_1 $= 100 \, mm$

       f_{cm} mean compressive strength of concrete $f_{cm} = f_{ck} + 8 \, N/mm^2$

b) Shrinkage strain

The shrinkage strain is expressed as:

$$\varepsilon_{cs}(t) = \varepsilon_{cas}(t) + \varepsilon_{cds}(t, t_s) \tag{C10}$$

the autogenous shrinkage strain is given as:

$$\varepsilon_{cas}(t) = \varepsilon_{cas0}(f_{cm}) \cdot \beta_{as}(t) \tag{C11}$$

the drying shrinkage strain is given as:

$$\varepsilon_{cds}(t) = \varepsilon_{cds0}(f_{cm}) \cdot \beta_{RH}(RH) \cdot \beta_{ds}(t - t_s) \tag{C12}$$

$$\varepsilon_{cas0}(f_{cm}) = \alpha_{as} \cdot \left(\frac{f_{cm}}{60 + f_{cm}} \right)^{2.5} \cdot 10^{-6} \tag{C12}$$

$$\beta_{as}(t) = 1 - \exp\left(-0.2\sqrt{t/t_1} \right) \tag{C13}$$

$$\varepsilon_{cds0} = \left[(220 + 110 \cdot \alpha_{ds1}) \cdot \exp\left(-\alpha_{ds2} \cdot \frac{f_{cm}}{10} \right) \right] \cdot 10^{-6} \tag{C14}$$

$$\beta_{RH}(RH) = \begin{cases} -1.55 \cdot \left[1 - \left(\frac{RH}{100} \right)^3 \right] & \text{for} \quad 40\% \leq RH < 99\% \cdot \beta_{s1} \\ & \text{for} \quad RH \geq 99\% \cdot \beta_{s1} \\ 0.25 \end{cases} \tag{C15}$$

$$\beta_{ds}(t - t_s) = \left[\frac{(t - t_s)/t_1}{350 \times (h_\circ/h_1)^2 + (t - t_s)/t_1} \right]^{0.5} \tag{C16}$$

$$\beta_{ds}\left(t-t_s\right)=\left[\frac{\left(t-t_s\right)/t_1}{350\times\left(h_\circ/h_1\right)^2+\left(t-t_s\right)/t_1}\right]^{0.5} \tag{C16}$$

$$\beta_{sl}=\left[\frac{35}{f_{cm}}\right]^{0.1}\le1.0 \tag{C17}$$

The values of α_{ds1} and α_{ds2} are listed in Table C.1

Table C.1 Cement coefficient for concrete shrinkage model [Da1]

	cement type	α	α_{as}	α_{ds1}	α_{ds2}
Slowly hardening cements (S)	SL	-1	800	3	0.13
Normal or rapidly hardening cements (N)	N, R	0	700	4	0.12
Rapidly hardening high strength cements (R)	RS	1	600	6	0.12
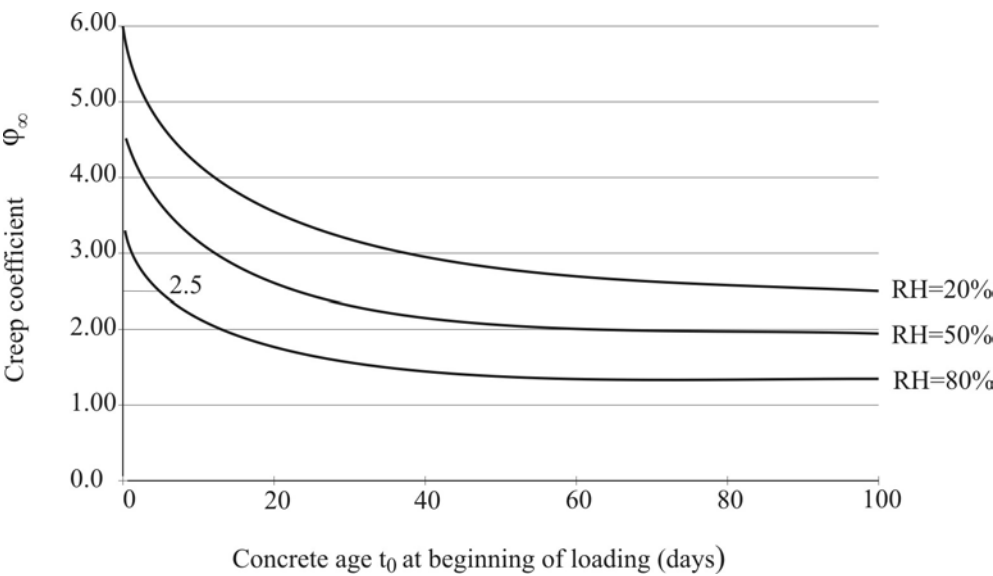
Figure C1   Coefficient of creep φ_∞ in relation to to the relative humidity and the age of the concrete at time of loading [EC2]
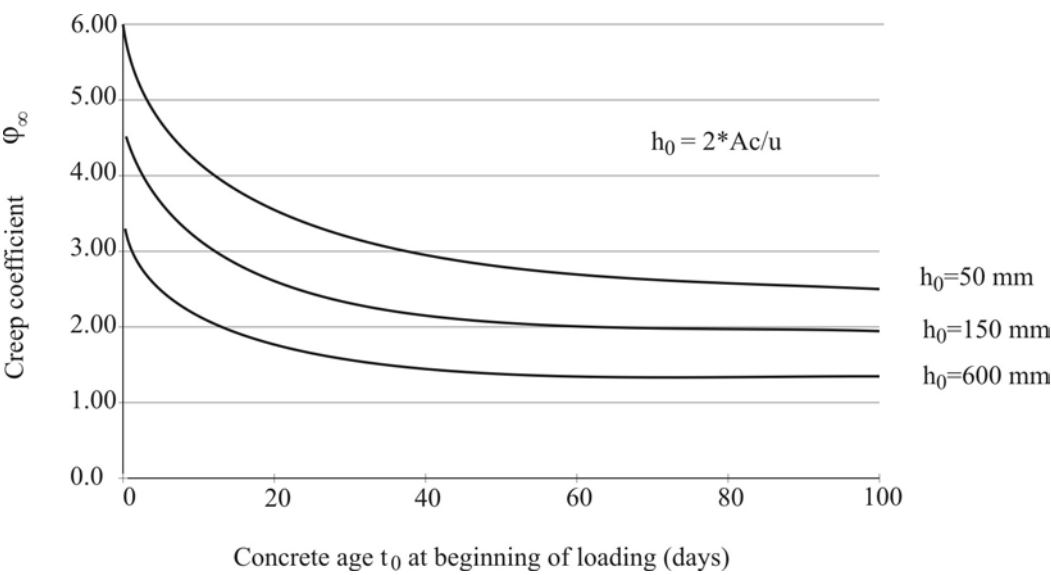

Figure C2   Coefficient of creep φ_∞ in relation to h_o and the age of the concrete at time of loading [EC2]
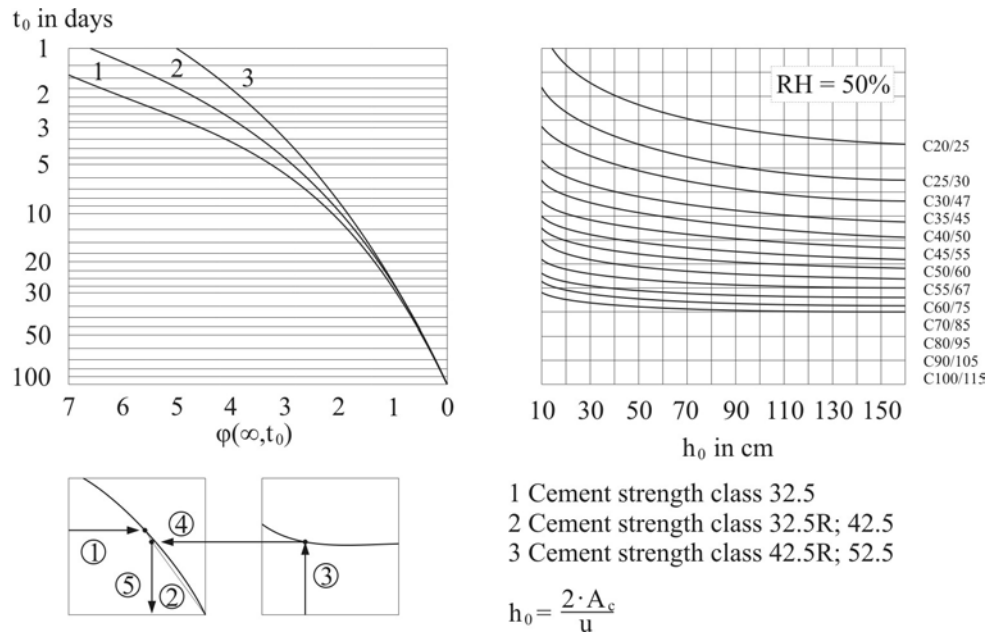
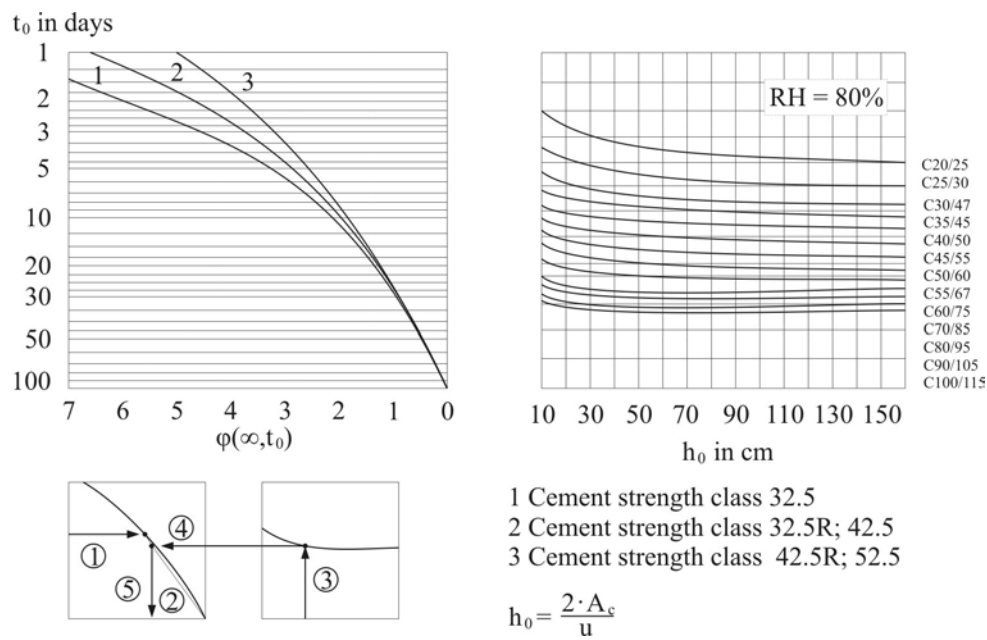**Figure C3**   Coefficient of creep at time infinity φ_∞ for a relative humidity of RH = 50 %
[DIN 1045-1]

Figure C4   Coefficient of creep at time infinity φ_∞ for a relative humidity RH = 80 %
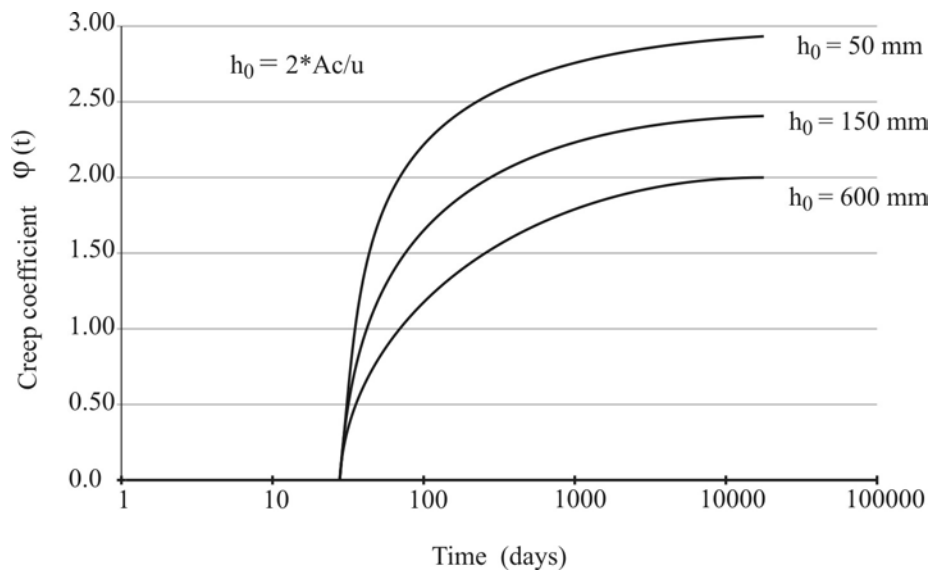[DIN 1045-1]

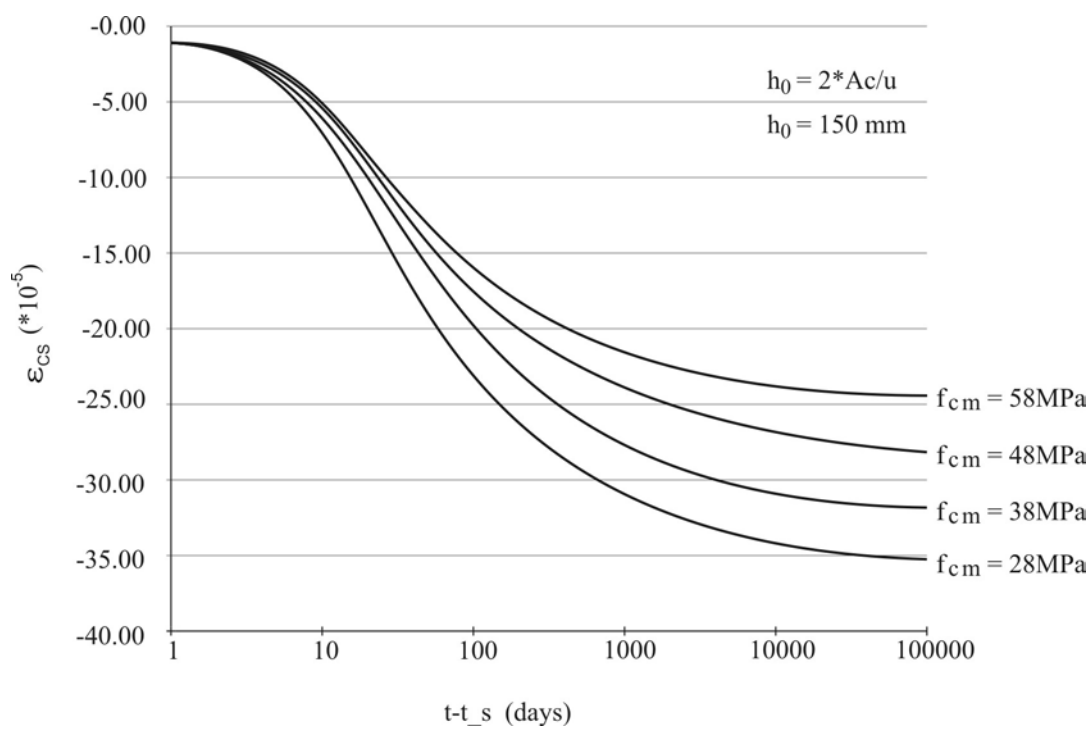**Figure C5**   Coefficient of creep $\varphi(t)$ versus time for different h_o [EC2]

Figure C6   Shrinkage value $\varepsilon_{cs}(t)$ versus time of start of l shrinkage for different concrete compressive strength [EC2]
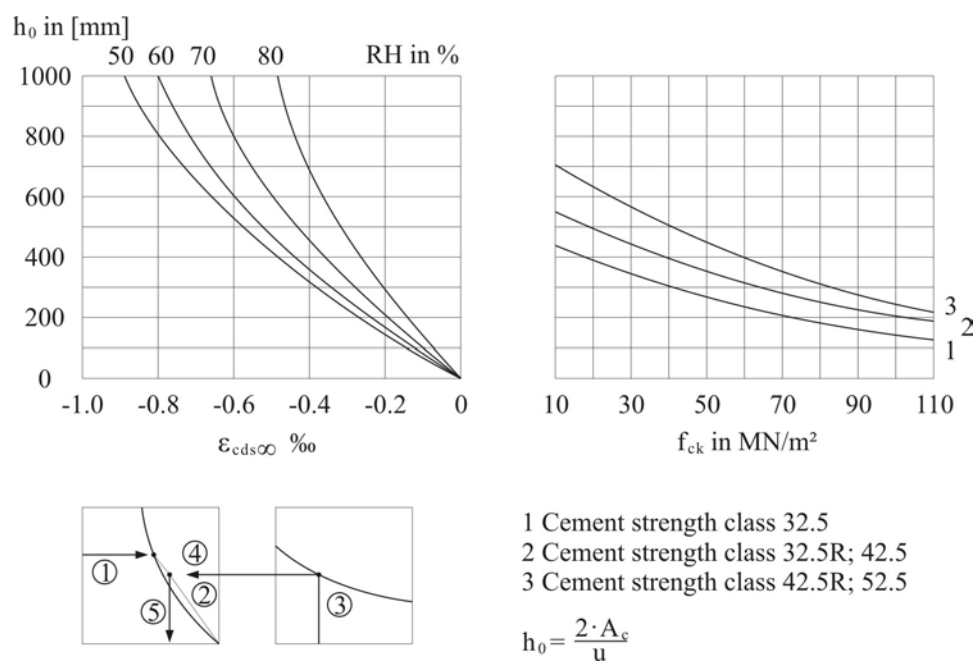
Figure C7   Shrinkage at time infinity $\varepsilon_{cds,\infty}$ [DIN 1405-1]

Verification of creep model used in the ANSYS analysis

Structure: $b\,/\,t\,/\,L = 5.0\,/\,1.0\,/\,10.0\ m$

$E_c = 43{,}000\ MPa$

Creep coefficient: $\varphi_\infty = 2.5$

Constant loading: $F_{ges} = 20 \cdot 5 = 100\ MN$

$$\varepsilon_{elastic} = \frac{\Delta l_{elastic}}{L}$$

$$\Delta l_{elastic} = \frac{F_{ges} \cdot L}{A_c \cdot E_c} = \frac{100 \cdot 10}{(5 \cdot 1) \cdot 43000} = 4.65 \cdot 10^{-3}\ m$$

$$\varepsilon_{creep} = \varepsilon_{elastic} \cdot \phi_{creep}$$

$$\varepsilon_{creep(\infty)} = \frac{4.65 \cdot 10^{-3}}{10} \cdot 2.5 = 1.16 \cdot 10^{-3}$$

$$\Delta l_{creep(\infty)} = \varepsilon_{creep(\infty)} \cdot L = 1.165 \cdot 10^{-3} \cdot 10 = 0.0116\ m$$

$$\Delta l_{total(\infty)} = \Delta l_{elastic} + \Delta l_{creep(\infty)} = 4.65 \cdot 10^{-3}\ m + 0.0116\ m$$
$$= 0.0162\ m$$

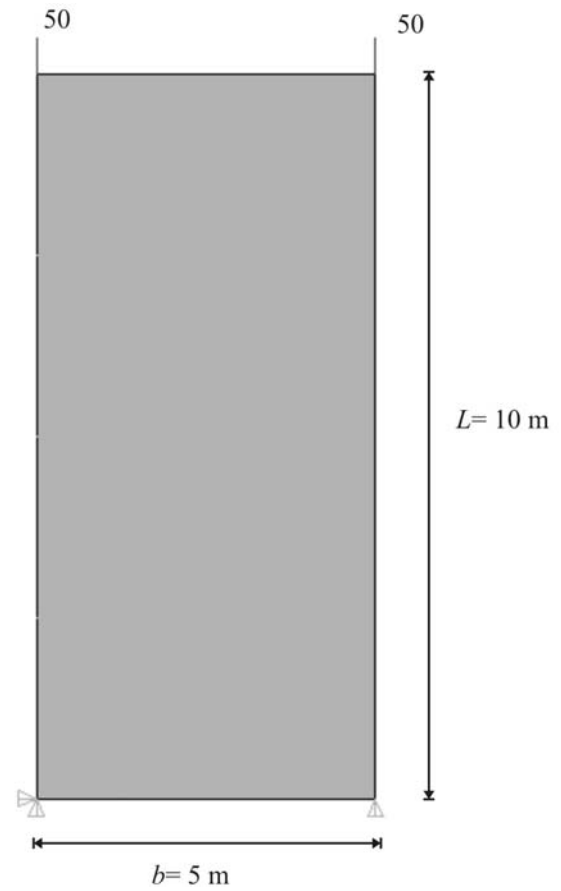numerical value: $\Delta l_{total(\infty)} = 0.0148\ m$

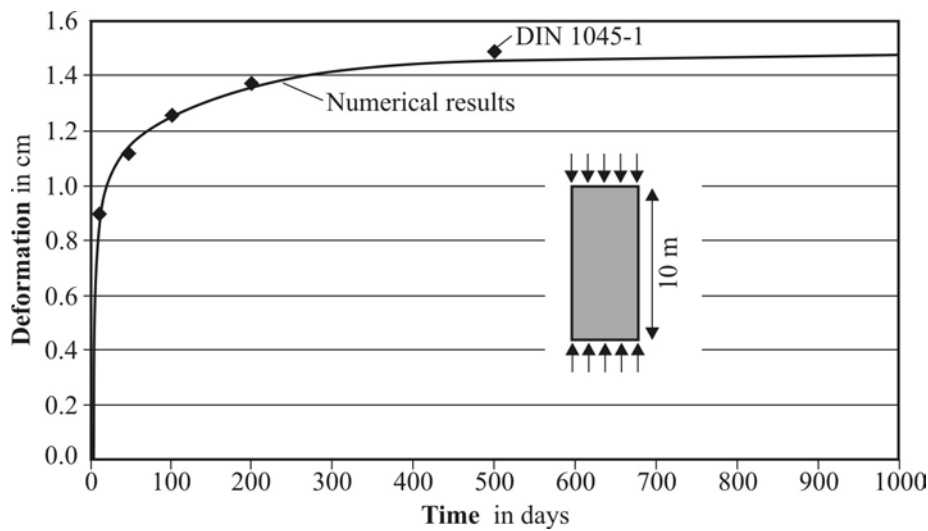**Figure C1** Example to verify numerical creep analysis

Figure C2 Creep deformation - ANSYS results versus German Code

Appendix D

Time dependant temperature distribution in a slab

The time dependant temperature distribution in a deck slab of a segment during match casting will be estimated in the following by simple analysis. The middle strip of the slab is taken as an equivalent system to reduce the problem to one dimension only.
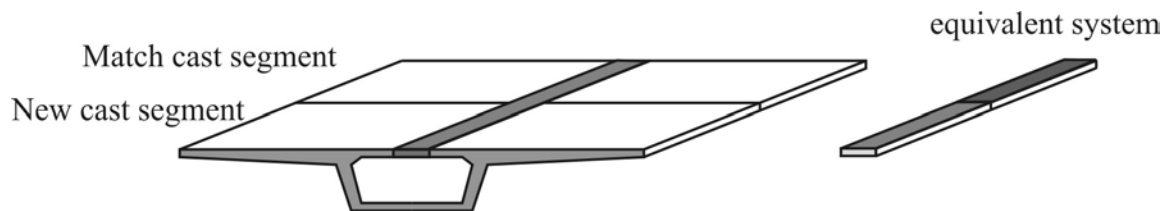

Figure D1 Equivalent system

The same parameters as in the finite element analysis are used (see table 3.2).

Table D 1 Heat transfer coefficients

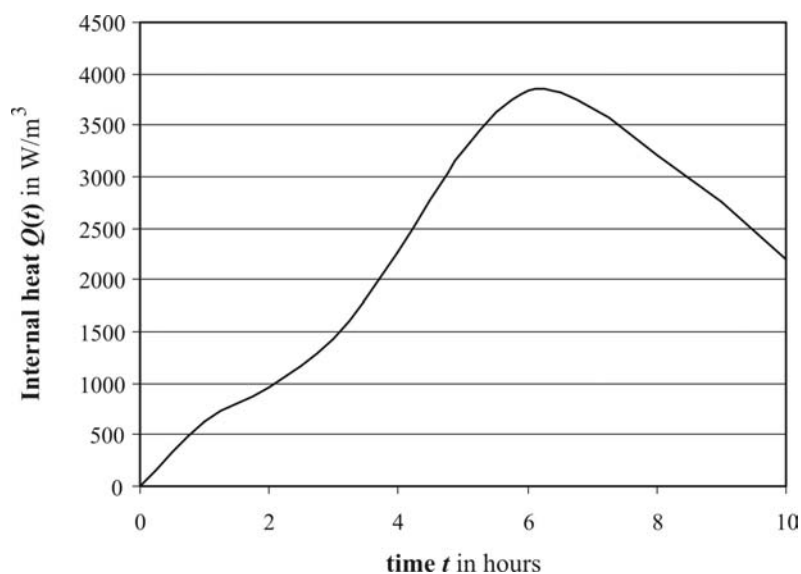|			
Thermal Conductivity Coefficient	$\lambda =$	2.65	$\left[W\,/(m\;^oC)\right]$
Specific Heat	$c =$	1128	$\left[W\;s\,/(kg\;^oC)\right]$
Convection Coefficient	$k\,/\alpha_k =$	2.59 /5.8[1]	$\left[W\,/(m^2\;^oC)\right]$
Concrete Density	$\rho =$	2,340	$\left[kg\,/\,m^3\right]$

[1] with / without formwork

Figure D2 Internal heat Q(t) over time

The finite element method is used for the analysis. The relevant equations has been derived in chapter B2.

global equilibrium:

$$\left(\frac{1}{\Delta t}\underline{M}\right)\underline{T}_{i+1} = \left[\frac{1}{\Delta t}\underline{M} - \underline{K}\right]\underline{T}_i + \underline{F}_i$$

element matrix:

$$k^{(j)} = \frac{A_c\lambda}{L^{(j)}}\begin{bmatrix} 1 & -1 \\ -1 & 1 \end{bmatrix} + \frac{\alpha_k P L^{(j)}}{6}\begin{bmatrix} 2 & 1 \\ 1 & 2 \end{bmatrix} + \iint \alpha_k \left[N^{(j)}\right]^T\left[N^{(j)}\right]dS$$

specific heat matrix:

$$m = \frac{c\rho A L_i}{6}\begin{bmatrix} 2 & 1 \\ 1 & 2 \end{bmatrix}$$

internal heat vector:

$$f = \frac{Q A_c L_i}{2}\begin{Bmatrix} 1 \\ 1 \end{Bmatrix}$$

The system is modelled by 6 elements whereby 3 elements represent the new segment and 3 the old match cast segment. The length of the elements has been chosen with regard to the high temperature gradient in the joint region. The finite element analysis and the measurements showed that the temperature in the match-cast segment decreased to the ambient temperature over a distance of ≈ 1 m from the joint.

The fresh concrete in the bottom face of the slab is covered by formwork. Convection takes only place at the top and bottom surfaces of the member and on the left side as the equivalent system is a part of the whole slab.
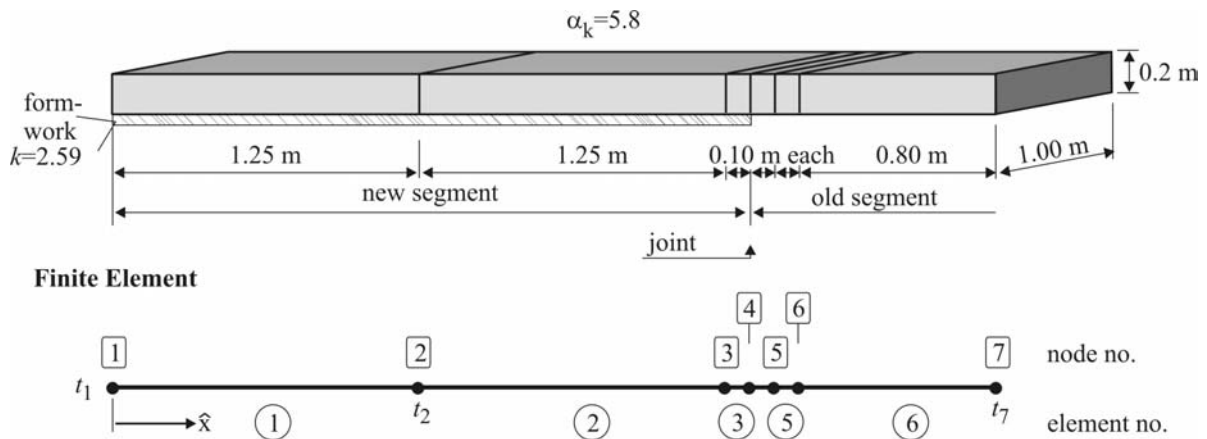

Figure D3 System and finite element model

$$\frac{1}{\Delta t}[m]_1 = \frac{1}{\Delta t}[m]_2 = \frac{c\rho A L_i}{6}\begin{bmatrix} 2 & 1 \\ 1 & 2 \end{bmatrix} = \frac{1128\cdot 2340\cdot 0.2\cdot 1.25}{3600\cdot 6}\begin{bmatrix} 2 & 1 \\ 1 & 2 \end{bmatrix} = \begin{bmatrix} 61.10 & 30.55 \\ 30.55 & 61.10 \end{bmatrix}$$

$$\frac{1}{\Delta t}[m]_3 = \frac{1}{\Delta t}[m]_4 = \frac{1}{\Delta t}[m]_5 = \frac{1128\cdot 2340\cdot 0.2\cdot 0.10}{3600\cdot 6}\begin{bmatrix} 2 & 1 \\ 1 & 2 \end{bmatrix} = \begin{bmatrix} 4.89 & 2.44 \\ 2.44 & 4.89 \end{bmatrix}$$

$$\frac{1}{\Delta t}[m]_6 = \frac{1128\cdot 2340\cdot 0.2\cdot 0.80}{3600\cdot 6}\begin{bmatrix} 2 & 1 \\ 1 & 2 \end{bmatrix} = \begin{bmatrix} 39.10 & 19.55 \\ 19.55 & 39.10 \end{bmatrix}$$

$$\frac{1}{\Delta t}[\underline{M}] = \begin{bmatrix} 61.10 & 30.55 & & & & & \\ 30.55 & 122.20 & 30.55 & & & & \\ & 30.55 & 65.99 & 2.44 & & & \\ & & 2.44 & 9.78 & 2.44 & & \\ & & & 2.44 & 9.78 & 2.44 & \\ & & & & 2.44 & 43.99 & 19.55 \\ & & & & & 19.55 & 39.10 \end{bmatrix}$$

$$[k]_1 = \frac{0.2\cdot 2.65}{1.25}\begin{bmatrix} 1 & -1 \\ -1 & 1 \end{bmatrix} + \frac{5.8\cdot 2\cdot 1.25}{6}\cdot\begin{bmatrix} 2 & 1 \\ 1 & 2 \end{bmatrix} + 2.59\cdot 0.2\begin{bmatrix} 1 & 0 \\ 0 & 0 \end{bmatrix} = \begin{bmatrix} 5.78 & 1.99 \\ 1.99 & 5.26 \end{bmatrix}$$

$$[k]_2 = \frac{0.2\cdot 2.65}{1.25}\begin{bmatrix} 1 & -1 \\ -1 & 1 \end{bmatrix} + \frac{5.8\cdot 2\cdot 1.25}{6}\cdot\begin{bmatrix} 2 & 1 \\ 1 & 2 \end{bmatrix} = \begin{bmatrix} 5.26 & 1.99 \\ 1.99 & 5.26 \end{bmatrix}$$

$$[k]_3 = [k]_4 = [k]_5 = \begin{bmatrix} 5.30 & -5.30 \\ -5.30 & 5.30 \end{bmatrix} + \begin{bmatrix} 0.39 & 0.19 \\ 0.19 & 0.39 \end{bmatrix} = \begin{bmatrix} 5.69 & -5.11 \\ -5.11 & 5.69 \end{bmatrix}$$

$$[k]_6 = \frac{0.2\cdot 2.65}{0.80}\begin{bmatrix} 1 & -1 \\ -1 & 1 \end{bmatrix} + \frac{5.8\cdot 2\cdot 0.80}{6}\cdot\begin{bmatrix} 2 & 1 \\ 1 & 2 \end{bmatrix} = \begin{bmatrix} 3.76 & 0.88 \\ 0.88 & 3.76 \end{bmatrix}$$

$$[\underline{K}] = \begin{bmatrix} 5.78 & 1.99 & & & & & \\ 1.99 & 10.51 & 1.99 & & & & \\ & 1.99 & 10.94 & -5.11 & & & \\ & & -5.11 & 11.37 & -5.11 & & \\ & & & -5.11 & 11.37 & -5.11 & \\ & & & & -5.11 & 9.44 & 0.88 \\ & & & & & 0.88 & 3.76 \end{bmatrix}$$

$$\left[\underline{\frac{1}{\Delta t}M - K}\right] = \begin{bmatrix} 55.32 & 28.56 & & & & & \\ 28.56 & 111.69 & 28.56 & & & & \\ & 28.56 & 55.04 & 7.55 & & & \\ & & 7.55 & -1.60 & 7.55 & & \\ & & & 7.55 & -1.60 & 7.55 & \\ & & & & 7.55 & 34.55 & 18.67 \\ & & & & & 18.67 & 35.35 \end{bmatrix}$$

$$[f]_1 = [f]_2 = \frac{Q \cdot A_c \cdot L_i}{2}\begin{bmatrix}1\\1\end{bmatrix} = \frac{623.2 \times 0.2 \times 1.25}{2}\begin{bmatrix}1\\1\end{bmatrix} = \begin{bmatrix}78\\78\end{bmatrix}$$

$$[f]_3 = \frac{Q \cdot A_c \cdot L_i}{2}\begin{bmatrix}1\\1\end{bmatrix} = \frac{623.2 \times 0.2 \times 0.1}{2}\begin{bmatrix}1\\1\end{bmatrix} = \begin{bmatrix}6.2\\6.2\end{bmatrix}$$

$$[f]_4 = [f]_5 = [f]_6 = 0$$

Time step 1 ($\Delta t = 1$ h):

$$\left(\frac{1}{\Delta t}M\right)\underline{T}_{i+1} = \left[\frac{1}{\Delta t}M - K\right]\underline{T}_i + \underline{F}_i \quad \text{with} \quad \underline{T}_0 = 0$$

$$\begin{bmatrix} 61.1 & 30.55 & & & & & \\ 30.55 & 122.2 & 30.55 & & & & \\ & 30.55 & 65.99 & 2.44 & & & \\ & & 2.44 & 9.78 & 2.44 & & \\ & & & 2.44 & 9.78 & 2.44 & \\ & & & & 2.44 & 43.99 & 19.55 \\ & & & & & 19.55 & 39.10 \end{bmatrix} \cdot \begin{Bmatrix} t_1 \\ t_2 \\ t_3 \\ t_4 \\ t_5 \\ t_6 \\ t_7 \end{Bmatrix} = \begin{Bmatrix} 77.9 \\ 155.8 \\ 84.1 \\ 6.2 \\ 0.0 \\ 0.0 \\ 0.0 \end{Bmatrix}$$

$t_1 = 0.9 \qquad t_2 = 0.8 \qquad t_3 = 0.9 \qquad t_4 = 0.4 \qquad t_5 = -0.1 \qquad t_6 = 0.0 \qquad t_7 = 0.0$

Time step 2 ($\Delta t = 2\ h$)**:**

$$
\begin{bmatrix}
61.10 & 30.55 & & & & & \\
30.55 & 122.20 & 30.55 & & & & \\
& 30.55 & 65.99 & 2.44 & & & \\
& & 2.44 & 9.78 & 2.44 & & \\
& & & 2.44 & 9.78 & 2.44 & \\
& & & & 2.44 & 43.99 & 19.55 \\
& & & & & 19.55 & 39.10
\end{bmatrix}
\cdot
\begin{Bmatrix}
t_1 \\ t_2 \\ t_3 \\ t_4 \\ t_5 \\ t_6 \\ t_7
\end{Bmatrix}
=
$$

$$
\begin{bmatrix}
55.32 & 28.56 & & & & & \\
28.56 & 111.69 & 28.56 & & & & \\
& 28.56 & 55.04 & 7.55 & & & \\
& & 7.55 & -1.60 & 7.55 & & \\
& & & 7.55 & -1.60 & 7.55 & \\
& & & & 7.55 & 34.55 & 18.67 \\
& & & & & 18.67 & 35.35
\end{bmatrix}
\cdot
\begin{Bmatrix}
0.9 \\ 0.8 \\ 0.9 \\ 0.4 \\ -0.1 \\ 0.0 \\ 0.0
\end{Bmatrix}
+
\begin{Bmatrix}
119.3 \\ 238.5 \\ 128.8 \\ 9.5 \\ 0.0 \\ 0.0 \\ 0.0
\end{Bmatrix}
=
\begin{Bmatrix}
190.5 \\ 382.0 \\ 204.0 \\ 14.5 \\ 3.6 \\ -0.7 \\ 0.0
\end{Bmatrix}
$$

$t_1 = 2.1 \qquad t_2 = 2.1 \qquad t_3 = 2.1 \qquad t_4 = 0.9 \qquad t_5 = 0.2 \qquad t_6 = 0.0 \qquad t_7 = 0.0$

In the following time steps the vectors $\underline{T}_i$ and $\underline{F}_i$ are changing only. Thus the analysis becomes very easy.

The results of the temperature distribution over time is summarized in the following table.

Table D 2 Temperature distribution over time

time	node 1	node 2	node 3	node 4	node 5	node 6	node 7
0 h	0.0	0.0	0.0	0.0	0.0	0.0	0.0
1 h	0.9	0.8	0.9	0.4	-0.1	0.0	0.0
2 h	2.1	2.1	2.1	0.9	0.1	0.0	0.0
3 h	3.8	3.9	3.8	2.1	0.2	0.0	0.0
4 h	6.6	6.7	6.5	3.2	0.8	0.0	0.0
5 h	10.4	10.7	10.2	5.6	0.9	0.1	0.0
6 h	14.7	15.2	14.3	7.4	2.4	0.1	0.0
7 h	18.3	19.2	17.6	10.4	2.7	0.4	-0.2
8 h	21.0	22.2	20.0	11.0	5.0	0.5	-0.3
9 h	22.8	24.5	21.4	13.9	4.3	1.2	-0.6
10 h	23.7	25.8	22.1	12.4	7.6	1.3	-0.6
				joint			

It should be noted that the size of the elements in the joint region in the previous example should be greater than 10 *cm*, otherwise numerical instabilities occur (see Fig. D 4, t_4 and t_5 curves). On the other hand, the temperature gradient in the match-cast segment is nearly independent of the element size in the joint region as the parametric studies have shown (Fig. D 6).
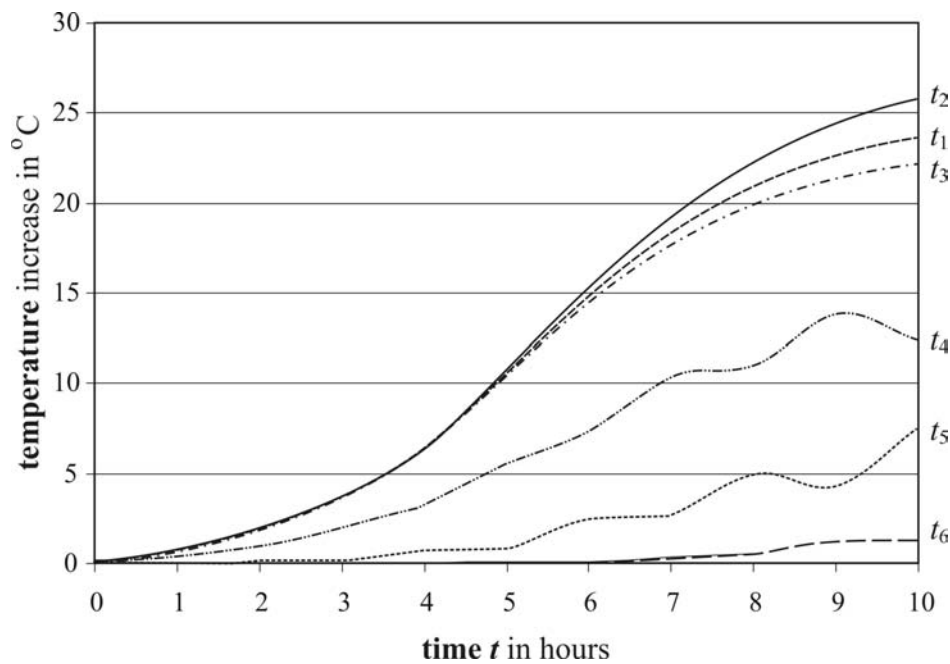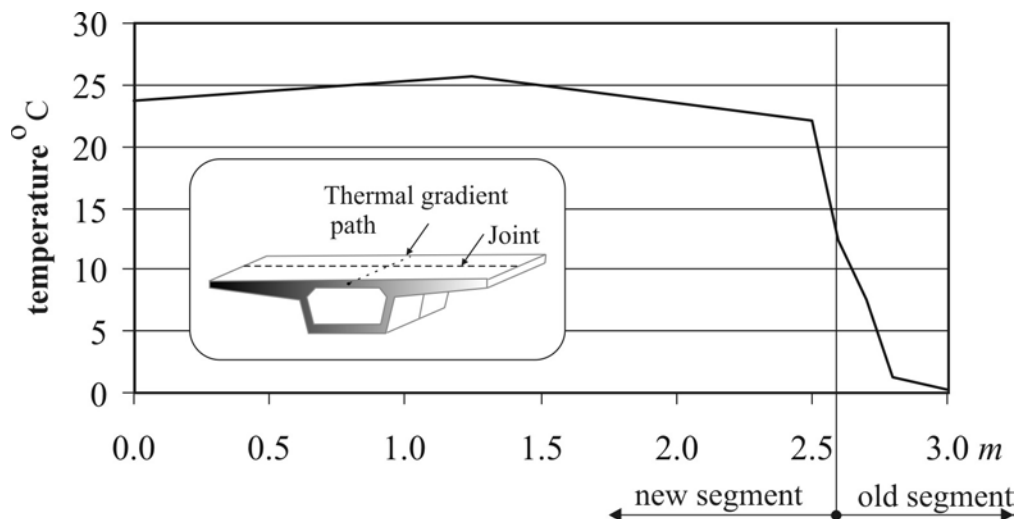
Figure D 4 Temperature distribution over time

Figure D 5 Temperature gradient after 10 *h*

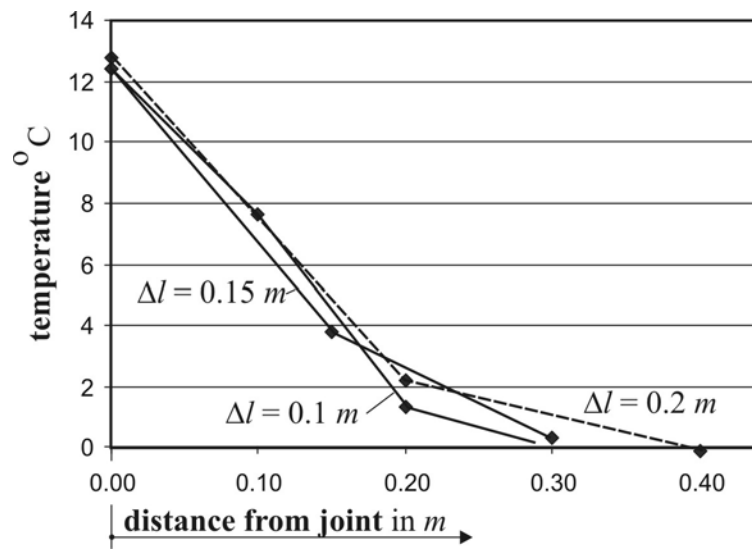**Figure D 6** Temperature gradient after 10 *h* for different element lengths

Lebenslauf

Persönliche Daten

Name: Ra'ed Abendeh

Geburtstag: 24.02.1975

Geburtsort: Irbid- Jordanien

Familienstand: Ledig

Staatsangehörigkeit: Jordanien

Schulausbildung

1981-1987   Abdel Rahman Schule in Irbid- Jordanien

1987-1993   Al-Ameer Hasan Schule in Irbid- Jordanien

Studium an der Jordan University of Science and Technology (Irbid, Jordanien)

1993-1998   Hochschulabschluss im Bauingenieurwesen

Abschluss: Bachelor- Ingenieur

(Degree of Bachelor of Science in Civil Engineering with a

specialization in Structural)

1998-2001   Abschluss: M.Sc.-Ingenieur

(Degree of Master of Science in Civil Engineering with a

specialization in Structural)

Berufliche Tätigkeit

08/2002-11/2005   Wissenschaftlicher Mitarbeiter im Institut für Massivbau der

Technischen Universität Hamburg-Harburg